Carderock Division
Naval Surface Warfare Center

Bethesda, Md. 20084-5000

AD-A273 302

CARDIVNSWC–CR–61—93/02   August 1993

Survivability, Structures, and Materials Directorate
Technical Report

Three-Dimensional, Inelastic Response of Single-Edge Notch Bend Specimens Subjected to Impact Loading

by
Pedro M. Vargas
Robert H. Dodds, Jr.

DTIC
ELECTE
NUV 3 0 1993
A

93-29245

93 1: 20 1 19

Approved for public release; distribution is unlimited.

Three-Dimensional, Inelastic Response of Single-Edge Notch Bend Specimens Subjected to Impact Loading

CARDIVNSWC–TR–61—93/02

Three-Dimensional, Inelastic Response of Single-Edge Notch Bend Specimens Subjected to Impact Loading

by
Pedro M. Vargas
Robert H. Dodds, Jr.

DTIC QUALITY INSPECTED 5

Accesion For		
NTIS CRA&I		☑
DTIC TAB		☐
Unannounced		☐
Justification		
By		
Distribution /		
Availability Codes		
Dist	Avail and / or Special	
A-1		

THREE-DIMENSIONAL, INELASTIC RESPONSE OF SINGLE-EDGE NOTCH BEND SPECIMENS SUBJECTED TO IMPACT LOADING

By

Pedro M. Vargas
Robert H. Dodds, Jr.
Department of Civil Engineering
University of Illinois

University of Illinois
Urbana, Illinois
August 1993

REPORT DOCUMENTATION PAGE

Public reporting burden for this collection of information is estimated to average 1 hour per response, including the time for reviewing instructions, searching existing data sources, gathering and maintaining the data needed, and completing and reviewing the collection of information. Send comments regarding this burden estimate or any other aspect of this collection of information, including suggestions for reducing this burden, to Washington Headquarters Services, Directorate for Information Operations and Reports, 1215 Jefferson Davis Highway, Suite 1204, Arlington, VA 22202-4302, and to the Office of Management and Budget, Paperwork Reduction Project (0704-0188), Washington, DC 20503.

1. AGENCY USE ONLY (Leave blank)	2. REPORT DATE	3. REPORT TYPE AND DATES COVERED
	AUGUST 1993	Final Oct 1988-Sep 1992

4. TITLE AND SUBTITLE	5. FUNDING NUMBERS
Three-Dimensional, Inelastic Response of Single-Edge notch Beend Specimens Subjected to Impact Loading	
6. AUTHOR(S)	N61533-88-C-0035 PE 62234N WU 8912814909
Pedro M Vargas and Robert H Dodds, Jr	

7. PERFORMING ORGANIZATION NAME(S) AND ADDRESS(ES)	8. PERFORMING ORGANIZATION REPORT NUMBER
University of Illinois at Urbana-Champaign Department of Civil Engineering 205 N. Mathews Avenue Urbana, Illinois 61801	UILU-ENG-93-2006

9. SPONSORING /MONITORING AGENCY NAME(S) AND ADDRESS(ES)	10. SPONSORING /MONITORING AGENCY REPORT NUMBER
Carderock Division, Naval Surface Warfare Center Metal and Welding Division, COde 610 Annapolis, Maryland 21402	CARDIV TR-61-CR-93-02

11. SUPPLEMENTARY NOTES

12a. DISTRIBUTION /AVAILABILITY STATEMENT	12b. DISTRIBUTION CODE
Approved for public relese; distribution is Unlimited	Statement A

13. ABSTRACT (Maximum 200 words)

Three-dimensional dynamic analyses are performed for three different specimen configurations (a/W=0.5, 0.15, 0.0725) of single edge bend, SE(B), fracture specimens subjected to impact loading.

14. SUBJECT TERMS	15. NUMBER OF PAGES
Finite-element analysis, three dimensional models, impact testing, strain-rate-effects, inertia, fracture toughness	16. PRICE CODE

17. SECURITY CLASSIFICATION OF REPORT	18. SECURITY CLASSIFICATION OF THIS PAGE	19. SECURITY CLASSIFICATION OF ABSTRACT	20. LIMITATION OF ABSTRACT
Unclassified	Unclassified	Unclassified	Same as Report

REPORT DOCUMENTATION PAGE	1. REPORT NO. UILU-ENG-93-2006	2.	3. Recipient's Accession No.

4. Title and Subtitle	5. Report Date
Three-Dimensional, Inelastic Response of Single-Edge notch Bend Specimens Subjected to Impact Loading	August 1993
	6.

7. Author(s)	8. Performing Organization Report No.
Pedro M. Vargas and Robert H. Dodds, Jr.	SRS 582

9. Performing Organization Name and Address	10. Project/Task/Work Unit No.
University of Illinois at Urbana-Champaign	
Department of Civil Engineering	11. Contract(C) or Grant(G) No.
205 N. Mathews Avenue	
Urbana, Illinois 61801	N61533-88-C-0035

12. Sponsoring Organization Name and Address	13. Type of Report & Period Covered
Carderock Division, Naval Surface Warfare Center	Final: 10-1-88 to 9-30-92
Metal and Welding Division, Code 281	
Annapolis, Maryland 21402	14.

15. Supplementary Notes

16. Abstract (Limit: 200 words)

Many significant problems in fracture mechanics of ductile metals involve surface breaking defects (cracks) located in structures that are subjected to short-duration loading caused by impact or blast. When the severity of impact loads is sufficient to produce large inelastic deformations, the assessment of crack-tip conditions must include the effects of plasticity, strain rate and inertia. This research examines the interaction of impact loading, inelastic material deformation and crack geometry with the goal of improving procedures for the engineering assessment of flaws located in critical structures. The work focuses on the bending-type test specimen employed to measure the inherent fracture toughness of a material. A thorough understanding of the test specimen behavior is a prerequisite to the application of measured material properties in structural applications.

Three-dimensional dynamic analyses are performed for three different specimen configurations (a/W=0.5, 0.15, 0.0725) of single edge bend, SE(B), fracture specimens subjected to impact loading. Loading rates obtained in routine drop tower tests (terminal load-line velocity of 100 in/sec) are applied in the analyses. The quarter-symmetric finite element models have 2000, 8-node elements. Such models are refined sufficiently to provide detailed information about overall load-displacement response, Crack Tip Opening Displacement values and J-integral values. The mesh refinement provides only a coarse prediction of crack tip stress fields over distances of a few CTODs. Explicit time integration coupled with an efficient element integration scheme is used to compute the dynamic response of the specimen. Strain-rate sensitivity is introduced via a new, efficient implementation of the Bodner-Partom viscoplastic constitutive model. Material properties for A533B steel (a medium strength pressure vessel steel) are used in the analyses. Static analyses of the same SE(B) specimens provide baseline results from which inertial effects are assessed. Similarly, dynamic analyses using a strain-rate insensitive material provide a reference for the assessment of strain rate effects. Strains at key locations and the support reactions are extracted from the analyses to assess the accuracy of static formulas commonly used to estimate applied J values. Inertial effects on the applied J are quantified by examining the acceleration component of J.

17. Document Analysis   a. Descriptors

Finite-element analysis, three-dimensional models, impact testing, strain-rate effects, inertia, fracture toughness testing, structural defect assessment, size effects, constraint, J, CTOD, Q, shallow cracks, viscoplasticity.

b. Identifiers/Open-Ended Terms

c. COSATI Field/Group

18. Availability Statement	19. Security Class (This Report)	21. No. of Pages
	UNCLASSIFIED	190
Release Unlimited	20. Security Class (This Page)	22. Price
	UNCLASSIFIED	

ABSTRACT

Many significant problems in fracture mechanics of ductile metals involve surface breaking defects (cracks) located in structures that are subjected to short−duration loading caused by impact or blast. When the severity of impact loads is sufficient to produce large inelastic deformations, the assessment of crack−tip conditions must include the effects of plasticity, strain rate and inertia. This research examines the interaction of impact loading, inelastic material deformation and crack geometry with the goal of improving procedures for the engineering assessment of flaws located in critical structures. The work focuses on the bending−type test specimen employed to measure the inherent fracture toughness of a material. A thorough understanding of the test specimen behavior is a prerequisite to the application of measured material properties in structural applications.

Three−dimensional dynamic analyses are performed for three different specimen configurations (a/W=0.5, 0.15, 0.0725) of single edge bend, SE(B), fracture specimens subjected to impact loading. Loading rates obtained in routine drop tower tests (terminal load−line velocity of 100 in/sec) are applied in the analyses. The quarter−symmetric finite element models have 2000, 8−node elements. Such models are refined sufficiently to provide detailed information about overall load−displacement response, Crack Tip Opening Displacement values and J−integral values. The mesh refinement provides only a coarse prediction of crack tip stress fields over distances of a few CTODs. Explicit time integration coupled with an efficient element integration scheme is used to compute the dynamic response of the specimen. Strain−rate sensitivity is introduced via a new, efficient implementation of the Bodner−Partom viscoplastic constitutive model. Material properties for A533B steel (a medium strength pressure vessel steel) are used in the analyses. Static analyses of the same SE(B) specimens provide baseline results from which inertial effects are assessed. Similarly, dynamic analyses using a strain−rate insensitive material provide a reference for the assessment of strain rate effects. Strains at key locations and the support reactions are extracted from the analyses to assess the accuracy of static formulas commonly used to estimate applied J values. Inertial effects on the applied J are quantified by examining the acceleration component of J.

ii

ADMINISTRATIVE INFORMATION

TABLE OF CONTENTS

LIST OF TABLES

LIST OF FIGURES

1 Introduction

1.1 Overview

Many significant problems in fracture mechanics of ductile metals involve surface breaking defects (cracks) located in structures that are subjected to short−duration loading caused by impact or blast. The duration of such loadings is often less than 0.005 seconds. Examples of structures under such short duration loads include pipelines, off−shore structures, railroad rolling stock and maritime vehicles. These structures experience severe impact loading during accidents. Failures initiated by fracture originating from pre−existing defects are generally catastrophic and may lead to environmental damage, economic loss and possibly loss of life. When the severity of impact loads is sufficient to produce large inelastic deformations, the assessment of crack−tip conditions must include the effects of plasticity, strain rate and inertia. This research examines the interaction of impact loading, inelastic material deformation and crack geometry with the goal of improving procedures for the engineering assessment of flaws located in critical structures. The work focuses on the bending−type test specimen employed to measure the inherent fracture toughness of a material. A thorough understanding of the test specimen behavior is a prerequisite to the application of measured material properties in structural applications.

Fracture mechanics provides a quantitative methodology to assess the significance of structural flaws. The relative safety of a structure containing a defect is determined by comparing the material's fracture resistance to the driving force for fracture caused by the loading. The prediction of fracture performance in general requires: 1) experiments to measure critical J−values and Crack−Tip Opening Displacement (CTOD) in simple geometries (e.g., bend bars), and 2) analytical/numerical procedures to predict the applied J and CTOD values in both laboratory specimens and structural components. The crack−tip parameters cannot be measured directly from experiments in the laboratory; they must be inferred from the measured loads, displacements and possibly strains measured at key locations on the specimen. The evaluation of fracture performance requires that the test method and the accompanying analytical procedures reflect the dynamic aspects of the impact loading. Numerical analyses play a key role in developing and validating the experimental procedures by providing the relationship between the fracture parameters and the quantities that are measurable in a fracture test.

Dynamic fracture testing is frequently performed with a drop tower arrangement as illustrated in Fig. 1.1−1. Specimens are fabricated with a through−thickness saw cut that is sharp-

1
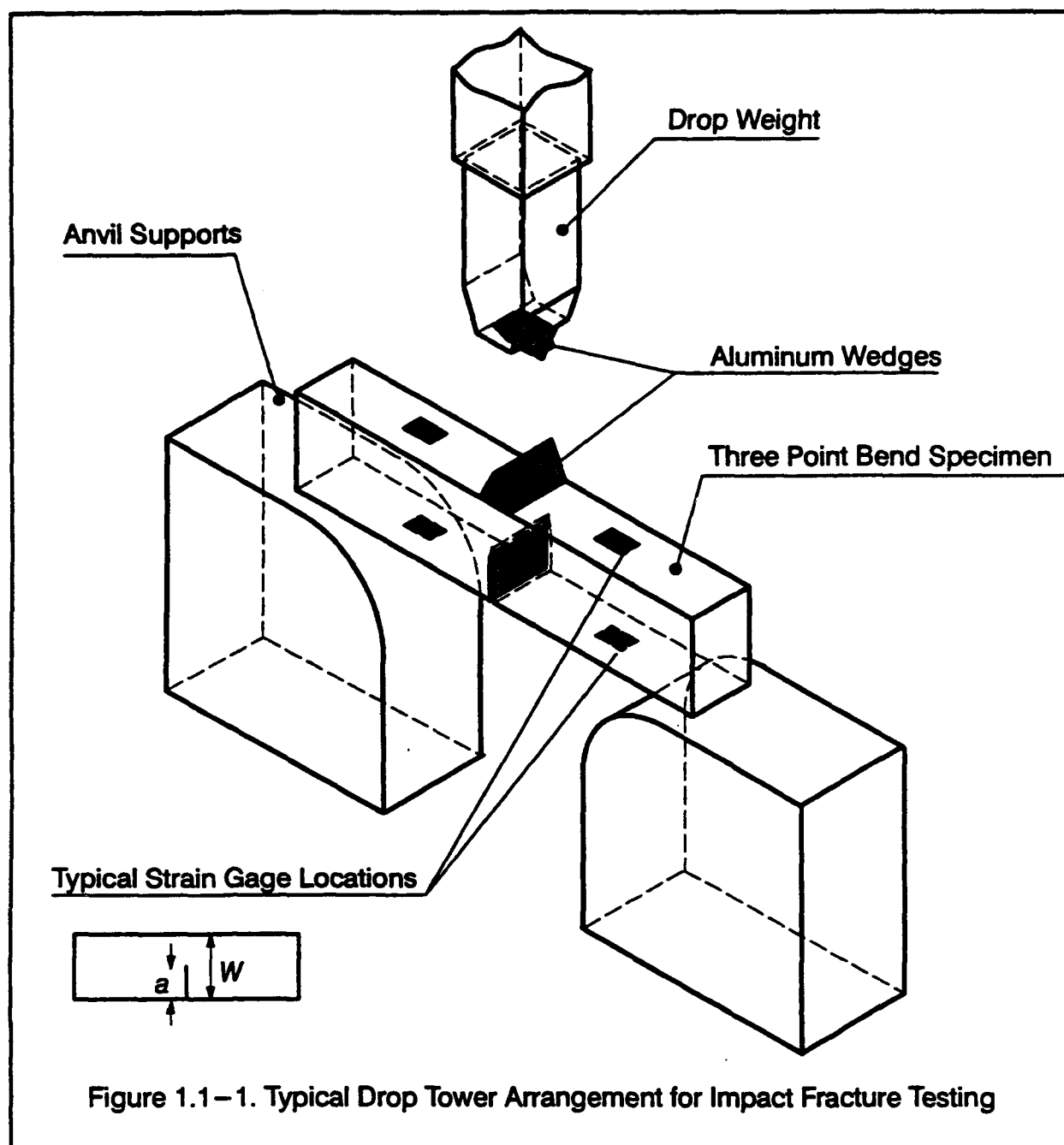
Figure 1.1−1. Typical Drop Tower Arrangement for Impact Fracture Testing

ened with fatigue loading. Three−point bending is accomplished with the support arrangement indicated in the figure. Deeply notched specimens (a/W=0.5, where a is the crack depth and W is the total specimen width) with 2 inch (50.8 mm) square cross−sections and 9 inches (228.6 mm) long have been successfully tested with a drop weight of 1200 pounds (544.3 Kg) having an impact velocity of approximately 20 f/s (6.1 m/sec). This impact velocity corresponds to a drop height of approximately 4 ft. (1.2m). The elapsed time from initial impact to specimen fracture is in the range of 0.001−0.006 seconds for ferritic materials with yield strengths of 60

to 100 ksi (413.7 to 689.5 MPa). Numerical studies [70,72,74] have demonstrated that the applied load vs. time for deeply notched specimens is predicted accurately using the ordinary static bending formula keyed to strains inferred at the quarter-span locations as indicated on the figure. Two factors enable this accurate correlation of strain gage readings with applied load: 1) the soft aluminum wedges minimize elastic rebounding of the drop weight upon initial impact, and 2) the large a/W ratio confines inelastic deformations to the net ligament on the crack plane.

Numerical analyses of the deeply notched specimens also demonstrate the adequacy of static bending formulas to predict the applied J-value from the measured load once the transition time, t_T, is exceeded (see Fig. 1.1-2) [70,71,72]. The transition time defines the point

Figure 1.1-2. Energy Ratio vs Time for a Three Point Bend Specimen
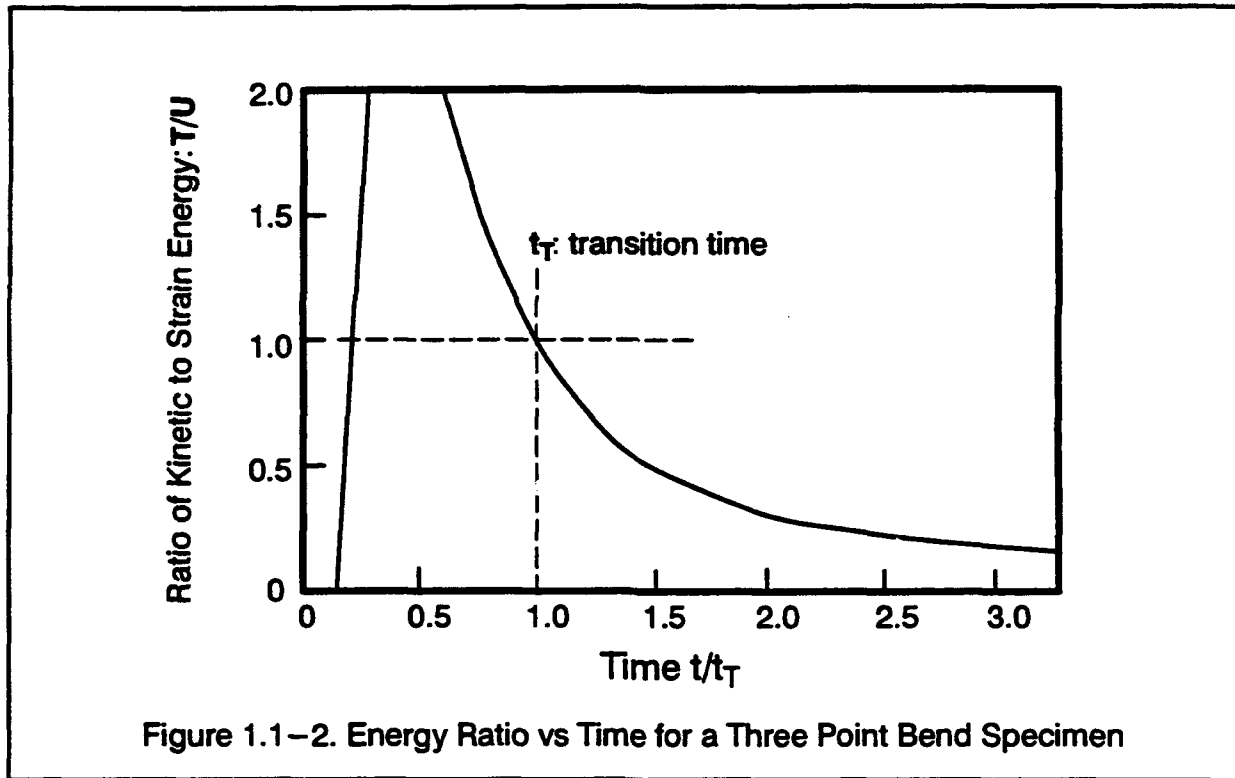
after impact at which the internal energy of deformation, U, equals the kinetic energy, T. Following the transition time, the deformation energy increases at a faster rate than the kinetic energy. For deeply notched specimens of medium strength steels (60 to 100 ksi, 413.7 to 689.5 MPa), the transition time occurs after stress-wave effects have dissipated but while strain rates at the crack tip remain quite large. These materials generally have sufficient toughness that first crack extension occurs when $t > 2 - 5 \, t_T$, a time sufficiently long for extensive plastic deformation to occur. The tests reveal a significant elevation of J-values required to initiate crack extension under impact loading compared to those for static loading [49]. The increase

of critical J-values for impact loading is attributed currently to the elevated yield stress caused by the viscoplastic response of the material.

Drop tower tests and parallel numerical analyses for deeply notched specimens have provided the first insights into dynamic fracture toughness under large−scale yielding conditions. However, practical applications must await a similar understanding of the behavior for shallow, rather than deeply, notched specimens. Real flaws in structures are most often shallow, surface breaking defects rather than deep, through−thickness cracks; moreover, the loading is predominantly tension rather than the severe bending present in the three−point bend specimen. Static tests and numerical analyses reveal substantial increases (factors of 3 to 5) in fracture toughness for bend specimens with shallow notches (a/W <0.15) caused by the lower constraint against plastic flow [6,30]. Similar increases in fracture toughness are anticipated for impact loading. Researchers currently believe it is desirable to employ bend bars containing shallow, through−thickness cracks to approximate the constraint conditions present at surface cracks subjected to tension loading [6,30].

This research presents the first detailed effort to address the effects of viscoplastic response and crack−tip constraint on the fracture driving force in deep and shallow notched three−point−bend specimens under impact loading. Specifically, the behavior of the specimens prior to crack initiation is investigated. By quantifying the different dynamic effects: viscoplasticity, inertia and the acceleration component of the J−integral, a much improved understanding of impact fracture is developed. A parallel evaluation of the techniques utilized in the testing procedures for the calculation of fracture driving force clarifies the extent of possible errors and inaccuracies in the measured fracture toughness.

The remainder of this chapter provides additional background material and concludes with the discussion of specific objectives for this research.

1.2 Crack−Tip Characterization

1.2.1 Crack−Tip Fields in Two−Dimensions

Characterization of the crack−tip stress−strain field by the J−integral is well understood for quasi−static loadings in two dimensions. J is a scalar parameter defined by a contour integral in two dimensions as shown in Fig. 1.2−1. Introduced by Rice [85], the J−integral is a measure of energy released per unit crack extension and is thus termed *energy release rate*. For linear elastic structures it is identical to G, the Griffith elastic energy release rate, and is related to the stress intensity factor K_I [85]. Hutchinson [47], Rice and Rosengren [87] (HRR) showed
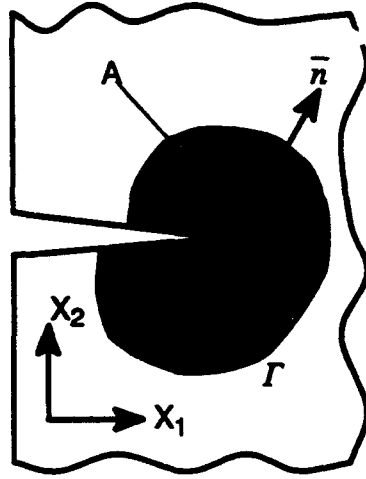
$$J = \lim_{\Gamma \to 0} \int_\Gamma \left(W n_1 - \sigma_{ij} \, n_j \frac{\partial u_i}{\partial x_1} \right) d\Gamma$$

where:

W = strain energy density

n_j = components of $\bar{n}$

$\bar{n}$ = outward normal

σ_{ij} = stress components

u_i = displacements

x_i = coordinate directions

Figure 1.2−1. Definition of the Two Dimensional J−integral

that the J−integral is a direct measure of the intensity of the stresses and strains ahead of a sharp crack tip for a nonlinear elastic, power−law hardening material under conditions of plane−strain, small−scale yielding and static loading. The power−law relation is expressed as:

$$\varepsilon/\varepsilon_0 = a(\sigma/\sigma_0)^n \tag{1.2−1}$$

where n is the hardening exponent, σ_0 is a reference yield stress, $\varepsilon_0 = \sigma_0/E$ is the associated reference strain with E denoting Young's modulus. The parameters a and n are chosen to fit the material's uniaxial $\sigma - \varepsilon$ curve. The first term of the asymptotic singular fields can then be written as:

$$\sigma_{ij} \to \sigma_0 \left(\frac{J}{a\sigma_0\varepsilon_0 I_n r} \right)^{\frac{1}{n+1}} \tilde{\sigma}_{ij}(\theta,n) \tag{1.2−2}$$

$$\varepsilon_{ij} \to a\varepsilon_0 \left(\frac{J}{a\sigma_0\varepsilon_0 I_n r} \right)^{\frac{n}{n+1}} \tilde{\varepsilon}_{ij}(\theta,n) \tag{1.2−3}$$

where r and θ are polar coordinates originating at the crack tip, $\bar{\sigma}$ and $\bar{\varepsilon}$ are dimensionless θ−variations and I_n is an integration constant that depends on n.

5

As the initially sharp crack tip blunts under increased loading, the opening displacement as shown in Fig. 1.2−2 is often used as a measure of crack−tip deformation. Shih [93] showed

Figure 1.2−2. Definition of the Crack−Tip Opening Displacement (CTOD)
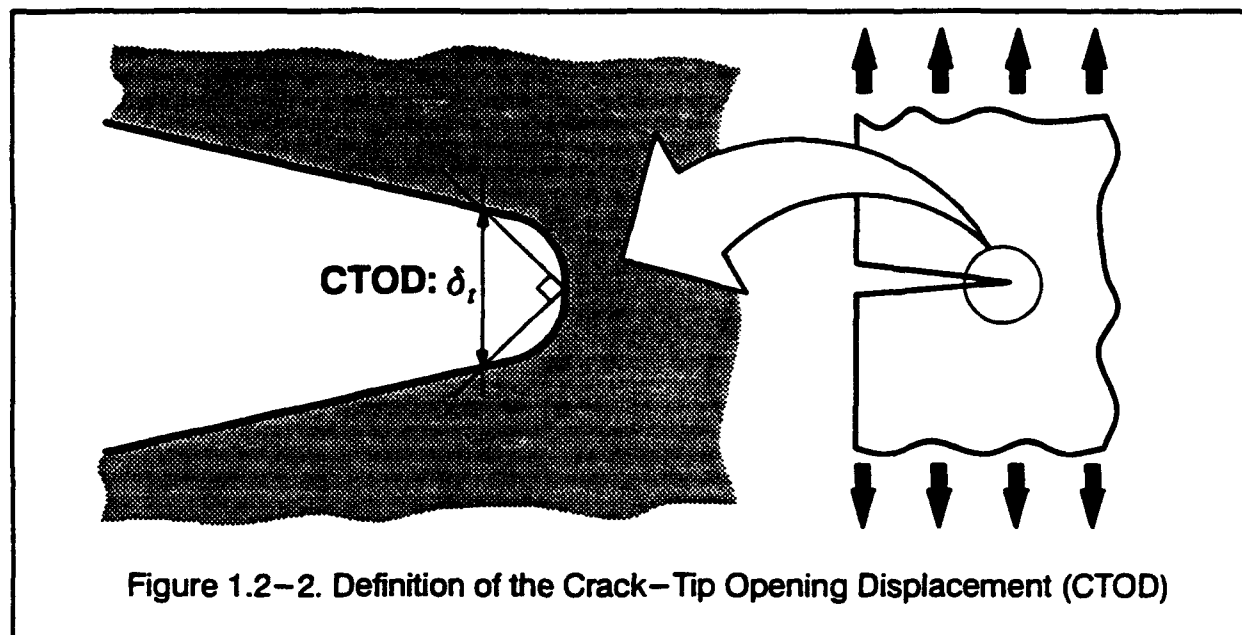
that the Crack−Tip Opening Displacement, (CTOD),varies linearly with the applied J−integral for a power−law hardening material:

$$\delta_t = d_n(a\varepsilon_0, n)\frac{J}{\sigma_0} \qquad (1.2-4)$$

where δ_t denotes the CTOD and d_n is a dimensionless coefficient dependent on material constants a, ε_0 and n.

The asymptotic fields exist rigorously under conditions referred to as "small−scale yielding" (SSY). SSY represents the conditions at a single−ended crack tip located in an infinite body subjected to remote loading. Regardless of the extent of plastic deformation, there always exists a surrounding linear−elastic, K_I field. In finite−sized test specimens and structures, SSY conditions exist only in the early stages of loading; once the plastic zones sense the presence of traction free boundaries the SSY field degenerates. Current research in this area couples the loss of constraint at the crack tip with a second parameter that quantifies near−tip stress triaxiality for cases in which the material and configuration restrictions for small−scale yielding are violated [63,30,6,80,81]. Two recently proposed models that have succeeded in quantifying the crack−tip stress fields under varying constraint conditions are the Dodds−Anderson model [30,6,7] and the Shih−O'Dowd $J-Q$ annulus [80,81] approach.

1.2.2 Crack-Tip Fields in Three-Dimensions

A rigorous definition of HRR crack-tip fields does not exist for the three-dimensional crack problem. However, remote from the free surfaces, it is argued and demonstrated from computational studies that near plane-strain conditions are approached leading to HRR-type fields. The variation of a local pointwise J-integral under static loading along a crack front in three dimensions has been studied in finite element analyses [17,29,28,41,99]. Most of these studies lack sufficient refinement of the finite element mesh near the crack tip to fully resolve the structure of the crack-tip fields. Correlation of the J-integral with stress-strain fields ahead of the crack tip is difficult due to the level of refinement necessary to examine the crack-tip fields. However, a few such studies are now being reported.

Parks [83] has performed very detailed, three dimensional finite element analyses of surface cracks in a tensile panel. A deformation-plasticity model (nonlinear elastic) in the form of a power-law relation (Equation 1.2-1), with small displacements was used. Two crack configurations (one semicircular and the other elliptical), each with two material hardening parameters ($a = 1.0, n = 5, 10$) were analyzed. Crack-tip fields were monitored in detail up to loading levels approaching gross section yield, $\sigma^{\infty}/\sigma_0 \to 1$. Parks et al. found excellent correlation of the crack-tip fields with J provided the conditions of SSY were satisfied. Correlation of the crack-tip fields with J degraded rapidly as the applied load produced gross section yielding and violated the SSY conditions.

This same study also demonstrated that the relationship between the local CTOD and the local J along the crack front retains the linear form described in Shih's study [93]. This observation enables the experimental evaluation of J from CTOD values obtained by infiltration and replica techniques.

1.3 J-integral Methods

Rice's original J-integral [85] has been generalized into a *total energy release rate* by Carpenter [19]. The general formulation includes the effects of inelastic strains (plastic and thermal) through area integrals defined over the *domain* enclosed by the planar contour (A in Fig. 1.2-1). The area integrals are a consequence of the explicit partial derivative of the work density which does not vanish for inelastic material response. Inertia forces within the domain, through-thickness stress gradients and crack face tractions require additional integrals [89].

A volume integral approach, initially derived by Parks [82] and Hellen [44] using the physical interpretation of a *virtual crack extension*, has been extended into a more general form using

7

continuum mechanics concepts by Nikishkov [76], Shih [91] and de–Lorenzi [22]. This approach is especially well suited for finite element models constructed of isoparametric elements. The required integrations over element volumes parallel closely the element stiffness calculations. Inelastic strains and body forces are accommodated through volume integrals similar in form to those required to generalize the contour integral method for these effects. This domain integral technique enables the computation of both pointwise values of J along the crack front and, for through–thickness cracks, a weighted mean value of J as well.

Extensions of these integrals to include dynamic effects have been presented by Nakamura [71]. Three additional integrals are necessary: a kinetic energy term, a velocity gradient term and an acceleration term. The kinetic energy term and the velocity gradient term are zero for a dynamically loaded specimen with a non–growing crack; only the acceleration (inertia) term is needed.

Computational aspects of the volume integral techniques are provided by de–Lorenzi [22,23], Nikishkov [76,77], Shih [90,91], Dodds [32,34] and others [64,98,65,45].

1.4 Dynamic Fracture Tests

Drop tower tests performed on three–point–bend specimens are often employed to evaluate elastic–plastic fracture toughness of a material under impact loading. Extensive studies on high strength, low alloy materials have been performed for deep cracks ($a/W>0.5$) [49,50,51,52,53,54]. More recently, the same approach for testing shallow crack specimens ($a/W \approx 0.1$) under impact loading has been studied [59,60]. The following sections summarize results of dynamic fracture tests for deep and shallow crack specimens.

1.4.1 Deep Crack Tests

Joyce et. al. [49,50,51,52,53,54] performed dynamic fracture tests to obtain J–resistance curves for high strength, tough steel alloys used in naval and nuclear power applications. Three–point–bend specimens with deep notches ($a/W \approx 0.5$) were tested in a drop tower apparatus illustrated in Fig. 1.1–1. The specimens had a 1 in. by 2 in cross–section (1T) with 20% side grooves. Aluminum wedges were used as impact absorbers to minimize high frequency load oscillations due to hammer rebounding. This setup produced a nearly linear rise of load with time [52,53,54]. An optical probe attached to the specimen monitored the load–line displacement. Strain gages located at the quarter span position (see Fig. 1.1–1) were calibrated in a corresponding static test to infer the applied load. The conventional static formula was applied to relate the measured external work to applied J. Supportive numerical analyses by

8

Nakamura et al. [70,72] confirmed the quasi−static nature of the drop tower test provided the fracture event occurred well after the transition time.

By using the drop tower testing apparatus together with the small aluminum wedges, Joyce et. al. were able to achieve essentially constant velocity loading of specimens over a wide range of specimen sizes. This result is obtained when the internal energy absorbed by the specimen remains vanishingly small compared to the kinetic energy of the hammer−tup assembly. Following an initial transient period, the displacement record exhibits a constant terminal velocity that is equal to the velocity of the hammer−tup assembly. These aspects of the drop tower test greatly simplify the generation of dynamic fracture toughness data for different materials and temperatures.

1.4.2 Shallow Crack Tests

Kirk et. al. [59,60] extended the drop tower procedure to include three−point bend specimens with shallow notches ($a/W < 0.15$). The fracture specimens had a 2 in. by 2 in. cross−section without side grooves. These much stiffer specimens, combined with an increased drop height, required modification of the double wedge impact absorber used in the deep crack testing. Kirk found that the two wedge system sliced through each other, which reduced the effectiveness in damping high frequency oscillations. A single pyramid shaped impact absorber solved this problem.

Unlike the deep notch specimens, the deflected shape for shallow notched specimens is not adequately modeled as two rigid arms rotating relative to each other about the crack plane. The overall bending deformation of the shallow notched specimen required that four non−contacting transducers be positioned along the underside of the bend specimen to evaluate the load−line displacement (see Fig. 1.4−1). Data from the four transducers, together with an empirical correlation derived from corresponding static tests, allowed the evaluation of the load−line displacement. Kirk et. al. anticipated extensive amounts of plasticity in the specimen due to shallow cracks and much larger loads. To capture potential nonlinear strain distributions remote from the crack plane, six equally spaced strain gages were placed at the quarter span location to estimate the applied load. Measured strains were converted to their corresponding stress from a uniaxial stress−strain curve of the material. The resulting stress distribution was integrated over the cross section to obtain a moment at the quarter span location from which the applied load was inferred for calculation of fracture parameters. The two strain gages placed near the crack tip signaled the onset of crack extension.

Kirk found that the empirical correlation used to evaluate the load−line displacement applies equally well to both high hardening and low hardening materials. Although the exper-

Figure 1.4—1.   Strain Gage and Eddy Current Gage Locations for
the Shallow Flaw Three—Point—Bend Specimen
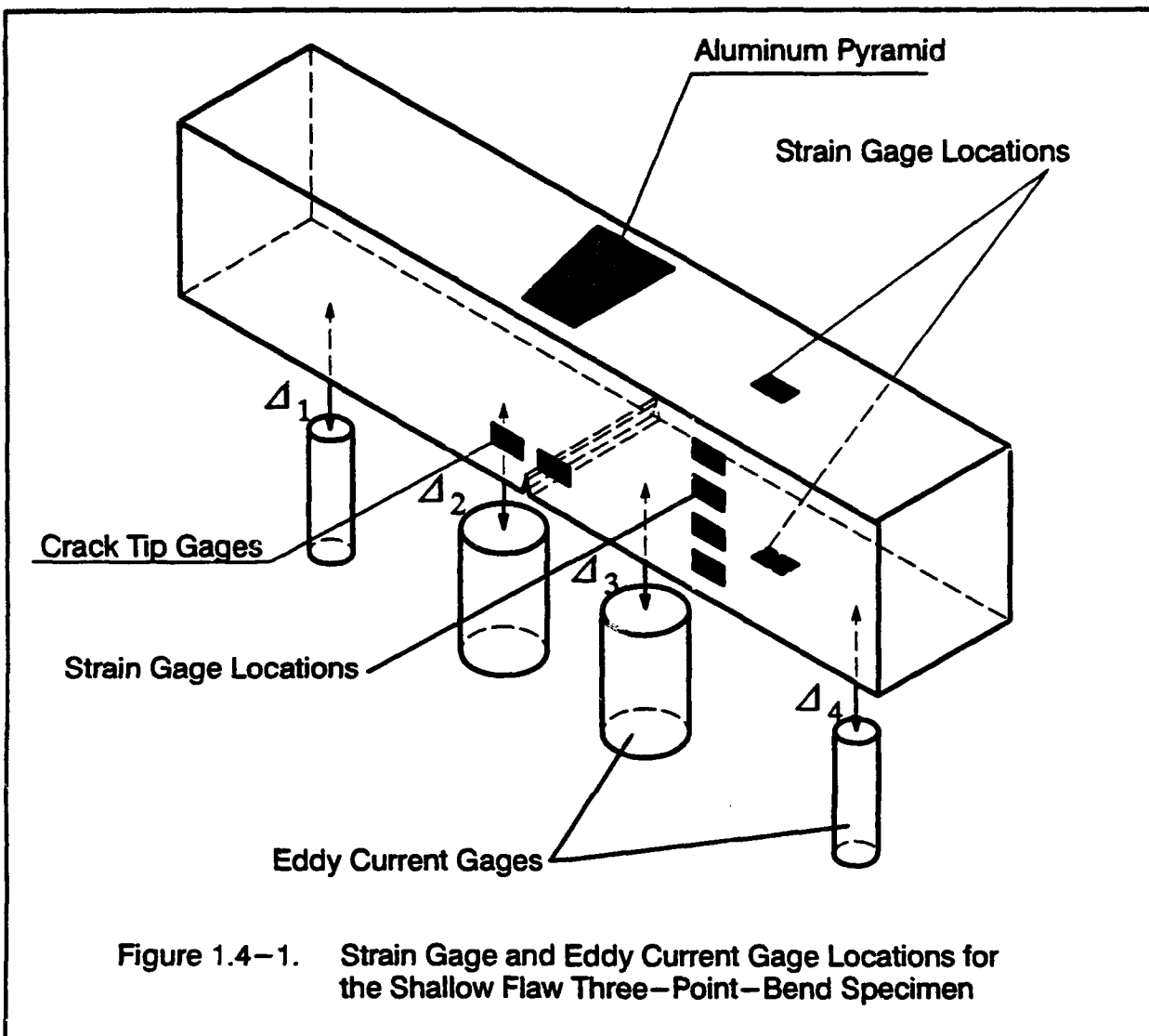
imental technique as modified for shallow—crack specimens appears successful, questions about the interpretation of results remain due to viscoplastic and inertial effects.

1.5 Calculation of *J*—integral from Measurable Quantities

Rice [86] showed that the *J*—integral for a deeply notched three—point bend specimen is given, to a good approximation, by integrating the product of the ligament moment and rotation of the specimen ends. By relating the moment to the applied load and the rotation to the load—line displacement, Sumpter [96] derived an expression that evaluates the *J*—integral from the load—displacement curve of the specimen. Although initially limited to deep cracks, extension of this approach to shallow cracks in an elastic—perfectly plastic material was achieved through a plastic proportionality factor, denoted η_p, that relates the internal plastic work to the plastic component of the applied *J* [96]. Kirk [61] studied Sumpter's formulas to

10

determine their applicability for different hardening materials. He found that for shallow flaws ($a/W < 0.25$) the relationship between the J−integral and the load−displacement curve is highly dependent on strain hardening properties of the material. By using the crack mouth opening displacement (CMOD) of the specimen for computation of internal plastic work, instead of the load−line displacement, the plastic component of J became essentially independent of material hardening.

1.6 Finite Element Studies of Impact Loading

Nakamura et. al. [70,72,74] performed both 2−D and 3−D finite element analyses of a three−point bend specimen with a deep crack ($a/W = 0.5$) under impact loading. Relatively coarse meshes were used in their studies, with crack−tip element sizes on the order of 0.1 inches (2.54 mm). An idealized ramp loading was applied to the finite element model. J−values were calculated over the complete loading history using domain integral techniques. The equations of motion were explicitly integrated (FEAP [100]). The material response was modeled with a strain−rate independent J_2−flow theory of plasticity with a hardening exponent, n, of 10 [70,72]. Subsequent work [74] employed a strain hardening, elastic−viscoplastic material model. Loading durations of approximately 0.001 seconds were considered. No attempts were made to compare numerically predicted responses with results of actual tests.

These computational studies by Shih and co−workers [70,71,72,73] assume *a−priori* characterization of the crack−tip fields by the J−integral even though no theoretically rigorous link exists between J and the stress−strain fields. (An HRR−type description of the crack−tip fields has yet to be developed for non−propagating cracks under dynamic loading.) Rather, they applied the energetic interpretation of J as the energy release rate to characterize the relative intensity of crack−tip deformation between the test specimen and structure. These studies focused on determining when the effects of impact loading become negligible in the computation of J. They introduced a transition time t_T at which the total energy of internal deformation exceeds the kinetic energy of the specimen (see Fig. 1.1−2). A simple strength of material model was developed to predict the transition time as:

$$\frac{T}{U} = \left[S \frac{W}{c_0} \frac{\dot{\Delta}_{LLD}(t)}{\Delta_{LLD}(t)} \right]^2, \text{ where } \quad S = \left[\frac{LBEC_s}{W} \right]^{\frac{1}{2}} \tag{1.2−5}$$

where T and U are the kinetic and internal energies respectively, W, B, and L are the specimen width, thickness and half the span length between the supports. C_s is the specimen compliance, c_0 is the unconfined dilatation wave speed of the material ($\sqrt{E/\varrho}$), Δ_{LLD} and $\dot{\Delta}_{LLD}$ are the

11

load–line velocity and displacement respectively. The predicted transition time from this model agrees well with the 3–D finite element results for deep notch specimens.

In these studies, J–integral values from the finite element analyses were compared with J–values computed using the conventional quasi–static formula to determine when the dynamic effects became negligible. In the quasi–static formula, the computed moment across the remaining ligament together with a rotation angle between the specimen ends were used to compute the internal work of the specimen, which was then related to the J–integral. Dynamic effects were found to be significant prior to twice the transition time ($2t_T$) in the deep crack specimens. The quasi–static formula predicted accurate values of the J–integral once the dynamic effects diminished sufficiently, i.e., $t > 2t_T$. Nakamura et al. normalized the J–integral with respect to the strain energy density at yield. The mid–section moment was normalized by the limit moment. Once normalized in this manner, both the static and the dynamic J–values collapse onto a single curve.

The transition time was found to be 27 × the time required for a longitudinal wave to travel the specimen width (W). For example, the transition time of the three–point bend specimen of two inch width, with the material properties of steel, is approximately 230 μs.

Nakamura also conducted a study incorporating a strain–rate sensitive material model in a deeply notched three–point bend specimen under impact loading [74]. Rate–sensitive and insensitive finite element analyses were compared for the idealized ramp loading. The loading duration was the same as in the previous studies, $\sim 10^{-3}$ seconds. Nakamura found that the rate–sensitive material consistently exhibited lower J–integral values than the rate–independent material model, even though the ligament moments were higher in the rate–sensitive specimen. The rate–sensitive model elevated the yield stress for material in the ligament. This forced deformation away from the crack–tip, thereby also lowering J compared to the rate–independent model at the same applied loading. The rate–sensitive model had a more nearly uniform distribution of applied J across the crack front. Nakamura also found that rate sensitivity of the material model did not affect the accuracy of J obtained from the quasi–static formula.

1.7 Objectives and Scope

Assessment of the fracture properties of a material under impact loading is possible only by quantifying the dynamic effects on the specimen response. Recent extension of testing procedures to examine shallow notched specimens introduces significant complexities for the interpretation of measurable quantities. The objective of this study is to develop a broader un-

derstanding of fracture parameters in the impact testing of notched bend-bars. The research focuses on numerical analyses with comparisons (where possible) to fracture tests recently completed at the David Taylor Research Center (Annapolis laboratory).

Impact testing produces three dynamic effects of interest: 1) stress waves and specimen oscillations; 2) high strain rates at the crack tip, and; 3) acceleration of material in the crack-tip region that may shield the crack tip. Direct experimental evaluation of these effects and their influence on the fracture parameters of the SE(B) specimen is not possible. In this study, numerical analyses are conducted to examine each of these effects. Corresponding quasi-static analyses provide a reference from which dynamic aspects are assessed. Dynamic analyses with two different materials, a rate-independent material and a rate-sensitive material, are used to quantify the strain rate effects. The validity of the transition time concept as it applies to shallow flaws is also examined through these analyses. Strains at key locations and the support reactions, quantities which are measurable in the laboratory, are extracted from the analyses and used in quasi-static methods for J computation. The time at which dynamic effects diminish sufficiently for these formulas to apply is determined and compared to the transition time.

Of particular interest in this work is the dynamic behavior of specimens as a function of crack depth, i.e. from deep cracks to shallow cracks. Three dimensional static and dynamic analyses are conducted for bend specimens with three different crack depths: $a/W = 0.5, 0.15, 0.0725$. Specimen dimensions are 2 inch by 2 inch cross section, 9 inches long, with an 8 inch loading span [59]. Stress-strain properties for A533B steel are used in all analyses. The effects of strain rate on the uniaxial stress-strain behavior of this material have been extensively studied. The present work focuses on the applicability of the quasi-static methodology employed in fracture testing to infer the applied fracture driving force J. Details of the near-tip stress-strain fields are not pursued in this work due to the prohibitive computational costs.

1.8 Outline

This report contains five chapters. Chapter 2 provides additional theoretical background. The dynamic J-integral is developed and its computation via domain integrals is outlined. The Bodner-Partom viscoplastic material model and its application to A533B steel are described. The procedure to calculate the fracture parameter J using quantities measured in the experiments is developed.

Chapter 3 describes the computational procedures employed in this research. The relevant details of the Spectrom finite element computer code are provided. Details of the implementation of J-integral calculations and the Bodner-Partom viscoplastic material model are pro-

13

vided. The methodology used to reproduce the load–line displacement history of the test specimen in the finite element simulations is developed.

Chapter 4 provides the results obtained from the finite element analyses. Comparisons between the different crack depths are developed for the various parameters studied. Transition time concepts and techniques to compute fracture parameters are also evaluated.

Chapter 5 provides the conclusions and recommendations derived from this research.

2 Theoretical and Experimental Background

This chapter presents the theoretical and experimental background material that forms the basis of this research. The first section develops extensions of the J-integral to include inertial effects and expands the formulation into a domain integral suited for finite element applications. This is followed by development of the quasi-static formula utilized for evaluation of J from measured load-displacement curves. In the third section, the Bodner-Partom viscoplastic material model is described. The effects of each material dependent parameter employed in the model are examined. The description of a material well characterized by the Bodner-Partom material model, A533B steel, is also included in this section. The last section provides some additional details of the drop tower test and their influence on the development of analysis procedures utilized in this work.

2.1 J-Integral with Inertia Loading Effects

Extensions of the J-integral to incorporate the effects of dynamic loading for non-growing cracks are established by including the kinetic energy density of material at the crack tip in the same manner as the strain energy density [70,71,72,73]. Thus,

$$J = \lim_{\Gamma \to 0} \int_{\Gamma} \left((W + T)n_1 - \sigma_{ij} n_j \frac{\partial u_i}{\partial x_1} \right) d\Gamma \tag{2.1-1}$$

$$W = \int_0^{\varepsilon_{ij}} \sigma_{ij} \varepsilon_{ij} \, d\varepsilon_{ij} \tag{2.1-2}$$

$$T = \frac{1}{2}\rho \left(\frac{\partial u_i}{\partial t} \right)^2 \tag{2.1-3}$$

where W and T are the strain and kinetic energy densities, respectively; n_i are components of an outward unit vector to the contour, Γ; σ_{ij} and ε_{ij} are the stress and strain components, respectively; ρ is the material mass density; u_i are the displacements; t denotes time and x_i are the coordinate directions (see Figs. 1.2-1 and 2.1-1). The positive direction of the contour is shown in Fig. 2.1-1. The integral becomes applicable for *arbitrary* material response in the limit as the contour shrinks to a point on the crack front. In two dimensions the contour Γ is defined in the plane. In three dimensions the contour integral is defined in a plane perpendicular to the crack front at point s as shown in Fig. 2.1-1.

15
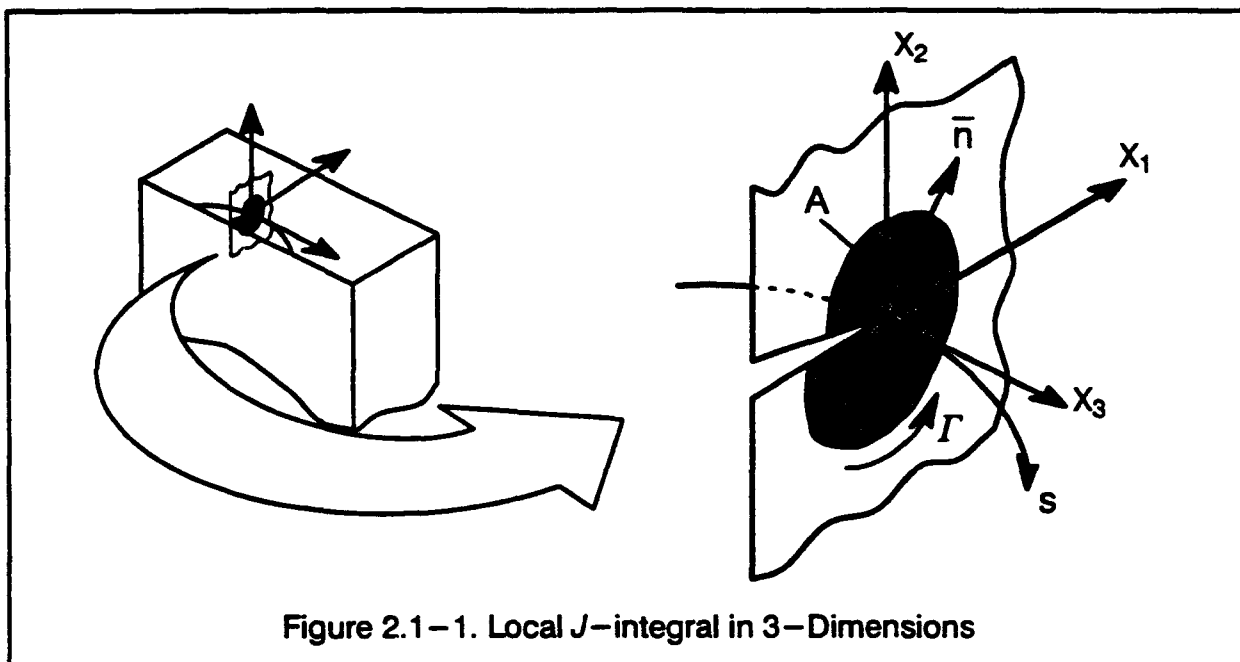
Figure 2.1−1. Local J−integral in 3−Dimensions

Work conjugacy is required for the stresses and strains (displacement gradients) in Eqns. 2.1−1 through 2.1−3. This requires use of the 1st Piola−Kirchoff stresses and the spatial rate of the displacements with respect to the undeformed coordinates. Alternatively, the integral can be expressed in terms of the Cauchy stress and the spatial rate of the displacements with respect to the current coordinates.

The direct evaluation of Eqn. 2.1−1 is cumbersome in a finite element model due to the geometric difficulties encountered in defining a contour that passes through the integration points. Such a contour is desired since the most accurate stress and strain quantities are available at the integration points. Moreover, the limiting definition of the contour requires extensive mesh refinement near the crack tip to obtain meaningful numerical results. The next section develops an approach much better suited for finite element models.

2.1.1 Domain Form of the J−Integral

By using a weight function which may be interpreted as a virtual displacement field, the contour integral is converted into an area integral for two dimensions and into a volume integral for three dimensions [32,23,76,77]. The resulting expressions are:

$$\bar{J}_{a-c} = \int_{s_a}^{s_c} [\, J(s)\, q_t(s)\,]\, dS \;=\; \bar{J}_1 + \bar{J}_2 + \bar{J}_3 \qquad (2.1−4)$$

16

$$J_1 = \int_V \left(\sigma_{ij} \frac{\partial u_i}{\partial x_k} \frac{\partial q_k}{\partial x_j} - W \frac{\partial q_k}{\partial x_k} \right) dV \qquad (2.1-5)$$

$$J_2 = - \int_V \left(\frac{\partial W}{\partial x_k} - \sigma_{ij} \frac{\partial^2 u_i}{\partial x_j \partial x_k} \right) q_k \, dV \qquad (2.1-6)$$

$$J_3 = - \int_V \left(T \frac{\partial q_k}{\partial x_k} - \varrho \frac{\partial^2 u_i}{\partial t^2} \frac{\partial u_i}{\partial x_k} q_k + \varrho \frac{\partial u_i}{\partial t} \frac{\partial^2 u_i}{\partial t \partial x_k} q_k \right) dV \qquad (2.1-7)$$

where q_k is the weight function in the k coordinate direction ($q_t(s)$ represents the resultant value of the weight function at point s on the crack front), V represents the volume of the domain surrounding the crack tip, and s denotes positions along the crack front segment. Body forces
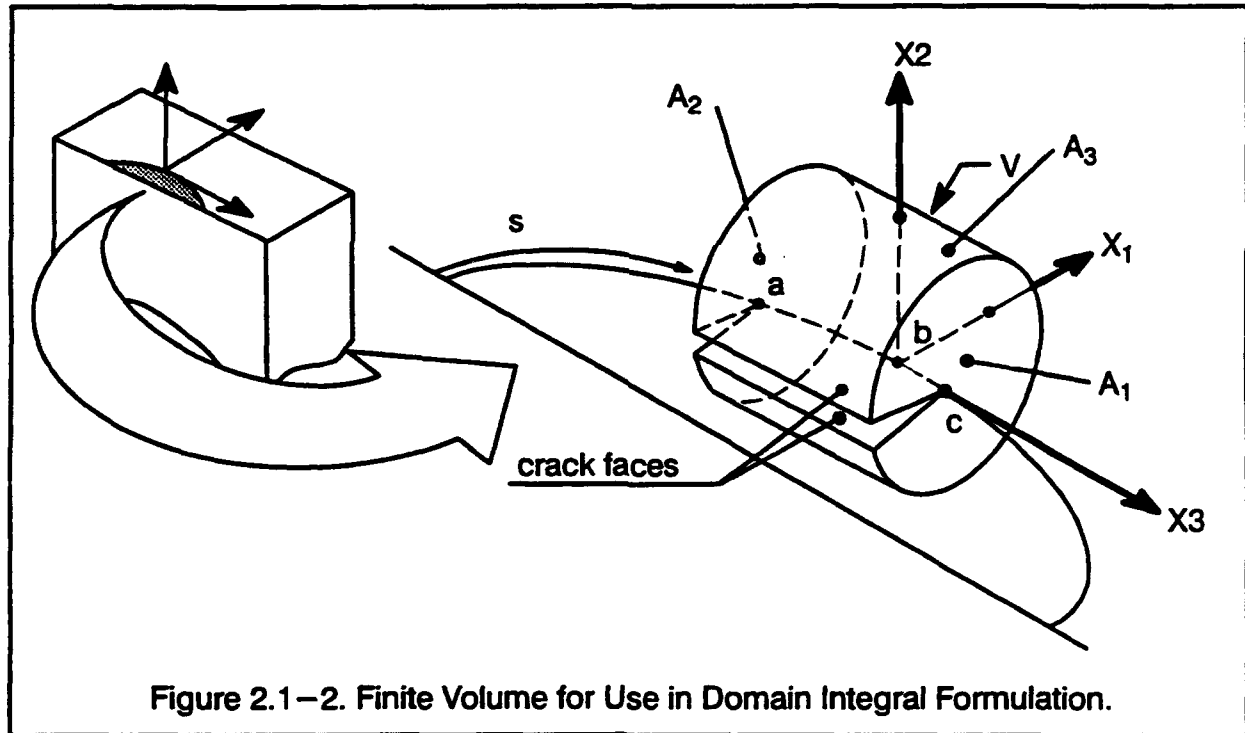
Figure 2.1−2. Finite Volume for Use in Domain Integral Formulation.

(other than inertial loading) and crack face tractions are assumed to be zero for simplicity. (The treatment of body forces, crack face tractions and thermal strains involve additional integrals discussed in [32].) $J(s)$ is the local energy release rate that corresponds to the perturbation at s, $q_t(s)$. Figure 2.1−2 shows a typical domain volume defined for an internal segment along a three−dimensional surface crack.

The q−function must vanish on the surfaces A_1, A_2 and A_3 in Fig. 2.1−2 for the development of Eqns. (2.1−5) through (2.1−6) from (2.1−4). This requirement makes area integrals

17

(line integrals in two dimensions) defined on these surfaces vanish in the derivation. Fig. 2.1−3 shows the variation of the amplitude of a valid q−function for the domain shown in Fig. 2.1−2. All material over which the q−function and its first derivative are non−zero must be included in the volume integrals. The value of q at each point in the volume, V, is readily interpreted as the virtual displacement of a material point due to the virtual extension of the crack front, q_t.
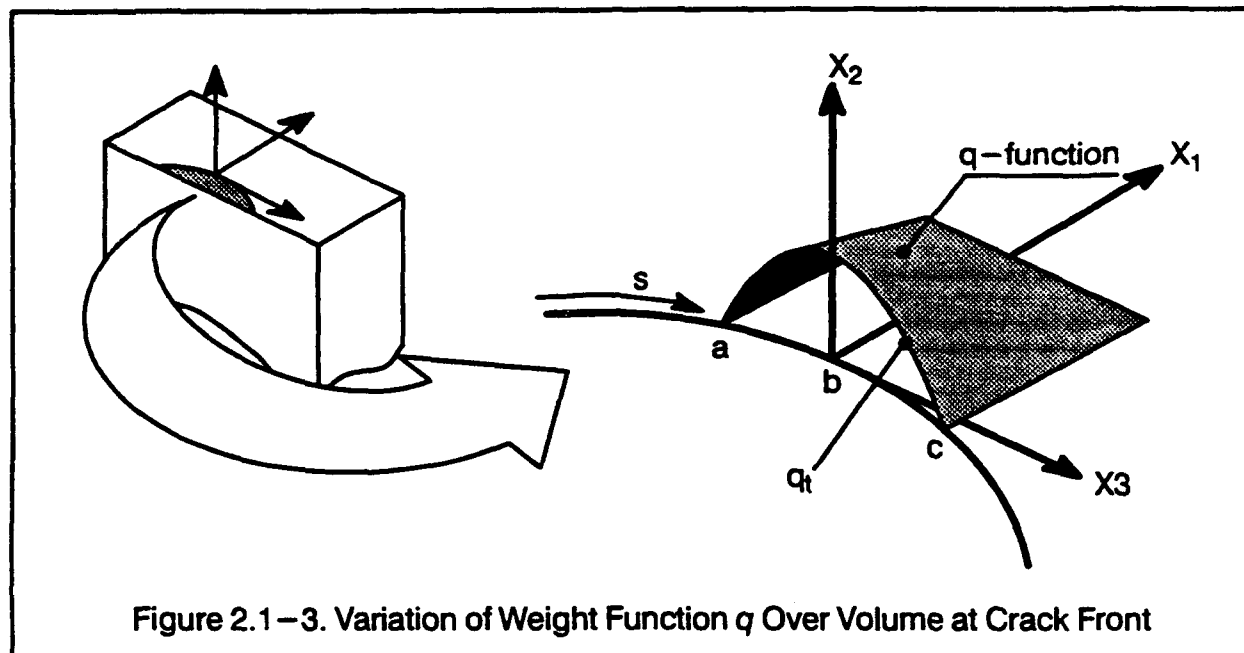
Figure 2.1−3. Variation of Weight Function q Over Volume at Crack Front

An approximate value of $J(s_b)$ is obtained by applying the mean−value theorem over the interval $s_a < s < s_c$. The pointwise value of the J−integral at s_b is given by (see Fig. 2.1−3):

$$J(s = b) \approx \frac{\int_{s_a}^{s_c} \left(J(s) \, q_t \right) ds}{\int_{s_a}^{s_c} q_t \, ds} = \frac{J}{A_q} \qquad (2.1-8)$$

where J is the energy released due to the crack−tip perturbation, $q_t(s)$; and A_q, the increase in crack−area corresponding to this perturbation, is simply the integral of q_t along the crack front from s_a to s_c.

For SE(B) specimens, the crack front is generally straight or only slightly curved. For such crack geometries, the average J for the entire crack front value is obtained by the application of a uniform q_t across the full crack front.

18

The above volume integrals are evaluated by Gauss quadrature. Derivatives of the $q-$ function over each finite element in V are computed by standard isoparametric techniques from specified values of q at element nodes. References [98,34] describe procedures for the evaluation of higher order derivatives of the integrands in J_2. The higher order derivatives are computed by either: 1) extrapolating Gauss point values to the element nodes and applying standard isoparametric techniques or, 2) interpolating the Gauss point values to a lower order integration within the element. Chapter 3 provides additional details on these procedures.

2.1.2 Domain form of the $J-$Integral: Discussion

The J_2 integral vanishes for an elastic material (linear or nonlinear) in the absence of thermal strains as shown in the following manner. By exchanging the order of differentiation and utilizing the (small displacement gradient) strain tensor definition, the second term in Eqn. 2.1$-$6 is rewritten as:

$$- \sigma_{ij}\frac{\partial^2 u_i}{\partial x_j \partial x_1} \ = \ - \sigma_{ij}\frac{\partial}{\partial x_1}\left(\frac{\partial u_i}{\partial x_j}\right) \ = \ - \sigma_{ij}\frac{\partial}{\partial x_1}\left(\varepsilon_{ij}\right) \ = \ - \sigma_{ij}\frac{\partial \varepsilon_{ij}}{\partial x_1} \qquad (2.1-9)$$

The chain rule is now evoked to expand the first term in Eqn. 2.1$-$6. The resulting derivative of strain energy density with respect to strain is the stress tensor for elastic materials. The result is:

$$\frac{\partial W}{\partial x_1} \ = \ \frac{\partial W}{\partial \varepsilon_{ij}}\frac{\partial \varepsilon_{ij}}{\partial x_1} \ = \ \sigma_{ij}\frac{\partial \varepsilon_{ij}}{\partial x_1} \qquad (2.1-10)$$

The two terms defining the integrand of J_2 thus sum to zero for elastic materials.

Dynamic loading effects appear in the J_3 term of the domain integral representation of the $J-$integral. The first term in J_3 provides the flux of the kinetic energy in the direction of the crack propagation. The second and third terms arise from the explicit partial derivative, $(\partial/\partial x_1)$, of the kinetic energy density. The second term contains material accelerations and the third term is identified with the spatial gradient of the velocities. The second term, containing the material accelerations, has been found to make significant contributions to the total $J-$integral for non$-$propagating cracks. This term is similar in form to domain integrals that accommodate ordinary body forces.

For an elastic structure under static loading (without any thermal strains), J_2 and J_3 are identically zero. For incremental (load path dependent) plasticity, the deviation of J_2 from

zero indicates the degree of non−proportional loading experienced over the domain of integration.

For many practical cases, the loading produces nearly proportional material histories within the domain of integration; in such cases the very small contribution of $\bar{J}_2$ is neglected [48,98]. Nakamura, et. al. neglected $\bar{J}_2$ for J−integral calculations in [70,71,72,73]. Vargas and Dodds [98] show that up to 15% of the J−integral in a 2−dimensional static case can be due to $\bar{J}_2$ for incremental plasticity models when the plastic strains and the elastic strains within the domain are similar in magnitude. For larger plastic strains, however, this difference diminishes to less than 0.1%, which justifies the use of $\bar{J}_1 + \bar{J}_3$ as an approximation to Eqn. 2.1−4 for large amounts of plastic deformation. The effects of thermal strains in the calculation of J are reported in [98,76]. The contribution of $\bar{J}_2$ in the presence of thermal strain gradients within the integration domain is significant.

The derivation of Eqns. 2.1−4 through 2.1−7 is mathematically rigorous. Provided sufficient resolution of the crack−tip stress−strain fields exists for accurate numerical integration, the calculated J−integral equals the weighted $J(s)$, where $J(s)$ is the contour definition in the limit as the contour shrinks onto the crack tip. For a given $q_t(s)$, i.e., the crack front variation of the weighting function, many combinations of domain volume and distribution of the q−function are possible. Thus, similar to *path independence* arguments for the contour J−integral, *domain independence* arguments apply for the domain J−integral. In practice, several domains defined concentrically about the crack tip are evaluated to insure domain independence of the computed J−integral. In the general case of thermal loading and inelastic material response all three components of the J−integral are required for the calculated value to be domain independent [76].

2.2 *J* Evaluation in Test Specimens

As shown by Rice [86], the J−integral is closely related to the work done by the ligament moment acting through the rotation angle for SE(B) specimens under static loading (see Fig. 2.2−1). For deeply notched specimens ($a/W > 0.5$), the J−integral for a SE(B) is given approximately by:

$$J = \frac{2}{bB} \int_0^{\Omega_f} M \, d\Omega \qquad (2.2-1)$$

where M is the moment on the remaining ligament at the crack plane, B is the specimen thickness, b is the ligament length and Ω is the relative angle between the specimen ends (see Fig. 2.2–1). This definition provides the average value of $J(s)$ across the entire crack front.
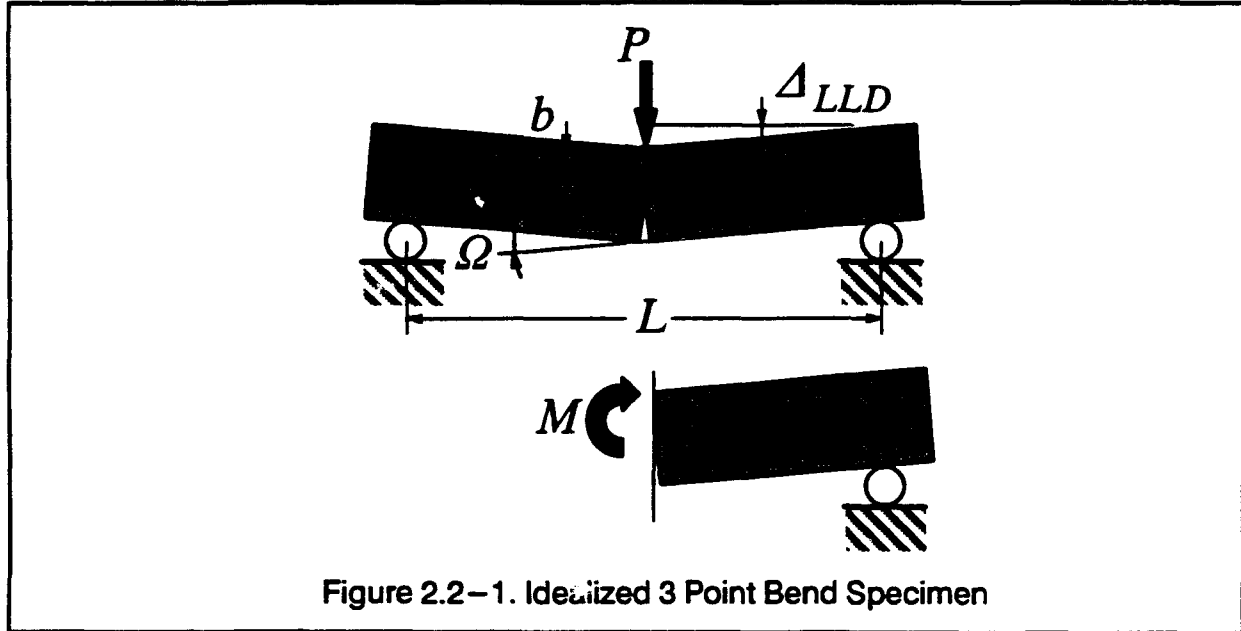
Figure 2.2–1. Ideaiized 3 Point Bend Specimen

By assuming the two ends of the specimen undergo a simple rigid–body rotation about the crack plane, the angle Ω is related directly to the load–line displacement Δ_{LLD}, $\Omega = \Delta_{LLD}/(L/2)$, where L is the total span between supports.. From equilibrium, the moment at the specimen center, M, is simply $(PL)/4$. Then Eqn. 2.2–1 can be rewritten:

$$J = \frac{\eta}{bB} \int_0^{\Delta_{LLD_f}} P \, d\Delta_{LLD} \qquad (2.2-2)$$

where η is the dimensionless constant that includes both the equilibrium condition that relates P to M and the kinematic relationship between Δ_{LLD} and Ω. For deep cracks the constant η is ≈ 2. This result is derived in the following manner. We assume that all the external work, W, done by the force P equals the increase in internal energy, U, of the specimen computed only from the ligament moment acting through the ligament rotation. Then:

$$U = \int_0^{\Omega_f} M \, d\Omega \qquad W = \int_0^{\Delta_{LLD_f}} P \, d\Delta_{LLD} \qquad (2.2-3)$$

and:

21

$$J = \frac{2}{bB} \int_0^{\Omega_f} M \, d\Omega = \frac{2}{bB} U = \frac{\eta}{bB} W \qquad \therefore \eta = 2 \qquad (2.2-4)$$

This simple model neglects small amounts of elastic energy stored remote from the crack plane. Finite element computations in plane strain verify that $\eta \approx 2$ for deeply notched specimens.

Eqn. 2.2−2 provides the basis for experimental evaluation of J in SE(B) specimens. The load, P, and the load−line displacement, Δ_{LLD}, are readily measured for static loading. The J−integral is then proportional to the area under the measured load−displacement curve.

To estimate J for shallow cracks in SE(B) specimens, Sumpter [96] separates the external work done by the applied load into elastic and plastic components, W_e and W_p:

$$J = J_e + J_p = \frac{\eta_e}{bB} W_e + \frac{\eta_p}{bB} W_p \qquad (2.2-5)$$

where η_e and η_p are the dimensionless constants that relate the elastic and plastic external work to the fracture driving force. W_p denotes the of external work of the applied load acting through the plastic component of the load line displacement. η_p indicates the relative amount of plastic deformation that contributes to crack−tip driving force rather than plasticity remote from the crack plane. By using the relationship between the J−integral and stress intensity factor K_I for plane strain, Eqn. 2.2−5 is rewritten as:

$$J = J_e + J_p = \frac{K_I^2(1 - \nu^2)}{E} + \frac{\eta_p}{bB} \int_0^{\Delta_f} P \, d\Delta_p \qquad (2.2-6)$$

This form for J insures compatibility between measured values of J and K_I when the deformation is predominantly linear. The plastic component of the load−line displacement, Δ_p, is computed by subtracting the elastic displacement from the total displacement. Sumpter used limit load solutions for plane−strain conditions to estimate η_p for different crack depths. Sumpter generated polynomial curve fits for η_p as follows [96]:

$$\text{for} \quad \frac{a}{W} < 0.282; \quad \eta_p = 0.32 + 12\frac{a}{W} - 49.5\left(\frac{a}{W}\right)^2 + 99.8\left(\frac{a}{W}\right)^3 \qquad (2.2-7)$$

$$\text{for} \quad \frac{a}{W} > 0.282; \quad \eta_p = 2.0 \qquad (2.2-8)$$

22

Kirk et. al. [61] performed 2−D finite element analyses to examine the applicability of Eqns. 2.2−7 and 2.2−8 for SE(B) specimens. A Ramberg−Osgood hardening material model with an exponent, $n = 13$, was used. For $a/W = 0.5$, Kirk et. al. obtained an η_p value of 1.924. Kirk et. al. noted that a modified form of Eqn. 2.2−6 in which the plastic work is calculated by integrating the applied load through the crack mouth opening displacement (CMOD) gave much better accuracy for shallow crack specimens ($a/W < 0.25$). Moreover, the use of CMOD, rather than Δ_{LLD}, removes much of the η_p dependence on strain hardening [61].

Eqns. 2.2−6, 2.2−7 and 2.2−8 are commonly used to calculate the value of J at fracture in test specimens.

2.3 Bodner−Partom Viscoplastic Material Model

The Bodner−Partom material model belongs to the family of viscoplastic theories of the "unified" approach, which combine both time−independent plasticity and time−dependent phenomena such as creep and stress relaxation into a single state variable [13,16,20,24,26]. Initially developed from a simple model attributed to Norton [79], the Bodner−Partom material model has since been modified to include isotropic and directional hardening effects [13,16]. The essential features of the Bodner−Partom model are: 1) the Prandl−Reuss flow rule, 2) a kinetic equation that relates the strain rate to the stress and the hardening variable, and, 3) an evolution law for the internal hardening variable.

The general formulation is based upon additive decomposition of the total strain rate, $\dot{\varepsilon}_{ij}$, into elastic, $\dot{\varepsilon}_{ij}^e$, and plastic components $\dot{\varepsilon}_{ij}^p$:

$$\dot{\varepsilon}_{ij} = \dot{\varepsilon}_{ij}^e + \dot{\varepsilon}_{ij}^p \tag{2.3−1}$$

where the superimposed dot indicates differentiation with respect to time. The elastic strain rates are related to the stress rates through standard linear−elastic, Hookean relations for small strain (hypoelasticity approach). The strain rates are in tensorial form, i.e. the shear strains are one−half the engineering strains. Extension of this approach to finite strains is valid only if plastic strains are much larger than the elastic strains (the additive decomposition of strains and precise treatment of material elasticity then have negligible effect) [43]. The inelastic strain rates, for both small and finite strain formulations, are related to the stress deviators, s_{ij}, through the flow rule:

$$\dot{\varepsilon}_{ij}^p = \lambda s_{ij} \tag{2.3−2}$$

where λ is defined as a plastic proportionality constant. This approach parallels the flow rule employed in incremental plasticity. The inner product of both sides of Eqn 2.3−2 is taken to yield the scalar result:

$$\lambda^2 = \frac{D_2^p}{J_2}$$ (2.3−3)

where J_2 and D_2^p are the second invariant of the stress tensor and plastic strain tensor, respectively. Again, this parallels the incremental plasticity formulation in which the plastic proportionality constant is related to the second invariant of the stress and increment of plastic strain tensors. A kinetic relationship is introduced to relate the overall plastic straining behavior, D_2^p, to the stresses, J_2, and the hardening variable, Z, as:

$$D_2^p = D_0^2 \exp(\beta) ; \qquad \beta = -\left(\frac{Z^2}{3J_2}\right)^n$$ (2.3−4)

where D_0 is the limiting plastic strain rate in shear, n determines the sensitivity to stress levels (strongly affecting the yield stress), and Z is a scalar hardening parameter. This relationship is motivated partially by work in the field of dislocation dynamics which has shown that the dislocation velocity is a function of the stress state [13]. Evolution of the hardening parameter is defined as:

$$\dot{Z} = m(Z_1 - Z)\dot{W}_p ; \qquad Z = Z_0 \text{ at } t = t_0$$ (2.3−5)

where W_p is the plastic work density, the superimposed dot implies differentiation with respect to time, m is the rate of hardening coefficient and the two parameters Z_0 and Z_1 determine the range of the hardening parameter Z. The material constants needed in the Bodner−Partom model are thus: D_0, m, n, Z_0, Z_1.

Figure 2.3−1 illustrates the qualitative effect of each parameter on uniaxial stress−strain curves. These effects are summarized below:

D_0: For a given strain rate, an increase in D_0 reduces the stresses at strains beyond the linear−elastic portion of the stress−strain curve. This reduction in stress is more pronounced at the higher strain rates, i.e., a higher strain rate generates a larger decrease in stresses than a lower strain rate for a given increase in D_0. Thus the difference between two uniaxial stress−strain curves at different strain rates decreases with an increase in D_0. Large values for D_0 reduce the overall rate sensitivity of the model.

Figure 2.3−1. Influence of the of the Bodner−Partom Material Model Coefficients on Uniaxial Stress Strain Curves
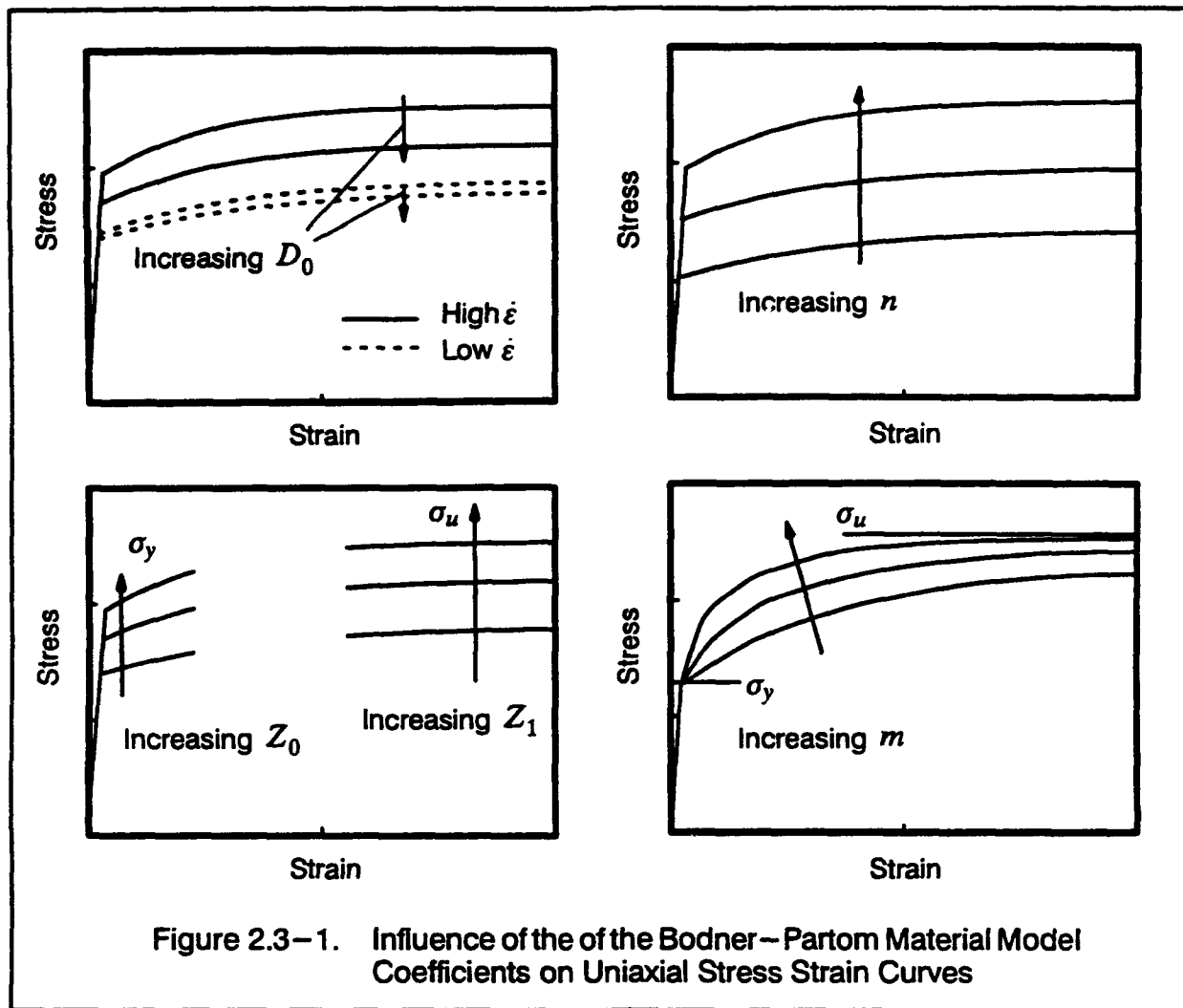
Z_0, Z_1: The parameters Z_0 and Z_1 define the range of the strain hardening parameter Z. The hardening parameter starts with $Z=Z_0$ at $t=0$; Z approaches Z_1 as the plastic strain energy density increases. Increases in the parameters Z_0 and Z_1 are accompanied by increases in the yield stress, σ_y, and saturation stress, σ_u, respectively.

n: The overall stress level increases with an increase in the parameter n.

m: The shape of the hardening curve is determined by m. As shown in the figure, an increase in m increases the hardening behavior of the stress−strain curve.

Unlike conventional rate−independent plasticity, the Bodner−Partom material model does not have an explicit yield function. Eqns. 2.3−1 through 2.3−5 predict the formation of plastic strain increments for all stress increments. It is this aspect of the model which enables the prediction of creep and stress relaxation effects. However, for a wide range of practical strain rates, e.g. 10^{-6}/sec to 10^6/sec for steels, a *yield stress* behavior does exist. To resolve this

25

issue, the following approach is adopted. The second invariant of the plastic strain rate and stress tensors are:

$$D_2^p = \tfrac{1}{2}\dot\varepsilon_{ij}^p\,\dot\varepsilon_{ij}^p = \tfrac{3}{4}\left(\dot\varepsilon_g^p\right)^2 \qquad J_2 = \tfrac{1}{2}s_{ij}\,s_{ij} = \tfrac{1}{3}\sigma_g^2 \tag{2.3-6}$$

where ε_g and σ_g are denoted the equivalent uniaxial strain and stress, respectively. By substituting Eqns. 2.3−6 into Eqn. 2.3−4, an expression for the equivalent stress is obtained:

$$\sigma_g = Z\left[\ln\frac{D_0^2}{\tfrac{3}{4}\left(\dot\varepsilon_g^p\right)^2}\right]^{-\frac{1}{2n}} \tag{2.3-7}$$

By assuming a plastic strain rate and a hardening parameter Z, a corresponding uniaxial stress is computed. Beyond yield, the plastic strain rate is approximately equal to be the total strain rate ($\dot\varepsilon_{ij}^e \to 0$). For most metals, the hardening parameter Z at yield remains very near the initial value of Z_0. Thus, an approximation for the yield stress at a given strain rate is determined by using Z_0 and the total uniaxial strain rate in Eqn. 2.3−7. Similarly, use of the maximum value for the hardening parameter, Z_1, in Eqn. 2.3−7 provides an estimate for the saturation stress. These two approximations are:

$$\sigma_y \approx Z_0\left[\ln\frac{D_0^2}{\left(\tfrac{3}{4}\dot\varepsilon_g^2\right)}\right]^{-\frac{1}{2n}} \qquad \sigma_u \approx Z_1\left[\ln\frac{D_0^2}{\left(\tfrac{3}{4}\dot\varepsilon_g^2\right)}\right]^{-\frac{1}{2n}} \tag{2.3-8}$$

2.3.1 Viscoplastic Parameters for A533B Steel

Viscoplastic characterization of a material with the Bodner−Partom material model requires multiple uniaxial tests of the material under widely varying strain rates. The extensive testing and associated expense have limited the number of materials for which constants are available.

Dexter, et. al., [24,26] have tested A533B steel to determine properties for the Bodner−Partom material model. Most vessels in U.S. pressurized water reactors (PWRs) are constructed of A533B steel. The A533B material tested by Dexter et. al. originated from the same quenched and tempered plate that was tested in the first series of wide plate crack−arrest experiments performed at the National Institute of Science and Technology (NIST) [75].

Chemical Composition Percent by Weight:						
0.19 C	1.28 Mn	0.012 P	0.013 S	0.21 Si	0.64 Ni	0.55 Mo

Quenched and Tempered: 1640°F (893°C) for 7.5 hours, water quenched
1150°F (621°C) for 50 hours
furnace cooled to 600°F (316°C)

Hardness: 89−91 HV (average) uniform through 7.36 in (18.7cm) thickness

Average Room Temperature Quasi−Static Properties:

Young's Modulus	$E = 30,000\ ksi\ (206.9\ GPa)$
Poisson's Ratio	$\nu = 0.3$
Yield Stress	$\sigma_y = 64.54\ ksi\ (445\ MPa)$
Ultimate Stress	$\sigma_u = 86.59\ ksi\ (597\ MPa)$
Elongation	24%
Area Reduction	69%
Thermal Expansion	$a_T = 6.1 \times 10^{-6}/F°\ \left(11 \times 10^{-6}/C°\right)$
Density	$\varrho = 7.35 \times 10^{-4}\ lb\text{-}sec^2/in^4\ \left(7850\ Kg/m^3\right)$

Table 2.3−1. Chemical Composition and Mechanical Properties for A533B Steel

The chemical composition and other physical properties are provided in Table 2.3−1. Tensile tests at four different strain rates, ranging from 10^{-3}/sec to 10^3/sec, were performed at five different temperatures in the range of −76° to 347°F (−60° to 175°C). All tensile tests were performed with the loading axis parallel to the rolling direction of the plate material. Following conventional uniaxial testing procedures in accordance with ASTM A370, stress−strain curves for the strain rates of 0.001, 0.01 and 1.0/sec were obtained. The Hopkinson tensile bar test [24] was used to obtain stress−strain curves for strain rates above 500 sec^{-1}. This test generates high rate tensile loading through a two−bar system with the specimen placed so that it acts as a tensile link between the two bars. The compressive wave generated by impacting the first bar is transmitted directly through to the second bar. At the end of the second bar the compressive stress wave is reflected into a tensile wave which then separates the two bars and loads the specimen [24].

Dexter, et. al., [24,26] outline methods utilized to define Bodner−Partom coefficients from the stress−strain data. To simplify the process, the limiting plastic strain rate in shear, D_0, is typically assigned an arbitrarily large value (e.g. $> 10^4$/sec). The model behavior is insensitive to the choice of D_0 for strain rates that are at least two orders of magnitude lower than D_0. The best estimate for D_0 is on the order of 10^8/sec [24,15]. Rearrangement of Eqns. 2.3−4, 2.3−5, and 2.3−6 yields expressions for the parameters m and n:

$$m = \frac{d\gamma}{d\sigma} \quad \text{where} \quad \gamma = \frac{1}{\sigma}\frac{d\gamma}{d\sigma} \qquad (2.3-9)$$

and

$$\frac{1}{n} = -2\frac{d(\ln \sigma_u)}{d(\ln S)} \quad \text{where} \quad S = 2\ln\left[2\frac{D_0}{\sqrt{3}\dot{\varepsilon}_g^p}\right] \qquad (2.3-10)$$

σ_s is the saturation stress. The hardening parameters, Z_0 and Z_1, are obtained readily from the relationships derived in Eqns. 2.3−8. Following these procedures, Dexter et. al. obtained the material constants for five different temperatures summarized in Table 2.3−2.

Temperature		m		n	Z_0		Z_1		D_0
(°C)	(°F)	(MPa^{-1})	(ksi^{-1})		(MPa)	(ksi)	(MPa)	(ksi)	(sec^{-1})
−60°	−76°	0.050	0.345	1.62	1772	257.0	2224	322.6	10^8
−10°	14°	0.053	0.365	1.68	1491	216.2	1992	288.9	10^8
50°	122°	0.064	0.441	1.75	1379	200.0	1804	261.6	10^8
100°	212°	0.066	0.455	2.57	907	131.5	1236	179.3	10^8
175°	347°	0.074	0.510	2.77	827	119.9	1112	161.3	10^8

Table 2.3−2 Bodner−Partom Constants for A533B Steel

The resulting stress−strain curves for different strain rates at three different temperatures, −76°F, 133°F, and 347°F (−60°C, 50°C, and 175°F), are shown in Fig. 2.3−2. (The stress−strain curves for intermediate temperatures in Table 2.3−2 are bounded by those shown in Fig. 2.3−2). The stress−strain curves show a definitive yield stress as discussed in the previous section. These yield stresses are predicted accurately by Eqn. 2.3−7. As expected, the yield stress increases significantly with strain rate. Contrary to typical behavior for most steels [24], the strain rate sensitivity increases with a decrease in temperature. Dexter et. al. speculate that this behavior may be due to dynamic strain−aging of the material [24,26].

Other materials similarily characterized for the Bodner−Partom model include: A537 steel, X46 and X70 pipeline steels [25], and B1900+Hf, a nickel based super−alloy [20].

2.4 Procedures for Impact Testing

As described in Section 2.2, the determination of a critical J−value from a test on an SE(B) specimen requires, at a minimum, the histories of the applied load and the load−line displace-
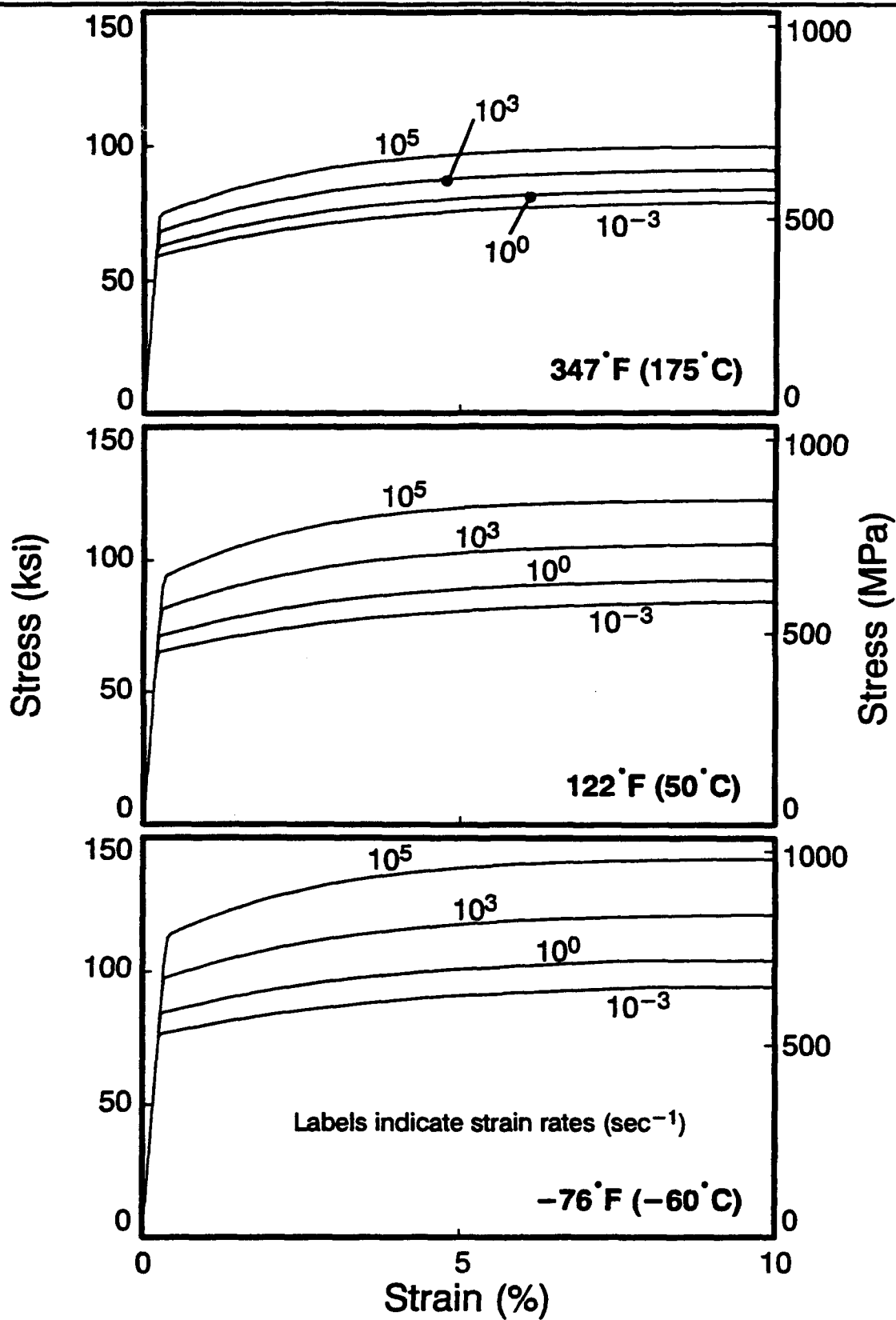
Figure 2.3-2. Bodner-Partom Stress Strain Curves for A533B Steel

ment. Procedures to obtain these measurements for impact loading are examined in this section. Discussion of the drop tower tests, highlighting the similarities and differences between deep crack tests [49,50,51,52,53,54] and shallow crack tests [59,60], follow.

2.4.1 Displacement History

The testing apparatus (see Fig. 1.1−1) is designed to generate a constant velocity response for all specimens (for a given drop height of the tup). To realize this, the potential energy of the tup must overwhelm the internal energy absorbed by the specimen prior to fracture. The

Figure 2.4−1. Load Line Displacement for Deep and Shallow Crack SE(B)
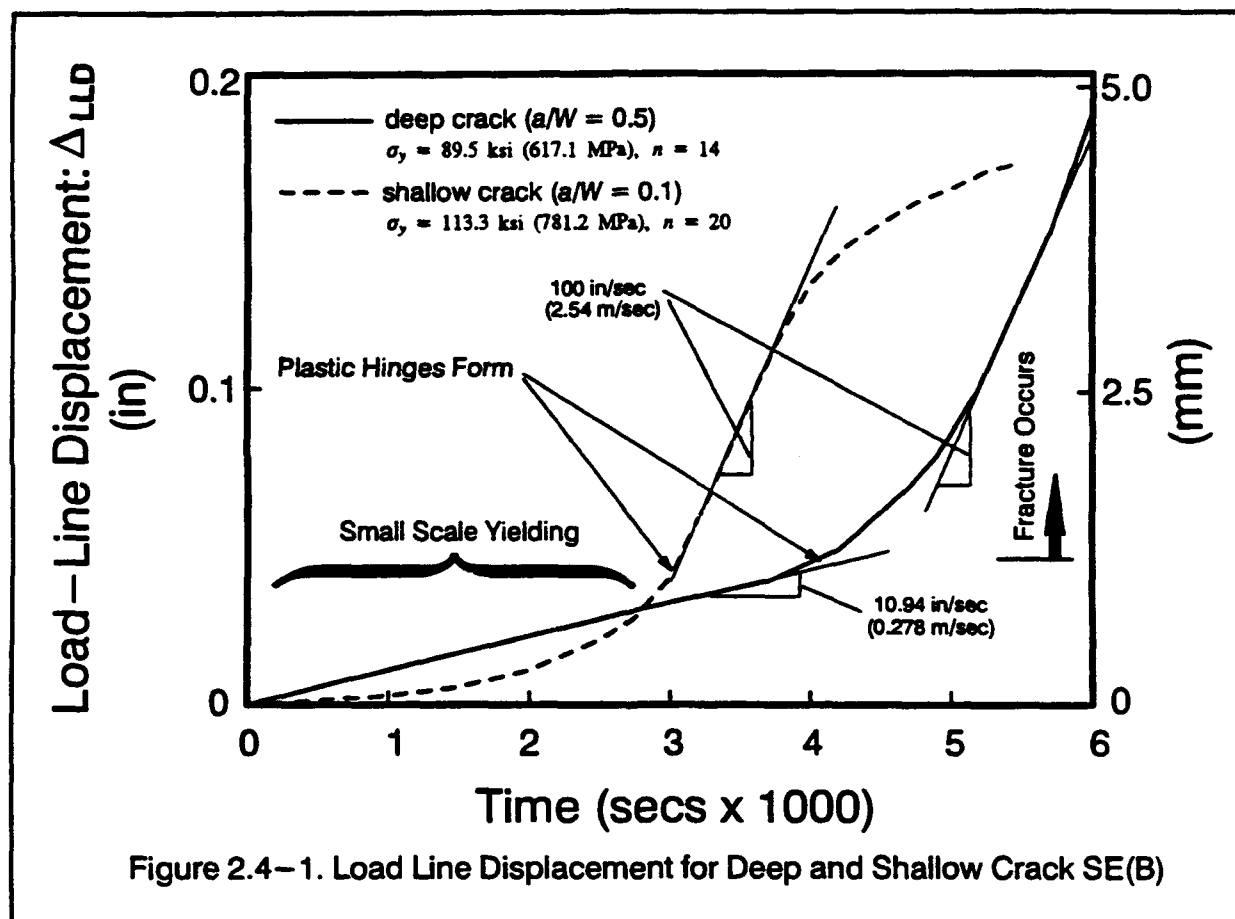
resulting constant velocity produces a final linear displacement−time loading of the specimen. Figure 2.4−1 compares the measured displacement−time curves for the different types of specimens.

An optical probe attached directly to the specimen measures the load−line displacement for the deep crack SE(B) specimens. Even at large deformations, the plastic zone in these specimens is confined to the remaining ligament, leaving a large portion of material remote from the crack plane elastic, with little deformation. This facilitates attachment of the optical light

30

probe (see Fig. 2.4−2). The plastic zone in shallow crack SE(B) specimens, however, spreads beyond the remaining ligament, occupying most of the mid−section of the entire specimen. Figure 2.4−2 shows the von Mises stresses on the two specimen types at the same load−line displacement, illustrating this phenomena. The attachment of a measuring device directly to the shallow crack SE(B) specimen near the crack plane is difficult due to the large strains in the plastic zone. An array of four eddy current gages placed underneath the specimen, is used to estimate the load−line displacement (see Fig. 1.4−1). An empirical correlation developed in Ref. [59] relates the measurements from the four eddy current gages to the load−line displacement. Typical displacement vs. time curves for a deep crack and a shallow crack specimen are given in [51,60] respectively.

Figure 2.4−2. von Mises Stress Contours for the Deep and Shallow Crack SE(B)
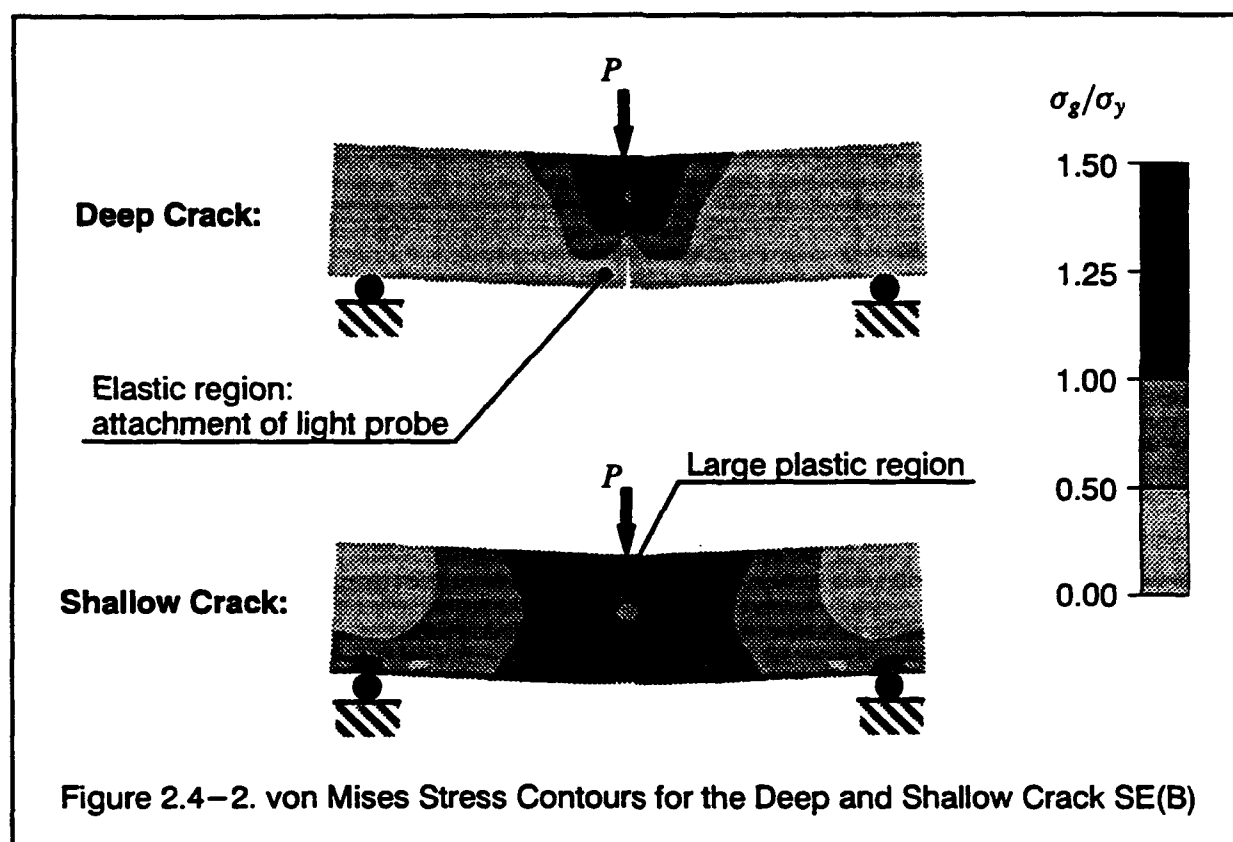
The different specimens, materials and testing procedures produce the deviation between the the two load−line displacement curves in Fig. 2.4−1. The deep crack specimens (a/W>0.5) have a 1 in. by 2 in. (25.4 mm by 50.8 mm) cross section with 20% side grooves. The load is applied by a 700 lb (320 Kg) hammer dropped from a height of 12.9 inches (0.33m). The free−falling velocity of the tup at impact was 100 in/sec (2.54 m/sec) [51]. The shallow crack specimens (a/W=0.1) have a 2 in by 2 in cross section, with no side grooves. The load is applied by a 1475 lb (669 Kg) hammer dropped from a height of 48 inches (1.22 m.). The free−falling

	Deep Crack a/W = 0.5	Shallow Crack a/W = 0.1
Specimen Dimensions:	1 in. by 2 in. by 9 in. (25.4 mm by 50.8 mm by 228.6 mm)	2 in. by 2 in. by 9 in. (50.8 mm by 50.8 mm by 228.6 mm)
Side Grooves:	20%	none
Material:	HY80 σ_y = 89 ksi (614 Mpa) σ_u = 106 ksi (731 Mpa)	HY100 σ_y = 113 ksi (779 Mpa) σ_u = 126 ksi (871 Mpa)
Tup Weight:	700 lbs (320 Kg)	1475 lbs (669 Kg)
Tup Drop Height:	12.9 in. (0.33 m)	48.0 in. (1.22 m)
Tup Impact Velocity:	100 in/sec (2.54 m/sec)	194 in/sec (4.88 m/sec)
Total Displacement:	0.20 in. (5.08 mm)	0.17 in. (4.32 mm)
Aluminum Absorbers:	2 wedges	1 pyramid

Table 2.4−1. Summaries of Impact Tests for Deep and Shallow Crack SE(B) Specimens

velocity of the hammer at impact was 194 in/sec (4.88 m/sec) for the shallow crack tests [60]. A stopping block fixture limited the total load−line displacement for the experiments. The maximum total load−line displacement was set at 0.2 inch (5.08 mm) for the deep crack experiments and at 0.17 inch (4.3 mm) for the shallow crack experiments. Table 2.4−1 summarizes the impact parameters for the two SE(B) specimen types.

Both shallow and deep notch tests employed aluminum wedges to minimize the high frequency content of the initial response immediately after impact. The load−line velocity of the specimen remained considerably below the impact velocity of the hammer until approximately 0.0045 sec for the deep crack and 0.003 sec for the shallow crack. The aluminum dampers absorb the early velocity difference between the loading tup and the specimen. As shown in Fig. 2.4−1, the deep crack specimen experiences nearly constant velocity while the shallow crack specimen experiences an increasing velocity during this period. The terminal velocity of the deep cracked bend specimens approaches the tup velocity of 100 in/sec (2.54 m/sec). The shallow flaw specimens, however, remain well below the intended terminal velocity (100 in/sec vs. 194 in/sec). Additional deformation taken by the absorbers reduces the maximum velocity experienced by the shallow crack specimens.

To generate meaningful comparisons for different crack depths in finite element analyses, the same displacement–time history is applied to the configurations included in the analysis matrix. The displacement history of the deep crack specimen is adopted for the finite element analyses. The very similar terminal velocity of 100 in/sec (2.54 m/sec) for the two specimen types suggests this approach (see Fig. 2.4–1).

2.4.2 Load History

Measurement of the applied load directly from an instrumented tup attached to the drop hammer is extremely difficult. Stress wave effects in the tup, combined with the complex interaction between the tup, the aluminum absorbers and the specimen, lead to significant uncertainties in the measured loads. Instead, the applied loads are inferred from strains measured at gages attached directly on the specimen [49,59]. Strain gages located midway between the crack plane and the specimen supports (1/4 point strains) provide a deformation history for both the deep crack and shallow crack SE(B) specimens. Figures 1.1–1 and 1.4–1 show the locations of these strain gages for the two types of specimens.

For the deep crack specimens, a static calibration relates the strain gage readings to an applied load. By assuming plane sections remain plane, two strain gages, (one on the top surface and one on the bottom surface,) quantify the deformation. Since material at the strain gage locations is remote from the crack plane and remains elastic for the entire loading history, the static calibration is valid in the absence of inertia effects.

For the shallow crack specimens, these strain gage locations are not expected to remain unyielded for the loading duration. Plasticity and spatially nonlinear strain distributions require a more detailed strain resolution over the specimen depth for the calculation of moments. Kirk et. al. [59] placed 6 strain gages at equally spaced locations (see Fig. 1.4–1). Corresponding stresses are computed using the static, uniaxial stress–strain curve. The moment was obtained by integration of the stress distribution. An inferred (static) load is calculated from the moment at the 1/4 point location using the model for a simply supported beam with a concentrated load at midspan.

In this study, the suitability of this technique to obtain the applied load is investigated using results of the finite element analyses. The strains at key locations in the finite element model are extracted and correlated to a (known) specimen load. In addition, researchers in fracture testing have expressed a desire to infer the applied load from measured support reactions. Such a proposal is also investigated in this study.

33

3 Computational Methods

Short duration impact loading of fracture specimens introduces a number of complications in the numerical modelling. This chapter addresses the following aspects of the 3−D nonlinear finite element analyses as outlined below:

- The dynamic response of the specimens is computed using an explicit time history integration technique. Explicit methods allow the local monitoring of discrete stress waves that occur immediately after impact and also provide the global response of the structure. The small time step required for stability of the solution, however, makes the explicit technique computationally expensive with respect to processor time required. Spectrom, the finite element program utilized in this study, minimizes processor time through a reduced integration order (one point) in the finite elements coupled with hourglassing suppression techniques.

- Strain−rate effects are introduced through a Bodner−Partom viscoplastic material model. This model was implemented in Spectrom as part of this study. The strong dependence of the plastic strain rate on the stresses required development of a new iterative stress−update algorithm. The development and implementation of an efficient updating scheme is essential to preserve the economy gained by the one−point integration of the elements.

- J−integral values are computed numerically by integrating quantities from the finite element analyses at specific time steps. Additional terms in the domain integrals that arise due to the dynamic response are included in the J computations.

- Impact testing, as conducted in a drop tower, imposes an essentially displacement controlled loading on SE(B) specimens. Direct application of the displacement history as a loading in the finite−element analyses produces unrealistic oscillations in the response. A technique is developed to define an equivalent loading that when applied to the finite−element model produces the desired displacement history.

The chapter is divided into four major sections corresponding to the topics listed above.

3.1 Spectrom: Dynamic Finite Element Program

Spectrom [57] is a Fortran−77 program that computes the dynamic response of arbitrary three−dimensional bodies under general loadings. The program utilizes an explicit scheme to integrate through time, which makes it ideal for the monitoring of stress−wave effects. Element formulations accommodate large displacements using an Updated Lagrangian approach. Several elements are available in the program including 4−node shell elements and three−dimensional 8−node bricks. The elements are integrated with one−point Gauss sampling coupled with zero−energy mode suppression. The low order of Gauss integration and the explicit time history integration reduce significantly the number of computations per time step . Elastic, inelastic and viscosity capabilities are available in the material models implem-

ented in the program. The program uses single precision storage for all variables and runs efficiently on 32−bit workstation environments as well as supercomputers.

The remainder of this section describes key aspects of the Spectrom software. Modifications performed on the original code for this study are first summarized. This is followed by a discussion of the variable step size approach utilized for the time history integration. The stress updating procedure and the element formulation of the single integration point, eight−node isoparametric element follow. This section concludes with a description of the technique adopted to suppress zero−energy deformation modes.

3.1.1 Spectrom Modifications

The source code for Spectrom as implemented on a DEC−VMS mini−computer was obtained from RE/SPEC [57]. Various modifications to the original source code were necessary to support this research. These modifications are:

1. *Machine dependencies*. The original source code was modified to upgrade machine dependant routines and file specifications for Unix workstations and a Convex C−240.

2. *Optimization*. The source code was optimized to run approximately 30% faster on the Unix workstations. This was done by *unrolling* all do−loops in the element computations.

3. *Hourglassing Energies*. Additional data structures and coding were implemented to monitor the hourglassing energy in the elements. The total amount of energy utilized for the hour glass control in the entire structure is output at specified time steps.

4. *Restart Capability*. The original restart features lacked the ability to change the applied loading. The modifications implemented allow load modification.

5. *Bodner−Partom Material Model*. The Bodner−Partom material model was implemented.

6. *Control Parameters*. Modifications to allow control over the time step size and hourglass parameters were implemented.

7. *Interface Programs*. Computer software to interface Spectrom with PATRAN [84] was designed and implemented.

3.1.2 Determination of Time Step Size

Spectrom utilizes a central difference method for time history integration. This technique, coupled with the use of lumped masses at the nodes, avoids triangulation of the global matrices (stiffness and mass matrix). In the absence of viscous damping effects, the equation of motion in matrix form is:

35

$$[M]\{\ddot{u}\}_t = \{F_{ext}\}_t - \{F_{int}\}_t \qquad (3.1-1)$$

where $[M]$ is the structural lumped mass matrix, $\{\ddot{u}\}_t$ are the nodal accelerations, $\{F_{ext}\}_t$ are the externally applied nodal loads, and $\{F_{int}\}_t$ are the element internal resisting forces. The subscript t identifies the current time.
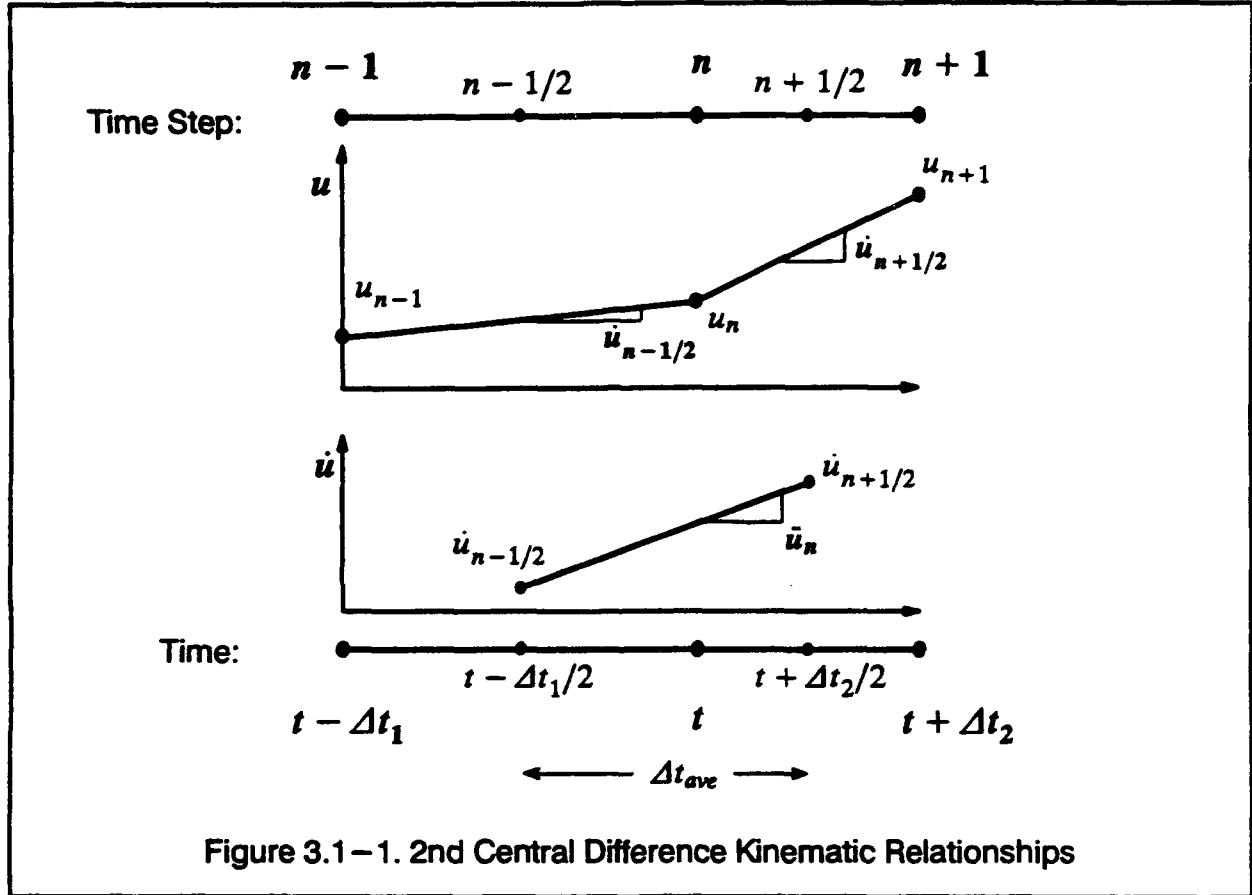
Figure 3.1−1. 2nd Central Difference Kinematic Relationships

Spectrom uses a variable time step as illustrated in Fig. 3.1−1. The central differencing scheme then becomes:

$$\{F_{int}\}_n = \sum_{i=1}^{nelem} \int_{Vol} [B]_n^T \{\sigma\}_n \, dV \qquad (3.1-2)$$

$$\{\ddot{u}\}_n = [M]^{-1}\left(\{F_{ext}\}_n - \{F_{int}\}_n \right) \qquad (3.1-3)$$

$$\{\dot{u}\}_{n+1/2} = \{\dot{u}\}_{n-1/2} + \{\ddot{u}\}_n \, \Delta t_{ave} \qquad (3.1-4)$$

36

$$\{u\}_{n+1} = \{u\}_n + \{\dot{u}\}_{n+1/2}(\Delta t_2) \tag{3.1-5}$$

where $[B]$ is the element divergence operator, $\{u\}$ and $\{\dot{u}\}$ are the nodal displacements and velocities, Δt_1 and Δt_2 are the time step sizes immediately before and after the current time t. Subscripts identify the time step, with mid-interval times, $t - \Delta t_1$ and $t + \Delta t_2$ symbolically defined as time steps $n - 1/2$ and $n + 1/2$. The displacement and velocity updating algorithm follows the order given above. Equation 3.1-2 defines the summation of internal forces at time t. The imbalance of the forces determines the nodal accelerations at time t (Equation 3.1-3). Inversion of the mass matrix as shown in Eqn. 3.1-3 is trivial for a diagonal mass matrix. By using the computed accelerations at time t, the velocities are calculated for the midpoint of the next time interval Δt_2 (Equation 3.1-4). These velocities are then used to update the displacements to the end of the next time step (Equation 3.1-5). The process is repeated for the duration of the analysis.

The central difference method is conditionally stable (energy balance is maintained) with respect to time step size [57,58,10]. To obtain a stable solution, the selected time step size must remain below the critical time step, Δt_{cr}, given by:

$$\Delta t_{cr} = \frac{T_n}{\pi} = \frac{2}{\sqrt{\lambda_n}} \tag{3.1-6}$$

where λ_n is the largest eigenvalue of the finite element model and T_n is the corresponding period. The period of the largest eigenvalue of a finite element model is closely related to the minimum time required for a dilatational stress wave to traverse an element [10,57]. Flanagan [38] developed an approximate technique to calculate the maximum eigenvalue for a 3-dimensional finite element model composed of 8-node finite elements with one-point integration:

$$\lambda_n \approx \left(\frac{2c_1}{\delta_{min}}\right)^2 ; \qquad c_1 = \sqrt{\frac{(1-\nu)E}{(1+\nu)(1-2\nu)\varrho}} \tag{3.1-7}$$

where δ_{min} is the smallest generalized element dimension of all elements in the model, and c_1 is the dilatation wave speed in an unbounded medium. (For special cases in 1-dimensional wave propagation, δ is the element length and the above relationship is exact.) For a given element, δ is defined by:

$$\delta = \frac{1}{\sqrt{2}}\left[\sum_{i=1}^{8}\left(\frac{\partial N_i}{\partial x}\right)^2 + \sum_{i=1}^{8}\left(\frac{\partial N_i}{\partial y}\right)^2 + \sum_{i=1}^{8}\left(\frac{\partial N_i}{\partial z}\right)^2\right]^{-\frac{1}{2}} \tag{3.1-8}$$

37

where N_i is the shape function corresponding to the ith local node. The shape function derivatives in Eqn. 3.1−8 are evaluated at the integration point of the element. The resulting approximation for Δt_{cr} is:

$$\Delta t_{cr} \approx \frac{\delta_{min}}{c_1} \tag{3.1−9}$$

Thus the estimated critical time step is simply the time required for an unconfined dilatational stress wave to travel the generalized element dimension. (For a simple unit cube, δ is equal to 0.577, or $1/\sqrt{3}$.) This approximation of the critical time step is much more economical than solving for the highest eigenvalue of the finite element mesh. The critical time step is calculated for each individual element in the finite element mesh at each time step. By choosing the smallest Δt_{cr} at each time step, a non−divergent solution is generated.

To account for distortional (shear) waves, an additional constraint is placed on selection of the time step size:

$$\Delta t_{shear} = \frac{\delta_{min}}{c_2} \; ; \qquad c_2 = \sqrt{\frac{G}{\varrho}} \tag{3.1−10}$$

where c_2 is the dilatational wave speed. The time step chosen must be smaller than Δt_{shear} for the distortional waves to be modelled adequately (otherwise an element with the minimum generalized dimension will not *sense* the deformation). The time step is then chosen as:

$$\Delta t = \min\left(\Delta t_{shear} , \Delta t_{cr}\right) \tag{3.1−11}$$

For nonlinear material behavior, a consistent tangent modulus approach is used to compute the elastic constants for use in Eqns. 3.1−7 and 3.1−10. Equivalent elastic constants that relate the total increments of stresses and strains for a given time step are used to calculate the dilatational and the distortional wave speeds. The solution process thus takes advantage of the increase in the critical time step size due to the softening of elements undergoing plastic deformation.

3.1.3 Stress Update Procedures

The Updated Lagrangian approach in Spectrom utilizes the configuration at time step n as the reference state (See Fig. 3.1−2.). Stresses, strains and internal forces are computed in this configuration. This section describes the strain−stress rates employed in the constitutive models and their numerical evaluation (see Healy and Dodds [10] for additional details).
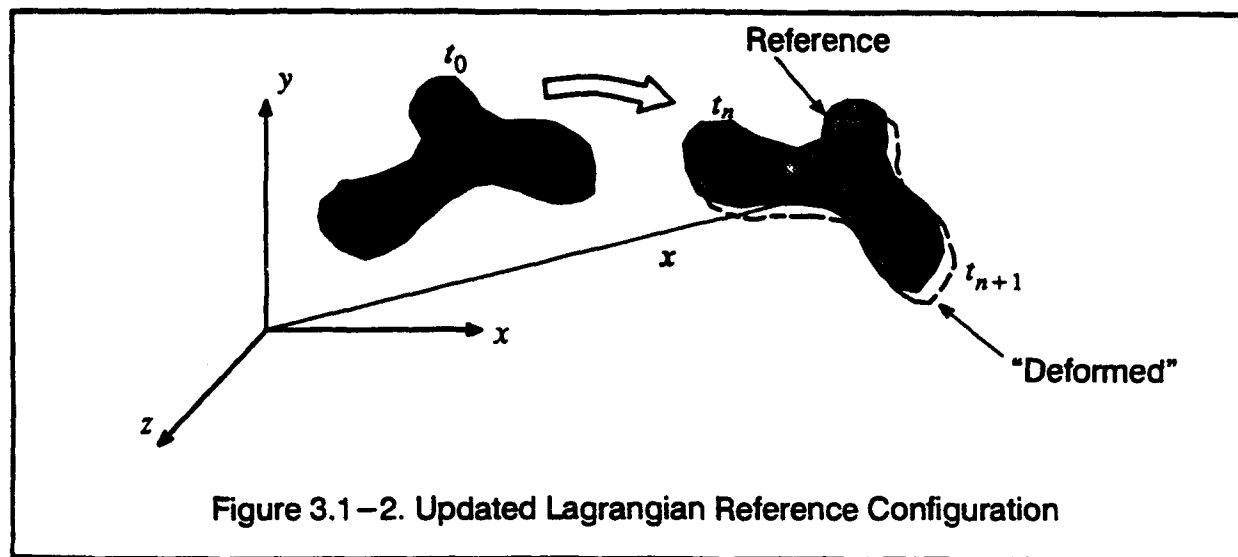
Figure 3.1—2. Updated Lagrangian Reference Configuration

The spatial gradient of the material velocities with respect to the current configuration is given by:

$$L = \frac{\partial v}{\partial x} \tag{3.1-12}$$

where in matrix form:

$$L = \begin{bmatrix} \dfrac{\partial v_x}{\partial x} & \dfrac{\partial v_y}{\partial x} & \dfrac{\partial v_z}{\partial x} \\[2mm] \dfrac{\partial v_x}{\partial y} & \dfrac{\partial v_y}{\partial y} & \dfrac{\partial v_z}{\partial y} \\[2mm] \dfrac{\partial v_x}{\partial z} & \dfrac{\partial v_y}{\partial z} & \dfrac{\partial v_z}{\partial z} \end{bmatrix} \tag{3.1-13}$$

The symmetric part of L is the spatial rate of the deformation tensor, D, and the skew—symmetric part, W, is the spin rate or the vorticity tensor. Thus,

$$L = D + W \tag{3.1-14}$$

where

$$D = \tfrac{1}{2}\left(L + L^T\right); \qquad W = \tfrac{1}{2}\left(L - L^T\right) \tag{3.1-15}$$

W represents the rate of rotation of the principal axes of the spatial rate of deformation, D. For the special case of zero rotation, i.e. $W = 0$, the principal values of D, integrated over time,

39

yield the logarithmic (true) strains of infinitesimal material fibers oriented in the principal directions of **D**. **L**, **D**, and **W** have no sense of the deformation history; they are instantaneous rates.

The rate of deformation tensor, **D**, is the energy conjugate strain−rate measure for the Cauchy stresses referred to the current configuration [10,43]. The Jaumann rate for Cauchy stress is used as a materially objective stress rate. A constitutive relation couples the Jaumann stress rate to the rate of deformation tensor. For simplicity, the constitutive behavior is assumed to be expressible as a tensor product. The Jaumann stress rate, $\dot{\mathbf{T}}_J$, is given by:

$$\dot{\mathbf{T}}_J = \dot{\mathbf{T}} - \mathbf{WT} + \mathbf{TW} = \mathbf{C} : \mathbf{D} \qquad (3.1-16)$$

where the symmetric, Cauchy stress **T** is:

$$\mathbf{T} = \begin{bmatrix} \sigma_{xx} & \tau_{xy} & \tau_{xz} \\ \tau_{xy} & \sigma_{yy} & \tau_{yz} \\ \tau_{xz} & \tau_{yz} & \sigma_{zz} \end{bmatrix} \qquad (3.1-17)$$

σ_{ii} and τ_{ij} are components of the Cauchy stress tensor referred to a Cartesian coordinate system defined on the current configuration. $\dot{\mathbf{T}}$ is the needed spatial rate of Cauchy stress due to the instantaneous motion defined by **L**. **C** is the modulus tensor and may depend on the stresses, strain rates and history dependent state variables. The process for updating the stresses in the current configuration then becomes:

$$\dot{\mathbf{T}} = \mathbf{C} : \mathbf{D} + \mathbf{WT} - \mathbf{TW} \qquad (3.1-18)$$

$$\Delta\mathbf{T} = \dot{\mathbf{T}}\Delta t \qquad (3.1-19)$$

$$\mathbf{T}_{new} = \mathbf{T}_{old} + \Delta\mathbf{T} \qquad (3.1-20)$$

where $\Delta\mathbf{T}$ is the increment of Cauchy stress that corresponds to the motion defined by **L** through a time increment of Δt. Various integration schemes can be applied to Eqns. 3.1−18 through 3.1−20. If all the terms in Eqn. 3.1−18 are evaluated at time t, $\dot{\mathbf{T}}$ is the Cauchy stress rate at time t and the integration procedure corresponds to a simple forward Euler scheme. Evaluation of Eqn. 3.1−18 at time $t + \Delta t$ corresponds to a backward Euler scheme. In general, the stresses and history dependent state variables are not known at time $t + \Delta t$. Consequently, the backward Eulerian approach requires an iterative technique to calculate the values at

$t + \Delta t$. Other tensorial state variables, such as the back−stresses for kinematic hardening plasticity, must also be updated according to Eqn. 3.1−16.

The relatively small time steps required for the globally explicit solution make the differences between the tensor at time t, $t − \Delta t$ (time step n, $n − 1$) or any intermediate time, insignificant (i.e. Δt is so small that the reference and the deformed configurations in Fig. 3.1−2 are almost identical). Computational economy determines the particular choice of the time corresponding to the individual tensors in Eqns. 3.1−21 and 3.1−22. For the computation of stresses at time step n, Spectrom utilizes the velocity gradient at the mid−interval of the previous time step, $n − 1/2$ (with respect to the configuration at time step n), together with the stresses at time step $n − 1$ to integrate Eqn. 3.1−18. In summary:

$$\dot{T} = C : D_{n-1/2} + W_{n-1/2}T_{n-1} − T_{n-1}W_{n-1/2} \tag{3.1−21}$$

$$L_{n-1/2} = B_n \, v_{n-1/2} \tag{3.1−22}$$

For the internal force calculation at time step n, the gradient operator B is needed at time t_n, and the nodal velocities are available at time $t_{n-1/2}$ (Eqns. 3.1−2 and 3.1−4). Use of these same tensor quantities for the stress updates reduces the computations required per time step.

The Jaumann rate of Cauchy stress has been widely applied in finite element codes due to its simplicity. For some deformations, in which shear strains exceed 100%, the Jaumann stress rate predicts an unacceptable response [43,27]. For a large range of finite shear strains, up to near 100%, however, the Jaumann stress rate predicts physically acceptable results [43]. Shear strains in this study are considerably below 100%, thus making use of the Jaumann stress rate acceptable.

3.1.4 Element Formulation

Spectrom utilizes the trilinear, eight−node isoparametric element for three−dimensional continuum models. A mean strain−rate quadrature scheme combined with hourglass control makes the computation of element internal forces very efficient [37,57,11]. For a globally explicit formulation, element internal force evaluation and stress updating are the major computational tasks.

The element displacement field and spatial configuration are related to the element nodal displacements and current coordinates through the trilinear isoparametric shape functions [21]:

$$u_i(\xi,\eta,\zeta) = \sum_{I=1}^{I=8} N^I(\xi,\eta,\zeta) \, u_i^I \quad or \quad u_i = N^I u_i^I \tag{3.1-23}$$

$$x_i(\xi,\eta,\zeta) = \sum_{I=1}^{I=8} N^I(\xi,\eta,\zeta) \, x_i^I \quad or \quad x_i = N^I x_i^I \tag{3.1-24}$$

where the superscript I refers to the element node and the subscript i refers to the coordinate direction (See Fig. 3.1–3). ξ, η, ζ are the isoparametric coordinates, N^I is the shape function
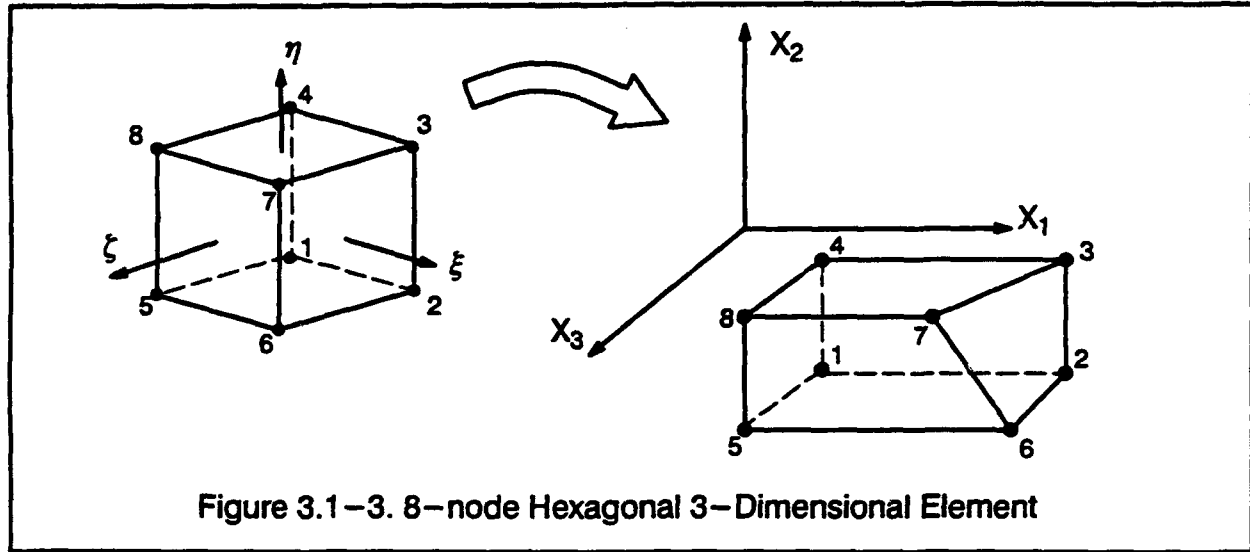
Figure 3.1–3. 8–node Hexagonal 3–Dimensional Element

corresponding to node I, and u_i^I and x_i^I are the element displacements and current coordinates respectively in the ith coordinate direction at node I. The right hand side of Eqns. 3.1–23 is expressed in incidicial notation where repeated subscripts imply summation over the range of that subscript. (i, j, k indicate coordinate directions with a range of 1 to 3; I, J, K indicate element nodes with a range of 1 to 8.) The isoparametric formulation eliminates the material–rate derivative when taking the time derivatives of Eqns. 3.1–23 and 3.1–24. Thus, the same interpolating functions provide the velocity field in the element:

$$v_i = N^I v_i^I \tag{3.1-25}$$

The velocity gradient is then defined as follows:

$$\frac{\partial v_i}{\partial x_j} = v_{i,j} = \sum_{I=1}^{I=8} \frac{\partial N^I}{\partial x_j} v_i^I = N_{,j}^I v_i^I \tag{3.1-26}$$

42

where v_i^I is the element velocity in the ith coordinate direction at node I. Using the principle of virtual work in the current configuration, the element nodal forces are computed from the divergence of Cauchy stress field as:

$$\delta v_i^I f_i^I = \int_V \sigma_{ij}\, \delta v_{i,j}\, dV \qquad (3.1-27)$$

where, $v_{i,j}$, and σ_{ij} are components of the velocity gradient tensor, L, and the Cauchy stress tensor, T, respectively. Since the Cauchy stress tensor is symmetric, the rate of virtual deformation tensor can be replaced with the virtual velocity gradient tensor. This integral is evaluated assuming a constant stress state and an average strain rate over the element for a time step. Eqn. 3.1−27 then becomes:

$$\delta v_i^I f_i^I = V\, \bar{\sigma}_{ij}\, \delta \bar{v}_{i,j} \qquad (3.1-28)$$

where f_i^I are the element nodal forces, V is the element volume, and $\bar{\sigma}_{ij}$ and $\delta \bar{v}_{i,j}$ are the mean stresses and mean virtual velocity gradient in the element. Mean kinematic quantities are defined over the element as follows:

$$\delta \bar{v}_{i,j} = \frac{1}{V} \int_V \delta v_{i,j}\, dV \qquad (3.1-29)$$

The gradient operator, B_i^I, is defined by integrating the shape function derivatives over the element volume:

$$B_i^I = \int_V N_{,j}^I\, dV = \frac{\partial V}{\partial x_i} \qquad (3.1-30)$$

The mean velocity gradient and the element internal nodal forces are then:

$$\delta \bar{v}_{i,j} = \frac{1}{V} B_j^I \delta v_i^I \qquad f_i^I = \bar{\sigma}_{ij} B_j^I \qquad (3.1-31)$$

Evaluation of the gradient operator is performed with a one−point Gaussian integration, which for the trilinear hexagonal element, produces a closed form expression. Algebraic details are found in [37]. For example, the gradient operator component B_x^1 is given explicitly by:

$$B_x^1 = \frac{1}{12}\left[y^2\left(z^{63} - z^{45}\right) + y^3 z^{24} + y^4\left(z^{38} - z^{52}\right) + y^5\left(z^{86} - z^{24}\right) + y^6 z^{52} + y^8 z^{45}\right] \quad (3.1-32)$$

where x^I, y^I, z^I, are the current Cartesian components of the element node I, and $z^{IJ} = z^I - z^J$. Nodal index and coordinate permutations simplify evaluation of the other gradient operator terms.

3.1.5 Zero–Energy Mode Suppression

Evaluation of the gradient operator by one–point Gaussian quadrature produces an element that admits, (in the addition to the rigid body modes), deformation patterns with no strain energy. These zero–energy modes, often called hourglass modes, if left unaltered, dominate

Figure 3.1–4. Orthogonal Displacement Modes for the
8–node Hexagonal Element
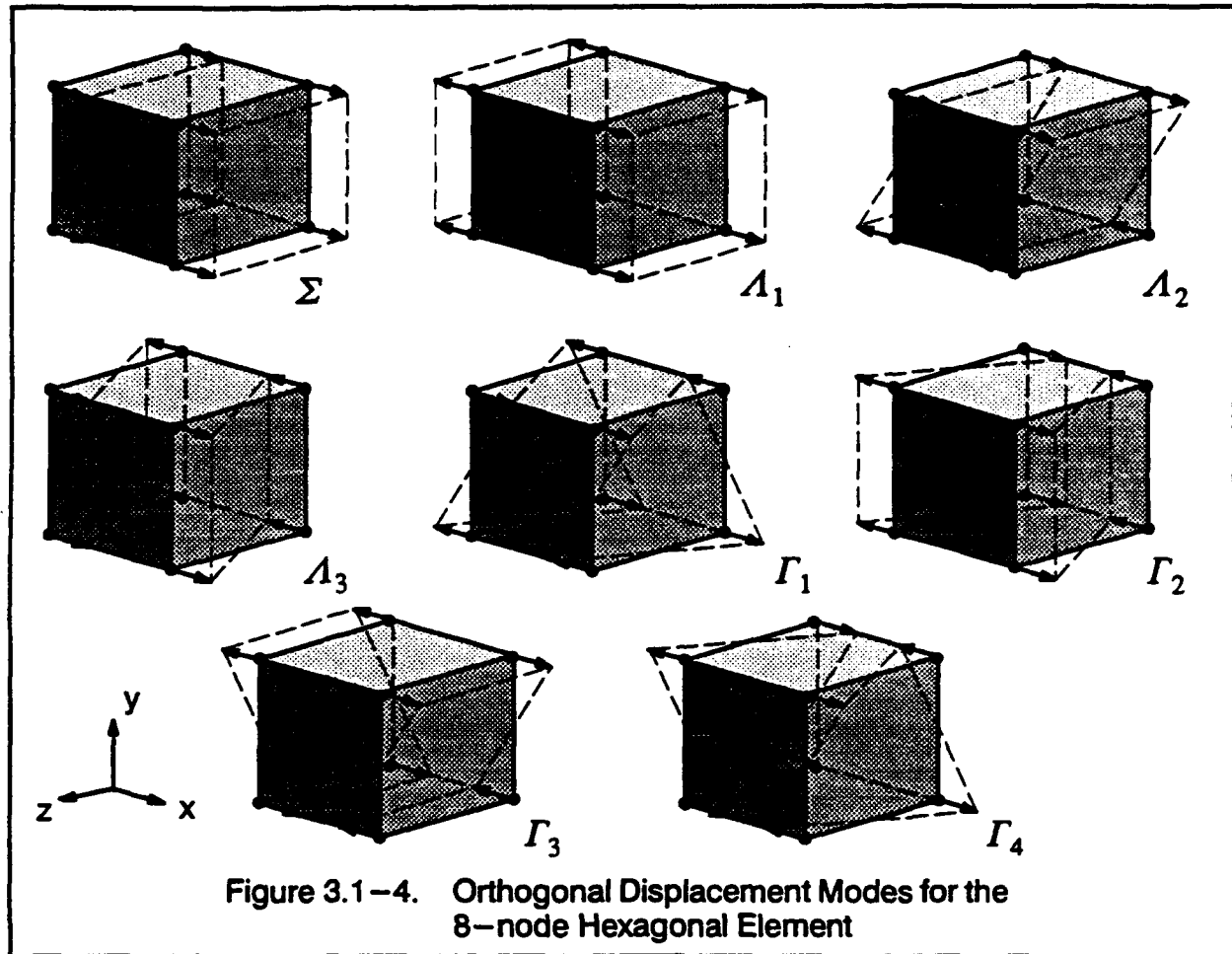
the element deformation thereby making the solution incorrect. Spectrom utilizes an efficient method for the suppression of the zero–energy modes [37,11].

The displacement patterns of the trilinear hexagonal element are expressed as a combination of orthogonal base vectors [37,11,57]. Figure 3.1–4 shows these orthogonal base vectors

for the x–coordinate direction. The first deformation mode, denoted Σ, is the rigid body translation. The next three modes, Λ_1 through Λ_3, represent uniform straining in the x–direction, uniform shear straining in the x–y plane and uniform shear straining in the x–z plane. The remaining four displacement modes, Γ_1 through Γ_4 are the zero–energy modes. Application of the gradient operator (Eqn. 3.1–30) to the zero–energy displacement shapes yields zero:

$$\frac{1}{V}B_i^I \Gamma_a^I = 0 \qquad (3.1-33)$$

where Γ_a^I is the element nodal displacement I corresponding to the zero–energy mode a. (a, β, γ indicate hourglassing modes with a range of 1 to 4.) Table 3.1–1 summarizes the vectorial representation of the orthogonal mode shapes.

Local Node	Σ	Λ_1	Λ_2	Λ_3	Γ_1	Γ_2	Γ_3	Γ_4
1	1	−1	−1	−1	1	1	1	−1
2	1	1	−1	−1	1	−1	−1	1
3	1	1	1	−1	−1	−1	1	−1
4	1	−1	1	−1	−1	1	−1	1
5	1	−1	−1	1	−1	−1	1	1
6	1	1	−1	1	−1	1	−1	−1
7	1	1	1	1	1	1	1	1
8	1	−1	1	1	1	−1	−1	−1

Table 3.1–1. Orthogonal Mode Shapes for the Trilinear Hexagonal Element

The zero–energy, displacement shapes produce no element resistance in the form of internal stresses. These modes are isolated and treated independently of the rigid body and the uniform straining modes. By subtracting the rigid body modes and the uniform straining modes from the velocity field, the field that corresponds to the zero–energy modes is isolated. The velocity at an element node I corresponding to the rigid body and the uniform straining modes, $\left(v_i^{R+S}\right)^I$, is [37,11,57]:

$$\left(v_i^{R+S}\right)^I = v_{i0} + \Delta x^I \frac{\partial v_i}{\partial x} + \Delta y^I \frac{\partial v_i}{\partial y} + \Delta z^I \frac{\partial v_i}{\partial z} \qquad (3.1-34)$$

where v_{i0} is the average velocity of all the element nodes in the coordinate direction i, Δx^I, Δy^I, and Δz^I are the deviation of the nodal coordinates from the coordinates of the integration

point. The first term is readily identified as the rigid−body component, while the remaining three terms are the uniform straining modes. (The rigid−body rotations result from combinations of the uniform shear straining modes in the different coordinate directions, i.e. rotation in the $x-y$ plane from $v_{x,y}$ and $v_{y,x}$). The remaining velocity field $\left(v_i^{HG}\right)^I$ defines the zero−energy modes:

$$\left(v_i^{HG}\right)^I = v_i^I - v_{i0} - \Delta x^I \frac{\partial v_i}{\partial x} - \Delta y^I \frac{\partial v_i}{\partial y} - \Delta z^I \frac{\partial v_i}{\partial z} \tag{3.1−35}$$

or:

$$\left(v_i^{HG}\right)^I = v_i^I - v_{i0} - \frac{1}{V}\left(x_j^I - x_{j0}\right)v_i^J B_j^J \tag{3.1−36}$$

where x_{i0} is the average coordinate of all the element nodes in the ith direction. B_i^J is the gradient operator defined in Eqn. 3.1−30.

An hourglass gradient operator is constructed from the zero−energy basis vectors, Γ_α^I, as follows [37,11,57]:

$$G_\alpha^I = \frac{V}{\delta}\Gamma_\alpha^I \tag{3.1−37}$$

δ is the generalized element dimension as defined in Eqn. 3.1−8, and V is the element volume. The factor V/δ provides the hourglass operator, G_α^I, with the same dimensional characteristics as the gradient operator B_i^I. G_α^I operates on the hourglass velocities to obtain the generalized hourglassing strain rates, $\dot{q}_{i\alpha}$:

$$\dot{q}_{i\alpha} = \frac{1}{V}G_\alpha^I\left(v_i^{HG}\right) \tag{3.1−38}$$

The orthogonal property of the G_α^I operators separate the hourglass velocity field into generalized hourglassing strain rates according to mode α. A constitutive relation is necessary to obtain a generalized stress from the generalized hourglassing strains. Spectrom utilizes a simple relation that has proven effective for most cases [57]:

$$\hat{Q}_{i\alpha} = \varepsilon 2\mu_{\tan}\dot{q}_{i\alpha} \tag{3.1−39}$$

where $\hat{Q}_{i\alpha}$ is the generalized stress of the hourglassing mode α in the ith coordinate direction, $2\mu_{\tan}$ is the tangent shear stiffness obtained from the constitutive model for the element, and

ε is a scaling parameter. In general, ε is taken arbitrarily small; 0.001 is used for this study. This assures that the level of the hourglass restoration forces remains below that of the internal forces due to element straining. For the invariant time derivative of the generalized stresses, finite rotations produce:

$$\hat{Q}_{ia} = \dot{Q}_{ia} - w_{ij}Q_{ja} \tag{3.1-40}$$

where w_{ij} are elements of the spin rate tensor, W, as defined in Eqn. 3.1-15.

The hourglass resisting forces are calculated by assuming energy conjugacy between the generalized stresses and strains. Thus:

$$\left(\delta v_i^I\right)^{HG}\left(f_i^I\right)^{HG} = VQ_{ia}\delta \dot{q}_{ia} \tag{3.1-41}$$

Using the definition of Eqn. 3.1-38 for the generalized hourglass strain rate and solving for the nodal hourglass resisting forces yields:

$$\left(f_i^I\right)^{HG} = Q_{ia}G_a^I \tag{3.1-42}$$

These hourglass resistance forces are added to the forces obtained from the element stress state (Eqn. 3.1-31). The total element resisting force is then:

$$f_i^I = \left(\bar{\sigma}_{ij}N_j^I + Q_{ia}G_a^I\right) \tag{3.1-43}$$

Calculation of the nodal accelerations (Eqn. 3.1-2) requires the accumulation of the resisting forces over all elements. Accumulation of the hourglass resisting internal forces was implemented into the program in a similar manner. Symbolically:

$$\{F_{int}\}_n = \sum^{elements} \{f\}_n \qquad \{F_{HG}\}_n = \sum^{elements} \{f^{HG}\}_n \tag{3.1-44}$$

where $\{F_{int}\}_n$ and $\{F_{HG}\}_n$ are the internal resisting forces and the hourglass resisting forces at the structural level for time step n. Total internal and kinetic energies of the structure are calculated as follows:

$$U = \int_0^{t_f} \{F_{int}\}_t^T \{v\}_n \, dt \qquad T = \frac{1}{2}\sum^{nodes} m(v_n)^2 \tag{3.1-45}$$

where U and T are the internal and kinetic energies respectively, and m, v_n are the lumped structural nodal mass and their velocities respectively. The amount of energy that can be attributed to the hourglass restoration forces indicates the extent of hourglassing in the solution process. The hourglassing energy, U_{HG}, is defined as:

$$U_{HG} = \int_0^{t_f} \{F_{HG}\}_n^T \{v\}_n \, dt \tag{3.1-46}$$

This energy is monitored throughout the solution process. The extent of hourglassing is identified by comparing the hourglassing energy to the total internal energy and kinetic energy.

Numerical studies reveal that the zero−energy suppression method degenerates for elements with large aspect ratios under relatively large deformations. Crack−tip elements, commonly employed in the finite element analysis of fracture mechanics problems, introduce stress and strain singularities through the use of collapsed nodes at the tip. These elements experience large deformation levels, and for 3−dimensional models, generally have large aspect ratios. The need to maintain an acceptable aspect ratio limits the in−plane refinement of conventional three dimensional finite element meshes (a maximum aspect ratio of approximately 20 for the crack tip elements was found to work for this study). The loading areas of SE(B) finite element models may also have elements with large aspect ratios. Localized loading, often applied to approximate a concentrated load, generates large deformations in these elements. The use of a finite width loading area reduces local deformations sufficiently for the zero−energy suppression technique to remain effective.

3.2 J−Integral Computations

This section describes the numerical procedures developed to evaluate the domain form of the J−integral as described in Eqns. 2.1−4 through 2.1−8. Volumetric integrals in finite elements are generally evaluated by Gaussian quadrature [21,100]. Element quantities in the integrand are evaluated at the integration points; a summation of the *weighted* values of the integrand, multiplied by the determinant of the Jacobian, approximates the desired integral:

$$\int_{Vol} \phi(x,y,z)dV \approx \sum_i \sum_j \sum_k \phi(x_i,y_j,z_k) w_i w_j w_k |J_{ijk}| \tag{3.2-1}$$

where i, j, k and w_i, w_j, w_k, correspond to the integration points and their respective weights in the ξ, η, ζ directions (see Fig. 3.1−3). $|J_{ijk}|$ is the determinant of the mapping Jacobian at the

48

integration point. The one−point integration scheme utilized for the trilinear hexagonal elements provides the most accurate element quantities at the integration point. As a natural extension of the element formulation, the one−point Gaussian quadrature is utilized for evaluation of the volumetric integrals in Eqns. 2.1−4 through 2.1−8. For a single integration point, Eqn. 3.2−1 simplifies to:

$$\int_{Vol} \phi(x,y,z)dV \approx \phi(x_0,y_0,z_0)V = \bar{\phi}V \qquad (3.2-2)$$

where x_0, y_0, z_0, are the average coordinates of the element, and V is the element volume. $\bar{\phi}$ is simply ϕ evaluated at the single integration point.

The q−function of Eqns. 2.1−4 through 2.1−8 is defined consistent with the isoparametric formulation. The q−function within an element is defined by the nodal q−values and the tri−linear isoparametric interpolation functions:

$$q_i(\xi,\eta,\zeta) = \sum_{I=1}^{I=8} N^I(\xi,\eta,\zeta) \, q_i^I \quad or \quad q_i = N^I q_i^I \qquad (3.2-3)$$

where q^I is the q−function value at node I, and N^I is the same function that is used for interpolation of displacements, coordinates and velocities (Eqns. 3.1−23, through 3.1−25). Spatial gradients of the displacements and the q−function are needed in addition to the spatial gradient of the velocities (Eqn 3.1−31). These quantities are available at the element nodes which again allows use of the gradient operator B_i^I defined in Eqn. 3.1−30:

$$\frac{\partial q_i}{\partial x_j} = \frac{1}{V}B_j^I q_i^I \qquad \frac{\partial u_i}{\partial x_j} = \frac{1}{V}B_j^I u_i^I \qquad (3.2-4)$$

The numerical evaluation of Eqns. 2.1−5 through 2.1−7 becomes:

$$\bar{J}_1 = \int_V \left(\sigma_{ij}\frac{\partial u_i}{\partial x_k}\frac{\partial q_k}{\partial x_j} - W\frac{\partial q_k}{\partial x_k} \right) dV$$

$$\approx \sum_{domain} \left[\bar{\sigma}_{ij}\left(\frac{1}{V}B_k^I u_i^I\right)\left(\frac{1}{V}B_j^I q_k^I\right) - \bar{W}\left(\frac{1}{V}B_k^I q_k^I\right) \right]V \qquad (3.2-5)$$

49

$$J_2 = -\int_V \left(\frac{\partial W}{\partial x_k} - \sigma_{ij} \frac{\partial^2 u_i}{\partial x_j \partial x_k} \right) q_k \, dV$$

$$\approx -\sum_{domain} \left[\left(\frac{1}{V} B_k^I W^I \right) - \bar{\sigma}_{ij} \left(\frac{1}{V} B_k^I u_{i,j}^I \right) \right] \bar{q}_k V \qquad (3.2-6)$$

$$J_3 = -\int_V \left(T \frac{\partial q_k}{\partial x_k} - \varrho \frac{\partial^2 u_i}{\partial t^2} \frac{\partial u_i}{\partial x_k} q_k + \varrho \frac{\partial u_i}{\partial t} \frac{\partial^2 u_i}{\partial t \partial x_k} q_k \right) dV$$

$$\approx -\sum_{domain} \left[\bar{T} \left(\frac{1}{V} B_k^I q_k^I \right) - \bar{\varrho} \left(\frac{1}{V} B_k^I a_i^I \right) \bar{q}_k + \bar{\varrho} \bar{v}_i \left(\frac{1}{V} B_k^I v_i^I \right) \bar{q}_k \right] V \qquad (3.2-7)$$

The superscript I indicates element nodal quantities. Quantities at the integration point are indicated by the superimposed bar. The summation extends over all finite–elements in the domain volume. The gradient operator, B_i^I, is defined with respect to the current coordinates thereby making the displacement derivatives and velocity gradients energy conjugate to the Cauchy stresses.

Element level values for the accelerations, a_i^I, velocities, v_i^I and the displacements, u_i^I, are extracted from global kinematic quantities. At time step n, the available quantities are: accelerations and displacements at time t, and the velocities at time $t - \Delta t/2$ (time step $n - 1/2$). The small time step size that results from the globally explicit solution makes the difference in velocities between time steps $n - 1/2$ and n negligible. These quantities, a_i^I, u_i^I at time t, and v_i^I, at time $t - \Delta t/2$, are used directly in the above integrations.

The material models provide the element quantities $\bar{\sigma}_{ij}$, $\bar{\varrho}$ and $\bar{W}$ (stress state, density and the strain energy density) at the element integration point. The strain energy density, $\bar{W}$, is obtained by integrating the stress–strain history of the integration point; the material density depends upon the volumetric strain of the element. A simple average of the element nodal values provides the element integration point values for the q–function and the element velocities ($\bar{q}_k$ and $\bar{v}_i$). The kinetic energy density, $\bar{T}$ in Eqn. 3.2–7, is computed from the element density, $\bar{\varrho}$, and the integration point velocities, $\bar{v}_i$, as follows:

$$\bar{T} = \frac{1}{2} \bar{\varrho} \sum_{i=1}^{3} (\bar{v}_i)^2 \qquad (3.2-8)$$

All of the terms needed for the evaluation of Eqns. 3.2–5 and 3.2–7 are computed, as described above, solely from nodal and integration point quantities available at the element level.

Loop over the local nodes of the element $I = 1, 8$

$$u_{i,j}^{total} = 0$$

$$W^{total} = 0$$

$$N = 0$$

For each element incident to element local node I:

Extract element quantities: u_i^J, x_i^J, W

Compute $B_i^J = B_i^J(x), V$

$$\overline{u}_{i,j} = \frac{1}{V} B_j^J u_i^J$$

$$u_{i,j}^{total} = u_{i,j}^{total} + \overline{u}_{i,j}$$

$$W^{total} = W^{total} + \overline{W}$$

$$N = N + 1$$

End element loop

$$u_{i,j}^J = u_{i,j}^{total}/N$$

$$W^I = W^{total}/N$$

End local node loop

Figure 3.2−1. Generation of Nodal Values for W and $u_{i,j}$

Additional consideration must be given for the evaluation of J_2 in Eqn. 3.2−6. This integral arises from the explicit derivative of the strain energy density in the application of the divergence theorem. The needed quantities are the spatial gradients of the strain energy density and the second derivatives of the displacements. The difficulties in the evaluation of these derivatives are summarized below:

$\dfrac{\partial^2 u_i}{\partial x_j \partial x_k}$: At the element level, the displacements are available at the nodes. Although formulation of a second−order gradient operator directly from the interpolation functions is possible, the low order of the trilinear fields precludes accurate computation of second−order derivatives in the element (element shape functions only permit linear variations along edges).

$\dfrac{\partial W}{\partial x_k}$: The strain energy density for the trilinear hexagonal element is available only at the single integration point. The numerical evaluation of a spatial gradient in an element from a single data value is not possible.

Thus, these derivatives cannot be evaluated directly from quantities available at the element level.

51

These gradients are computed by first generating nodal values of the displacement deriva-
tives, $u_{i,j}^I$, and the strain energy densities, W_k^I. Standard isoparametric techniques are then ap-
plied (gradient operator, B_k^I) to compute the spatial gradients (Eqn. 3.2−6). The strain ener-
gy density corresponding to a given node, W_k^I, is computed at the global level as the average
of the strain energy densities of all the elements incident to that node. Similarly, the average
spatial gradient of the displacements of all the elements incident to the node is used as $u_{i,j}^I$.
Figure 3.2−1 summarizes the algorithm.

Loop over the elements in the domain

      Compute element nodal quantities: $u_{i,j}^J, W^J$ (See Fig. 3.2−1)

      Extract element nodal quantities: $u_i^J, x_i^J, v_i^J, a_i^J, q_i^J$

      Extract element integration point: $\bar{\sigma}_{ij}, \overline{W}, \bar{\varrho}$

      Compute at element integration point: $\bar{q}_i, \bar{v}_i, \overline{T}$

      Compute gradient operator and volume: $B_i^J = B(x), V$

      Compute spatial gradients:

$$\overline{u}_{i,j} = \tfrac{1}{V}B_j^J u_i^J \quad \overline{q}_{i,j} = \tfrac{1}{V}B_j^J q_i^J$$

$$\overline{W}_{,k} = \tfrac{1}{V}B_k^J W^J \quad \overline{(u_{i,j})}_{,k} = \tfrac{1}{V}B_k^J u_{i,j}^J$$

$$\overline{v}_{i,j} = \tfrac{1}{V}B_j^J v_i^J$$

      Compute element $J-$integrals:

$$J_1 = \left(\bar{\sigma}_{ij}\overline{u}_{i,k}\bar{q}_{j,k} - \overline{W}\bar{q}_{k,k}\right)V$$

$$J_2 = -\left(\overline{W}_{,k} - \bar{\sigma}_{ij}\overline{(u_{i,j})}_{,k}\right)\bar{q}_k V$$

$$J_3 = -\left(\overline{T}\bar{q}_{k,k} - \bar{\varrho}\bar{a}_{i,k}\bar{q}_k + \bar{\varrho}\bar{v}_i\bar{v}_{i,k}\bar{q}_k\right)V$$

End element loop

Figure 3.2−2. Computation of $J-$Integrals

Once the nodal quantities of W_k^I and $u_{i,j}^I$ are generated, all spatial variations in Eqns. 3.2−5
through 3.2−7 are computed by application of the gradient operator as shown in Eqn. 3.2−4.
Figure 3.2−2 summarizes the procedure to compute the $J-$integral.

Spectrom creates a binary database that contains the structural response (displacements,
stresses etc.) at user−specified times. A post−processing program computes the $J-$integrals
over the time history by extracting solution data from this database.

3.3 Bodner–Partom Viscoplasticity Model

This section outlines the implementation of the Bodner–Partom viscoplastic material model developed specifically to support this study. The material model advances the stress history from time step $n-1$ to n given the kinematic state and the history of key parameters. The global kinematic solution provides the spatial rates of deformation at each material point. The rate of the deformation gradient tensor (See Eqns. 3.1–22, 3.1–14 and 3.1–15) relative to the configuration at time step n is utilized as the total strain rate for the time step:

$$\dot{\varepsilon}_{ij} = d_{ij} = \dot{\varepsilon}^e_{ij} + \dot{\varepsilon}^p_{ij} \tag{3.3-1}$$

where additive decomposition of the total strain rate into elastic and plastic components is assumed to remain valid (Eqn. 2.3–1). The stress rates are coupled to the elastic strain rates through a hypoelastic form of the elastic constitutive relation:

$$\dot{\sigma}_{ij} = \lambda_{Lame}\dot{\varepsilon}^e_{kk}\delta_{ij} + 2G\dot{\varepsilon}^e_{ij} \tag{3.3-2}$$

where λ_{Lame} is Lame's constant, G is the shear modulus:

$$\lambda_{Lame} = \frac{vE}{(1+v)(1-2v)} \qquad G = \frac{E}{2(1+v)} \tag{3.3-3}$$

This Hookean relationship provides the component of the Jaumann stress rate caused by material deformation in Eqns. 3.1–16 and 3.1–18. The plastic strain rates are defined by Eqns 2.3–2 through 2.3–5:

$$\dot{\varepsilon}^p_{ij} = \lambda s_{ij} \qquad \lambda = \lambda(J_2, Z) \tag{3.3-4}$$

The lack of a closed form solution for the nonlinear system of equations given in Eqns. 2.3–2 through 2.3–5 requires the application of numerical integration techniques. The dependency of the plastic strain rates on the stresses (which are in turn dependent on the plastic strain rates, Eqns. 3.3–4) necessitates an iterative solution for the stresses. Alternatively, a non–iterative forward Eulerian approach can be employed; the stresses, strains and hardening variables at the beginning of the time step are used to calculate the plastic strain rates for the step.

A mean value approach is best suited for accurate evaluation of the plastic strain rates and element stress state. Using a central difference scheme, the rate form of the Bodner–Partom equations is recast as:

$$\dot{\varepsilon}^p_{ij} = \lambda_{n-1/2}\left(s_{ij}\right)_{n-1/2} \tag{3.3-5}$$

$$\left(\lambda_{n-1/2}\right)^2 = \frac{\left(D^p_2\right)_{n-1/2}}{\left(J_2\right)_{n-1/2}} \tag{3.3-6}$$

$$\left(D^p_2\right)_{n-1/2} = D^2_0\, e^{a_{n-1/2}} \qquad a_{n-1/2} = -\left[\frac{\left(Z_{n-1/2}\right)^2}{3\left(J_2\right)_{n-1/2}}\right]^n \tag{3.3-7}$$

$$Z_{n-1/2} = Z_{n-1} + \dot{Z}_{n-1/2}\frac{\Delta t}{2} \tag{3.3-8}$$

$$\dot{Z}_{n-1/2} = m(Z_1 - Z_{n-1})\left(\dot{W}_p\right)_{n-1/2} \tag{3.3-9}$$

where subscripts identify the time step. ($n-1/2$ symbolically refers to the mid−interval be-tween time step $n-1$ and n, or at $t - \Delta t/2$.) The strain rates are assumed to remain constant for the time step in accordance with the global solution at $n-1/2$. Stresses at the mid−interval are computed using the stress rate predicted by the hypoelastic relation, Eqn. 3.3−2, times $\Delta t/2$:

$$\left(\sigma_{ij}\right)_{n-1/2} = \left(\sigma_{ij}\right)_{n-1} + \left(\lambda_{Lame}\dot{\varepsilon}^e_{kk}\delta_{ij} + 2G\dot{\varepsilon}^e_{ij}\right)\frac{\Delta t}{2} \tag{3.3-10}$$

The plastic strain energy density in Eqn. 3.3−9 is evaluated using the mid−interval stresses and plastic strain rates:

$$\left(\dot{W}_p\right)_{n-1/2} = \dot{\varepsilon}^p_{ij}\left(\sigma_{ij}\right)_{n-1/2} \tag{3.3-11}$$

Updating of the stresses thus involves use of a starting estimate for the mid−interval plastic strain rate followed by a computation of the corresponding mid−interval stresses. These stresses are then used to determine a corresponding plastic strain rate from the Bodner−Par-tom material model. The correct material state is found once the plastic strain rates from the predicted stress state match the plastic strain rate assumed to generate the stress rate. Finally the hardening parameter Z, and the stresses are updated to the end of the time step:

$$\left(\sigma_{ij}\right)_n = \left(\sigma_{ij}\right)_{n-1} + \left(\lambda_{Lame}\dot{\varepsilon}^e_{kk}\delta_{ij} + 2G\dot{\varepsilon}^e_{ij}\right)\Delta t \qquad (3.3-12)$$

$$Z_n = Z_{n-1} + \dot{Z}_{n-1/2}\Delta t \qquad (3.3-13)$$

The iteration process implemented to resolve the plastic strain rate is summarized in Fig. 3.3−1. The computations are initialized with the converged plastic strain rates of the previous time step. The corresponding elastic strain rates are given by the additive decomposition of the total strain rates. The hypoelastic relationship provides stress rates for the interval from the elastic strain rates. The plastic work rate and the hardening parameter at the mid−interval are computed with the mid−interval stress state. The computed plastic strain rates and the assumed plastic strain rates are compared for convergence of the iterations. To continue in the next iteration, an updated estimate of the plastic strain rates is necessary. Two approaches to improve the estimate of plastic strain rates are developed in subsequent sections.

Convergence of the iterative solution occurs when the assumed plastic strain rates at the beginning of an iteration are within a specified tolerance of the computed plastic strain rates. The norm of the difference in plastic strain rates is compared to the norm of the average of the assumed and calculated plastic strain rates:

$$\Delta\dot{\varepsilon}^p_{ij} = \left(\dot{\varepsilon}^p_{ij}\right)^i_{calc} - \left(\dot{\varepsilon}^p_{ij}\right)^i \qquad (3.3-18)$$

$$\left|\Delta\dot{\varepsilon}^p_{ij}\right| = \Delta\dot{\varepsilon}^p_{ij}\Delta\dot{\varepsilon}^p_{ij} \qquad (3.3-19)$$

$$\left(\dot{\varepsilon}^p_{ij}\right)_{ave} = \frac{1}{2}\left[\left(\dot{\varepsilon}^p_{ij}\right)^i_{calc} + \left(\dot{\varepsilon}^p_{ij}\right)^i\right] \qquad (3.3-20)$$

$$\left|\left(\dot{\varepsilon}^p_{ij}\right)_{ave}\right| = \left(\dot{\varepsilon}^p_{ij}\right)_{ave}\left(\dot{\varepsilon}^p_{ij}\right)_{ave} \qquad (3.3-21)$$

The convergence criteria becomes:

$$\left|\Delta\dot{\varepsilon}^p_{ij}\right| < tol \times \left|\left(\dot{\varepsilon}^p_{ij}\right)_{ave}\right| \qquad (3.3-22)$$

where *tol* is a tolerance value sufficiently small to insure that the difference between the assumed and computed plastic strain rates is negligible. Section 3.3.3 studies the numerical con-

Initialize:
$$\left(\dot{\varepsilon}^p_{ij}\right)^0 = \left(\dot{\varepsilon}^p_{ij}\right)_{n-1}$$

Note: $n^* = n - 1/2$

Begin Iteration:
$$i = i + 1$$

Stress State:

$$\left(\dot{\varepsilon}^e_{ij}\right)^i = \left(\dot{\varepsilon}_{ij}\right) - \left(\dot{\varepsilon}^p_{ij}\right)^i$$
$$\left(\sigma_{ij}\right)^i_{n^*} = \left(\sigma_{ij}\right)_{n-1} + \left(\lambda_{Lame}(\dot{\varepsilon}^e_{kk})^i \delta_{ij} + 2G(\dot{\varepsilon}^e_{ij})^i\right)\frac{\Delta t}{2}$$
$$\left(s_{ij}\right)^i_{n^*} = \left(\sigma_{ij}\right)^i_{n^*} - \tfrac{1}{3}\left(\sigma_{kk}\right)^i_{n^*}\delta_{ij}$$
$$\left(J_2\right)^i_{n^*} = \tfrac{1}{2}\left(s_{ij}\right)^i_{n^*}\left(s_{ij}\right)^i_{n^*}$$

(3.3−14)

Hardening Variables:

$$\left(\dot{W}_P\right)^i_{n^*} = \left(\dot{\varepsilon}^p_{ij}\right)^i\left(\sigma_{ij}\right)^i_{n^*}$$
$$\dot{Z}^i_{n^*} = m(Z_1 - Z_{n-1})\left(\dot{W}_P\right)^i_{n^*}$$
$$Z^i_{n^*} = Z_{n-1} + \dot{Z}^i_{n^*}\frac{\Delta t}{2}$$

(3.3−15)

Plastic Strain Rates:

$$\left(D^p_2\right)^i_{n^*} = D_0^2 \exp(\beta^i_{n^*}) \quad \beta^i_{n^*} = -\left[\frac{(Z^i_{n^*})^2}{3(J_2)^i_{n^*}}\right]^n$$
$$\left(\dot{\varepsilon}^p_{ij}\right)^i_{calc} = \lambda^i_{n^*}\left(s_{ij}\right)^i_{n^*} \quad \left(\lambda^i_{n^*}\right)^2 = \frac{\left(D^p_2\right)^i_{n^*}}{\left(J_2\right)^i_{n^*}}$$

(3.3−16)

Convergence Check:

$$\frac{\left|\Delta \dot{\varepsilon}^p_{ij}\right|}{\left|\left(\dot{\varepsilon}^p_{ij}\right)_{ave}\right|} < tol$$

No → **Estimate new Plastic Strain Rates:**
$$\left(\dot{\varepsilon}^p_{ij}\right)^{i+1}$$

Yes

Update Stresses:

$$\left(\sigma_{ij}\right)_n = \left(\sigma_{ij}\right)_{n-1} + \left(\lambda_{Lame}\dot{\varepsilon}^e_{kk}\delta_{ij} + 2G\dot{\varepsilon}^e_{ij}\right)\Delta t$$
$$Z_n = Z_{n-1} + \dot{Z}_n\Delta t$$

(3.3−17)

Next Element

Figure 3.3−1. Material Model Iterations

vergence of the iterative scheme summarized in Fig. 3.3−1. A tolerance value of 0.01%, was found to be adequate.

As previously noted, the iterative solution requires an updated set of plastic strain rates to continue the next iteration. Two such methods are developed in the following sections.

3.3.1 Iterative Substitution

The first technique implemented to update the plastic strain rates for the next iteration uses a linear combination of the assumed plastic strain rates at the beginning of the iteration and the computed strain rates at the end of the iteration:

$$\left(\dot{\varepsilon}_{ij}^{p}\right)^{i+1} = a\left(\dot{\varepsilon}_{ij}^{p}\right)^{i} + (1 - a)\left(\dot{\varepsilon}_{ij}^{p}\right)_{calc}^{i} \tag{3.3−23}$$

where a is a weight factor between 0 and 1. $a = 1$ provides a non−convergent material model; the assumed plastic strain rates at the beginning of each iteration remain unchanged and equal to the converged plastic strain rates of the previous step. For $a = 0$ the computed plastic strain rates at the end of the iteration are adopted as the assumed plastic strain rates in the next iteration.

For a given time step in which the initial plastic strain rates are overestimated, the elastic strain rates, (and therefore the stresses) are underestimated (see Eqn. 3.3−14); in extreme cases a sign reversal may occur. The plastic strain rates computed with these stresses, Eqn. 3.3−16, also underestimate the correct strain rates. Conversely, initially underestimated plastic strain rates cause computed plastic strain rates to be overestimated. This behavior occurs when the time step size is reasonably small. The assumed plastic strain rates and the computed ones bracket the correct strain rates. This response of the material model makes the scheme expressed in Eqn. 3.3−23 a good predictor for the plastic strain rates.

Limited numerical studies reveal that the number of iterations required for convergence is relatively insensitive to the choice of a for $0.3 < a < 0.7$. Generally, for $a \rightarrow 0$ or $a \rightarrow 1$ a larger number of iterations was required for convergence. An a value of $a = 0.5$ was utilized for all finite−element analyses.

3.3.2 Decoupled Differential Equations

Dexter et. al. [26,55] describe an iterative process for integration of viscoplastic rate equations. The hypoelastic equations relating the stresses and strain rates are cast in deviatoric space, which decouples the stress and strain components:

$$s_{ij} = 2G\left(\dot{e}_{ij} - \dot{e}_{ij}^p\right) \tag{3.3-24}$$

where G is the shear modulus, $\dot{s}_{ij}$ are the stress deviators and $\dot{e}_{ij}$ and $\dot{e}_{ij}^p$ are the total deviatoric and plastic deviatoric strains respectively:

$$\dot{s}_{ij} = \dot{\sigma}_{ij} - \frac{1}{3}\dot{\sigma}_{kk} \qquad \dot{e}_{ij} = \dot{\varepsilon}_{ij} - \frac{1}{3}\dot{\varepsilon}_{kk} \qquad \dot{e}_{ij}^p = \dot{\varepsilon}_{ij}^p \tag{3.3-25}$$

The flow rule, Eqn. 3.3−5, relates linearly the plastic strain rates and the stress deviators. (The plastic strain rates are deviatoric by definition.) Substituting the flow rule, Eqn. 3.3−5, into Eqn. 3.3−24 and rearranging yields:

$$\dot{s}_{ij} + 2G\lambda s_{ij} = 2G\dot{e}_{ij} \tag{3.3-26}$$

Assuming that λ is constant, and independent of the stress deviators over the time increment, a closed form solution for the resulting nonhomogeneous, first−order ordinary differential equation can be obtained:

$$\left(s_{ij}\right)_{t+\Delta t} = \left(s_{ij}\right)_t \exp(-2G\lambda\Delta t) + \frac{1}{\lambda}\dot{e}_{ij}(1 - \exp(-2G\lambda\Delta t)) \tag{3.3-27}$$

where the stresses at time $t + \Delta t$ are expressed in terms of the stresses at the beginning of the time step and the total strain rate deviators over the time step. Rewriting Eqn. 3.3−24 in terms of the plastic strain rates:

$$\dot{e}_{ij}^p = \dot{e}_{ij} - \frac{1}{2G}\dot{s}_{ij} \tag{3.3-28}$$

The stress rate is calculated using:

$$\dot{s}_{ij} = \frac{\left(s_{ij}\right)_n - \left(s_{ij}\right)_{n-1}}{\Delta t} \tag{3.3-29}$$

By substituting the differential equation solution for the stresses at the end of time step n and rearranging, the solution for the plastic strain rates is:

$$\dot{e}_{ij}^p = \frac{1}{2G}(1 - \exp(-2G\lambda\Delta t))\left(s_{ij}\right)_{n-1} + \left(1 + \frac{\exp(-2G\lambda\Delta t) - 1}{2G\lambda\Delta t}\right)\dot{e}_{ij} \tag{3.3-30}$$

Eqn. 3.3–30 expresses the plastic strain rates for the interval in terms of the stress deviators at the beginning of the time step and the total strain rates. The evaluation of λ is as shown in Eqn. 3.3–6, with the stresses and hardening variables evaluated at the mid–interval as expressed in Eqns. 3.3–14 through 3.3–16. The expression for the plastic strain rates shown in Eqn. 3.3–30 is used as the assumed plastic strain rate for the next iteration.

3.3.3 Verification of Convergence

The convergence behavior of the two methods for integrating the Bodner–Partom viscoplastic material model is examined in this section. A material point is subjected to uniaxial loading as shown in Fig. 3.3–2. An initial tensile strain rate of 1000 sec^{-1} is applied for 50

A   Tensile Elastic Loading

B   Tensile Plastic Loading

C   Tensile Elastic Unloading
     Compressive Elastic Loading

D   Compressive Plastic Loading

Figure 3.3–2. Uniaxial Loading for Convergence Comparison
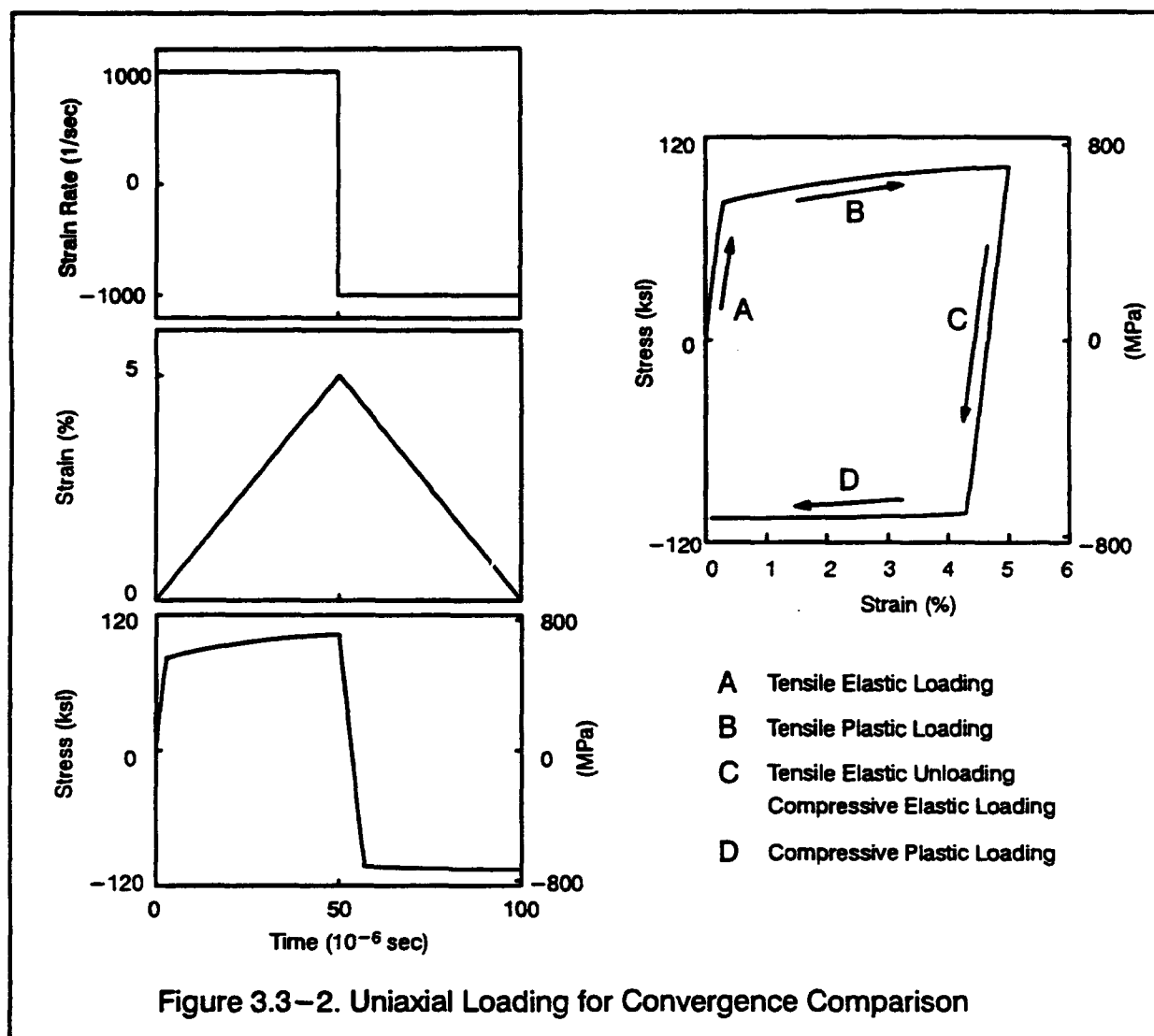
μ–sec, followed by a strain reversal at a compressive strain rate of 1000 sec^{-1} for 50 μ–sec, for a total response history of 100 μ–sec. The applied strain rate represents the upper range

59

of rates expected in near—tip elements of the impact loaded SE(B) specimens. The material properties typical of A533B steel at $50°C$ ($133°F$) are used in these convergence studies (See Table 2.3—2 for the Bodner—Partom material constants).

The material response is expressed in Fig. 3.3—2. Initially, the material is elastic, exhibiting the initial steep slope in the stress—strain diagram labelled A in the figure. Once plastic deformation dominates the response, the material exhibits a shallow slope labelled B in the figure. The strain—rate reversal creates the elastic unloading curve labelled C, and after sufficient deformation, plastic deformation in compression again dominates the response, producing the curve labelled D. The severe slope changes that occur between the different material loading states make this a demanding test case for evaluation of the convergence behavior of the two iterative methods. The differences between the assumed plastic strain rates and the converged plastic strain rates are the largest at these slope changes.

Three different iteration schemes are examined:

1) Differential equation solution (DES), Eqn. 3.3—30

2) Iterative substitution with $\alpha = 0.0$ (IS_0.0), Eqn. 3.3—23

3) Iterative substitution with $\alpha = 0.5$ (IS_0.5), Eqn. 3.3—23

A constant time step of $\Delta t = 1.0 \times 10^{-7}$ sec with a tolerance of $tol = 0.01\%$ (Eqn. 3.3—22) is used for the convergence study.

Portions of the stress—strain curve with relatively constant slopes require very few iterations (usually one or two iterations) for convergence. This is expected since the initial estimate of the plastic strain rates, the converged values of the previous time step, is nearly identical to the current values. All three schemes required at most 2 iterations at times within the smooth sections of the stress—strain curve labelled A through D in Fig. 3.3—2. However, the transition between these labelled portions of the curve, require more iterations for convergence in all three methods.

Examples of the convergence behavior of the different iterative schemes for the transitions between the different smooth curves are found in Fig. 3.3—3. A scalar measure of convergence is introduced using the second invariant of the plastic strain rates, (See Eqn. 3.3—16), as follows:

Figure 3.3−3. Convergence Comparison, $\Delta t = 1.0 \times 10^{-7}$
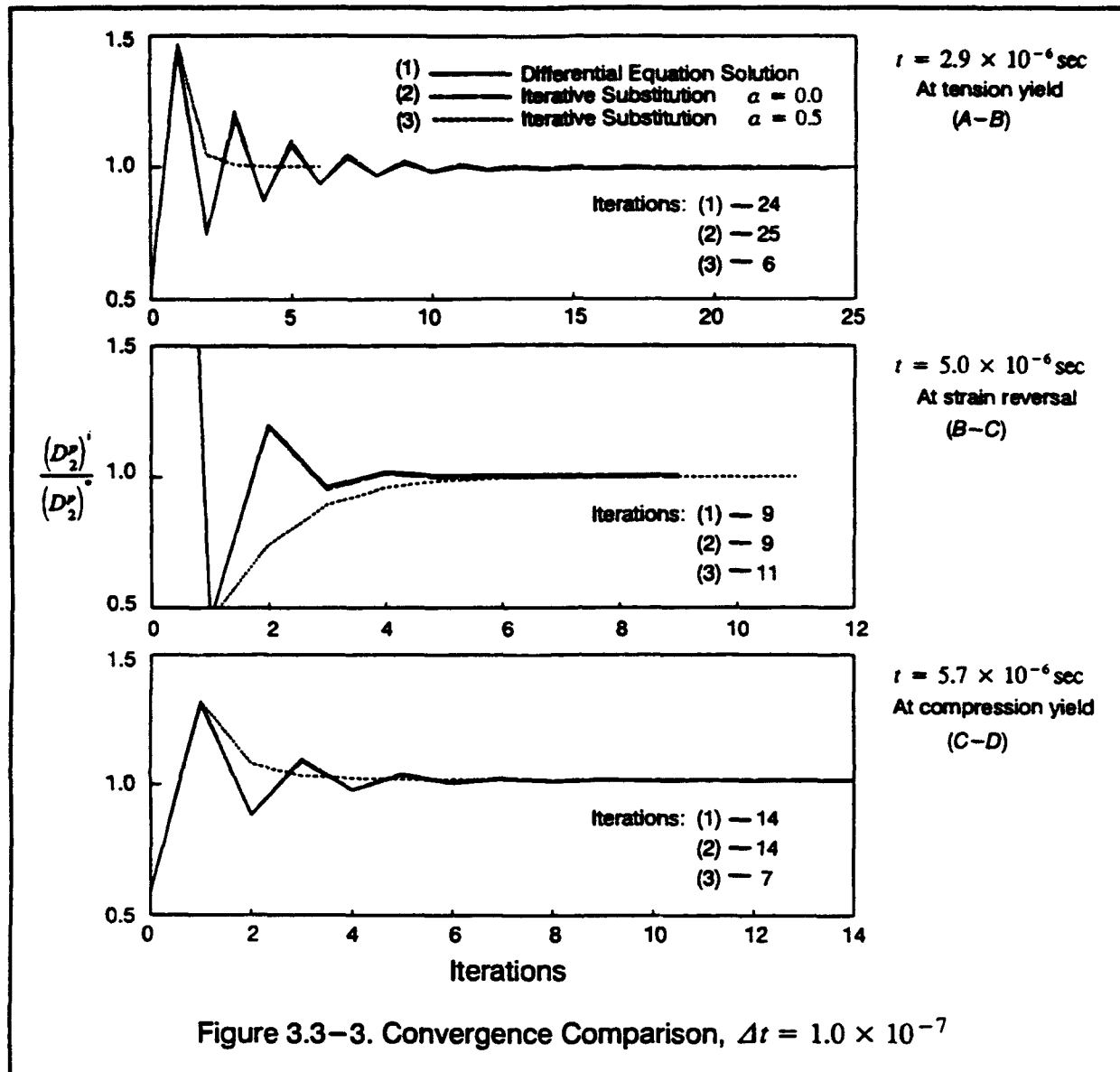
$$\frac{\left(D_2^p\right)^i}{\left(D_2^p\right)^*}$$

where: $\left(D_2^p\right)^i$ = ith iteration result

and: $\left(D_2^p\right)^*$ = converged value

(3.3−31)

The above ratio equals unity once convergence is achieved.

As shown in Fig. 3.3−3. both the DES method and the IS_0.0 method behave nearly identical at all three transitions. These methods experience large oscillations about the converged value, with the oscillations dropping in magnitude as the number of iterations increases. The IS_0.5 method converges monotonically towards the correct value for all three transitions. The

number of iterations required for convergence is summarized in the figure for the given time step. The total number of iterations required for the entire time history is 1208, 1260 and 1220 for the DES, IS_0.0, and IS_0.5, respectively. Although the total number of iterations required for the convergence favors the DES method, the monotonic convergence behavior of the IS_0.5 is considered preferable.

The time step size employed of the material model strongly affects the convergence rate. For a relatively large time step, the material state at the beginning and the end of the integration time step can be very different (the change in material states as shown in Fig. 3.3−2. for example). In these cases an intermediate stress state (Eqn. 2.3−1), that can define the plastic strain rates for the time step may not exist or may be numerically difficult to converge upon. For these cases, all three iterative methods diverge. Sub−incremental schemes, in which the time step is subdivided into smaller time steps, may be needed to enable the integration of the material model.

Section 3.1.2 outlines the variable time step selection of the global time history integration. Using Eqns. 3.1−7 through 3.1−9 as a guide, and recalling that the generalized dimension, δ, for a unit cube is equal to to 0.577, or $1/\sqrt{3}$, an upper bound estimate for the time step size is developed. In the finite element model with the largest δ_{min}, the smallest element is of the order of $h = 0.1$ inches (2.54 mm) where h is the edge of a hexahedron element cube. The critical generalized dimension is then:

$$\delta_{min} = \frac{h}{\sqrt{3}} = 5.774 \times 10^{-2} \text{in.} \quad (1.467 \text{mm})$$

(3.3−32)

By substituting the elastic properties for steel, $E = 30000$ ksi (206844 MPa), $\nu = 0.3$, and $\varrho = 7.345 \times 10^{-4}$ lb−sec^2/in^4 (7.85×10^{-3} Kg/mm^3) into Eqn. 3.1−7, the unbounded dilatational wave speed, c_1, is 2.345×10^5 in/sec (5.133×10^6 mm/sec). The maximum time step expected for analyses of the SE(B) is then:

$$\Delta t_{max} = \frac{\delta_{min}}{c_1} = 2.462 \times 10^{-7} \text{sec}$$

(3.3−33)

The convergence behavior of the three different schemes is studied with a time step of Δt_{max} to determine the best scheme to integrate the constitutive rate equations. The uniaxial loading example shown in Fig. 3.3−3 was re−analyzed with a time step of $\Delta t = 2.5 \times 10^{-7}$ sec, and a tolerance of $tol = 0.01\%$ (Eqn. 3.3−22). For the initially elastic segment of the stress−strain curve, (A in Fig. 3.3−3), all three methods converge in one or two iterations. At

Figure 3.3−4. Convergence Comparison $\Delta t = 2.5 \times 10^{-7}$
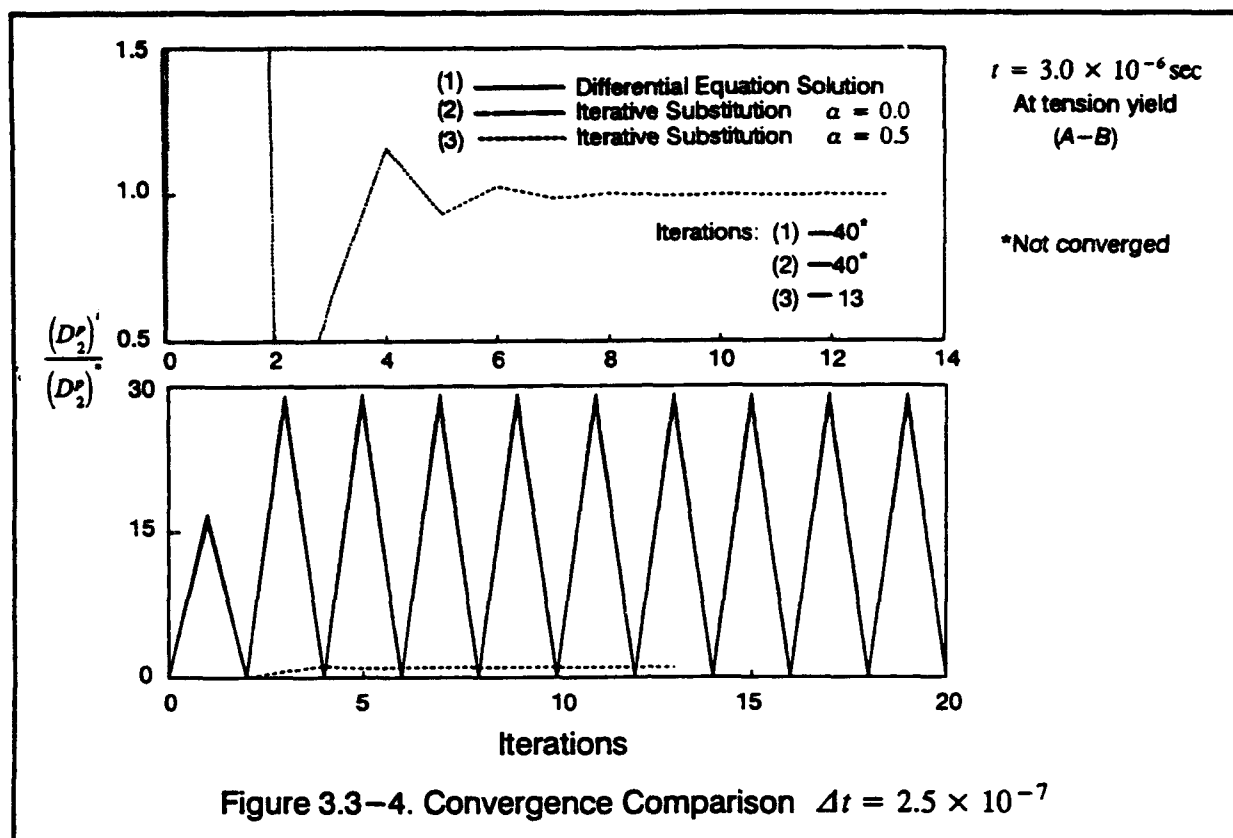
the yield point, however, the DES and the IS_0.0 methods both diverge. The IS_0.5 method accurately integrates the entire stress−strain history. Figure 3.3−4 shows the convergence behavior of the three methods at the tensile yield point. The lower graph in the figure shows the large oscillations of the nonconvergent methods. The DES and the IS_0.0 show nearly identical behavior. Although the IS_0.5 method generates a few, small oscillations, the method converges quickly.

Additional verification of these updating schemes is accomplished by comparison with numerical results presented by Dexter et. al. [24,25]. Dexter modeled a uniaxial loading of A533B steel at 100 ^{0}C for two strain rates, 10^{-2} sec^{-1} and 500 sec^{-1}. A series of constant strain rates were applied each followed by a period over which the total strain was held constant. During the holding periods, the viscoplastic effects cause stress relaxation. Figures. 3.3−5 and 3.3−6 summarize the two different applied strain histories and the computed stresses.

The computation was repeated using the IS_0.5 method with a $\Delta t = 0.05$ sec. for the 10^{-2} sec^{-1} strain rate and $\Delta t = 2.0 \times 10^{-7}$ sec for the 500 sec^{-1} strain rate loading. Creep behavior causes stress relaxation during the constant strain regions. This is responsible for the small dimples observed in the stress−strain diagrams. As expected, the higher strain rate loading exhibits both higher stresses and larger amounts of stress relaxation than the lower strain rate

63
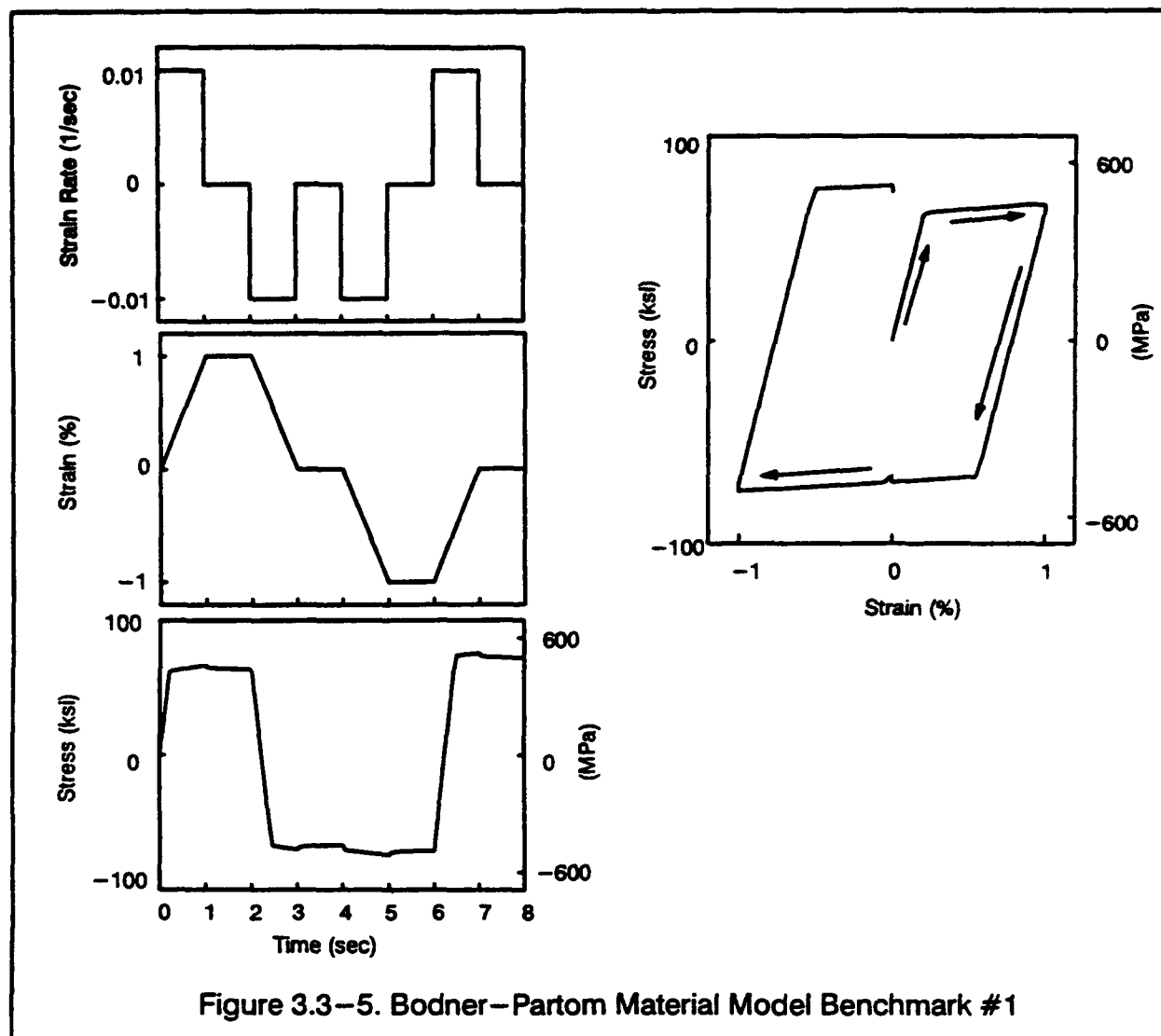
Figure 3.3–5. Bodner–Partom Material Model Benchmark #1

loading. The stresses computed with the current model match very closely those reported by Dexter et. al. [24,25].

The IS_0.5 method ($\alpha = 0.5$) is used for the integration of the Bodner–Partom material model. Except for the extreme cases of $\alpha = 1$ and $\alpha = 0$, little variation in the convergence occurs with the parametric variation of α in Eqn. 3.3–23. The explicit time history integration severely limits the time step size and simplifies the integration of the viscoplastic rate equations by eliminating the need for sub–incrementation. For larger time step sizes, used in implicit finite element codes, sub–incrementation may be needed for the accurate integration of the material model.

Figure 3.3−6. Bodner−Partom Material Model Benchmark #2
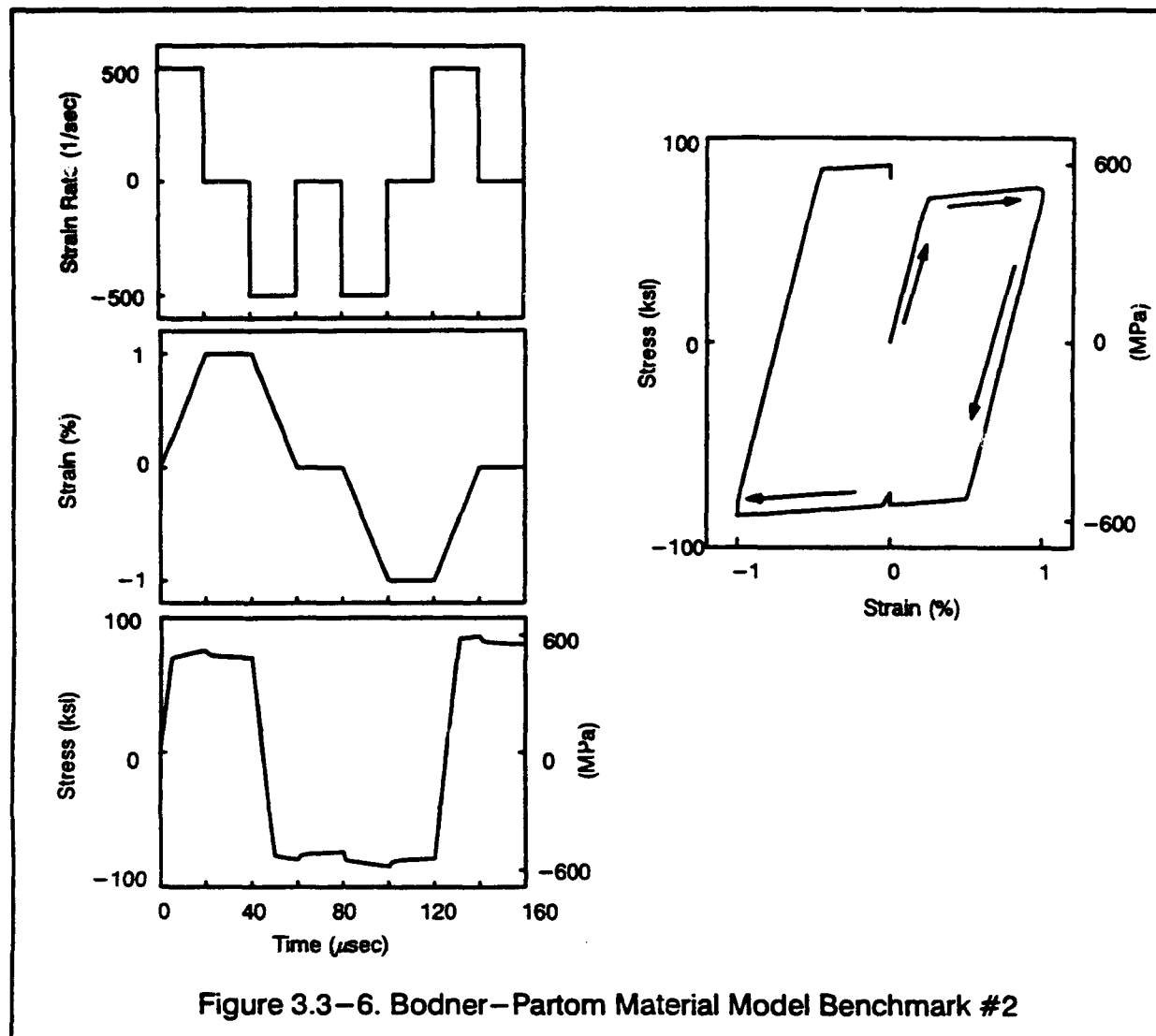
3.4 Loading of Finite Element Models

The physical apparatus and instrumentation for impact testing in a drop tower are described in Section 2.4. Realistic assessment of the dynamic effects requires matching of the specimen's load history (See Fig. 2.4−1) in the finite element analyses. However, the applied load on the specimen is not measured directly; the reliability of the inferred load using strains measured at the quarter−point location is unknown. This suggests loading of the finite element model by an imposed displacement history.

Direct application of non−zero displacements, however smooth, as constraints in an explicit dynamic analysis creates large oscillations of the element stresses. The spatial distribution of displacements to be applied across the loaded surface is unknown. An arbitrary dis-

tribution of displacements imposed across the loaded edge artificially stiffens the SE(B) specimen. This generates high frequency stress waves and their reflections from the boundaries. Moreover, application of the displacements to a single line of nodes across the specimen thickness creates a "butter knife" effect in which severe local deformations develop.

Figure 3.4−1. Methodology to Determine Applied External Loads
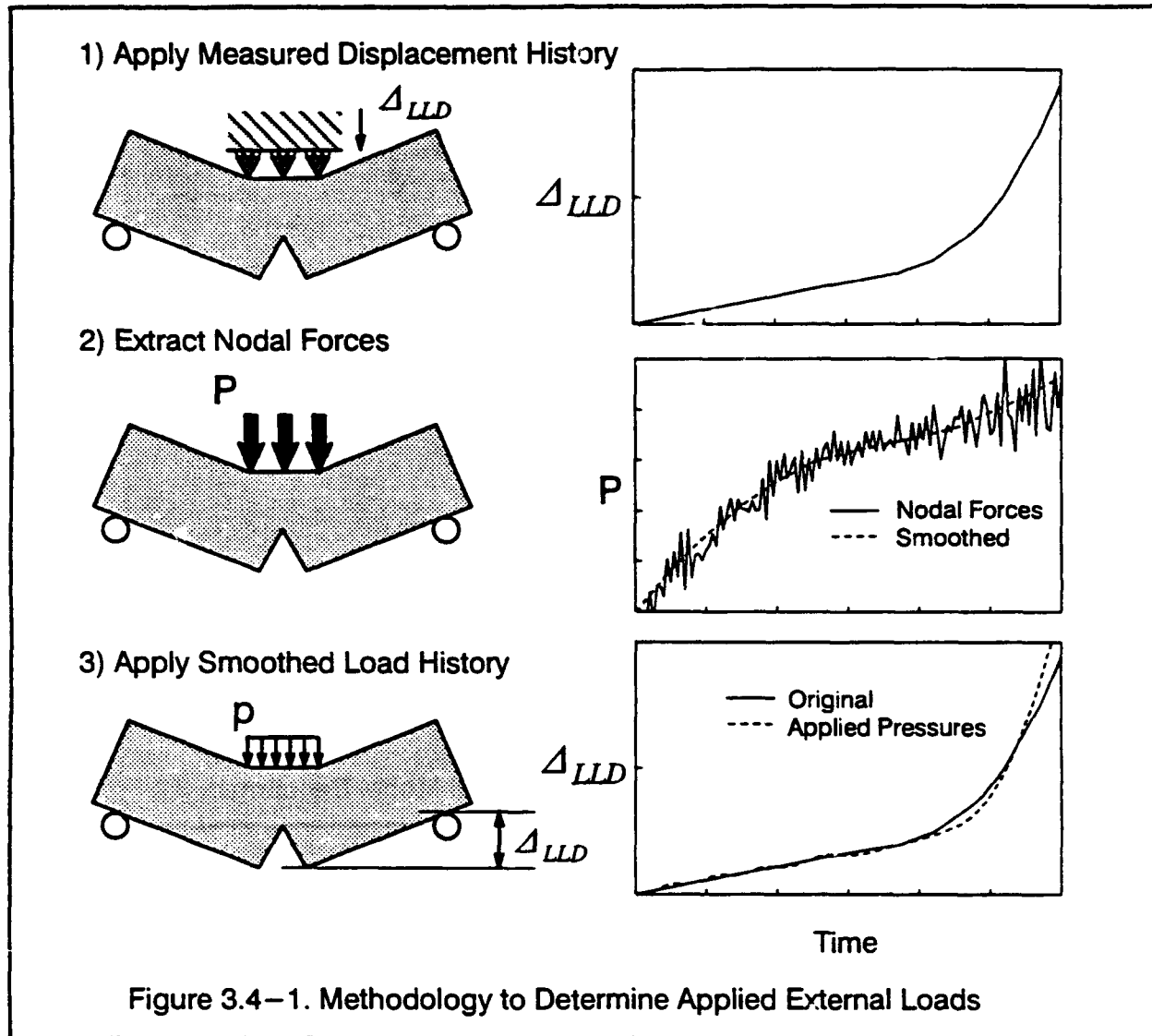
The application of time dependent external forces is the preferred method of loading a finite element model. However, the lack of information on the applied loading requires a procedure to generate a loading that when applied to the finite element model, reproduces the displacement history measured in tests. This loading is generated by first executing a displacement controlled analyses in which the loaded area is uniformly displaced according to the displacement history (Fig. 2.4−1). Application of the uniform displacement across the loading area effectively creates a rigid boundary that causes high frequency stress oscillations.

Reactions at the displaced nodes are extracted and smoothed to generate an equivalent external loading history. These external loads are applied to the model over the loading area as an equivalent uniform pressure. The computed displacement history of the specimen under the smoothed loading history is compared for agreement with the measured displacement history. Figure 3.4−1 illustrates the steps of this procedure.

3.4.1 Application to an A533B SE(B) Specimen

Reference [54] describes impact fracture toughness testing of a specific A533B steel over a range of loading rates, temperatures and specimen sizes. The A533B material used for these tests is the same plate utilized by Dexter et. al. for the viscoplastic characterization of A533B steel [24,26]. Results are presented for drop tower tests conducted on 20% sidegrooved, 1T SE(B) specimens with the crack oriented in the L−T direction [2,4]. Generation of the applied loading as described in the previous section is demonstrated using data for specimen H15 in reference [54].

Figure 3.4−2 shows the geometry and the finite element model utilized for this analysis. The dimensions comply with standard ASTM specifications for the 1T SE(B) specimen used in $J-R$ testing [4]. Due to symmetry, only one quarter of the specimen is modeled. The crack tip consists of collapsed hexagonal elements in which nodes along the front are free to displace to model blunting. Five element layers of 0.1 in (2.54 mm.) each form the specimen half−thickness. In order to model the sidegrooves, the thickness of the outer most layer of elements is set equal to the sidegroove depth (see Fig.3.4−2). The finite element model consists of 1030 elements with 1428 nodes. The mesh gradation minimizes stress reflections at element boundaries. A six millisecond analysis requires a total of 33,227 time steps, with an average time step of 1.8×10^{-7} seconds. The analysis required 4.1 hours of CPU on the HP/Apollo DN−10000 workstation.

The H15 specimen was tested at a temperature of 150°F (66°C). The available parameters for the Bodner−Partom viscoplastic material model are at the discrete temperatures shown in Table 2.3−2. For this analysis, estimates of the Bodner−Partom parameters at 150°F (66°C) were obtained by linearly interpolating from those available at 122°F (50°C) and 212°F (100°C). The interpolated Bodner−Partom parameters for 150°F (66°C) are: $m=0.44568$ ksi^{-1} (0.06464 MPa^{-1}), $n=2.0124$, $Z_0=178.0994$ ksi (1227.96 MPa), $Z_1=235.2846$ ksi (1622.24 MPa), and $D_0=1.0 \times 10^3$ sec^{-1}.

The measured history for the drop tower tests is not presented for the A533B specimens in reference [54]. However, both the specimen and the drop tower setup utilized for the A533B

Figure 3.4−2. Specimen Dimensions and Finite Element Mesh

Within the figure:

H15 Specimen:

W = 2.0 in. (50.8 mm.)
a /W = 0.6
L = 9.0 in. (228.6 mm.)
B = 1.0 in. (25.4 mm.)
Span = 8.0 in. (203.2 mm.)
20% Sidegrooved
150°F (66°C)

Loading Area:
0.436 in. (11.1 mm.)

Finite Element Model:

1030 elements
1428 nodes

Side Grooves:
0.1 in. (2.54 mm)
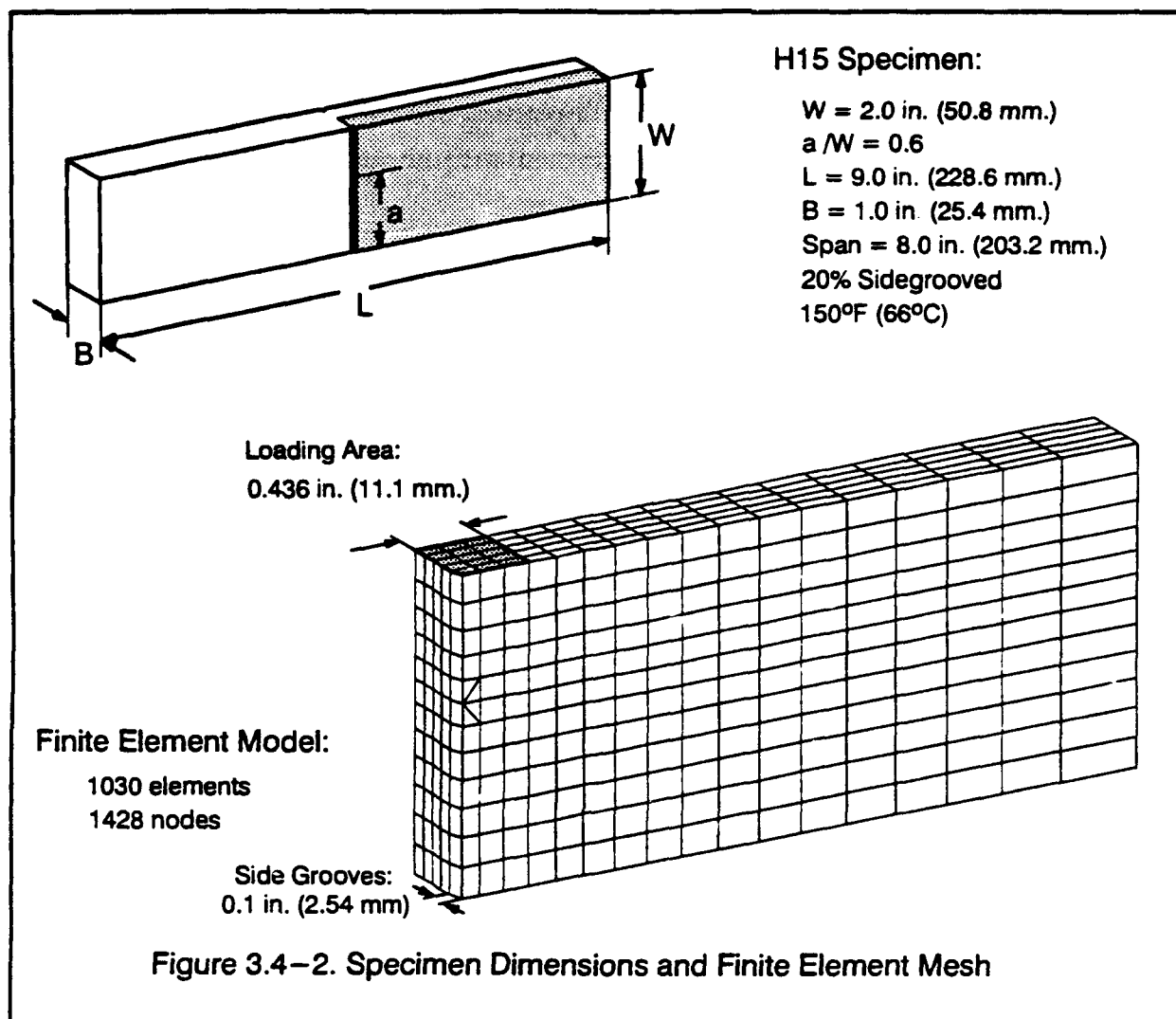
SE(B) specimens in [54] are similar to the setup reported in [52] for the fracture testing of HY80 steel. This similarity, and the tendency of the drop tower to impart a displacement history that is independent of the specimen, suggests the use of the displacement history reported in [52] for the A533B specimen. (This displacement history is shown as a solid line in Fig. 2.4−1 and is repeated in Fig. 3.4−3).

The displacements are applied on a small loading area in the finite element model. Using the dimensions of the aluminum wedges, 1 inch by 1 inch at the base, as a guide (see Section 2.4.1), the loading area is chosen as the first three rows of elements in the finite element mesh. This corresponds to a total loading width of 0.874 inches (22.2 mm.). As shown in Fig. 3.4−2, the loading width on the finite element model is one−half of the total loading width, 0.436 inches (11.1 mm). The displacement history shown in Fig. 2.4−1 is applied to the specimen over

Figure 3.4-3. Load Determination for H15 A533B Steel SE(B) Specimen
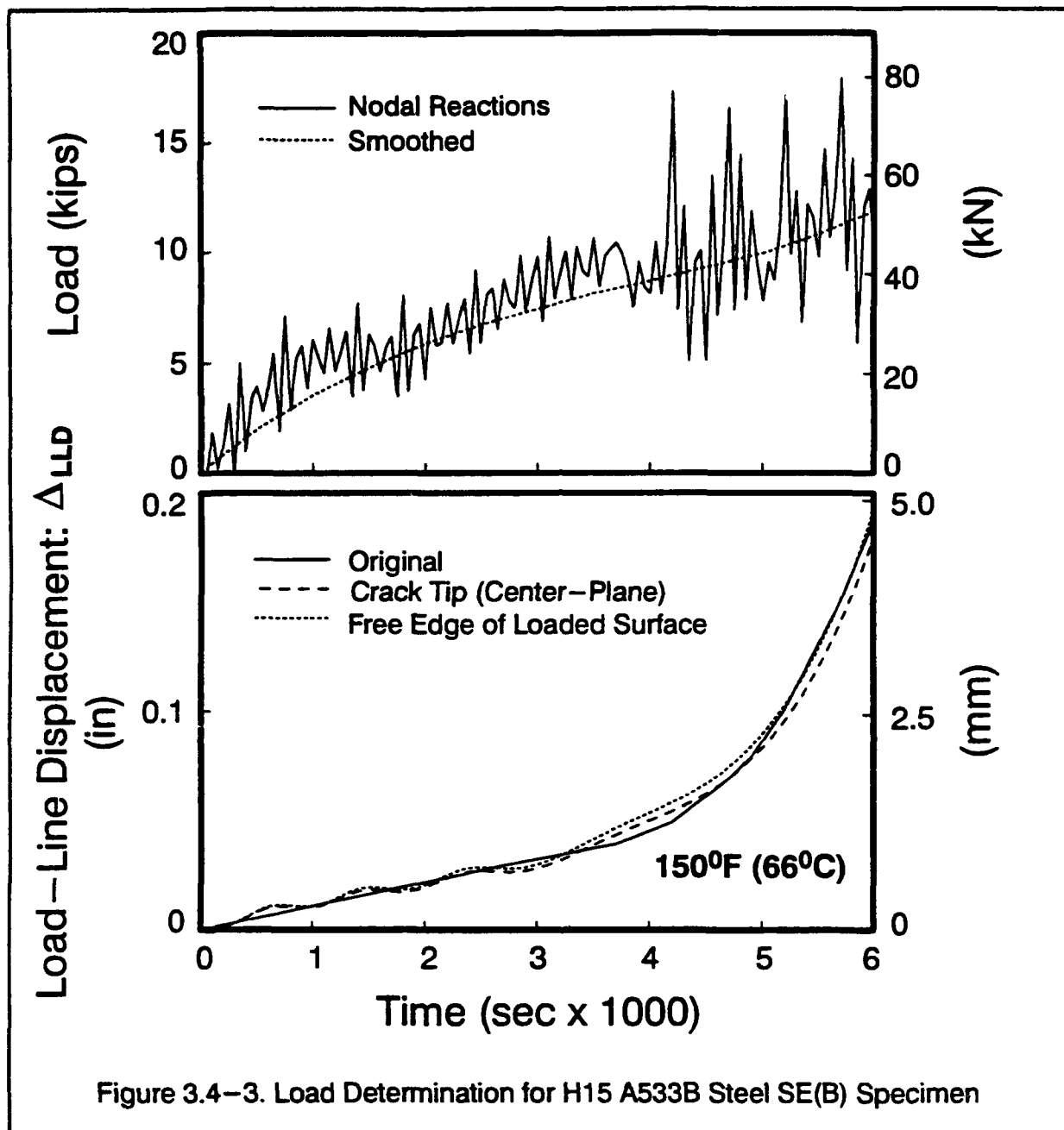
the area indicated in Fig. 3.4-2. The summed reactions at these nodes provide the total external load shown in Fig. 3.4-3.

The rigid boundary created by the applied displacement field produces the large amplitude, high frequency oscillations shown in Fig. 3.4-3. The applied displacements constrain the specimen to a deformation mode of higher strain energy than the actual specimen. The actual deformation pattern of the deep crack SE(B) specimen reveals that both arms rotate about the plane of the remaining ligament as rigid bodies (See Fig. 2.2-1). The rigid deformation across

69

the loading area forces the ends of the specimen to deform about a finite region defined by the rigid loading area. This causes both a high frequency content of the nodal reactions and a stiffer response of the specimen. The real specimen, however, does not experience either the rigid boundary condition or the large amplitude oscillations. The only purpose of the applied displacement simulation is to obtain a guide for the actual applied forces.

For shallow flaw SE(B) specimens ($a/W \approx 0.1$), the natural deformation pattern is more of a *beam−bending* pattern rather than the *rigid−arm* pattern of the deep crack SE(B) specimens. For these specimens, the applied displacement pattern is a better approximation to the true deformation pattern of the specimen. As shown in the next chapter, the applied displacement analysis for these specimens shows less oscillatory behavior in the extracted nodal reactions than is observed for the deep crack SE(B) specimens.

Figure 3.4−3 shows the smoothed version of the extracted nodal forces that is applied to the specimen. A trail−and−error approach is used for smoothing the nodal force oscillations

Figure 3.4−4. Load Displacement for H15 A533B Steel SE(B) Specimen
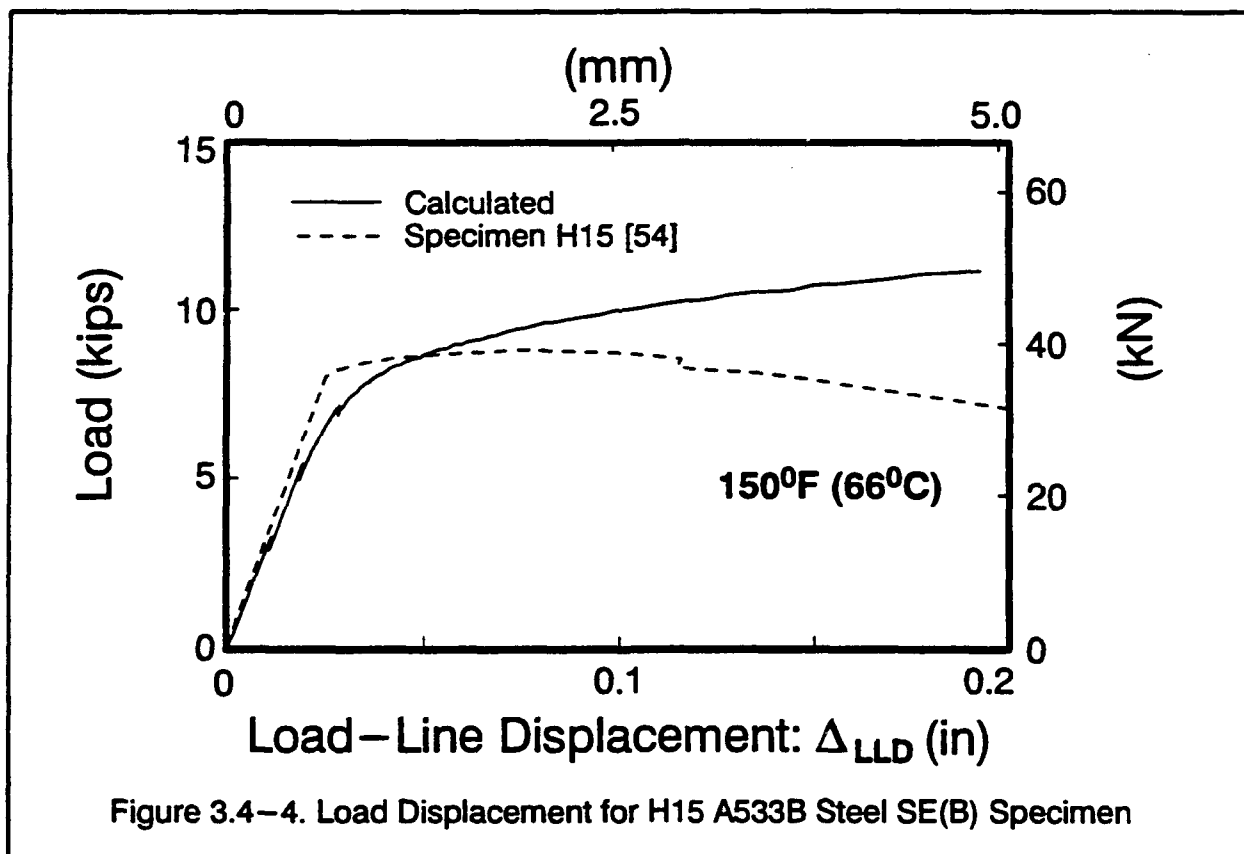
to obtain an applied load that produces the displacement history. To begin, a cubic fit of the extracted nodal loads is used as a guide to establish the smoothed loading. This loading is applied to the finite element model, and the displacements are monitored. If the computed dis-

placements deviate significantly from the measured values, the loads are modified to obtain a better match in the next analysis with the measured displacements. Several trail−and−error cycles are needed to accurately match the measured displacement history.

The measured displacement history and the resulting displacements from the smoothed extracted nodal loads are shown together in Fig. 3.4−3. The crack plane experiences a range of displacements from a minimum at the crack−tip center−plane to a maximum at the loaded−surface free−edge. These two displacements are shown in Fig. 3.4−3. The computed response from the smoothed loadings matches the measured displacement history very well. Elastic vibration of the specimen in the first fundamental mode causes the small−amplitude oscillations in the computed response for the first half of the analyses. This phenomena is examined in detail in the following chapter.

Figure 3.4−4 shows the resulting load−displacement curve for the analysis. The experimental curve is obtained from strain gages placed at the 1/4 point as explained in Section 2.4.2. General trends of the analysis, such as the limit load and initial slope, match well with reported values [54]. Up to 0.3 inches (7.6 mm) of crack growth in the laboratory specimen is responsible for the decreasing load after 0.05 inches of displacement.

4 Computational Results and Discussion

This chapter presents the computational details and results of the research. Three−point bend specimens with three different crack depths, a/W = 0.0725, 0.15, and 0.50 (subsequently referred to as *shallow*, *medium*, and *deep* respectively), are investigated to quantify constraint effects. The three specimens have the same overall dimensions, 2.0 inch by 2.0 inch cross−section, 9.0 inches long, with an 8.0 inch loading span (50.8mm by 50.8mm by 228.6 mm, 203.3 mm span). The Bodner−Partom constitutive model is employed to examine the effects of high strain rates. A loading history characteristic of drop tower testing is imposed on the three specimens. Analyses are conducted using both rate−sensitive and rate−insensitive material models. Additional static analyses are performed to provide baseline responses for assessment of dynamic effects.

Three dynamic effects are of interest: 1) kinematic effects in the form of stress waves and specimen oscillations; 2) strain rate effects on material constitutive behavior, and; 3) acceleration of material in the crack tip region that possibly shields the crack tip from deformation. These effects are quantified and presented in this chapter for the three specimens.

This chapter is organized into the following twelve sections:

4.1 *Finite Element Meshes:* The finite element modelling details and computational parameters for the SE(B) specimens are presented.

4.2 *A533B Steel Rate−Insensitive Material Model:* Bodner−Partom coefficients are developed to model a rate−insensitive stress−strain curve of A533B steel. This material model provides a basis to isolate strain−rate effects.

4.3 *Determination of Applied Loading:* The procedure described in Section 3.4 is applied to simulate drop tower loading of the specimens using time−dependent nodal forces.

4.4 *Transition Times:* Transition times for the six analyses are determined. Single degree of freedom models of the SE(B) specimens are developed to estimate transition times. An analysis with a much higher loading rate is conducted to examine the significance of the transition time for characterizing dynamic effects.

4.5 *Strain Rates and Stresses:* Distributions are presented for strain rates and the plastic deformation in the SE(B) specimens.

4.6 *Applied Load Inferred from Measurable Quantities:* Laboratory measurements are simulated through the extraction of key numerical values from the dynamic analyses. Three methods of inferring the applied load from laboratory measurements are examined. Dynamic results are compared with static analyses to quantify dynamic effects in the specimens. The dis-

tribution of longitudinal strains at the quarter−span gage location is studied for the shallow crack specimen.

4.7 *J−integral Values:* Thickness average values of the J−integral computed from finite element results are compared with J−values computed from static formulas using the inferred loads. Values of the plastic proportionality constant, η_p, in the static formulas are computed. The time at which dynamic effects become negligible and the time after which static formula yields accurate J−values is compared to the transition time.

4.8 *Crack Front Variation of the Pointwise J−Integral:* The variation cf the J−integral along the crackfront is examined to determine the effects of strain rate and crack−tip inertia loading.

4.9 *Crack Tip Opening Displacements:* Both dynamic and static CTOD values are determined. Distributions of the pointwise values of the constraint parameter m along the crack front are obtained.

4.10 *Near Crack Tip Stresses:* Opening mode stresses along the crack front are compared for the three SE(B) specimens. Near−tip fields are examined to estimate values of the deviation of mean stress from small−scale yielding (Q).

4.11 J_{acc} *Term:* The relative contribution of the J_{acc} term to the total J−integral is studied. The magnitude of this term indicates the relative importance of material accelerations at the crack tip.

4.12 *Summary:* Major conclusions and observations are summarized.

4.1 Finite Element Meshes

Figures 4.1−1 through 4.1−3 show the finite element meshes developed in this study. Two mesh refinements, denoted coarse and refined, are shown for each specimen. Due to symmetry, only one quarter of the specimen is modelled. The shaded region indicates the portion of the specimen actually modelled. Figure 4.1−4 shows the symmetric boundary conditions for the specimen on a typical finite element mesh. All elements are trilinear hexagonal bricks (8−noded), with a one point Gaussian integration and hourglass control. The number of elements and nodes for each of the finite element models are also shown in the figures. The end support is modelled by constraining the vertical displacement of the nodes 1.0 inch (25.4 mm) from the specimen ends. The specimen "overhang" from the supports is included in the finite element model.

Section 3.4 describes the need to apply load over a finite width. Utilizing dimensions for the base of the aluminum absorbers as a guide (see section 2.4.1), a strip of approximately 1.0 inch width (25.4 mm), over the thickness of the specimen is specified for the loading area. Due to the differences in mesh refinement, the loading area varies slightly among the models. Figures 4.1−1 through 4.1−3 indicate the loading areas for each of the finite element models.

73

W = 2.0 in. (50.8 mm)
a/W = 0.5
L = 9.0 in. (228.6 mm)
B = 2.0 in. (25.4 mm)
Span = 8.0 in. (203.2 mm)
No Sidegrooves

Modelled Region

0.454 in. (11.5 mm.)

Loading Area:
0.436 in. (11.1 mm.)

Refined Model
2920 elements
3834 nodes

Coarse Model
860 elements
1212 nodes

Trilinear Brick

Figure 4.1 – 1. Finite Element Mesh for Deep Crack Specimen
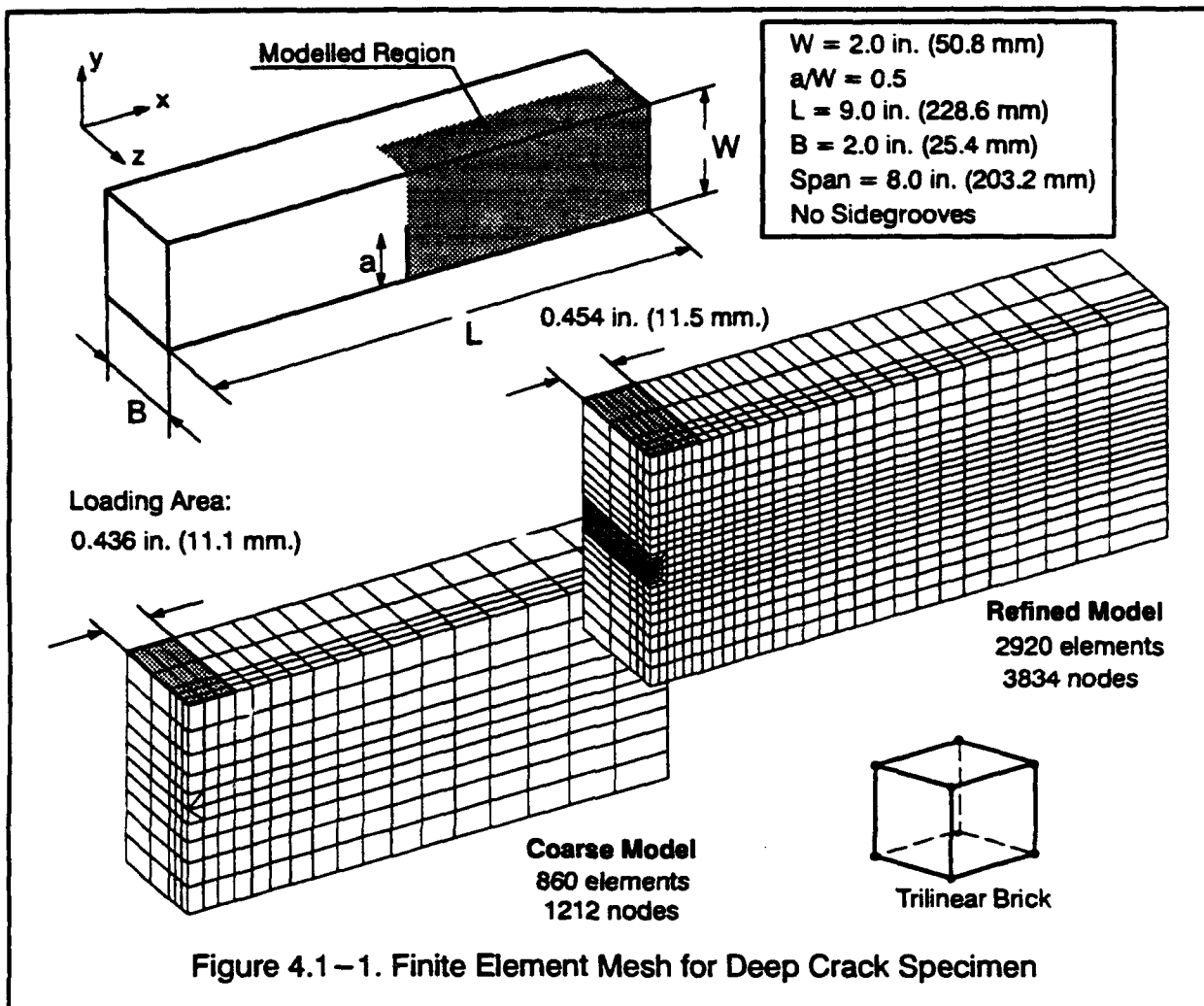
Previous work by Nakamura et. al. [71,70,74] was used as a guide for developing the coarse model. For specimens of size similar to those examined here, Nakamura's smallest element dimension was 0.1 inches (2.54 mm). The coarse meshes in this study employ elements of size 0.1 inch in the $X-Y$ plane near the crack front, while the refined models use elements of size 0.025 inch (0.635 mm) at the crack front. The gradual refinement in the $X-Y$ plane toward the crack front helps to minimize spurious reflections of stress waves. All models have five layers of elements in the $Z-$direction. Each layer has the same mesh layout in the $X-Y$ plane. From the specimen centerplane to the free surface, the layer thicknesses are: 0.4, 0.3, 0.1, 0.1, 0.1 inches (10.16, 7.62, 2.54, 2.54, 2.54 mm). The increased refinement near the free surface captures the severe gradients.

Hexagonal elements collapsed into wedges are defined along the crack front for both the coarse and the refined models. The coarse models contain four collapsed elements at each layer, forming a ring one element deep around the crack tip. The refined models contain eight

Figure 4.1−2. Finite Element Mesh for Medium Crack Specimen
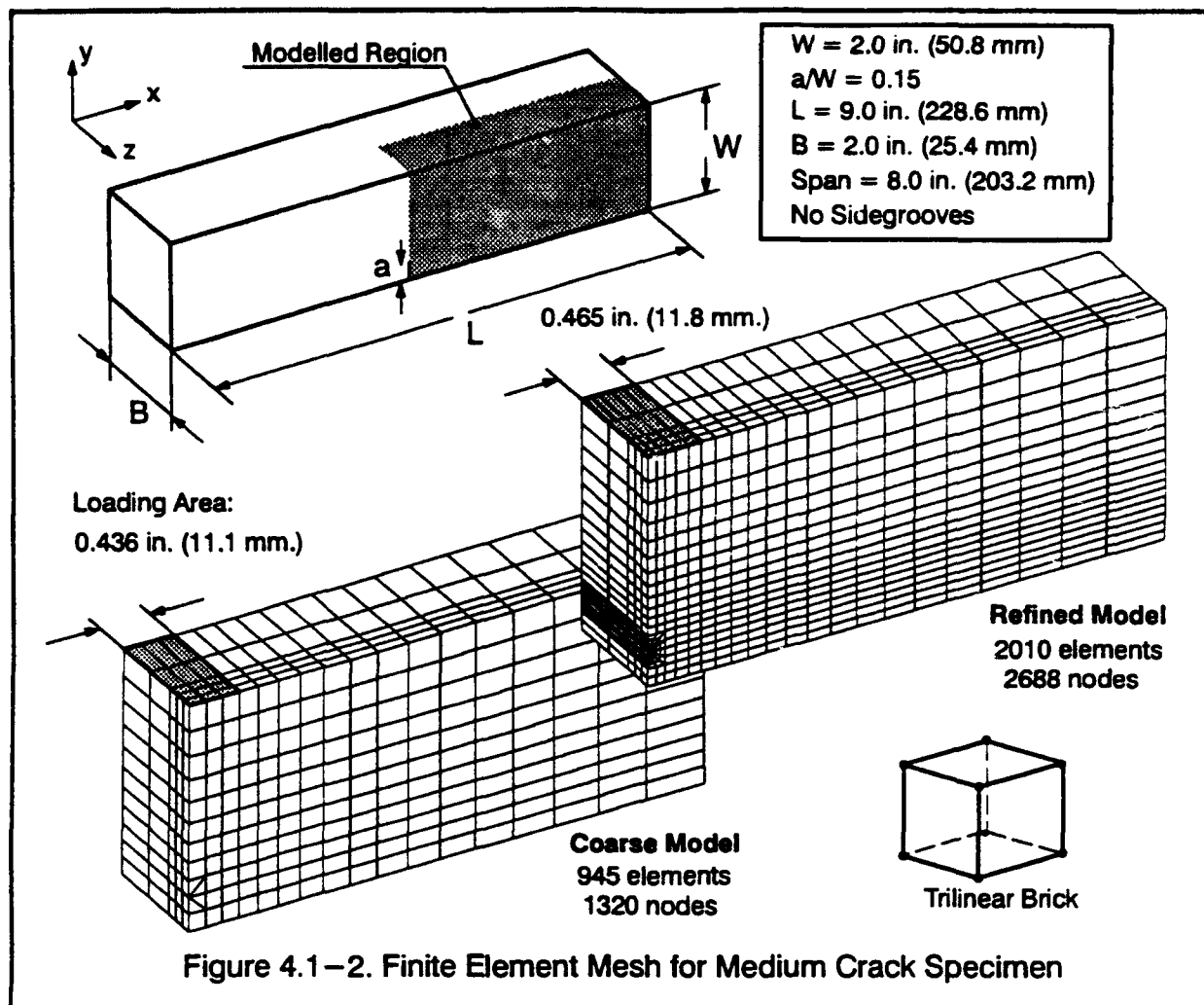
collapsed elements in each layer, surrounded by three rings of conventional elements, forming a four deep ring of elements around the crack tip. The coincident nodes of the collapsed elements at the crack tip are free to displace independently. Figure 4.1−5 shows the displacement pattern of the crack−tip elements in the fine mesh as the crack opens under loading. Displacement gradients in these elements contain singular terms of the order of $1/r$ in the $X-Y$ plane [86,66].

Section 3.1.2 describes the explicit integration scheme and the requirements for a stable time step size. Time step sizes for a typical coarse model range from 1.5×10^{-7} to 2.2×10^{-7} seconds, with an average time step of 1.8×10^{-7} seconds. A total of 33,000 time steps is required to compute the 0.006 second response. Nakamura et. al. report similar time step sizes for their analyses [70,72].

Figure 4.1−3. Finite Element Mesh for Shallow Crack Specimen
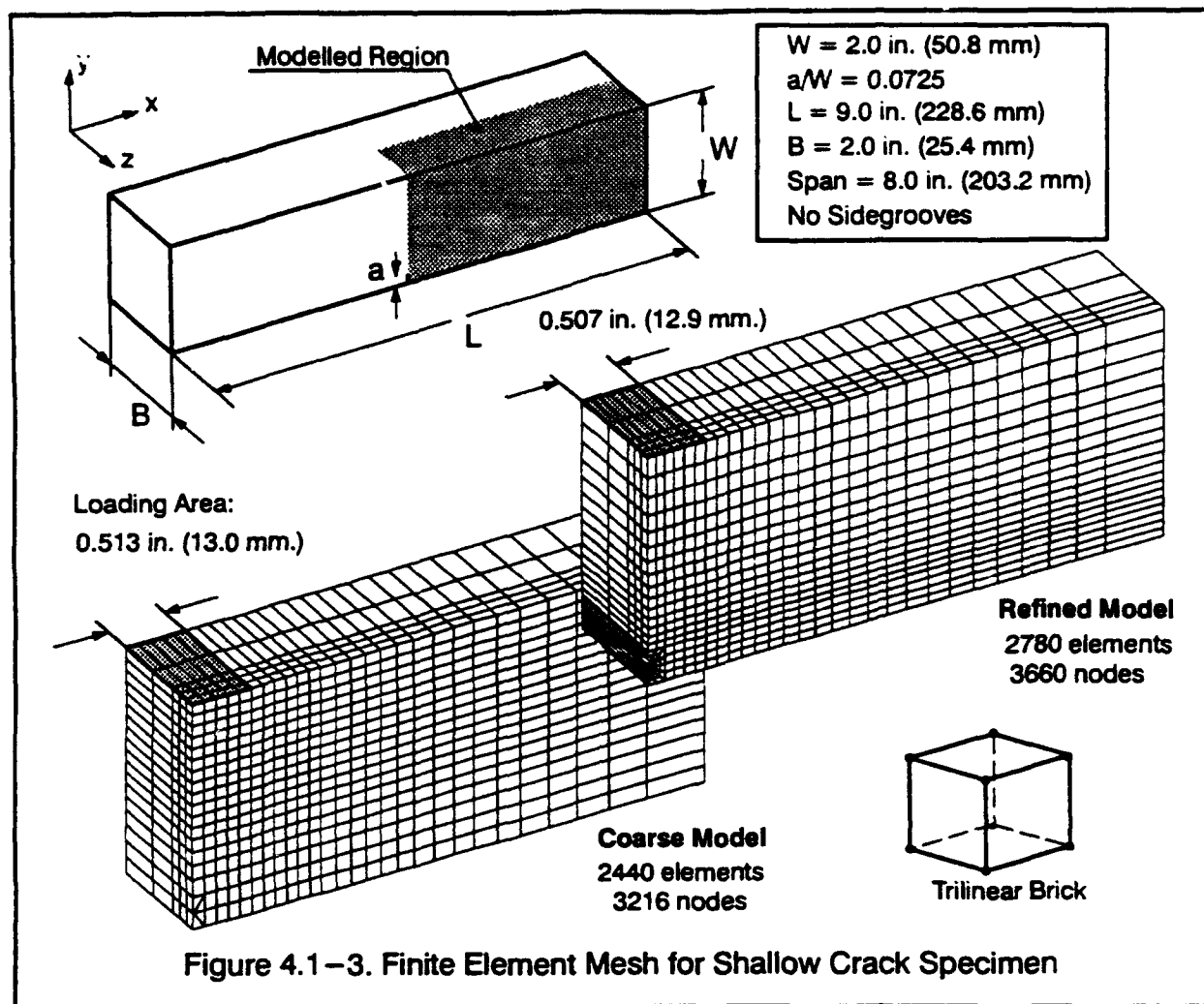
Time steps for a typical refined model analysis range from 1.6×10^{-8} to $2.4 \times 1\iota^{-8}$ seconds, with an average time step size of 2.2×10^{-8} seconds. Approximately 300,000 time steps are required to compute the 0.006 second response. As described in Section 3.1, the Spectrom code utilizes single precision storage for all floating point variables. Single precision (32 bits) representation of floating point numbers provides six to seven decimal digits of precision. Each time step requires the addition of computed changes in kinematic variables (e.g. nodal displacements) and accumulated time. A loss of precision occurs when increments in the variables are on the order of the least significant digit of the accumulated value. Thus, numerical precision of the hardware provides an upper limit on the total number of time steps. Assuming constant size increments, the single precision limit is on the order of $10^6 - 10^7$ time steps. The number of time steps required for the analyses are well below these limits.

A 0.006 second coarse model analysis requires 10 CPU hours on a HP/Apollo DN−10000 workstation; 4 CPU "days" are required for a refined model. The same analyses on a HP/Apol-

76

Figure 4.1−4. Boundary Conditions for the Finite Element Models
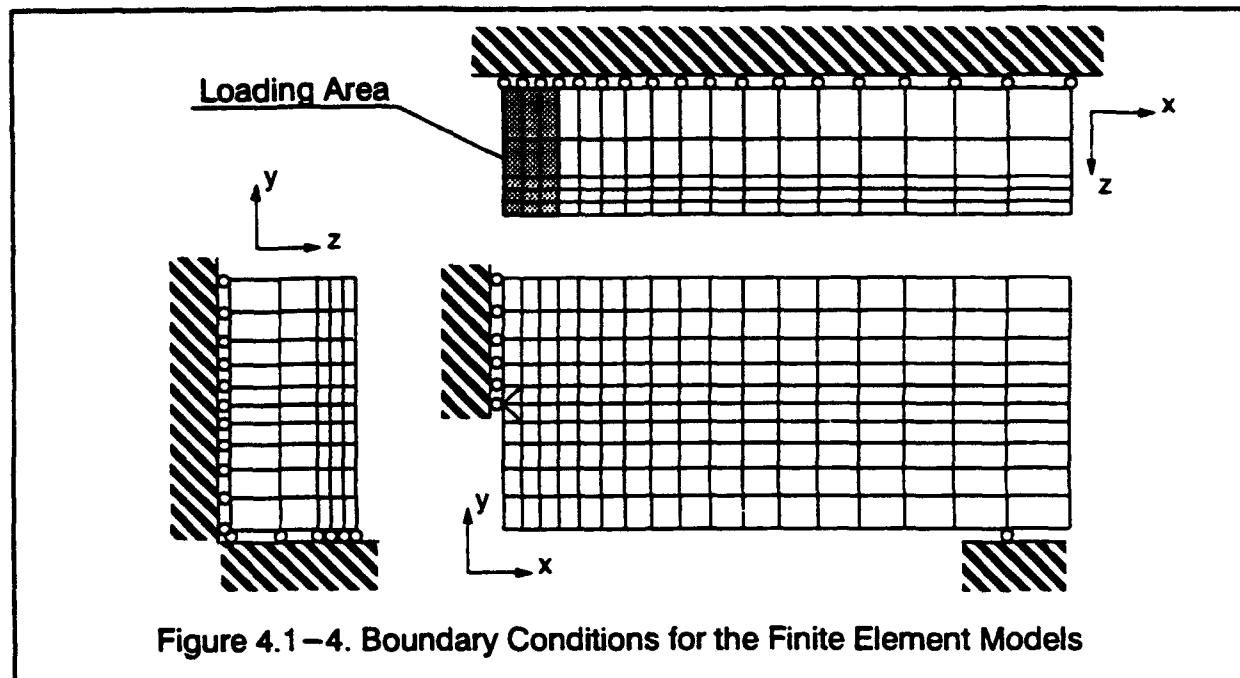
lo 9000/720 workstation run in 1/3 the CPU time. Nakamura [74] reports CPU use for a model similar in size and mesh density to the coarse deep crack model in this study. Hexagonal elements with the $\bar{B}$ method [46,69] were employed in their model which was analyzed for a duration of 0.0012 seconds. Utilizing an explicit dynamic code, their analysis required over 8 hours of CPU on a Cray XMP supercomputer. Drastic savings in CPU utilization are achieved in this study with the one−point Gaussian quadrature and hourglass suppression.

Figure 4.1−5. Crack Tip Detail for Refined Meshes
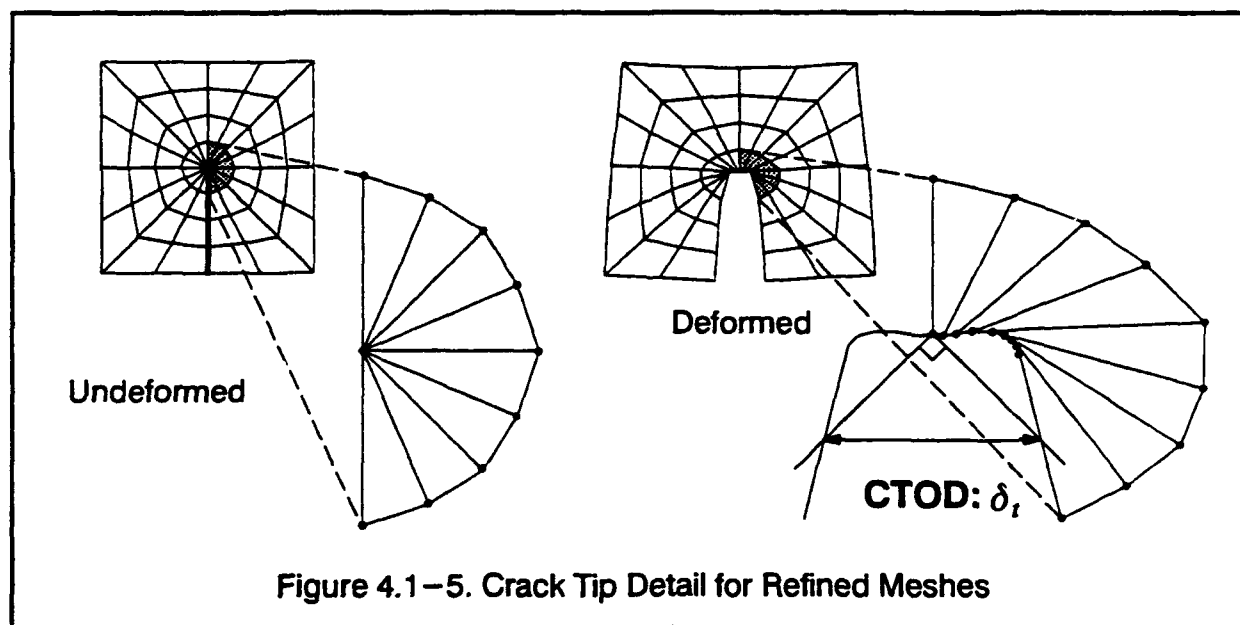
4.2 Rate–Insensitive Material Model

The investigation of strain rate effects requires a comparison of results for analyses conducted with materials exhibiting different degrees of rate sensitivity. Bodner–Partom parameters representative of A533B steel at 50°C (122°F) are used to evaluate strain rate effects. The 25% increase in the yield stress of this material for a strain rate of 1000 sec^{-1} is typical of a wide range of medium to high strength steels. The Bodner–Partom constants for A533B steel are provided in Table 2.3–2. Figure 2.3–2 shows the uniaxial response of this material at different strain rates and temperatures.

The lowest strain rate in Fig. 2.3–2, $1.0 \times 10^{-3} sec^{-1}$ at 50°C (122°F), establishes the quasi–static behavior for the A533B steel. This rate is less than the maximum rate of $8.33 \times 10^{-3} sec^{-1}$ specified in ASTM E8 for the determination of static yield strength in tension. (At a strain rate of $1.0 \times 10^{-3} sec^{-1}$, a typical uniaxial test specimen requires two and a half minutes to reach 15% elongation). The yield and ultimate stress for the $1.0 \times 10^{-3} sec^{-1}$ strain rate curve at 50°C (122°F) are 65.1 ksi (449 MPa) and 84.4 ksi (582 MPa) respectively. (The stress at 10% elongation is taken as the ultimate stress.) These values agree closely with published values of 64.5 ksi (445 MPa) and 86.6 ksi (597 MPa) for the yield and ultimate stresses, respectively [24,26].

The rate–insensitive material model must match the quasi–static response at the low strain rate of $1.0 \times 10^{-3} sec^{-1}$, and yet must not deviate significantly from the static response at higher strain rates on the order of 1000 sec^{-1} expected in the SE(B) analyses. Section 2.3.1 describes the general effect that the individual parameters have on the stress–strain curves predicted by the Bodner–Partom material model. The choice of D_0 strongly influences the rate sensitivity of the material. As D_0 increases, the rate sensitivity decreases as does both the yield and ultimate stresses. Equation 2.3–8 provides relationships between Z_0, Z_1, D_0, n and the yield and ultimate stresses. Thus an increase in D_0 relative to the actual value is sought, together with appropriate values of Z_0, Z_1, m and n to model the quasi–static, stress–strain curve at the higher strain rates.

The following iterative procedure is employed to determine parameters for the quasi–static Bodner–Partom model. First, an arbitrarily large D_0 is chosen to minimize the strain rate sensitivity. Using Eqn. 2.3–8, values for Z_0 and n are chosen to match the quasi–static yield stress at the lower strain rate of $1.0 \times 10^{-3} sec^{-1}$. Eqn. 2.3–8 and the ultimate stress determine the value for Z_1. Finally, a value for m is chosen to match the overall hardening behavior. Once these values are determined, the response of the material model is computed at the higher strain rate of 1000 sec^{-1}. The cycle is repeated for progressively larger values of D_0

Figure 4.2−1. Stress−Strain Curve for Rate−Insensitive Material Model
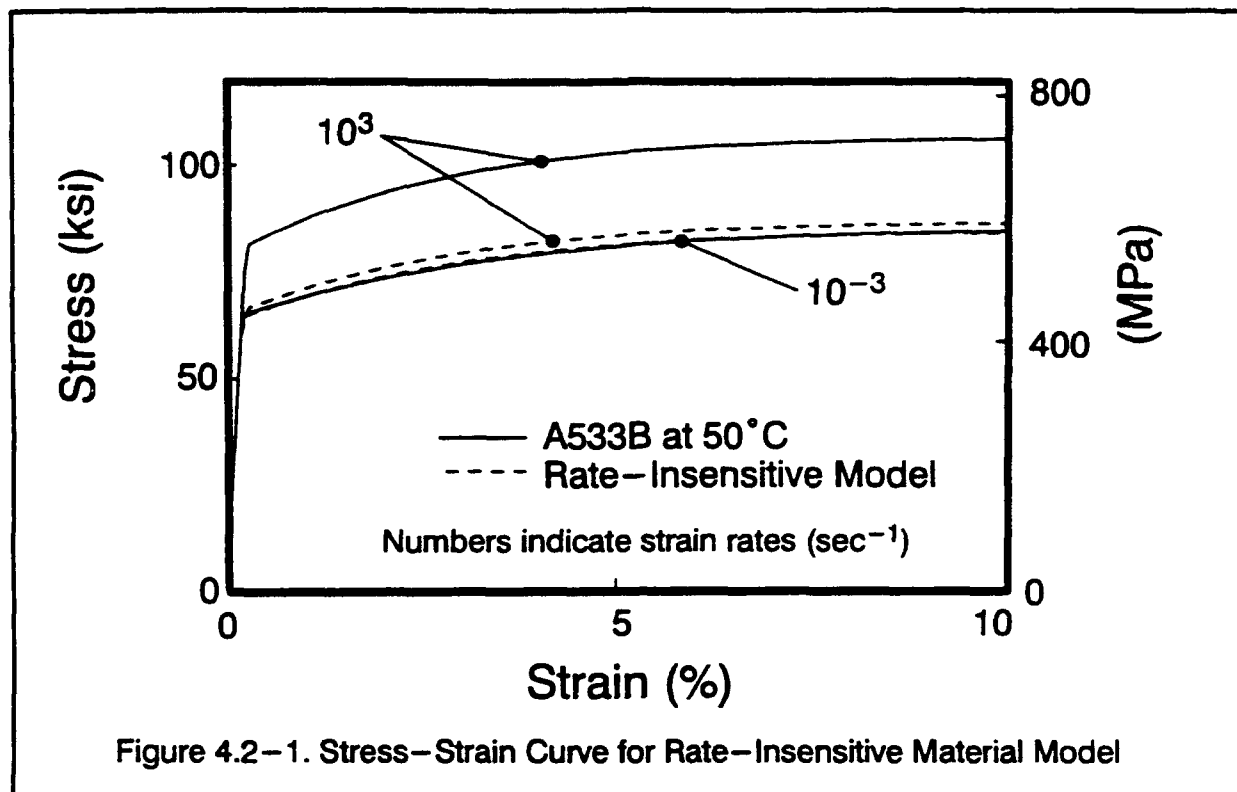
until the difference in the stress−strain curves at the two strain rates becomes small enough to model a rate−insensitive material. The resulting Bodner−Partom parameters for the rate−insensitive model of A533B are: m=0.51022 ksi^{-1} (0.0750 MPa^{-1}), n=10, Z_0=79.77 ksi (550.0 MPa), Z_1=104.426 ksi (720.0 MPa), and D_0= 1.0 × 10^{12} sec^{-1}.

Figure 4.2−1 shows the resulting stress−strain curve for the rate−insensitive model at the two strain rates: 1.0 × 10^{-3} sec^{-1} and 1000 sec^{-1}. Also shown in the figure are the stress−strain curves for A533B steel at 50°C (122°F) for the same two strain rates. For the rate−insensitive material, the maximum difference of the stresses for the two strain rates is less than 2%. This compares to a 25% difference in the stresses shown for the actual rate−sensitive material.

4.3 Determination of Applied Loading

Section 3.4 describes the method which was used to develop loadings for the finite element models. For each specimen and material, two separate analyses of 0.006 second duration are necessary: 1) an analysis in which the desired load−line displacement (observed in tests) is applied to the loading area to extract nodal reactions, and 2) an analysis in which a uniform pressure (computed from the nodal reactions obtained in 1) is applied to the loading area. The second analysis yields the kinematic quantities and fracture parameters of interest. The coarse

79

mesh models shown in Section 4.1 provide sufficient accuracy for resolution of global quantities such as the nodal loads resulting from the applied displacements. Considerable computational economy is achieved by using the coarse mesh models for the first set of analyses (i.e. the extraction of nodal loads from the load−line displacement application). The fine mesh models are analyzed with the smoothed loadings.

Figures 4.3−1 and 4.3−2 show the normalized loads obtained from analyses with imposed displacements for the rate−insensitive and rate−sensitive materials, respectively. The loads are normalized with respect to the limit load given by the plane−strain, plastic solution for pure bending [39,36]. The three−point bending produces a non−zero shear force at the crack ligament and alters the limit moment, however, this small effect is neglected here [68]. The limit moment on the ligament, M_L, is given by:

$$M_L = 0.364 \sigma_y b^2 B \qquad a/W > 0.295 \qquad (4.3-1)$$

$$M_L = \frac{1.155}{4}\left[1 + 1.686\frac{a}{W} - 2.72\left(\frac{a}{W}\right)^2\right]\sigma_y b^2 B \qquad a/W \leq 0.295 \qquad (4.3-2)$$

where σ_y is the yield stress, 65.5 ksi (452 MPa), b is the ligament length, B is the thickness of the specimen, a is the crack depth and W is the specimen width. This moment is related to the applied load by $P_L = 4M_L/L$, where P_L is the limit load and L is the span between the supports, 8 inches (203.2 mm). The limit loads are 23.5 kips (162.0 MPa) for the deep crack specimen, 64.2 kips (442 MPa) for the medium crack specimen and 71.1 kips (490 MPa) for the shallow crack specimen.

The time after impact is normalized by the time required for an unbounded dilatational wave to travel the width of the specimen, t_W [70,72]. Using the elastic properties for A533B steel in Eqn. 3.1−7, the unbounded dilatational wave speed, c_1, is 2.34×10^5 in/sec (5.13×10^6 mm/sec). For a specimen width, W, of 2.0 inches (50.8 mm), t_W is then:

$$t_W = \frac{W}{c_1} = 8.5 \times 10^{-6} \text{ sec} \qquad (4.3-3)$$

The normalized time scale is displayed at the top of Figs. 4.3−1 and 4.3−2. As shown in the figures, the duration of the analyses equals approximately 700 wave traversals over the specimen width. Spatial diffusion after several traversals reduces the discrete wave effects in the specimen. The large normalized times indicate that discrete wave effects are negligible for most of the specimen response.

Figure 4.3-1. Load Determination for Rate-Insensitive Material

Figure 4.3-2. Load Determination for Rate-Sensitive Material
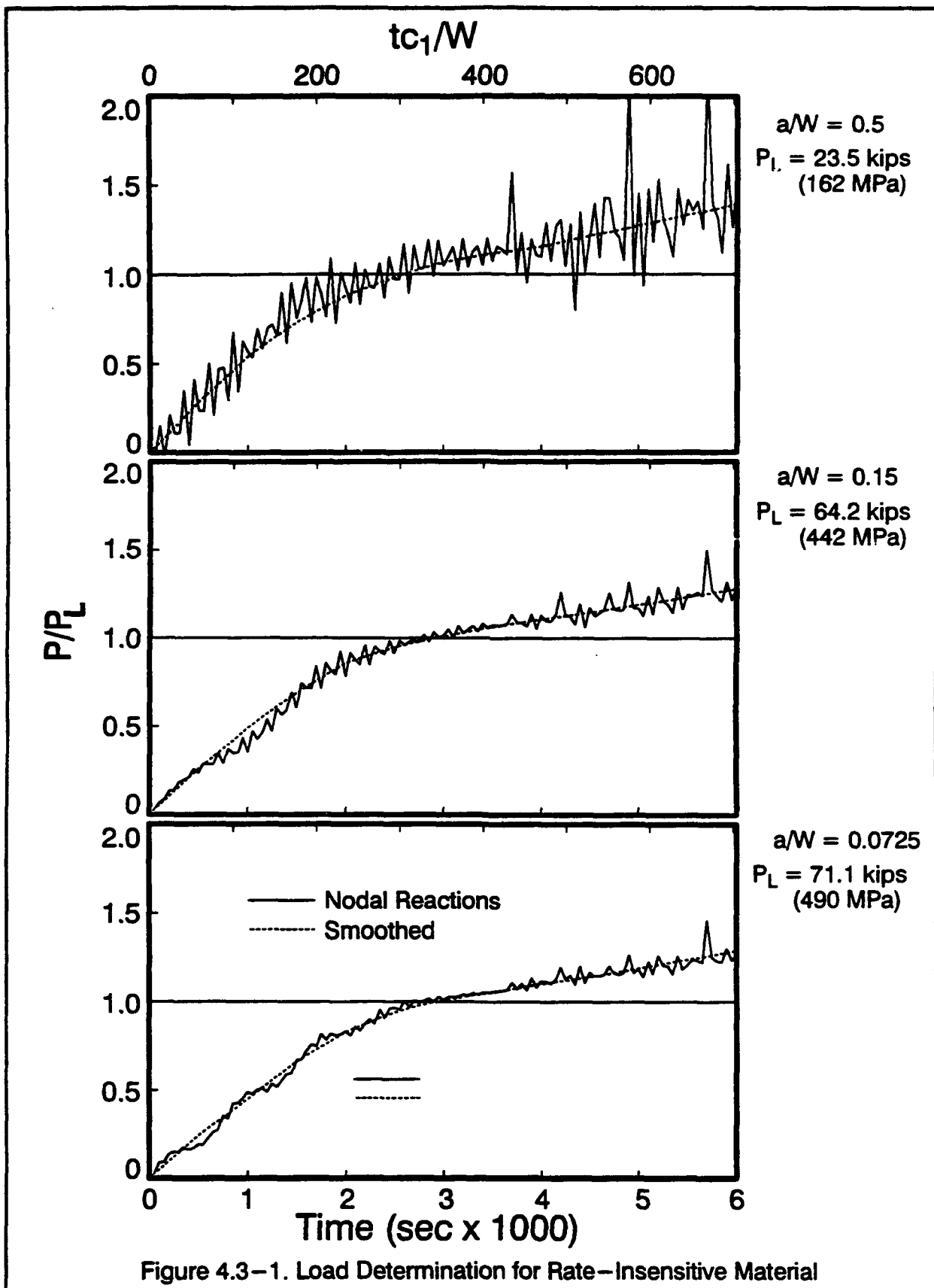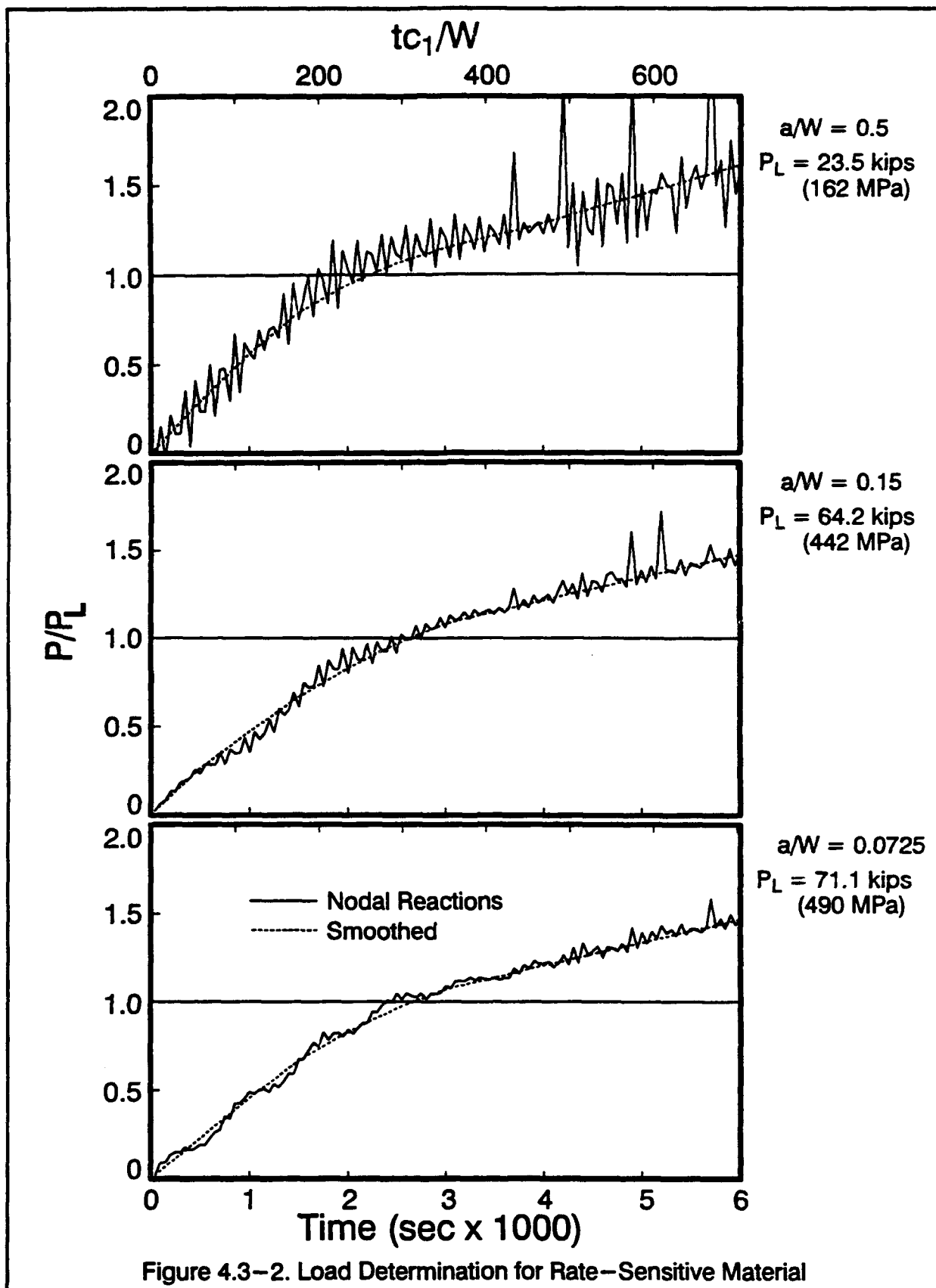
Figures 4.3−1 and 4.3−2 show relatively large oscillations of the nodal forces for the deep crack SE(B) specimen. These oscillations decrease considerably for the medium crack specimens and nearly vanish for the shallow crack specimens. As described in Section 3.4.1, application of the displacements uniformly on the loaded area creates a rigid boundary on that portion of the specimen. Enforcement of this deformation constraint generates oscillations on the order of the time required for a stress wave to traverse one of the elements on the rigid boundary. The amplitude of these oscillations indicates the extent to which the enforced deformation deviates from the deformation pattern consistent with an applied normal pressure.

Figure 4.3−3. Deformation Patterns for the Deep and Shallow SE(B) Specimens
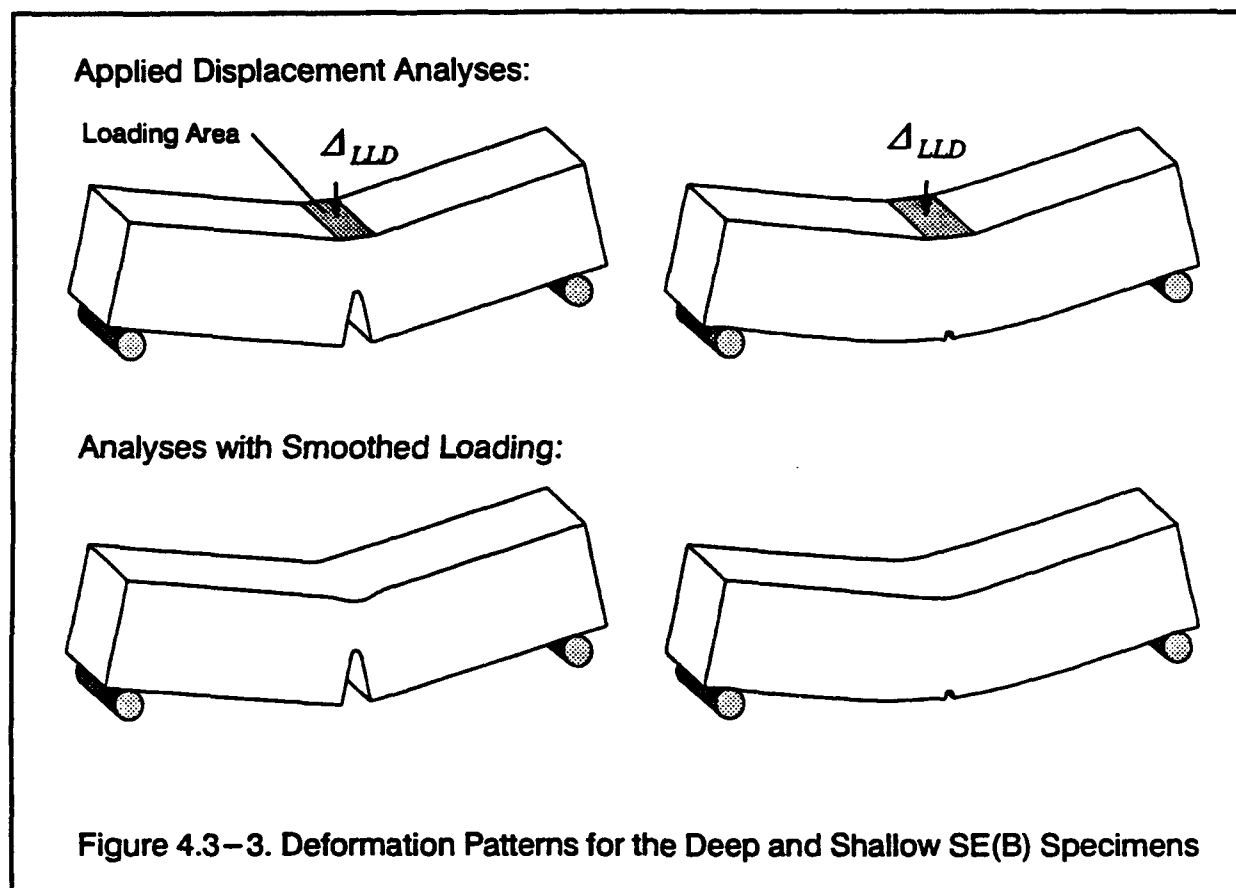
Figure 4.3−3 shows the deformed shapes of the deep and shallow crack specimens for the two groups of analyses: 1) the analyses using applied displacements, and 2) the analyses using the smoothed nodal loads. The conventional bending deformation of the deep crack specimen, (represented by the analyses with the smoothed nodal loadings), concentrates deformation in the ligament region. The displacement boundary conditions create a rigid surface defined by the loading area. The specimen ends rotate about a finite width defined by this surface. This difference in the deformation pattern creates the large oscillations of the nodal forces shown in Figs. 4.3−1 and 4.3−2. For the medium and shallow crack specimens, the deformation is

83

more of a beam−bending pattern rather than the concentrated ligament deformation of the deep crack specimen. For these specimens the applied displacement deformation deviates less from the natural deformation pattern, resulting in a lower amplitude of the nodal force oscillations.

Figures 4.3−4 and 4.3−5 show the vertical displacements at mid−span for the analyses conducted with the smoothed pressure loadings. Nodes on the ligament experience a range of vertical displacements. The minimum vertical displacement occurs at the crack tip on the centerplane of the specimen; the maximum vertical displacement occurs at nodes on the loaded area at the free surface. Figures 4.3−4 and 4.3−5 show these displacements together with the original load−line displacement measured in the drop tower tests. As shown in the figures, good agreement exists between the finite element analyses and the drop tower tests for all six cases.

The vertical displacement histories shown in Figs. 4.3−4 and 4.3−5 reveal well defined periodic oscillations during the initial 0.003 seconds. Elastic vibration in the first dynamic mode is responsible for these periodic oscillations. The first two modes and their frequencies were computed for the finite element models using the POLO−FINITE system [35]. The eigenvalue analyses were performed using the refined models with trilinear hexagonal elements, lumped nodal masses, and a 2 by 2 by 2 Gaussian quadrature with the B−bar technique for generating the element stiffness matrices [46,69]. Due to symmetry, the first two modes correspond to the first and third modes of the full specimen.

		Deep Crack	Medium Crack	Shallow Crack
Mode 1	T_1	0.621×10^{-3} sec	0.416×10^{-3} sec	0.404×10^{-3} sec
	ω_1	0.101×10^5 rad/sec	0.151×10^5 rad/sec	0.156×10^5 rad/sec
Mode 3	T_3	0.120×10^{-3} sec	0.913×10^{-4} sec	0.898×10^{-4} sec
	ω_3	0.523×10^5 rad/sec	0.689×10^5 rad/sec	0.700×10^5 rad/sec

Table 4.3−1 Elastic Periods and Frequencies for the SE(B) Specimens

Table 4.3−1 summarizes the periods and the frequencies obtained for the three different SE(B) specimens. Figures 4.3−4 and 4.3−5 indicate the first fundamental period on the load−line displacement for each specimen. The period of oscillations in the displacement response matches closely the first fundamental period up to 0.002 seconds into the response. Beyond this time, plastic deformation in the specimens causes the period of the oscillations to elongate, and finally, after approximately 0.004 seconds these oscillations disappear altogether.

84
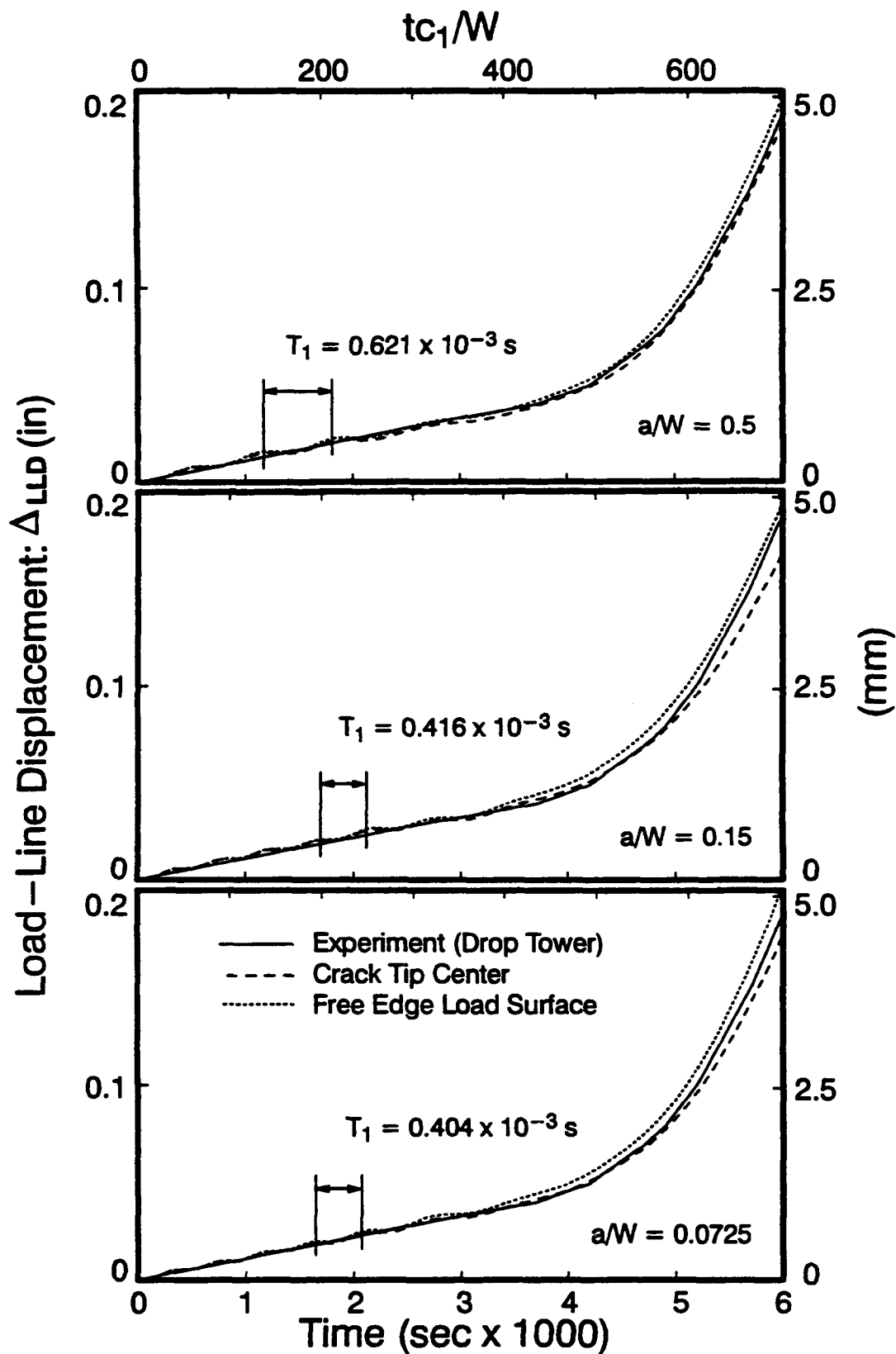
Figure 4.3—4. Mid—Span Displacements for Rate—Insensitive SE(B)

Figure 4.3−5. Mid−Span Displacements for Rate−Sensitive SE(B)
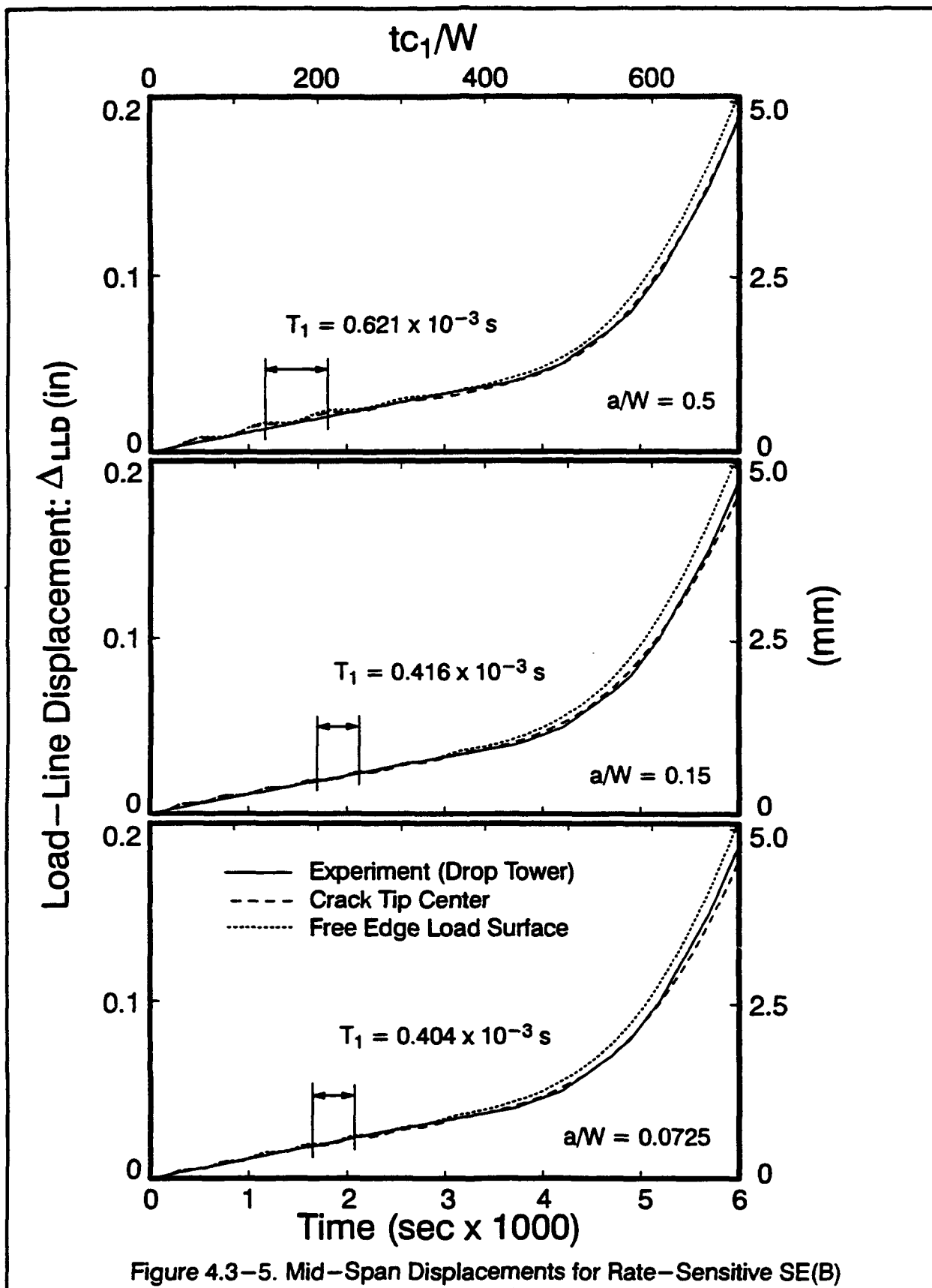
Figure 4.3−6 summarizes the derived load−time histories for the six cases: three SE(B) specimen a/W ratios with both a rate−insensitive and a rate−sensitive material. Once the derived loads are normalized with respect to the limit load, the three specimens behave in a quantitatively similar manner. During the initial elastic response of the specimen, strain rate sensitivity does not affect the predicted loading. Once sufficient plastic deformation occurs, high strain rates elevate the loading of the rate sensitive specimens. This causes the derived loading for the two material models to diverge. The rate sensitivity provides load elevations of approximately 20% relative to the strain rate−insensitive material model for each of the three specimens.

In previous computational work, Nakamura et. al. [70,74,72] assum⁓d a loading history based upon experimental results obtained prior to the adoption of aluminum wedges [50]. Nakamura used simple load ramps with a total duration of 0.0012 seconds. They report a maximum load of 1.2 × the static limit load (1.45 × in [70]), and faster loading rates (0.00006 to 0.0005 second ramps to maximum load). As shown in Fig. 4.3−6, the current study predicts the applied load to reach the limit load between 0.002 and 0.003 seconds, indicating less severe dynamic effects than those reported in Nakamura's work. The faster loading rates adopted by Nakamura approximate loading durations observed in Charpy V−Notch (CVN) test specimens [78,9].

4.4 Transition Times

Nakamura and Shih [70] introduced the concept of a *transition time*, t_T, which denotes the time after which dynamic effects are decreasing in the specimen. The initial impact of the tup rapidly increases the specimen velocity, thereby increasing the kinetic energy. As the specimen deforms, the internal energy also increases rapidly. For the range of practical loading rates of interest, the internal energy eventually overtakes the kinetic energy of the specimen due to extensive plasticity. The transition time is defined as the time after which the total kinetic energy of the specimen becomes less than the internal energy of the specimen, and indicates the duration of initial dynamic effects from the impact. After the transition time, the kinetic energy continues to increase, but at a much diminished rate relative to the increasing internal energy. Nakamura proposed and validated a limit of 2 × t_T as a time beyond which the evaluation of the fracture parameters (J−integral) with static formulas yields acceptable accuracy [72].

4.4.1 Single Degree of Freedom Model

Direct measurements of the kinetic and internal energies of the specimen are not possible during an experiment. Eqn. 1.2−5 summarizes the model, proposed by Nakamura in [70],
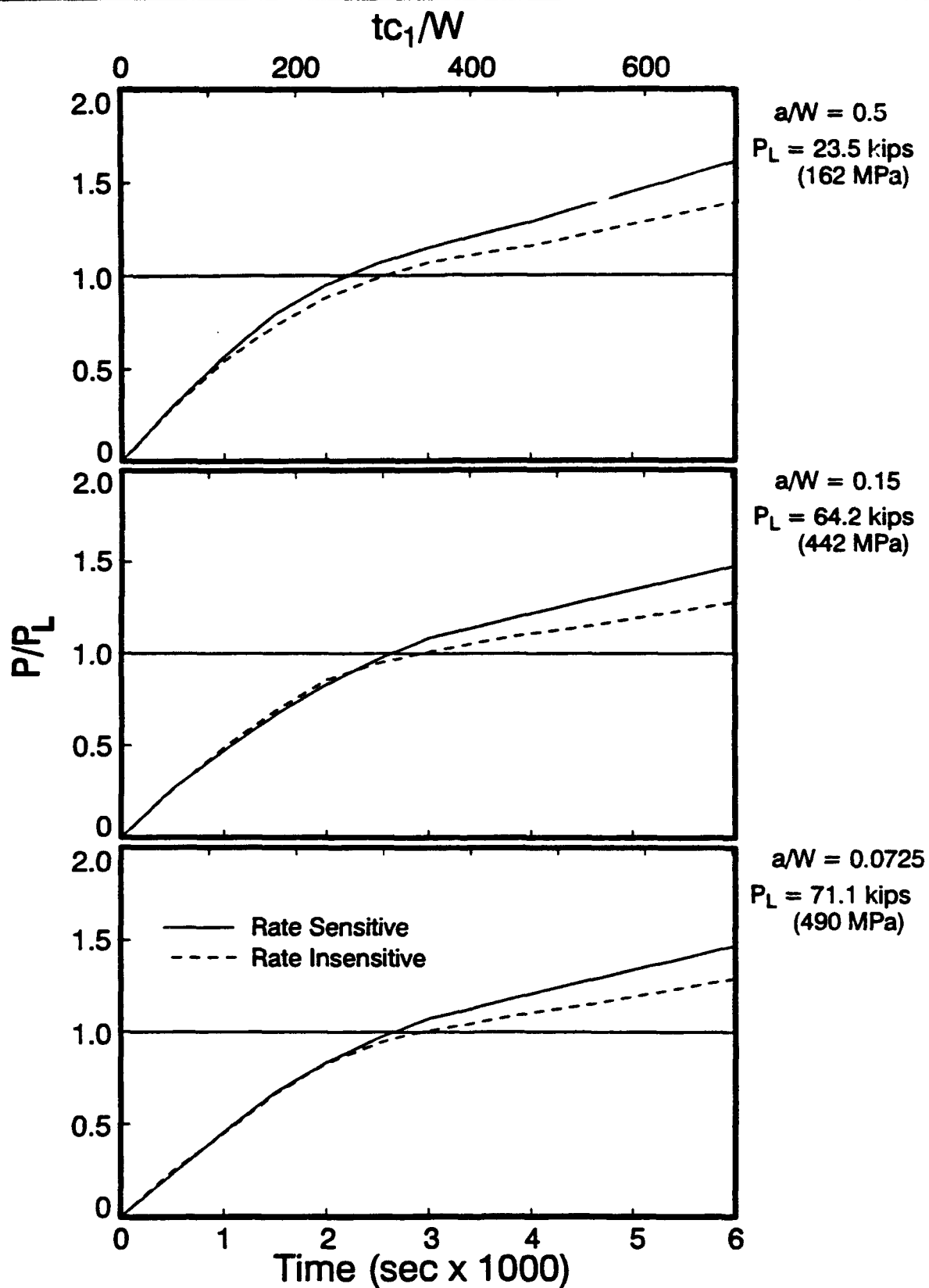
Figure 4.3–6. Smoothed Nodal Forces for Different Rate Sensitivities

which estimates these energies from the load–line displacement curve. Figure 4.4–1 shows

Figure 4.4–1. Single Degree of Freedom SE(B) Model
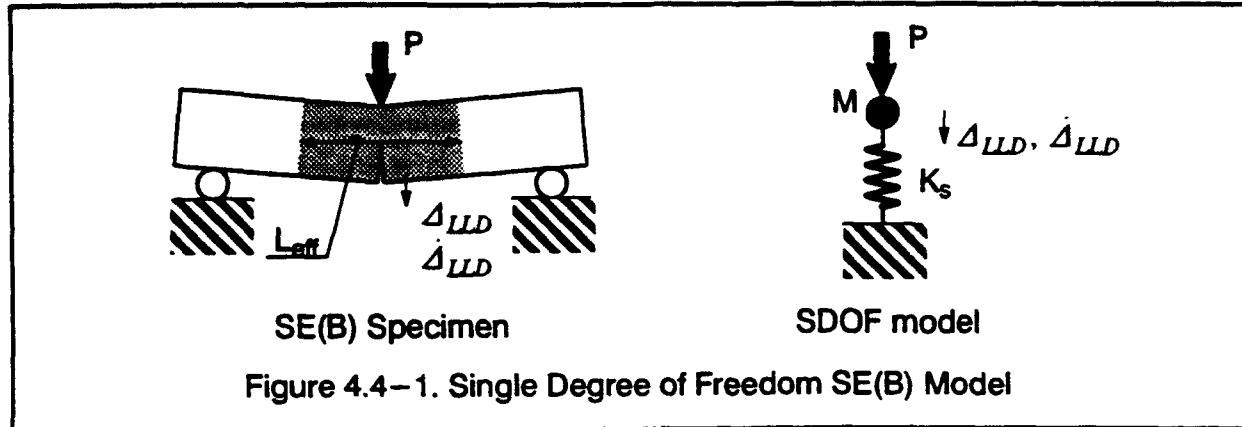
the single degree of freedom (SDOF) idealization of the SE(B) specimen model used to esti-
mate the transition time. The globally elastic behavior of the specimen prior to the transition
time allows elastic parameters to be used in the derivation of the model. Equating static rela-
tions for the internal and external work yields:

$$U = \int_{Vol} \sigma_{ij}\varepsilon_{ij}dV = \tfrac{1}{2}P\Delta_{LLD} = \tfrac{1}{2}K_s \,\dot{\Delta}^2_{LLD} \qquad (4.4-1)$$

where U is the internal energy and σ_{ij} and ε_{ij} are the stresses and strains. Figure 4.4–1 shows
P and Δ, the load and the load–line deflection. The elastic stiffness, K_s, of the SE(B) specimen
relates the applied load to the load–line displacement. Formulas for the computation of K_s
for a range of SE(B) specimens are given in [97].

Computation of the kinetic energy for the SDOF model requires an equivalent lumped
mass for the specimen. A contributory volume approach allocates the middle–half of the load-
ing span as mass for the SDOF model. This volume is defined by the specimen width and depth,
W and B, together with an effective length, L_{eff}, as shown in Fig. 4.4–1. The kinetic energy,
T, is then:

$$T = \tfrac{1}{2}M\dot{\Delta}^2_{LLD} = \tfrac{1}{2}\varrho WBL_{eff} \,\dot{\Delta}^2_{LLD} \qquad (4.4-2)$$

where M is the effective mass, $\dot{\Delta}_{LLD}$ is the load–line velocity, and ϱ is the material density.
The ratio of the kinetic energy to the internal energy becomes:

$$\frac{T}{U} = \frac{\varrho WBL_{eff} \dot{\Delta}_{LLD}^2}{K_s \Delta_{LLD}^2} \qquad (4.4-3)$$

Substitution of the relationship for the unconfined dilatational wave speed of the material, $\varrho = E/c_o^2$, into Eqn. 4.4−3 and the structural compliance, C_s, for the reciprocal of the specimen stiffness, K_s, yields Eqn. 1.2−5:

$$\frac{T}{U} = \left[S \frac{W}{c_o} \frac{\dot{\Delta}_{LLD}(t)}{\Delta_{LLD}(t)} \right]^2 \quad \text{where} \quad S = \left[\frac{LBEC_s}{W} \right]^{\frac{1}{2}} \qquad (4.4-4)$$

Nakamura [70,72] reports excellent agreement of the energy ratio given by Eqn. 4.4−4 with 3−D finite element results for deep crack specimens.

4.4.2 Comparison of SDOF Model with Finite Element Results

Static analyses using the POLO−FINITE system [35] were conducted to determine K_s, the equivalent SDOF stiffness, for the deep, medium and shallow crack specimens. (Although values of K_s for SE(B) specimens are presented in [97], these are computed using two−dimensional models and as a result are not sufficiently accurate to evaluate the SDOF model against the 3−D finite element results.) The static analyses utilized the fine meshes with the trilinear hexagonal elements and the B−bar technique to generate the element stiffness matrices. Ap-
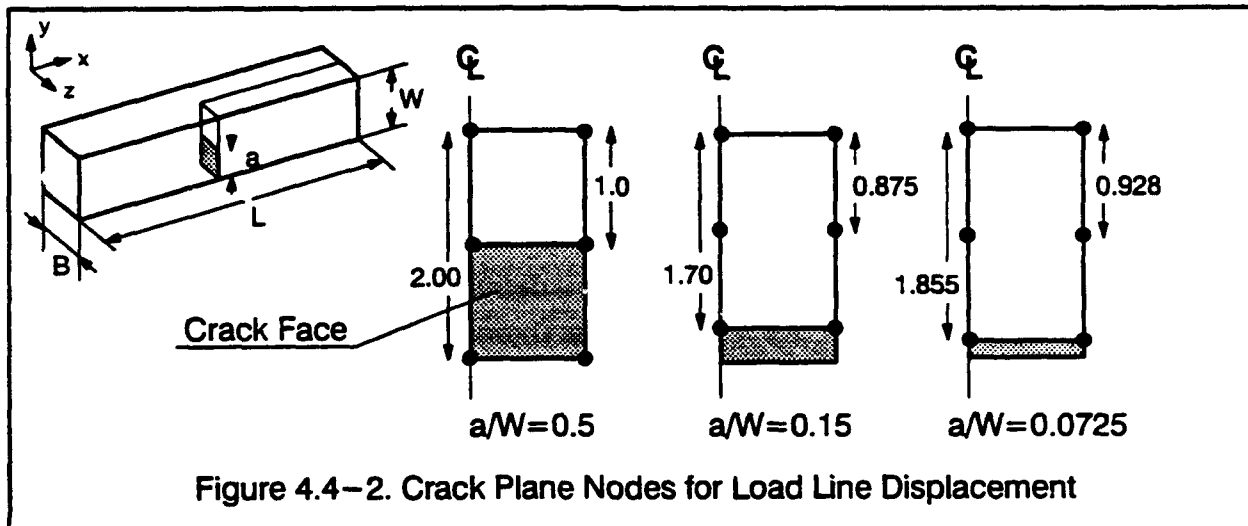
Figure 4.4−2. Crack Plane Nodes for Load Line Displacement

plication of a total load of 1 kip as a uniform pressure on the loading area provides the crack-plane displacements utilized to calculate K_s. As shown in Figs. 4.3−4 and 4.3−5, points on the crack plane experience a range of displacements. Also, the loading surface of the SE(B) speci-

men exhibits local deformation, making the definition of a single–valued load–line displacement non–trivial (see Fig. 4.3–3). The single displacement value for use in defining K_s for the SDOF model is obtained by averaging values at key points on the ligament as shown in Fig. 4.4–2. Load–line velocities are determined in the same manner. The mass for the SDOF model is computed with an L_{eff} of 4.0 inches for all three specimens. The resulting SDOF parameters are summarized in Table 4.4–1.

A comparison of the fundamental frequencies for the SE(B) specimens with those for the SDOF models confirms the accuracy of the simplified models. Table 4.4–1 shows the computed frequencies of the SDOF models, $\omega = \sqrt{K_s/M}$, together with the percent deviation from the finite element computations reported in Table 4.3–1. The maximum error is approximately 5%.

		Deep Crack	Medium Crack	Shallow Crack
Static	K_s	$0.107 \times 10^7 \text{lb/in}$	$0.273 \times 10^7 \text{lb/in}$	$0.298 \times 10^7 \text{lb/in}$
Dynamic	M	$0.0118 \text{ lb sec}^2/\text{in}$	$0.0118 \text{ lb sec}^2/\text{in}$	$0.0118 \text{ lb sec}^2/\text{in}$
	ω_1	$0.956 \times 10^4 \text{rad/sec}$	$0.152 \times 10^5 \text{rad/sec}$	$0.159 \times 10^5 \text{rad/sec}$
ω_1 error		-5.3%	$+0.9\%$	$+2.1\%$

Table 4.4–1 SE(B) SDOF Model Properties

Figure 4.4–3 compares the energy ratios for the SDOF and finite element models for the three specimens. (Finite element computation of the energies follows Eqns. 3.1–45, while the SDOF models use Eqn. 4.4–3 with load–line displacements and velocities taken from the finite element results.). The transition time occurs early in the response while the structural response is predominantly elastic. Strain rate effects are negligible during this early stage, and both material models produce the same results. The finite element curves shown in Fig. 4.4–3 are identical for the rate–sensitive and rate–insensitive models.

Figure 4.4–3 shows that the energy ratio decreases rapidly for all three models, approaching zero soon after the transition time. The corresponding transition times are: 0.240×10^{-3}, 0.161×10^{-3} and 0.157×10^{-3} seconds for the deep, medium, and shallow crack specimens respectively. (Normalized with respect to t_W, these are: 28.1, 18.9, and 18.4 respectively.) Nakamura [72] reports a normalized transition time of 28 for a deep crack specimen, identical to the results reported here for the deep crack SE(B) specimen. As shown in the figure, the SDOF models predict accurately the specimen energy ratios for the early elastic response of the SE(B) specimens.

91
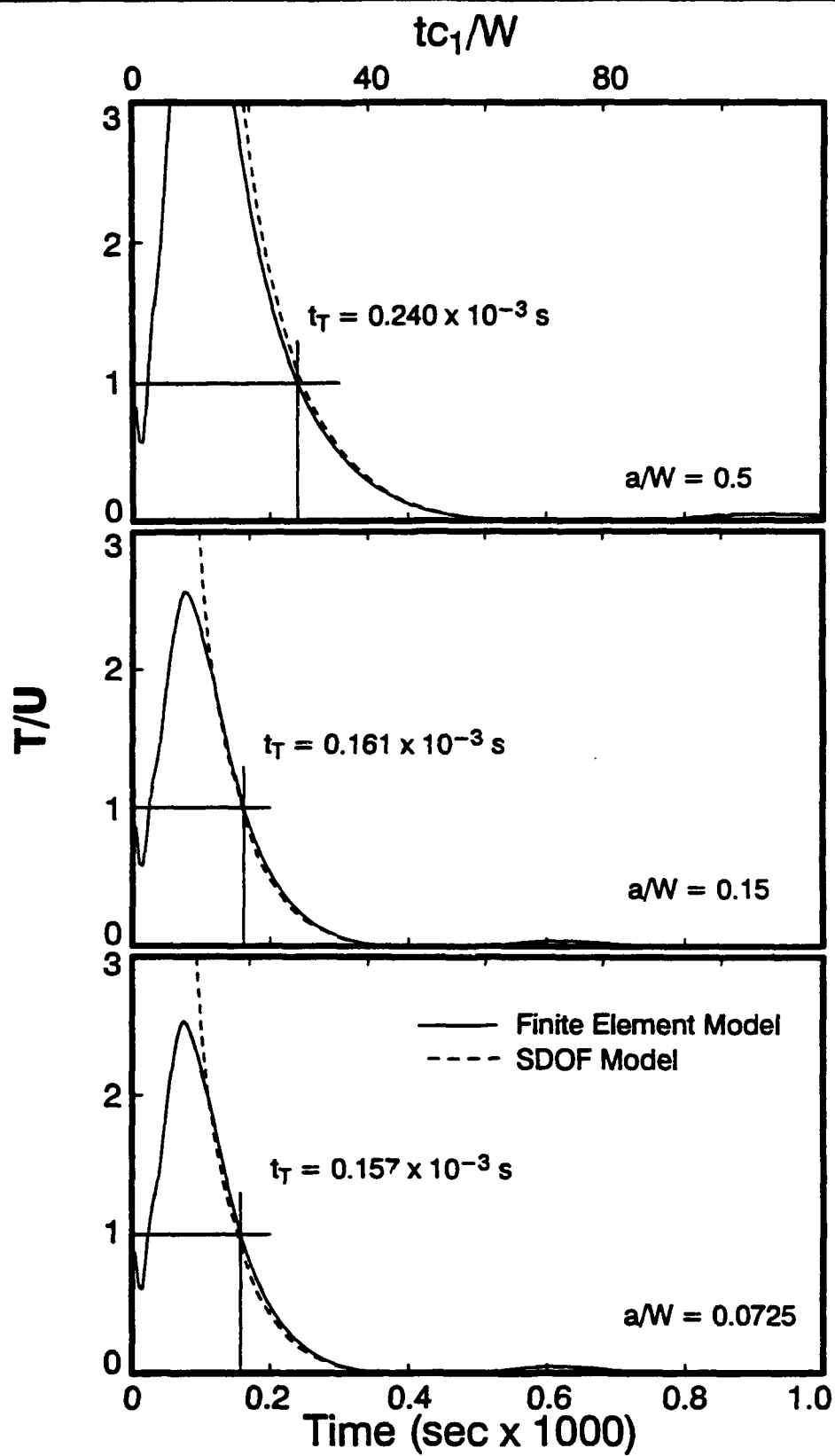
Figure 4.4–3. Transition Time for the SE(B) Specimens

4.4.3 Transition Times: Discussion

By writing Eqn 4.4−3 in terms of the SDOF mass and by recognizing that $\omega = \sqrt{K_s/M}$, the energy ratio simplifies to:

$$\frac{T}{U} = \frac{\dot{\Delta}^2_{LLD}}{\omega^2_1 \Delta^2_{LLD}} \qquad (4.4-5)$$

At the transition time the ratio is equal to unity, giving:

$$\frac{\dot{\Delta}_{LLD}}{\omega_1 \Delta_{LLD}} = 1 \qquad (4.4-6)$$

Thus, the transition time occurs when the product of the frequency and the load−line displacement is equal to the load−line velocity. If the velocity is constant, $\Delta_{LLD} = \dot{\Delta}_{LLD} \, t$, the transition time is then:

$$t_T = \frac{1}{\omega_1} = \frac{T_1}{2\pi} \qquad (4.4-7)$$

This indicates that for a constant load−line velocity, regardless of magnitude, the transition time is defined uniquely by the fundamental period of the system.

Figure 2.4−1 shows the displacement−time history utilized in this study. The initially constant velocity of 10.9 in/sec (0.278 m/sec) suggests the use of Eqn. 4.4−7 to estimate the transition time. Utilizing the frequencies of the SDOF models, the transition times computed via Eqn. 4.4−7 are: 0.105×10^{-3}, 0.066×10^{-3} and 0.063×10^{-3} seconds for the deep, medium, and shallow crack specimens respectively. (Normalized with respect to t_W, these are: 12.3, 7.7, and 7.4 respectively.) These transition times are only 40% of those computed from the finite element models. The inability of the finite element analyses to match the initially constant velocity produces these differences. The use of finite element displacements and velocities in the SDOF model, however, provides very accurate comparisons with the finite element energy predictions as shown in Fig. 4.4−3. Thus, the accurate determination of transition times from displacement records using the SDOF model requires precise measurements of the specimen displacement and velocity early in the response.

For the loading rates experienced in drop tower tests, the transition time is a small fraction of the fundamental period of the system. This is illustrated in Eqn. 4.4−7 for a constant velocity

93

response, and is confirmed for the three specimens of this study (the transition time is consistently 39% of the first period of each respective specimen). *The specimens respond in a manner analogous to an elastic SDOF system subjected to a ramp loading.* The SDOF system vibrates about the static equilibrium position defined by the stiffness and the instantaneously applied loading. The SDOF system thus experiences harmonic oscillations. At approximately one half of the fundamental period following the application of the ramp loading, the first crest of harmonic motion occurs (i.e. zero velocity and kinetic energy) which defines the transition time. The zero energy ratios of the finite element analyses at exactly half of their respective periods confirm this behavior (see Fig. 4.4-3). These observations suggest that the transition time is more indicative of the first mode vibration of the specimen rather than a global time scale to assess the significance of dynamic effects.

4.4.4 Loading Rate Dependence of the Transition Time

Nakamura [72] performed a finite element study of an SE(B) specimen using a loading rate considerably higher than those considered here. The in−plane dimensions of the SE(B) specimen are identical to the deep crack specimen in this study, but with a thickness of $B=1.0$ inches, rather than the $B=2.0$ inches used in this study. Nakamura reports a transition time identical to that found for the deep crack SE(B) specimens of this study, thus confirming the observations described in the previous section. The finite element analyses reported by Nakamura [72] are repeated here for comparison. (These analyses also provide verification of the computational techniques employed here.) Figure 4.4−4 shows the finite element mesh and parameters of interest. Element layers of equal thickness are defined over B. A linear eigenvalue analysis of this model provides:

$$\omega_1 = 0.101 \times 10^5 \text{rad/sec} \quad T_1 = 0.621 \times 10^{-3} \text{sec}$$
$$\omega_3 = 0.529 \times 10^5 \text{rad/sec} \quad T_3 = 0.119 \times 10^{-3} \text{sec}$$

$$(4.4-8)$$

These values agree very closely with values reported in Table 4.3−1 for the deep crack specimen. Although Nakamura utilized a strain−hardening, nonlinear−elastic Ramberg−Osgood material model, the rate−sensitive Bodner−Partom material is used in this analyses. Figure 4.4−5 shows the loading and the load−line displacement for analyses with the high loading rate. For comparison, the figure also shows the corresponding results for the deep crack SE(B) specimens analyzed with the 0.006 second drop−tower loading ($B=2.0$). The higher loading rate and thinner specimen employed in Nakamura's analysis yields a terminal velocity of 185 in/sec. Specimen oscillations corresponding to the first elastic mode do not occur with Naka-

Figure 4.4−4. Specimen Dimensions for High Loading Rate Analyses
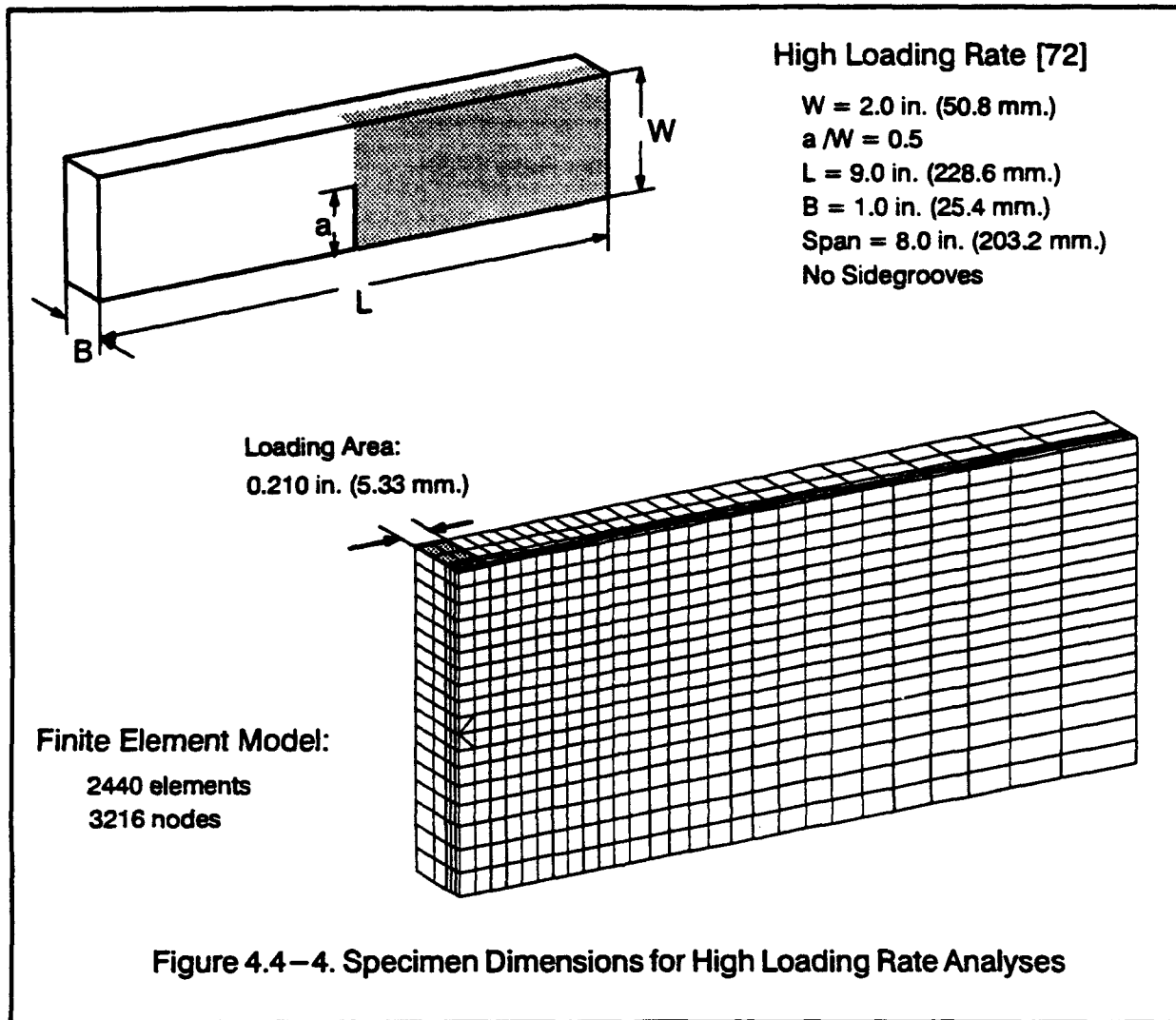
mura's loading rate. Figure 4.4−5 shows some rebounding of the thinner specimen beyond the maximum load line displacement of 0.122 inches (3.09 mm).

Figure 4.4−6 compares the energy ratios for the two analyses. The sum of internal and kinetic energies for these two specimens differ significantly at the transition time. The total energy for the specimen under the high rate loading is 96.5 lb−in (10.9 Nm), while the total energy for the deep crack SE(B) under the drop−tower loading is only 5.7 lb−in (0.64 Nm). However, the evolution of the energy ratio for the two analyses is very similar and yields nearly identical transition times. This confirms the analogy of the elastic SDOF system responding to a ramp load. For the loading rates examined, the transition time is completely determined by the first elastic period of the specimen.
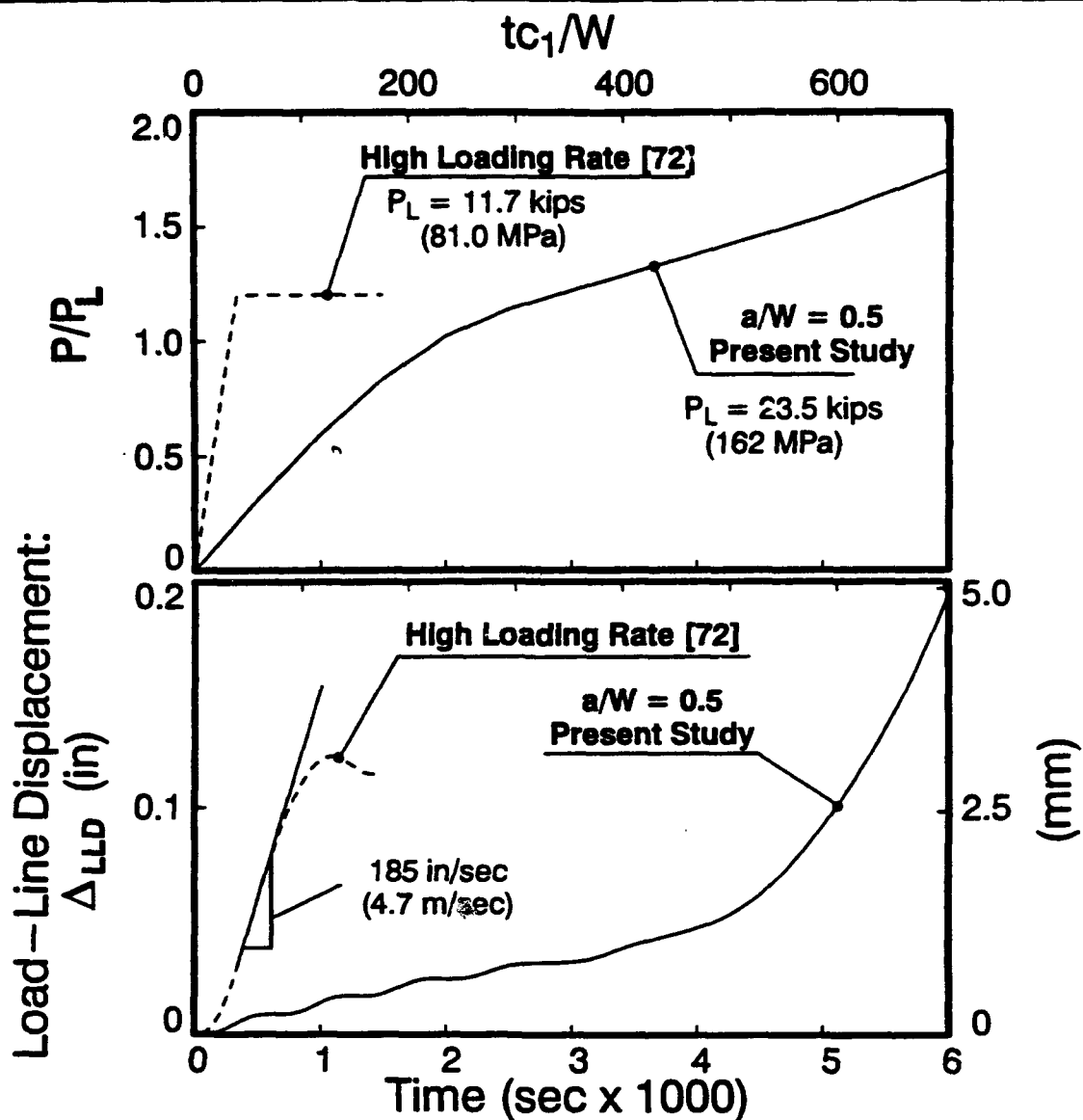
Figure 4.4−5.   Load and Displacement Response for Two Deep Crack SE(B)
Specimens Under Different Loading Rates

4.4.5 Transition Time: Experimental Results

Kirk [59] uses Eqn. 1.2−5 together with the history of load−line displacement and load−line velocity of a shallow crack specimen (a/W = 0.1) measured in a drop tower test to determine the extent of dynamic behavior. Kirk reports large fluctuations and considerably higher values (as high as 10) for the ratio of internal energy to the kinetic energy of the specimen. As late as 0.0014 seconds into the test (approximately 9 times the transition time for the shallow crack specimen) the energy ratio exhibits peaks that exceed unity.
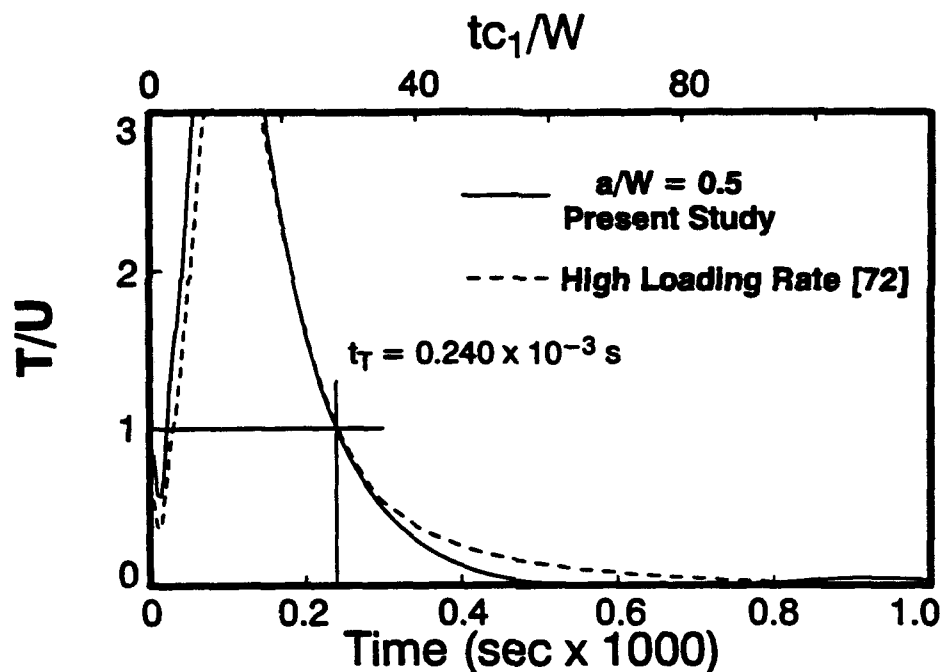
Figure 4.4—6.   Energy Ratio of Two Deep Crack Specimens Under Different
Loading Rates

Figure 2.4—1 shows the load—line displacement record of Kirk's test. The relatively smooth nature of the displacement curve provides no indication of erratic changes in the energy ratio. Such large fluctuations in the energy ratio are due to the initial impact and possibly to some noise in the measurements. Kirk recommends use of a transition time at which the energy ratio declines to less than 0.1, (1.75 milliseconds) as the time after which dynamic effects are negligible. This value is approximately 10 times greater than the transition times obtained in this study.

4.5 Strain—Stress Distributions in SE(B) Specimens

This section examines the distribution of strain rates and stresses throughout the three SE(B) specimens. The effect of visco—plastic material response is of specific interest.

4.5.1 Strain Rates

Fig. 4.5—1 shows the distribution of generalized strain rates (See Eqn.2.3—6) for the three specimens. The visible surfaces include the crack plane, the vertical free surface and the top surface of the specimens. The strain rates indicated on the specimen are taken from analyses using the rate sensitive material. Results for the rate—insensitive analyses are indistinguish-

97

Figure 4.5–1. Strain Rates shown on Quarter Symmetric Models
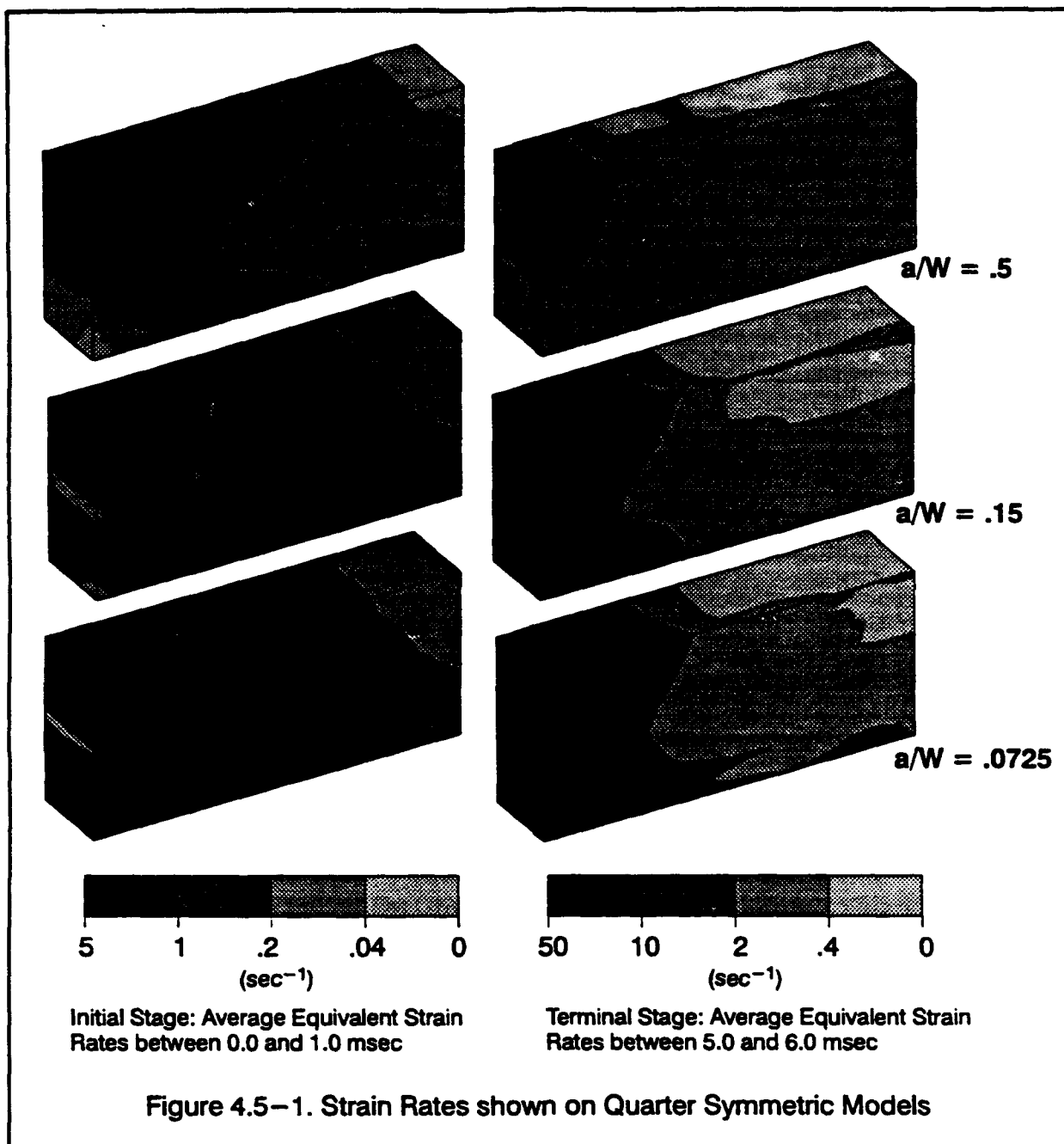
able from those in Fig. 4.5–1. The identical strain rates are expected since the loading is defined to produce nearly constant velocity response in all specimens.

The strain rate distributions shown in Fig. 4.5–1 correspond to two loading stages of interest: 1) the strain rates from zero to 0.001 seconds represent the initial loading stage, and 2) the strain rates from 0.005 to 0.006 seconds represent the terminal loading stage. These stages correspond to portions of the displacement history of the specimen that exhibit constant velocity (see Figs. 4.3–5 and 4.3–4): a constant load line velocity of 10.94 in/sec (0.278 m/sec) up to

0.004 seconds and a constant terminal velocity of 100 in/sec (2.54 m/sec) after approximately 0.005 seconds.

The load—line velocity at the terminal loading stage is ten times larger than in the initial stage. The strain rates shown in Fig. 4.5—1 also reveal the same factor of ten in the strain rates. The distribution of strain rates in the terminal stage of the response reveal the different deformation patterns of the three specimens. During the terminal velocity stage, relatively large strain rates, (above 50/sec,) are concentrated in the remaining ligament for the deep crack specimen. The shallow crack specimen, however, experiences these elevated strain rates that extend to the top and bottom surfaces of the specimen.

4.5.2 Stresses

Figures 4.5—2, 4.5—3 and 4.5—4 show the distribution of von Mises stress, normalized with respect to the static yield value of 64.5 ksi (445 MPa), for the three specimens. Results for both rate—sensitive and rate—insensitive analyses are shown in the figures. Rate sensitivity does not affect the von Mises stress distributions prior to 0.003 seconds for the three specimens. The specimen behavior is predominantly elastic prior to this point. At 0.004 seconds into the response, all three specimens show full plastic zone development across the ligament for both material models. This agrees with Fig. 4.3—6 in which the specimens are shown to be near limit load at 0.004 seconds. Figures 4.3—5 and 4.3—4 also confirm that the elastic oscillations of the specimens cease after this time. Once plastic deformation becomes extensive, the rate sensitive material model shows significant increases in the von Mises stress levels for all three specimens corresponding to the increased yield stress.

The plastic zones developed after initial ligament yielding parallel the formation of high strain rate zones reported in Section 4.5.1. The plastic zone for the deep crack specimen is confined to the remaining ligament, while the plastic zone breaks through to the free surface behind the crack for the shallow SE(B) specimen. For static loading, this phenomena strongly affects the levels of opening mode stress near the crack tip [33]: confinement of plastic deformation to the remaining ligament in the deep crack specimen maintains the crack tip constraint while the breakthrough of the plastic zone to the free surface in the shallow crack specimen significantly reduces crack—tip constraint.

The plastic zones in the medium and shallow crack specimens approach the strain gage locations near the quarter—span at 0.004 seconds. Consequently, the through—depth variation of longitudinal stress may not conform to the simple, linear distribution of beam theory

99

Figure 4.5−2. von−Mises Stress Distributions for the Deep Crack SE(B) Specimen
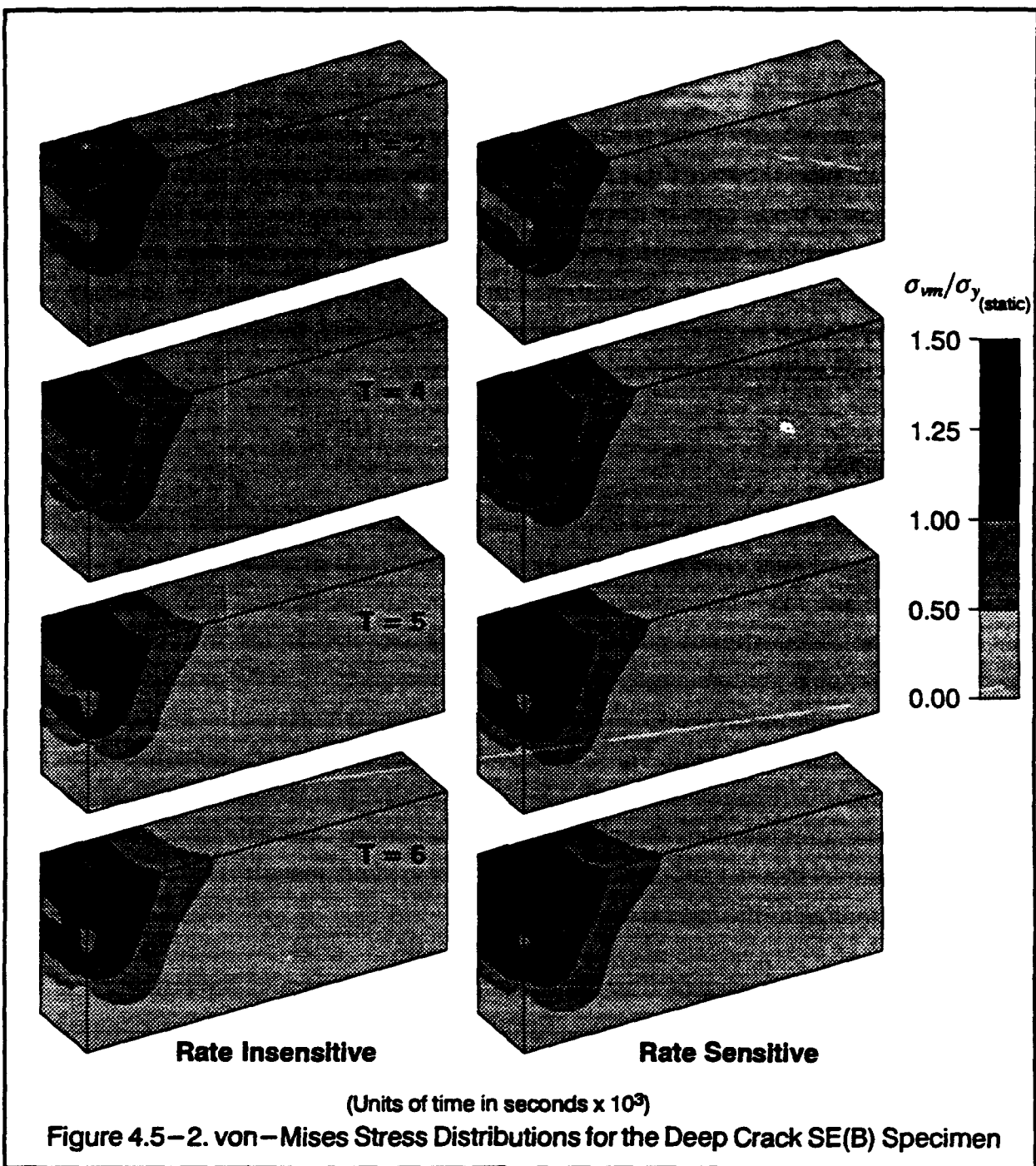
after this time. The plastic zone for the deep crack specimen, however, is confined to the re-maining ligament. Recall that the quarter−span strain gages used in tests to infer applied loads are located at 2.0 inches from the crack plane. The edge of the plastic zone on the top surface of the medium crack specimen extends to approximately 1.8 inches (45.7 mm) beyond the crack plane for the rate−sensitive material model, and extends 1.5 inches (38.1 mm) beyond the crack plane for the rate−insensitive material model. This distance for the shallow cracks

Rate Insensitive   Rate Sensitive

(Units of time in seconds x 10³)

Figure 4.5−3. von Mises Stress Distributions for the Medium Crack SE(B) Specimen
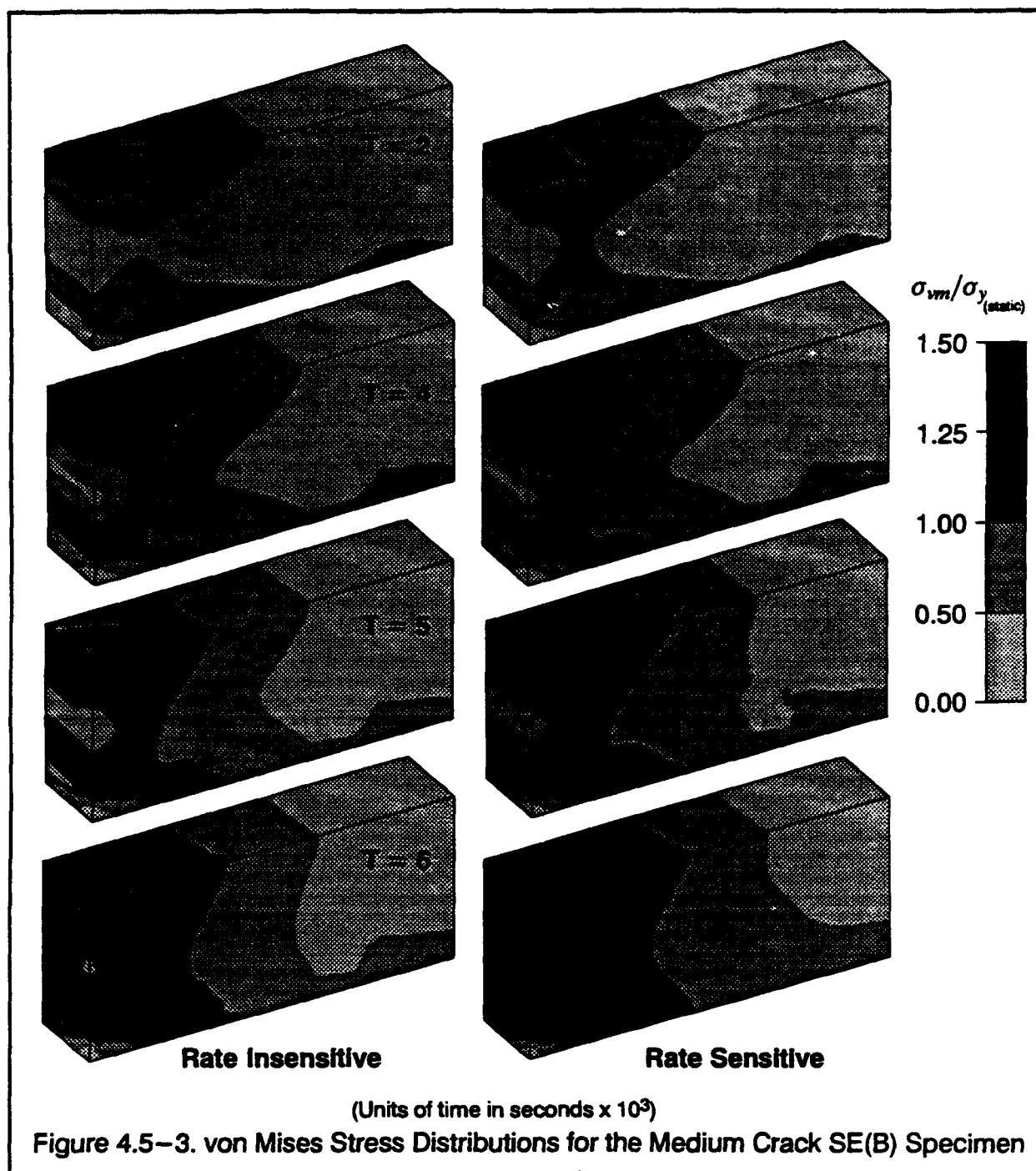
is 2.1 inches (53.3 mm), and 1.8 inches (45.7 mm) for the rate sensitive and insensitive material models, respectively. Quarter−span gage locations for the shallow crack specimens thus undergo plastic deformation. Section 4.6.5 examines strain distributions at the quarter−span location of the shallow crack specimen.

Rate Insensitive   **Rate Sensitive**

(Units of time in seconds x 10³)

Figure 4.5−4. von Mises Stress Distributions for the Shallow Crack SE(B) Specimen
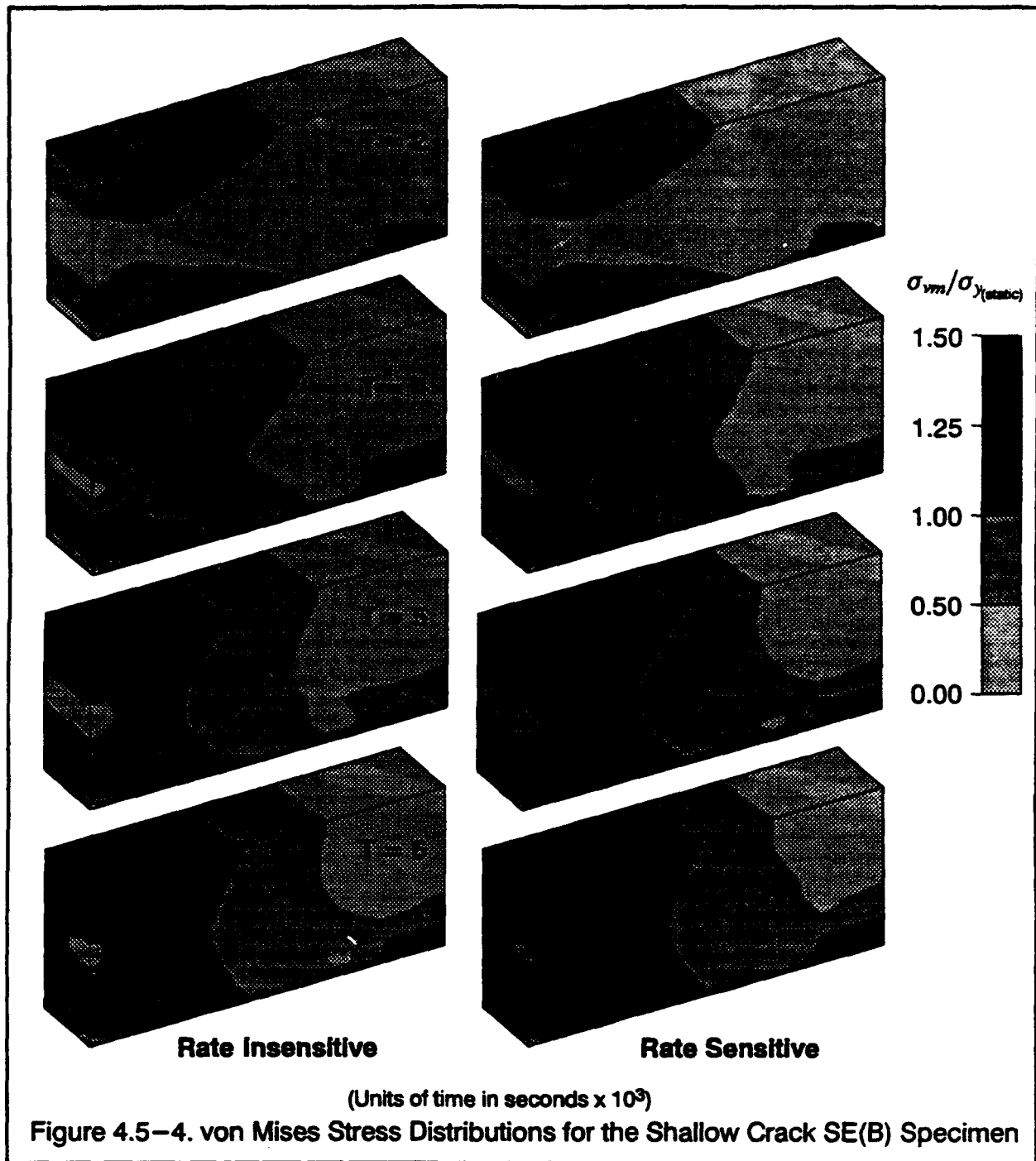
4.6 Procedures to Infer the Applied Loads

Direct measurement of the applied loading is often impractical in a dynamic test such as the drop tower. Indirect methods to infer the applied loads from more easily measured quantities are investigated in this section. For the deep crack specimens, strains measured at the

quarter—span locations are correlated in a static test to provide a direct load—strain relationship. Although this technique neglects the effects of inertia on the measured response, it has proven very successful in practice and provides accurate predicted loads as confirmed by dynamic finite element analyses. Shallow crack specimens introduce uncertainties to this procedure as outlined in Section 2.4.1.

This section compares alternate methods to obtain the applied load from more easily measured quantities (e.g., quarter—span strains) in an impact test. The finite element analyses provide information to evaluate each method: computed strains and reactions are treated as experimental data for input to each method from which inferred loads are compared to the corresponding known loads in the finite element model. The inferred loads and measured displacements at the load—line and crack mouth provide the necessary information to compute the J—integral for an actual impact test.

The following methods to infer applied loads are evaluated:

1. Applied loads are evaluated from the support reactions. Experimentalists have proposed to use instrumented supports to measure reactions.

2. Applied loads are evaluated from the quarter—span strains measured on the top and bottom surfaces of the specimen that are calibrated against a static linear—elastic analysis. Because the specimen is statically determinate, the moment at the quarter—span location is one—half the centerplane moment and is equal to the applied load × $L/8$ (neglecting inertial effects). For deep notch specimens, plastic deformation remains remote from the quarter—span locations leading to a simple, linear—elastic stress—strain response at the strain gage locations and a linear variation of bending strain over the specimen width. This approach fails if nearby plastic deformation affects the through width linear strain variation.

3. Applied loads are evaluated from the moment computed at the crack plane using nodal reactions. This moment, which includes inertial effects, is compared to the crack plane moment for a simply supported beam with a statically applied mid—span load. This method predicts a quasi—static, equivalent load needed to achieve the same moment across the ligament that occurs under dynamic loading.

As shown in Section 2.2, integration of the ligament moment through the specimen end rotation provides the basis for calculation of an applied J—value in a statically loaded specimen. For dynamic conditions, however, inertial effects in the specimen may nullify the simple relationship between the load—load line displacement and the ligament moment—specimen end rotation. The third method to infer applied loads defines an equivalent quasi—static load that parallels the static procedure for calculation of applied J. This equivalent load is more indicative of the conditions at the crack plane and therefore represents a better measure of loading for computation of J in the specimen.

4.6.1 Use of Support Reactions

At each time step, reaction forces at the constrained end nodes are extracted from the finite element results. The total of these nodal reactions across the half–thickness of the model are multiplied by four to estimate the instantaneous load applied to the specimen. (Due to symmetry, only a quarter of the specimen is modelled). Use of support reactions to estimate the applied load in this manner neglects completely the inertial response of the specimen. The accuracy of this technique for application in testing is investigated by comparing the reactions with the actual applied loads.

4.6.2 Use of Strains at the Quarter–Span Location

During a test, strain gages attached to the top and bottom surfaces of the specimen at quarter span measure the longitudinal bending strains at these locations. In the finite element models, the actual locations to define the quarter span strains vary slightly due to meshing differences. Two nodes that lie on the longitudinal center plane of the specimen are used to compute *gage* strains from the finite element models. These nodes are chosen so that they lie near the quarter–span location and are separated by a suitable distance (a *gage length*). The longitudinal displacements of these nodes together with their undeformed separation (*gage length*) provide the engineering strain at the gage for both the linear elastic calibration and the dynamic analyses. Figure 4.6–1 provides the specific locations to define strains at the quarter–span locations for each finite element model.

On test specimens, a Wheatstone bridge connects the top and bottom strain gages to produce a single reading from the two strain gages. This resulting strain is effectively the difference of strains on the top and bottom surface of the SE(B) specimen. Elastic deformations for a prismatic beam in pure bending produce equal magnitudes of bending strain on both surfaces with opposite signs, negative on the compression side and positive on the tensile side. The difference of the two strains is thus twice the magnitude of the individually measured bending strains. By using the difference of the two surface strains, any uniform axial deformations are eliminated. Thus, half of the difference of the two surface strains defines the *effective bending strain*, ε_b. This experimental technique is followed to compute ε_b from finite element values of the quarter–span surface strains. Figure 4.6–1 summarizes the linear–elastic, load–ε_b relationships computed for the three specimens.

The static relationship utilized to correlate the quarter–span strains to the applied load suffers from the same deficiencies as the procedure to infer applied load from the support reactions. The quarter span strains measure the deformation in the specimen only at that one loca-

Figure 4.6–1. Quarter–Span Strain Gage Locations

	Shallow Crack a/W=0.0725	Medium Crack a/W=0.15	Deep Crack a/W=0.5
d_1	1.923 in. (48.84 mm)	1.821 in. (46.25 mm)	1.955 in. (49.66 mm)
d_2	2.266 in. (57.56 mm)	2.323 in. (59.00 mm)	2.322 in. (58.98 mm)
L_g	0.343 in. (8.71 mm)	0.501 in. (12.73 mm)	0.367 in. (9.32 mm)
ε_b/P	2.38×10^{-5}/kip $(5.34 \times 10^{-6}$/kN)	2.39×10^{-5}/kip $(5.38 \times 10^{-6}$/kN)	2.32×10^{-5}/kip $(5.21 \times 10^{-6}$/kN)
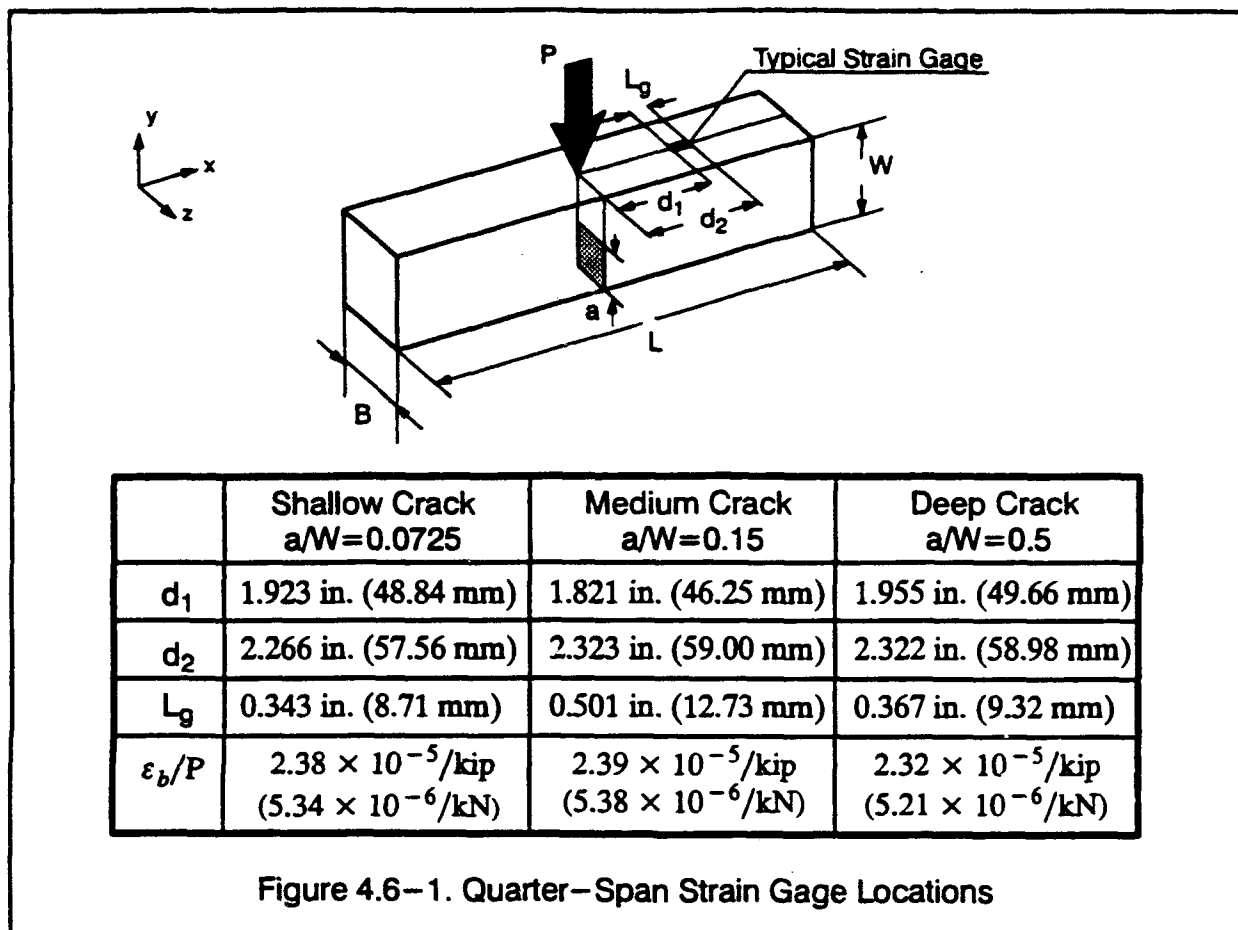
tion. The simple linear moment distribution over the span for static loading may be altered by inertial loading. Thus loads inferred from strain gage readings include inertial effects experienced by the specimen, but the *static* quarter–span strain vs. mid–span load relationship may be incorrect.

The linear–elastic relationship used to estimate applied loads from the quarter–span strains also neglects the influence of plasticity near the strain gage locations. Once plasticity reaches the quarter–span locations, the linear relationship between strains and load may no longer apply. The use of additional gages applied over the specimen width to capture the strain distribution in shallow crack specimens is discussed later.

4.6.3 Use of Ligament Moments

The calculation of moment on the remaining ligament proceeds with the extraction of global X–direction nodal forces on the crack plane from the finite element analyses at each time step. The algebraic sum of these nodal forces provides the total longitudinal force present in the specimen. (The total longitudinal force may not be zero due to inertial effects in the speci-

men). This longitudinal force does not contribute to the ligament moment; it's effect is removed prior to calculation of the ligament moments. An equivalent uniform pressure, equal to the negative of the net longitudinal force, is added to the nodal forces to isolate that portion of nodal forces contributing to the ligament moment (the corrected nodal forces). The ligament moment is then calculated about any global Z-direction axis in the crack plane using the corrected nodal forces. The instantaneous neutral axis is also estimated from the distribution of the corrected nodal forces.

The quasi-static load necessary to produce the same moment is computed using a simply supported beam model with a uniform load extending over the length of the loading area employed in the 3-D finite element models. While this quasi-static applied load reflects the inertial response of the specimen, the linear moment-load relationship implied by the simple beam model neglects inertial effects on the moment distribution over the span. Although not necessarily an accurate estimate of the applied load, the load inferred from the ligament moment does represent conditions at the crack plane, and would appear to provide a good candidate for use in the computation of J-values from load-displacement curves. Unfortunately, direct measurement of the ligament moment in an SE(B) specimen is not possible.

Both the support reactions and the quarter span strains quantify the specimen response in a manner that includes the overall inertial effect. However, inertial response of the volume of material between the measurement locations may contribute to discrepancies in the predicted applied loads for the three techniques. The inertia of material between the crack plane and the quarter span location contributes to differences between estimates of the applied load from ligament moments and quarter-span strains. Similarly, the inertial response of the entire specimen from the supports to the crack plane contributes to differences in estimates of the applied load from ligament moments and support reactions.

4.6.4 Comparison of Methods to Infer Applied Loads

Figures 4.6-2 and 4.6-3 compare the inferred loads with the actual applied loads for the three different methods. For the deep and medium crack specimens, all three methods predict identical applied loads over the complete response history ($0 \leq t \leq 0.006$ seconds). For the shallow crack specimen, however, the load inferred from quarter-span strains deviates from the other two methods for $t > 0.003$ seconds. This method underpredicts the applied load by approximately 6%. The ability of each method to predict the applied load is independent of the material's strain rate sensitivity; the assumptions needed to infer the applied loading are not dependent on the material model.

Figure 4.6-2. Inferred Loads for Rate-Insensitive Material

Figure 4.6-3. Inferred Loads for Rate-Sensitive Material
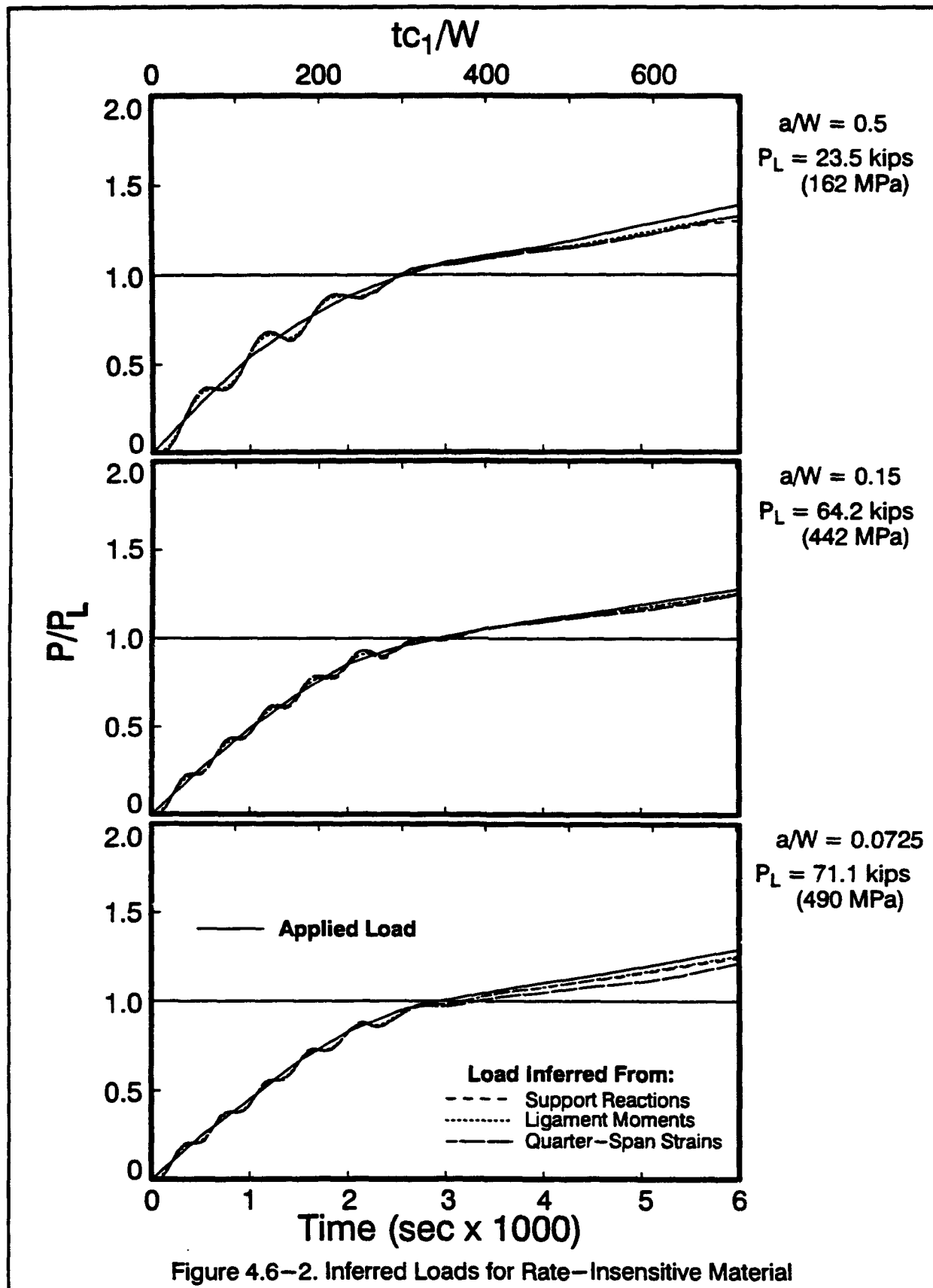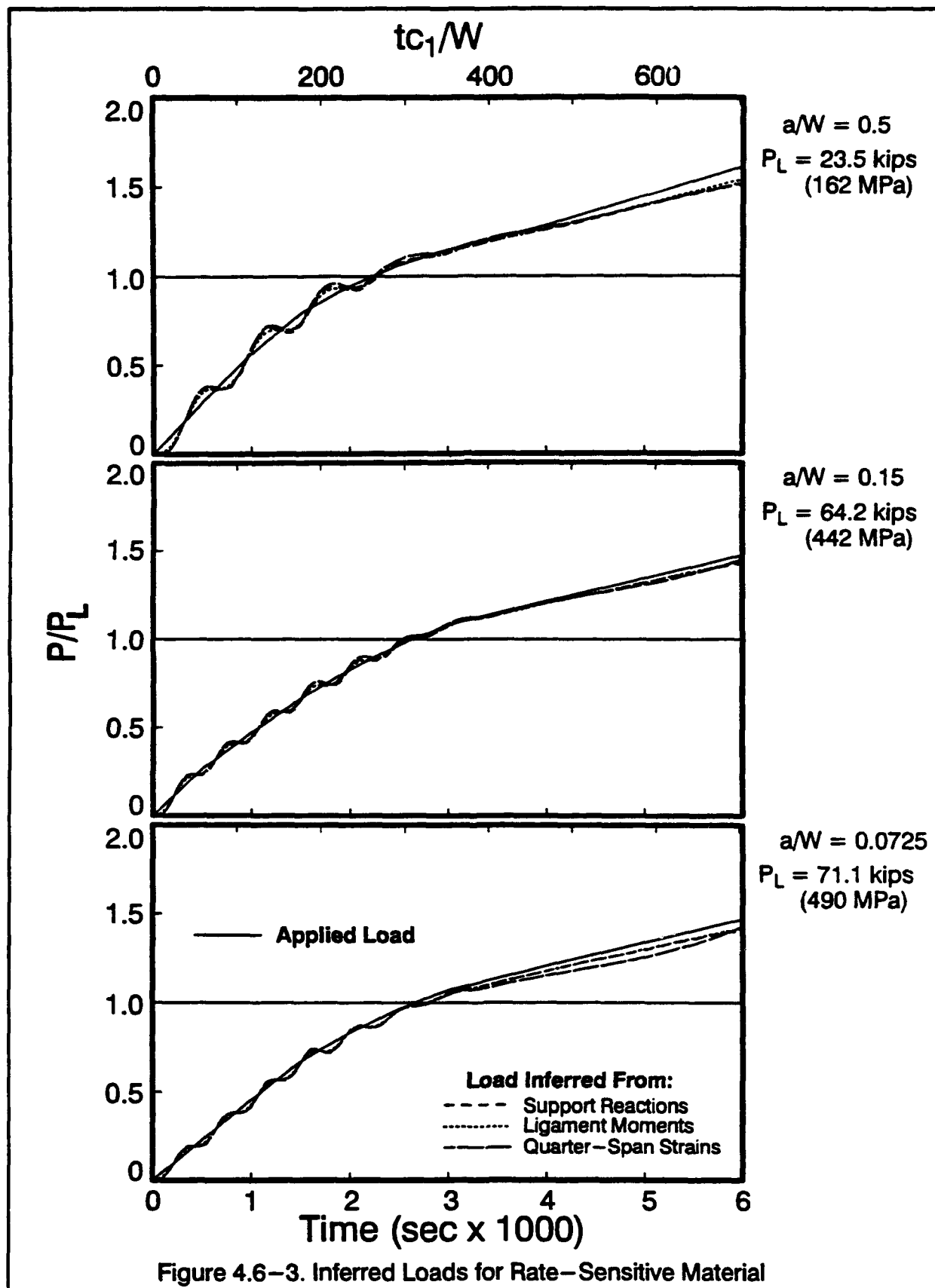
The initial elastic oscillations of the specimens are clearly indicated by the inferred loads shown in Figs. 4.6−2 and 4.6−3. All three methods correctly translate the instantaneous value of some quantity (e.g. reactions) of the specimen into an inferred load assuming a static response. This confirms the very small magnitude of inertial loads relative to applied loads at the loading rates of these analyses.

The good agreement among the three methods supports the adoption of measured quarter−span strains and the measured reactions in experimental work to infer applied loads, especially for deep and medium notch specimens. In shallow crack specimens, plastic zones extend to the quarter−span strain locations, producing small errors in the inferred loads.

4.6.5 Strain Distributions at the Quarter−Span Location

Section 1.4.2 describes the additional strain gage measurements utilized by Kirk et al. [59] to address the distortion of through−width strain distributions for the shallow flaw specimens. Six strain gages, equally spaced over the width of the specimen at the quarter span location, capture the strain distributions through the specimen width (see Fig. 1.4−1). The strain measured at each gage is converted to a stress using the quasi−static, uniaxial stress−strain curve of the material. Integration of these stresses, yields a moment at the quarter span. Strains measured at mid−thickness on the top and bottom surface are assumed to remain constant over the specimen thickness. This computed moment is employed to infer the applied load as described in the previous section.

Three−dimensional finite element analyses provide data to check the potential improvements in the inferred loads by using the additional strain gages. Figure 4.6−4 shows the longitudinal strain distributions versus width position in the different specimens for the rate−sensitive material model. The rate−insensitive distributions show similar overall trends, but with slightly smaller magnitudes, and are not given here. The longitudinal strains are normalized by the quasi−static yield strain of $\varepsilon_y = 2.185 \times 10^{-3}$. The position is expressed as a fraction of the specimen width, W. The strain distributions on the centerplane and on the specimen surface are shown in the figure at increasing times after impact. Each curve represents the strain distribution at increments of 0.001 seconds. Longitudinal strains in the deep crack specimen remain in the linear−elastic range over the full 0.006 second response. The maximum strain value is less than $\varepsilon_y/2$. The outer fibers for both the medium and shallow crack specimens experience strains approaching ε_y during the last stages of the response.

The through−width distribution of longitudinal strain at the specimen centerplane remains essentially linear for all three specimens over the entire loading history. Surface strains,
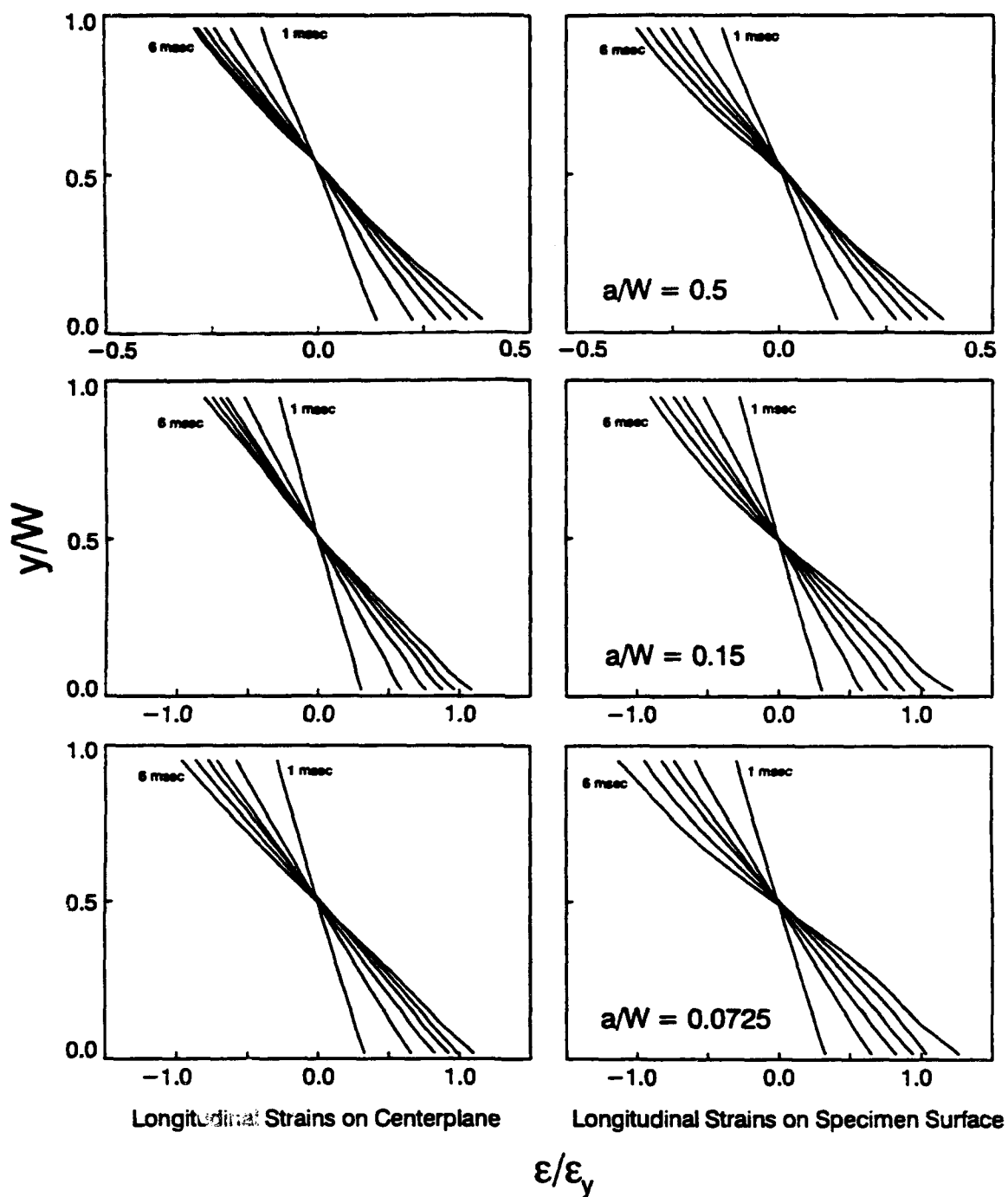
Figure 4.6−4. Longitudinal Strains at the Specimen Quarter−Span Location

however, show distinctive deviations from linearity late in the response. These surface strains deviate from the linear distribution in a manner that resembles an 's'−curve. Longitudinal strains on the surface are consistently larger than those at the centerplane, approaching a 20% difference on the outer fibers.

The quasi-static stress-strain curve shown in Fig. 4.2-1 is used to convert the strain distributions to stress distributions. Figure 4.6-5 shows the resulting loads inferred from these stress distributions for the shallow flaw specimen together with the loads inferred from the crackplane moment and the quarter-span strain gages.

Figure 4.6-5. Applied Load Inferred Using Strain Distributions
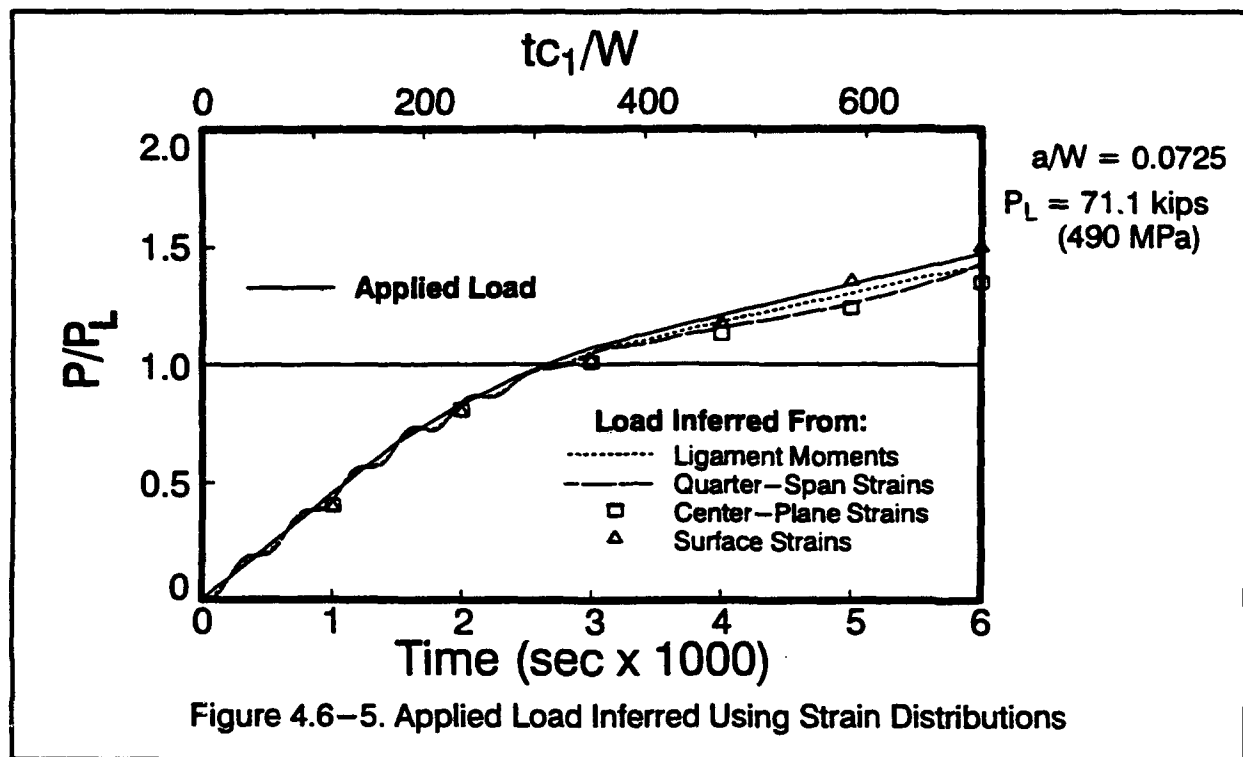
During the early linear response, both strain distributions yield loads that are identical to the applied loads. After extensive plasticity, loads inferred from the centerplane and surface strain distributions reveal some differences. Strains on the specimen surface predict a larger load that eventually exceeds the actual applied loading. The loads inferred from the strain distributions bound the load inferred from the ligament moment. This explains why the six strain gage system utilized by Kirk [59], which is a hybrid between the two methods shown in Fig. 4.6-5, gave relatively accurate loads. For static tests, Kirk reports errors below 4% for a low hardening steel (similar hardening characteristics to the material used in this study), and errors below 10% for a high hardening steel.

Finite element predictions of strain distributions at the quarter span location indicate that the through-width distribution changes significantly with increased load for the shallow notch specimen. While the specimen behavior remains predominantly elastic, the simple correlation between the quarter span strains (centerplane or through-width gages) and the inferred load is very accurate. Once the quarter span location experiences plasticity, the outer surfaces ex-

111

hibit larger strains than at the centerplane, and as a result, a larger moment is inferred at the quarter span location with the surface strains. Figure 4.6−5 demonstrates that measured surface strains, converted to stresses and integrated to yield a moment produce the most accurate prediction of applied load.

4.7 J−Integral Calculations

The quasi−static relationship in Eqn. 2.2−6 used with the load−displacement curve obtained from an SE(B) specimen provides an average, through−thickness J−value. This section examines the accuracy of this procedure to compute J for impact tests.

4.7.1 Finite Element J−Integral Calculations

Figure 4.7−1 shows the domains and q−functions utilized in the finite element computation of the average, through−thickness J−values. The finite element mesh near the crack tip for the three specimens is shown in the figure. Four element domains are used for J evaluation. Each domain comprises a larger annular arrangement of elements beginning with the first ring of elements surrounding the crack tip. The shaded elements in the figure indicate the domains utilized for the finite element evaluation of the J−integral. The q−function is constant through the thickness with the trapezoidal, in−plane distribution indicated. A constant q−value is specified at each point on the crack front. Eqn. 2.1−8 establishes the average J as the domain integral value divided by the area under the q−function along the crack front.

Figure 4.7−1. q−functions and Domains for J_{fem}
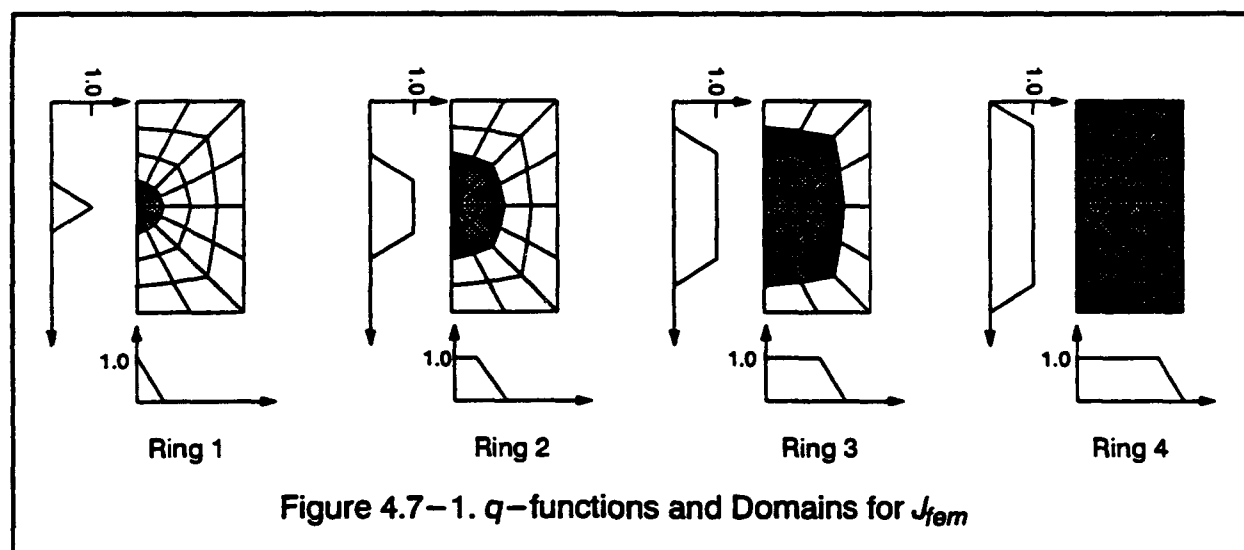
Finite element computation of the J−integral follows the methodology outlined in Section 3.2. Neglecting terms from the explicit derivative of the strain energy density, the finite element J−integral is:

$$J_{fem} = J_1 + J_3 \qquad (4.7-1)$$

where J_1 and J_2 are defined in Eqns. 2.1−6 and 2.1−7, respectively. Computed values of J vary less than 4% between the domains denoted *Ring 2, Ring 3* and *Ring 4* in Fig. 4.7−1 for all the specimens. Severe stress−strain gradients in the crack−tip elements, coupled with the numerical difficulties expected in integrating over the degenerate elements, make the accuracy of J−values computed with *Ring 1* less reliable [98]. Nevertheless, the maximum deviation of J−values between the crack tip domain, *Ring 1*, and the remaining domains is approximately 8%. The average of J−values for domains *Ring 2,3 and 4* is selected to define the finite element value.

Figure 4.7−2 shows the computed J−values in the three specimens for the rate sensitive and insensitive material models. The average J−values are normalized by the product of the flow stress, σ_{fl}, and the remaining ligament, $b = W - a$. The flow stress is the average of the yield and ultimate stresses. Using the stresses tabulated for A533B steel in [75] (See Table 2.3−1), $\sigma_{fl} = 75.6$ ksi (521 MPa). This normalization removes both the absolute size and the material flow stress effect in the J−values [6]. All three specimens show higher J values for the rate sensitive material model. Eqn. 2.2−2 implies a linear relationship between the area under load−displacement curve and J. Rate sensitivity increases the applied loading at a load−line displacement, thereby increasing the area under the load−displacement curve and the applied J.

Rate sensitivity elevates the J−values for deep and medium crack specimens by approximately 17%, while the shallow crack specimen exhibits a smaller elevation of 5%. The kinematic response of the deep and medium crack specimens is a deformation pattern dominated by rotation of the specimen ends, acting as rigid arms, which concentrates deformation near the crack−tip. For these specimens, the elevation in crack−tip stresses due to strain rate sensitivity translates directly to an increase in J. Strain rate sensitivity in the shallow crack specimen stiffens the ligament sufficiently to force deformation away from the crack tip. This shields the crack tip from the elevation of J due to strain rate sensitivity.

Figure 4.7−3 shows the J−values for the rate−sensitive models of the three specimens together. Both the medium and the deep crack specimens show nearly identical magnitudes for J, while the shallow crack specimen experiences significantly lower values. The medium and shallow crack specimens both require much higher loading (approximately a factor of 2.7) than the loading of the deep crack specimen to reach the same global deformation levels. However, while the load levels of the medium crack are much higher than the deep crack specimen, J−

Figure 4.7–2. J_{fem} from Domain Integrals for the SE(B) Specimens
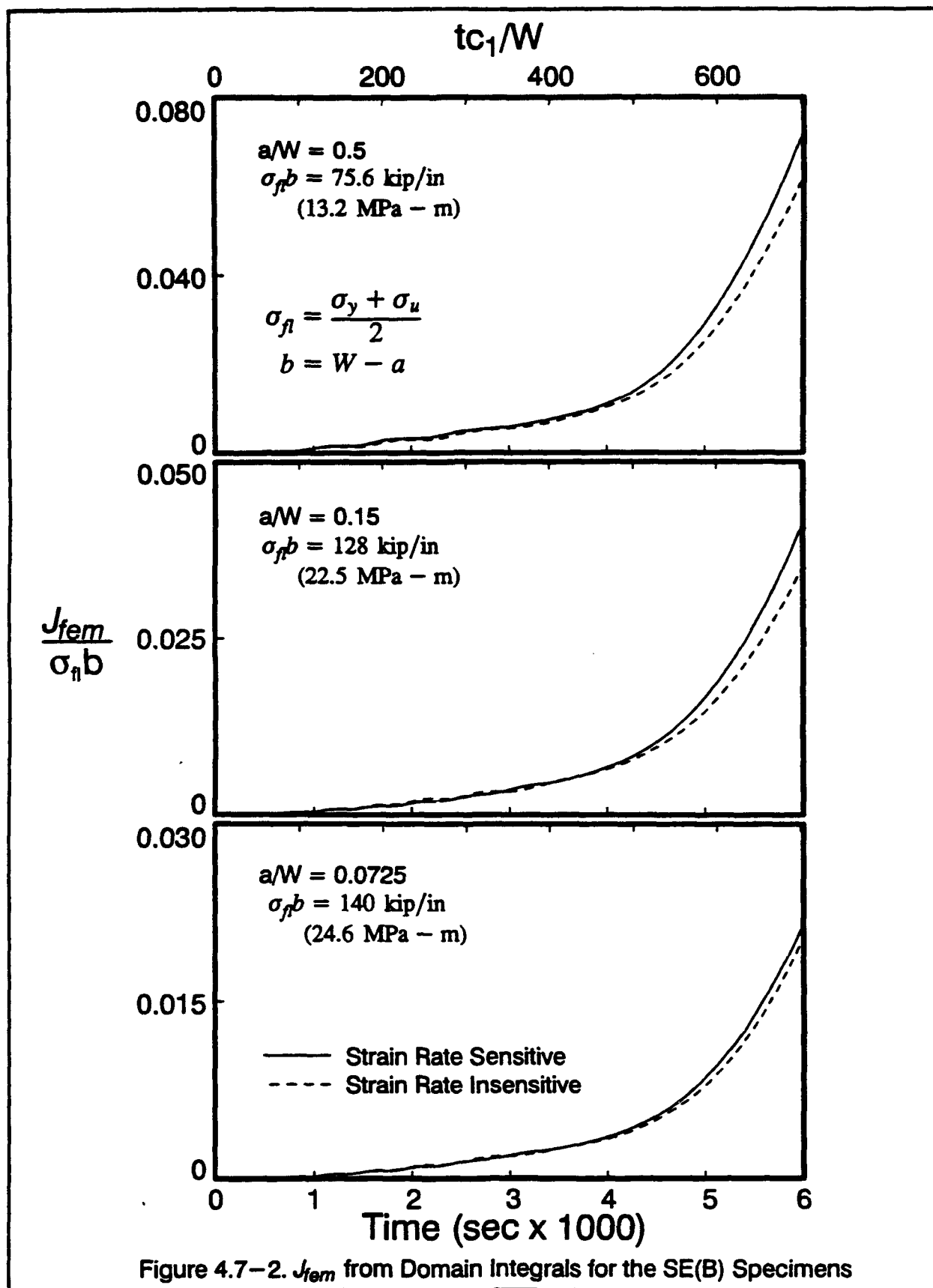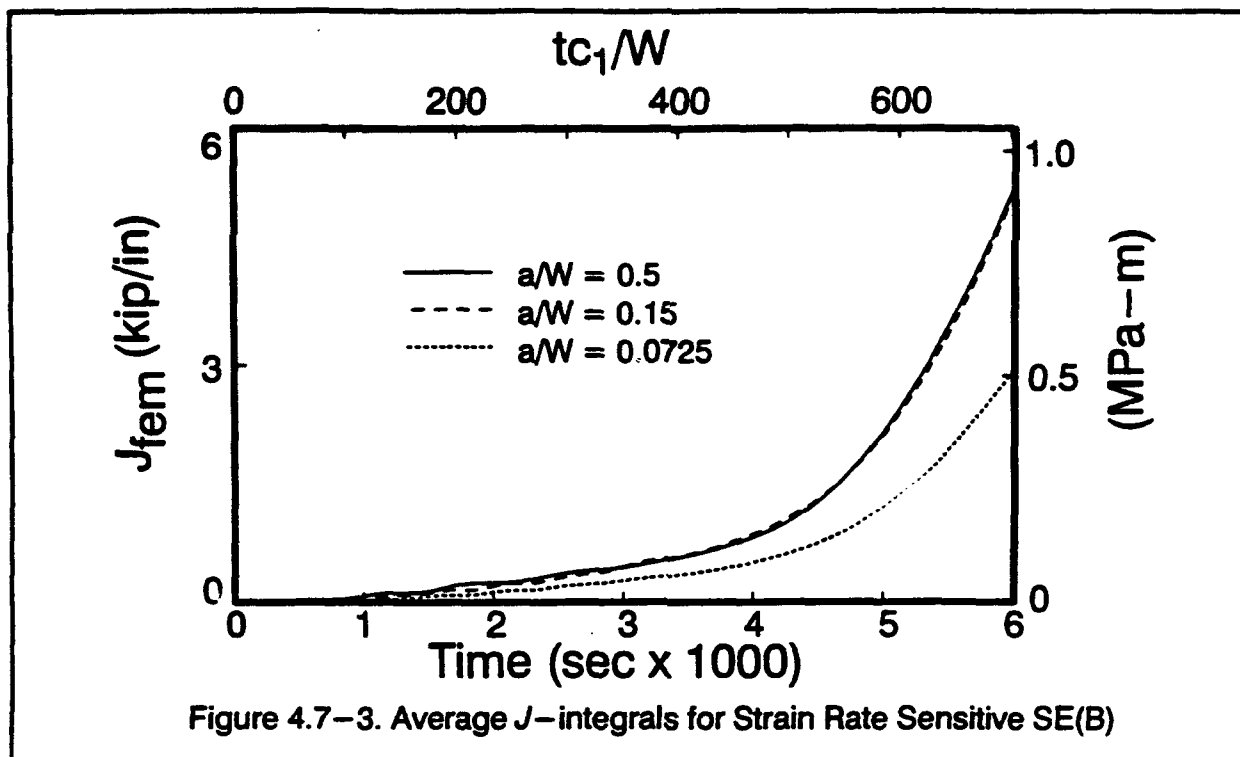
Figure 4.7−3. Average J−integrals for Strain Rate Sensitive SE(B)

values for the medium crack specimen equal the J−values for the deep crack specimen. Although the load levels for the medium and shallow crack specimen are equal, a much smaller J−value is observed for the shallow crack specimen. Thus, as a/W decreases (i.e. from deep to shallow cracks), the applied loading increases and at the same time, the applied J decreases. This phenomena illustrates the crack tip shielding commonly observed [33] for specimens with medium to shallow cracks.

Joyce [54] reports J_{Ic} values (J at the onset of stable ductile crack growth) for A533B steel in the range of 1.0 to 2.0 kip/in (0.175 to 0.35 MPa−m) for quasi−static loading of deep notch specimens. In drop tower testing, J_{Ic} values up to 3.0 kip/in (0.525 MPa−m) are reported. In addition, Joyce reports J_c values (J at cleavage fracture after significant plasticity and possibly some stable tearing) of up to 6.0 kip/in (1.05 MPa−m) for both quasi−static and drop tower testing. The computed J values for the analyses in this study are in this range (see Fig.4.7−3).

Nonlinear static analyses of the three specimens provide verification of the fracture parameter computations and a basis to quantify dynamic effects. The POLO−FINITE system [35] is used for the static analyses with the same finite element meshes and loading area utilized for the dynamic analyses. A 2 x 2 x 2 Gaussian quadrature with the B−bar method is utilized for computations. A von Mises model with isotropic hardening is adopted which matches the Bodner−Partom material model at slow strain rates. Small strain and small displacement as-

115

sumptions are utilized in the analyses. Approximately 25 variably sized load steps are defined to load each specimen to the load line displacement of 0.2 inches (5.08 mm). Two to three full Newton iterations are needed to achieve convergence at each load step.

The quasi−static stress−strain curve in Fig. 4.2−1, used to develop the rate−insensitive model for dynamic analyses, is used as the stress−strain curve for the von Mises material model in the static analyses. Static analyses with the static stress−strain curve provide the counterpart for the rate−insensitive dynamic analyses. In addition, static analyses are performed using a stress−strain curve indicative of the strain rates experienced by the specimen. Figure 4.7−4 shows the equivalent uniaxial stress−strain history experienced by a typical crack−tip
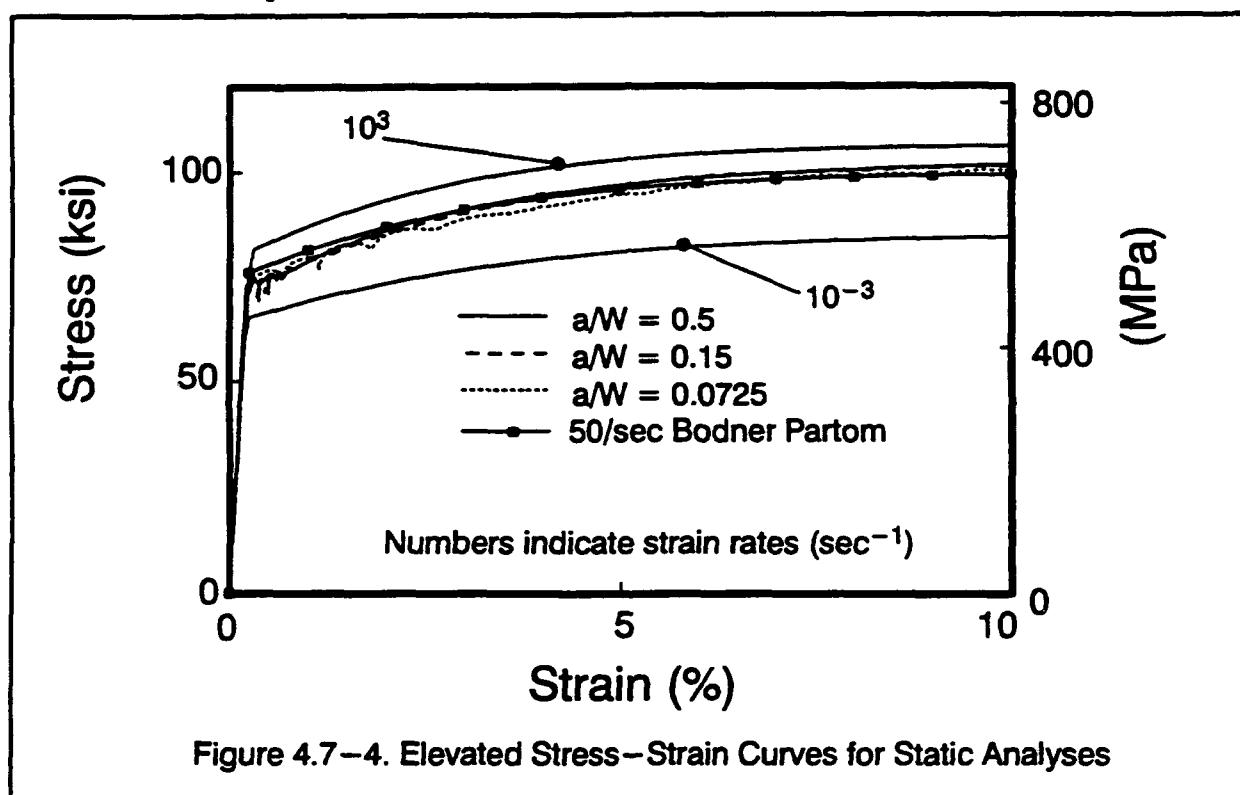
Figure 4.7−4. Elevated Stress−Strain Curves for Static Analyses

element in each of the three specimens. For each specimen, the crack−tip element utilized for the stress−strain history in the figure corresponds to the element located at the centerplane, directly ahead of the crack tip. All three specimens show similar magnitudes of equivalent stress levels. Also shown in the figure is the equivalent uniaxial stress−strain curve for A533B steel at 50°C, at a strain rate of 50 sec^{-1}. This stress−strain curve closely matches the crack−tip stress−strain response shown and is used in the second set of static analyses.

Figure 4.7−5 compares the finite element J−values for the dynamic analysis with the corresponding static analyses. The static J−values are computed from the same domains and q−functions as shown in Fig. 4.7−1. Again, the average J from the domains denoted Ring 2

116
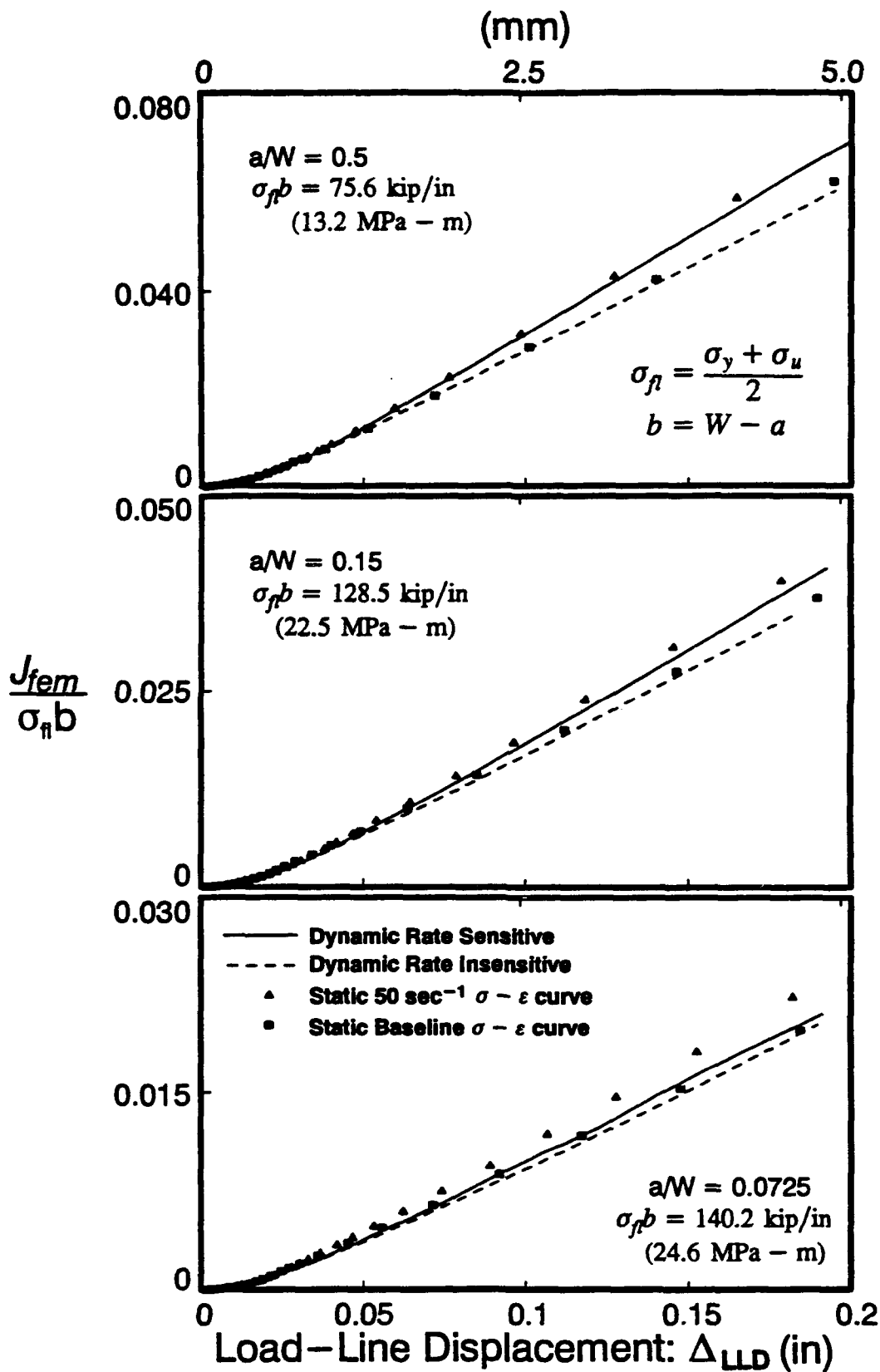
Figure 4.7-5. J_{fem} vs. Load-Line Displacement

117

through *Ring 4* defines the computed J_{fem} for both the static and dynamic analysis. Domain dependencies of the J–values for the static analyses are smaller than for the dynamic analyses, with all domains showing less than 2% deviation from J_{fem}. This is attributed to the different Gaussian integration scheme of the static analyses ($2 \times 2 \times 2$ with B–bar vs. 1 point with hour–glass control). For a given load–line displacement, the J–values for the static analyses performed with the quasi–static stress–strain curve are nearly identical to those for the rate–insensitive dynamic analyses in all three specimens. Global inertia effects on thickness average J–values are thus found to be negligible.

J values for the second set of static analyses, labelled by the corresponding strain rate of the equivalent Bodner–Partom material model, are also shown in the figure. For the deep crack specimen, these static results closely match the rate–sensitive dynamic analyses. For the medium crack specimen, the static J_{fem} with the simulated rate sensitivity exceeds the computed J_{fem} of the dynamic analyses by approximately 4%. For the shallow crack specimen, the static J_{fem} with the simulated rate sensitivity exceeds the computed J_{fem} of the dynamic analyses by nearly 10%.

## 4.7.2 Load Displacement Curves

The use of Eqn. 2.2–6 to estimate J–values requires integration of the load–displacement response. Figures 4.7–6 and 4.7–7 show the load–displacement curves for the SE(B) analyses in this study. The load–line displacement is taken as the average vertical displacement of six nodal points on the ligament plane as explained in Section 4.4. The figures show the actual applied loading together with the three different inferred loadings presented in Section 4.6. Results from static analyses are also included in the figures. Figure 4.7–6 shows the rate–insensitive dynamic analysis together with static analyses using the baseline stress–strain curve. Figure 4.7–7 shows the rate–sensitive dynamic analysis together with static analyses using the elevated stress–strain curve that corresponds to a strain rate of 50/sec.

Beyond a load–line displacement of 0.05 inches, (1.27 mm), the applied load is approximately 2 to 5% larger than the various inferred loads. The quasi–static analysis nearly matches the inferred loads from the ligament moment, verifying that the specimen experiences negligible global dynamic effects, other than the increase in kinetic energy near the end of the 0.006 second response.

The static analysis with the elevated stress–strain curve predicts larger loads than those for the rate–sensitive dynamic analyses (after the initial linear–elastic response) for all three
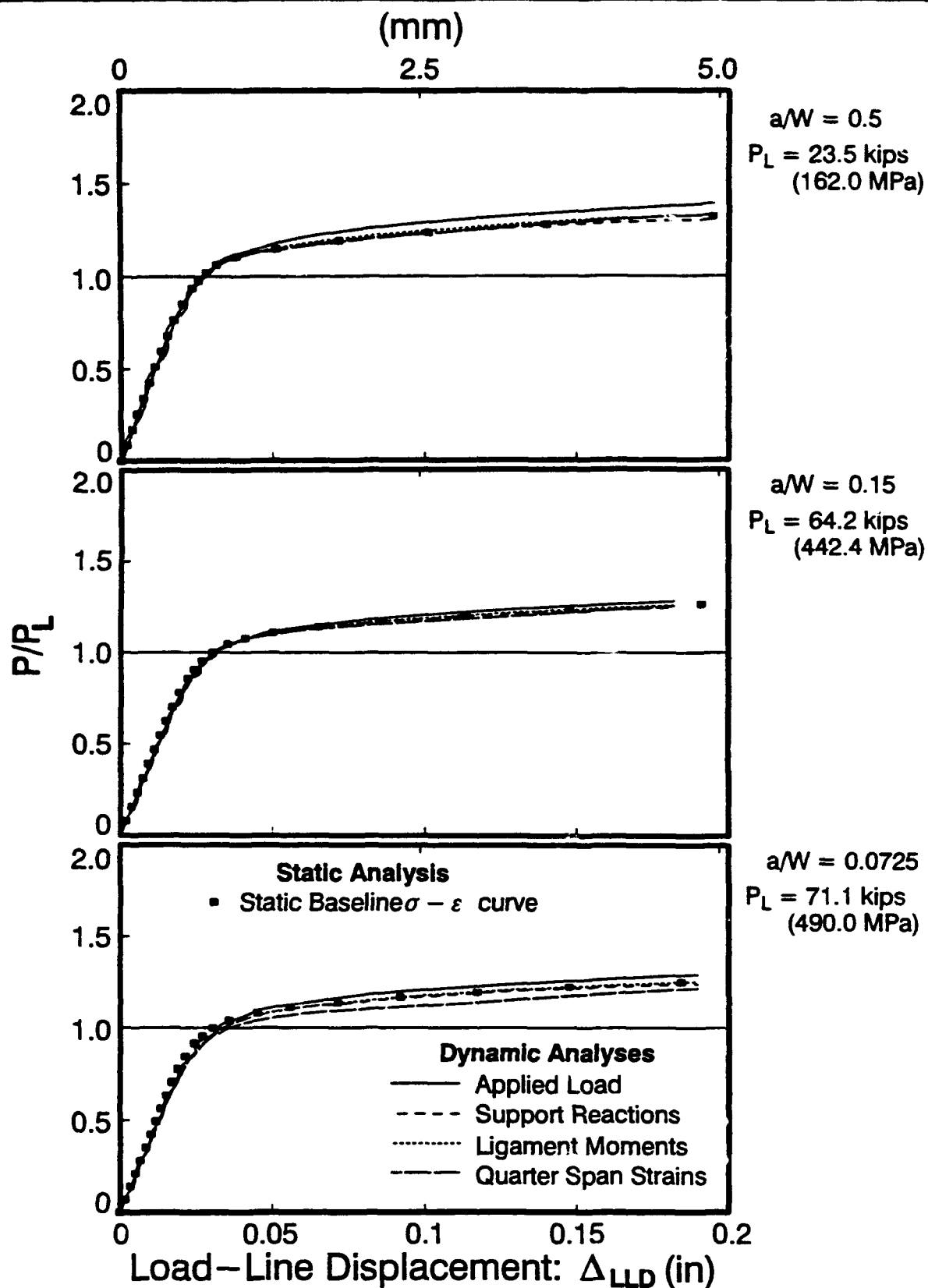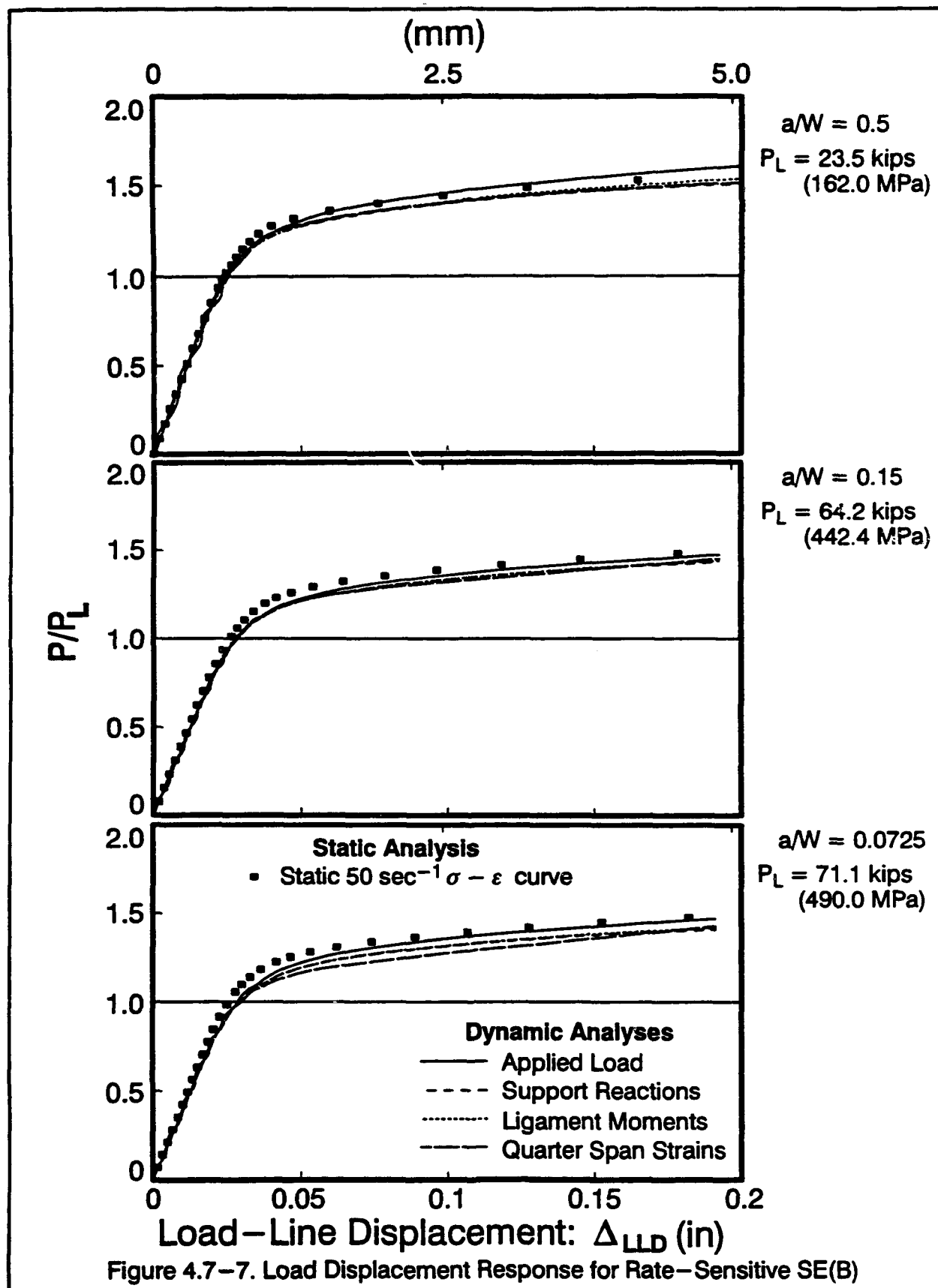
118

Figure 4.7-6. Load Displacement Response for Rate-Insensitive SE(B)

Figure 4.7−7. Load Displacement Response for Rate−Sensitive SE(B)

specimens. Use of a stress–strain curve with a higher yield stress elevates the stiffness of the specimen and thus higher loads are required to achieve the same deformation. For the deep crack specimen, most of the deformation is concentrated in the remaining ligament, and the elevated stress–strain curve of the crack tip is a good indicator of the straining behavior of the material that controls the global behavior of the specimen. Thus the load obtained from the static analysis with the elevated stress–strain curve matches the rate–sensitive response of the deep crack specimen very well. For the medium and shallow crack specimen, plastic deformation spreads beyond the ligament. In material remote from the crack tip, the strain–rates are well below rates at the crack tip. For these two specimens, the elevated stress–strain curve does not represent a large portion of the material undergoing deformation. Thus the static load obtained with the elevated stress–strain curve predicts loads larger than those for the rate–sensitive medium and shallow crack specimens. Nevertheless, all three static analyses with the elevated stress–strain curves agree well with the rate–sensitive analyses.

4.7.3 Calculation of J_e

Eqn. 2.2–6 outlines the computation of J from experimental measurements. J is divided into elastic and plastic parts. The elastic component is calculated from the elastic stress intensity factor K_I:

$$J_e = \frac{K_I^2(1 - \nu^2)}{E} \text{ for } P_\varepsilon, \qquad J_e = \frac{K_I^2}{E} \text{ for } P_\sigma \qquad (4.7-2)$$

where K_I is typically computed from 2–dimensional models. P_ε and P_σ denote plane strain and plane stress, respectively. Reference [97] provides a comprehensive collection of 2–dimensional solutions for various structural configurations. The elastic component is dependent only on the loading of the specimen. Using a 1 kip (4.448 kN) reference load, and correcting the applied loading for the finite loading area, (described in detail below), reference [97] yields the values tabulated in Table 4.7–1 for J_e. For the full 3–dimensional model, a linear elastic analysis yields an average through–thickness J for a 1 kip loading. (Details of the linear–elastic analysis and the J computations are found in Sections 4.4 and 4.7.1.) The resulting J_e values from the finite element analyses are also shown in Table 4.7–1.

The J_e–values computed from the full–field finite element solutions lie between those from the plane–stress and plane–strain idealizations, and are approximately equal to the average of these two values for all three specimens. To insure compatibility between the static equation (Eqn. 2.2–6) and the computed J_{fem} from the finite element computations in the

121

	Shallow Crack a/W=0.0725	Medium Crack a/W=0.15	Deep Crack a/W=0.5
P_σ	3.175×10^{-5} kip/in (5.560×10^{-6} MPa – m)	6.374×10^{-5} kip/in (1.116×10^{-5} MPa – m)	4.441×10^{-4} kip/in (7.777×10^{-5} MPa – m)
P_ε	2.889×10^{-5} kip/in (5.059×10^{-6} MPa – m)	5.801×10^{-5} kip/in (1.016×10^{-5} MPa – m)	4.042×10^{-4} kip/in (7.079×10^{-5} MPa – m)
FEM	3.034×10^{-5} kip/in (5.313×10^{-6} MPa – m)	6.086×10^{-5} kip/in (1.066×10^{-5} MPa – m)	4.236×10^{-4} kip/in (7.418×10^{-5} MPa – m)

Table 4.7–1 J_e for Plane Stress, Plane Strain idealizations, and the 3–Dimensional Finite Element Model (1 kip load).

elastic range, a relationship is developed for J_e values from the finite element J–values in shown in Table 4.7–1. This eliminates errors due to the 2–dimensional approximations in Eqn. 4.7–2. Denoting the J_e value from the linear–elastic analysis with a unit load as $J_e^{1\,kip}$, and recognizing that J_e is proportional to the square of the applied load:

$$J_e(P) = P^2 J_e^{1\,kip} \qquad (4.7\text{–}3)$$

where P is the loading in kips. This equation is exact for the specimen geometries in this study under linear–elastic conditions and small displacements; it is the 3–dimensional counterpart to Eqn. 4.7–2.

4.7.4 Calculation of J_p

The plastic component of J is calculated from the area under the plastic load–line displacement curve. ASTM E813 recommends modification of the load–line displacements to account for local deformation near the supports of specimens [3]. Following Kirk's procedure [62], the vertical displacement of a nodal point directly above the support on the free surface, and midway through the width of the specimen establishes a reference for support deformation. The displacement of this reference point is subtracted from the load–line displacement (see Section 4.4) to remove deformation at the support. Removal of the elastic displacement corresponding to the applied load isolates the plastic component of the load–line displacement. The linear–elastic analyses provide a compliance value for each specimen. The compliance value relates the elastic load–line displacement (as modified to exclude the support deformations) to the applied load. The plastic component, Δ_p, is then:

122

$$\Delta_p = \Delta_{LLD} - \Delta_{support} - \Delta_{elastic} = \Delta - \Delta_{support} - C_\Delta P \qquad (4.7-4)$$

where Δ_{LLD} is the load−line displacement, $\Delta_{support}$ is the vertical displacement of the nodal point directly above the support, and C_Δ is the elastic compliance. From the elastic static analyses, $C_\Delta = 3.172 \times 10^{-4}$, 3.495×10^{-4}, 9.134×10^{-4} in/kip (1.811×10^{-3}, 1.996×10^{-3}, 5.217×10^{-3} mm/kN) for the shallow, medium and deep crack, respectively.

For a given total load, the finite width over which loads are applied produces a smaller ligament moment th: a concentrated load. The finite width of loading used in this study requires adjustment of the load used to compute the plastic component of J with published values of η_p. An equivalent concentrated load that produces the same ligament moment as the load applied over the finite loading width is utilized in the computation of J_p in Eqn. 2.2−6. This correction makes the computation of fracture parameters independent of the smaller ligament moment caused by the finite loading width. The resulting correction is given by:

$$P_{equiv} = P(1 - l_{load}/L) = P\alpha_{load} \qquad (4.7-5)$$

where P is the total load applied load, L is the span length between supports, l_{load} is the length of the loading area along the span, and P_{equiv} is the equivalent concentrated load for use in Eqn. 2.2−6. α_{load} is defined as the load correction factor. The plastic component of J is then computed by:

$$J_p = \frac{\eta_p}{bB} \int_0^{\Delta_f} P_{equiv}\, d\Delta_p \qquad (4.7-6)$$

where the integral is numerically evaluated with the trapezoidal rule. The sum of J_e (Eqn. 4.7−3) and J_p (Eqn. 4.7−6) is considered here as the J−value (J_{lab}) that would be predicted for an experiment conducted in the laboratory for an SE(B) specimen.

4.7.5 Calculation of J with η_p from 2−D Solutions

Sumpter [96] obtained values for η_p using 2−dimensional, slip−line solutions for SE(B) specimens with pure moment loading on the crackplane. Eqns. 2.2−7 and 2.2−8 summarize Sumpter's results. For the crack depths utilized in this study, the corresponding η_p−values are 2.0, 1.343, 0.9678 for the deep, medium and shallow crack specimens, respectively. Figures 4.7−8 and 4.7−9 show the predicted J_{lab} values, normalized by the finite element values, J_{fem},

123
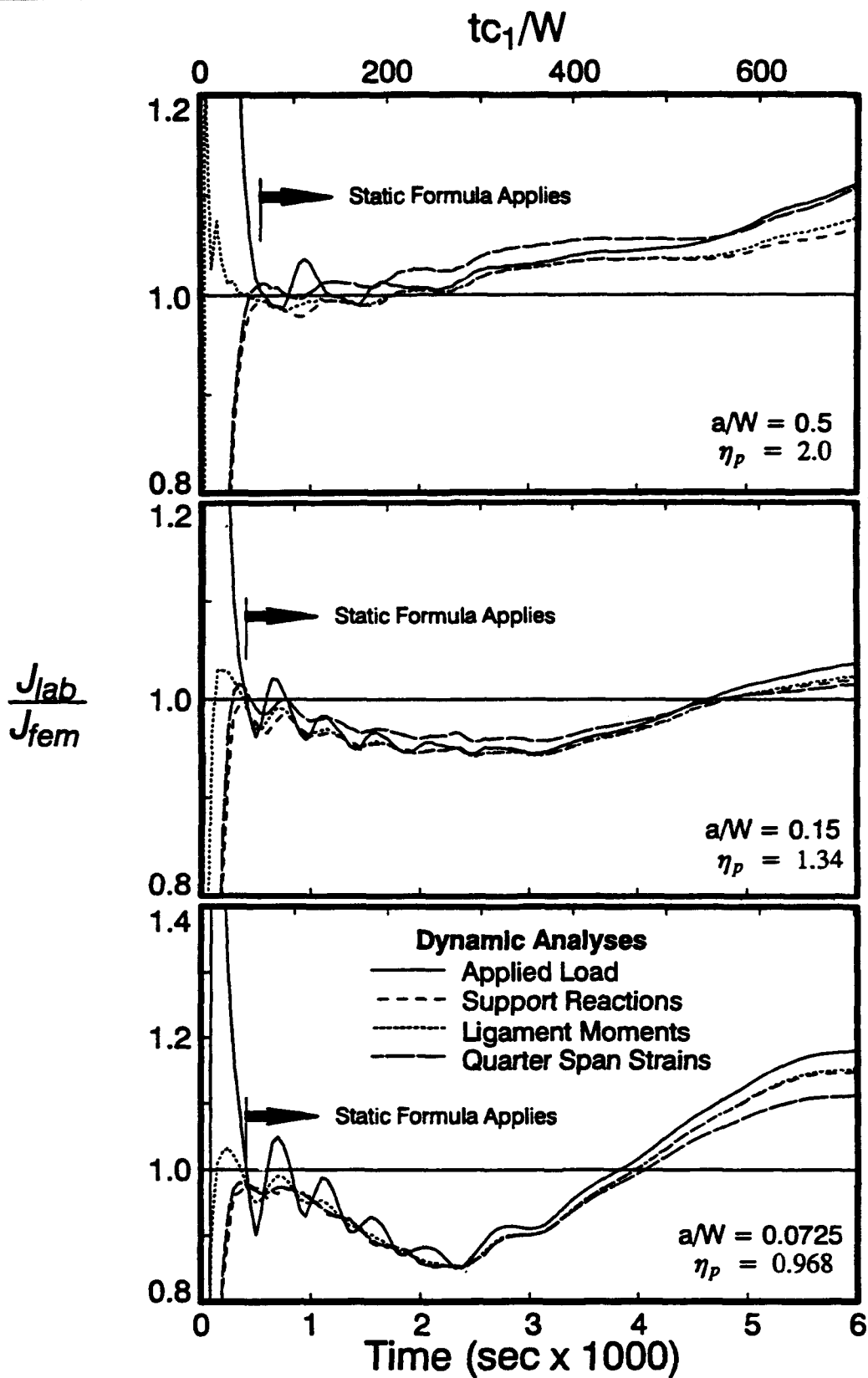
Figure 4.7−8. J_{lab}/J_{fem} for Rate−Insensitive SE(B) Using η_p from Sumpter [96].
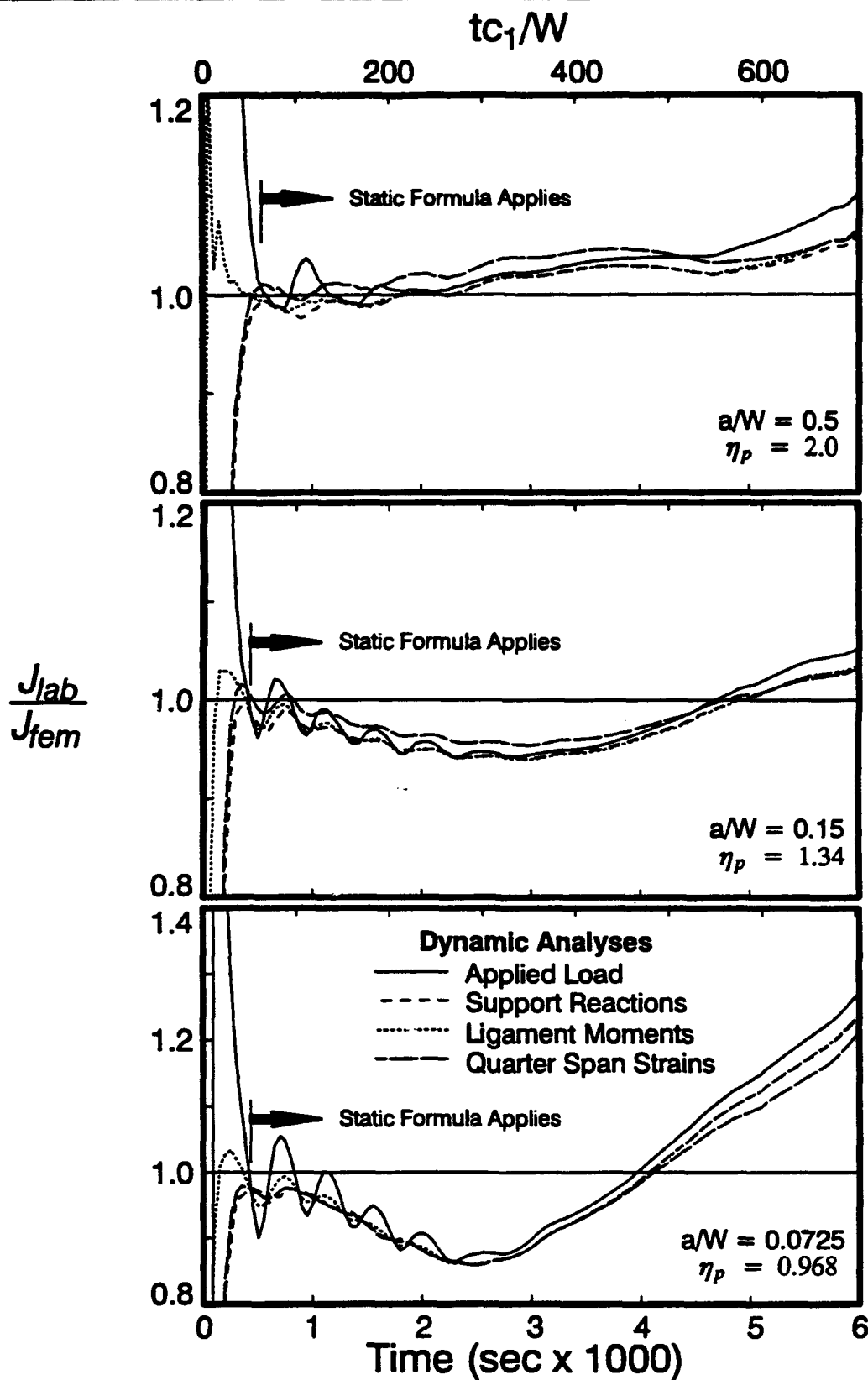
Figure 4.7–9. J_{lab}/J_{fem} for Rate–Sensitive SE(B) Using η_p from Sumpter [96].

for the rate insensitive and sensitive simulations. J_{lab} values computed from the different inferred loads, together with those computed from the applied loads in the analyses, are included in the figures. Deviations of the normalized J-values from unity, shown on the figures as a horizontal reference line, indicate the degree of error incurred in the using static formulas for the evaluation of J.

The deep crack specimen exhibits significant dynamic effects up to prior to 0.0006 seconds, while the medium and shallow cracks show similar effects prior to 0.0004 seconds. These times are approximately 2.5 × the transition times for the respective specimens, and are approximately equal to the first period of the SE(B) specimens. After these times, the simple static formula for J computation predicts accurate results. This agrees with the findings reported in [70], where similar agreement is reported to occur after 2 × t_T. These observations suggest use of the first period of vibration as a practical time after which the static formulas apply. Some oscillatory behavior continues up to approximately 0.003 seconds into the response which indicates elastic vibration in the first mode. The computed J_{lab} with the applied load shows the largest amplitudes of these oscillations, while the inferred loads show lower oscillation amplitudes.

Figure 4.7–10. Ramberg–Osgood Model for Static Base–Line
Stress–Strain Curve for A533B Steel at 50°C.
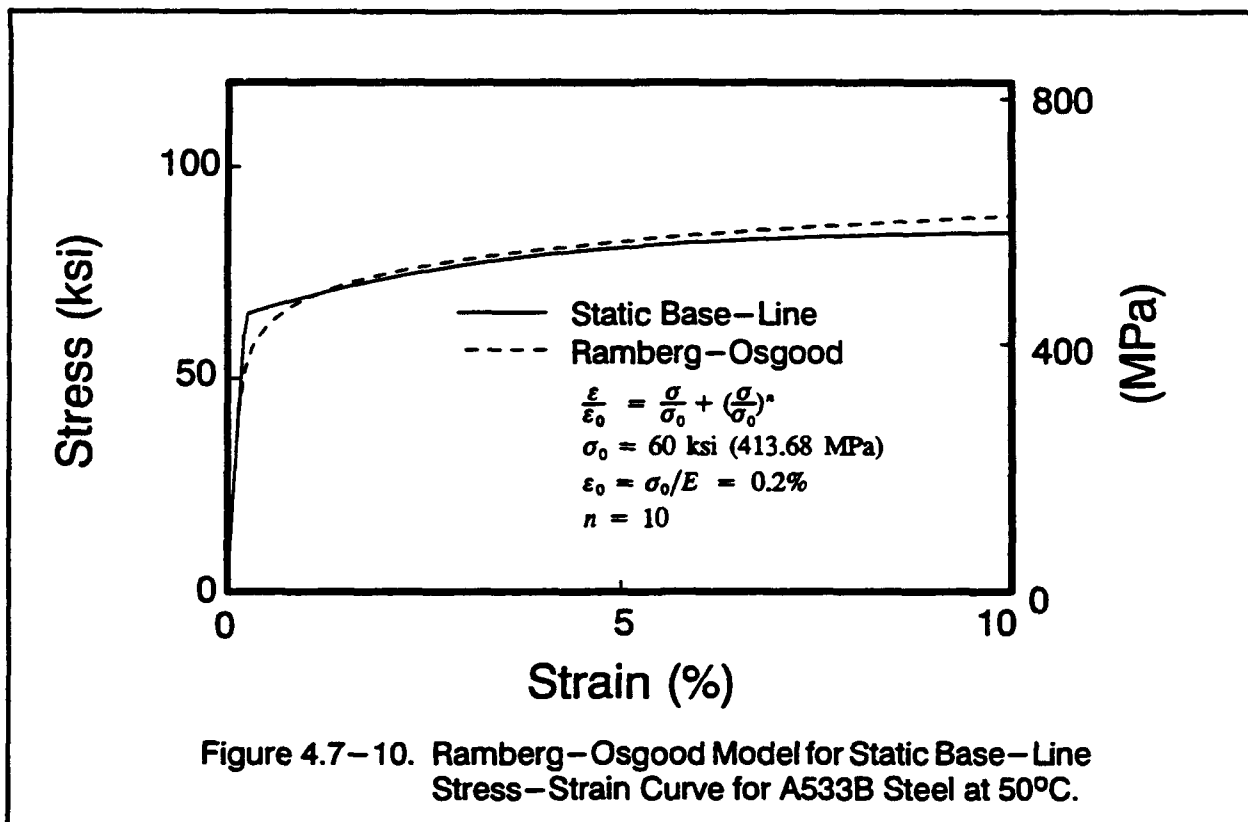
Good predictions (less than 10% error after the initial dynamic effects) of J-values are obtained for the deep and medium crack specimens using Sumpter's relationship for η_p. For the shallow crack specimens, the errors approach 20% with Sumpter's η_p-values once plastic deformation dominates the response. These errors are material model independent, i.e., both material models, rate sensitive and rate insensitive, exhibit the same errors in J-values for the shallow crack specimens.

Kirk [62] computed values of η_p for various specimens and material hardening exponents using plane-strain finite element models. Figure 4.7-10 shows a Ramberg-Osgood stress-strain curve with a material hardening exponent of 10 and a reference stress, σ_0, of 60 ksi (413.68 MPa) superimposed on the baseline stress-strain curve used in this study. As shown in the figure, a material hardening exponent of $n=10$ characterizes the baseline stress-strain curve very well. Kirk reports η_p-values of 1.924, 1.542, and 1.0452 for the deep, medium and shallow crack, respectively. (η_p for the shallow crack is obtained by linear interpolation between tabulated values). Figures 4.7-11 and 4.7-12 show the predicted J-values normalized by the finite element results.

The J-values computed using Kirk's η_p-values are more accurate for the deep crack specimen. Errors in the medium and shallow crack specimens, however, are increased. Maximum errors approach 20% and 30% for the medium and shallow crack, respectively. Rate sensitivity has no influence on the magnitude of the errors.

Figures 4.7-13 through 4.7-16 show the predicted J-values normalized by the finite element values, plotted against the load-line displacement (corrected for the support deformation). This format simplifies the comparison of J-values for dynamic and static analyses. The first two figures, 4.7-13 and 4.7-14, show J-values using Sumpter's values for η_p, while the last two figures show J-values using Kirk's values for η_p.

Deep crack J-values obtained using η_p from Kirk's study [62] match the finite element values well over the entire range of deformation, with errors less than 5%. However, both sets of η_p-values lead to 20 to 30% overestimation of J for the shallow crack specimen.

The following section addresses the use of η_p-values determined from 3-dimensional finite element analyses rather than the plane-strain values used to this point in the discussion.

4.7.6 Calculation of J with η_p Derived from 3-D Analyses

By setting Eqn. 2.2-6 equal to J computed from finite element analyses, η_p may be found directly by:

Figure 4.7–11. J_{lab}/J_{fem} for Rate–Insensitive SE(B) Using η_p from Kirk [62].
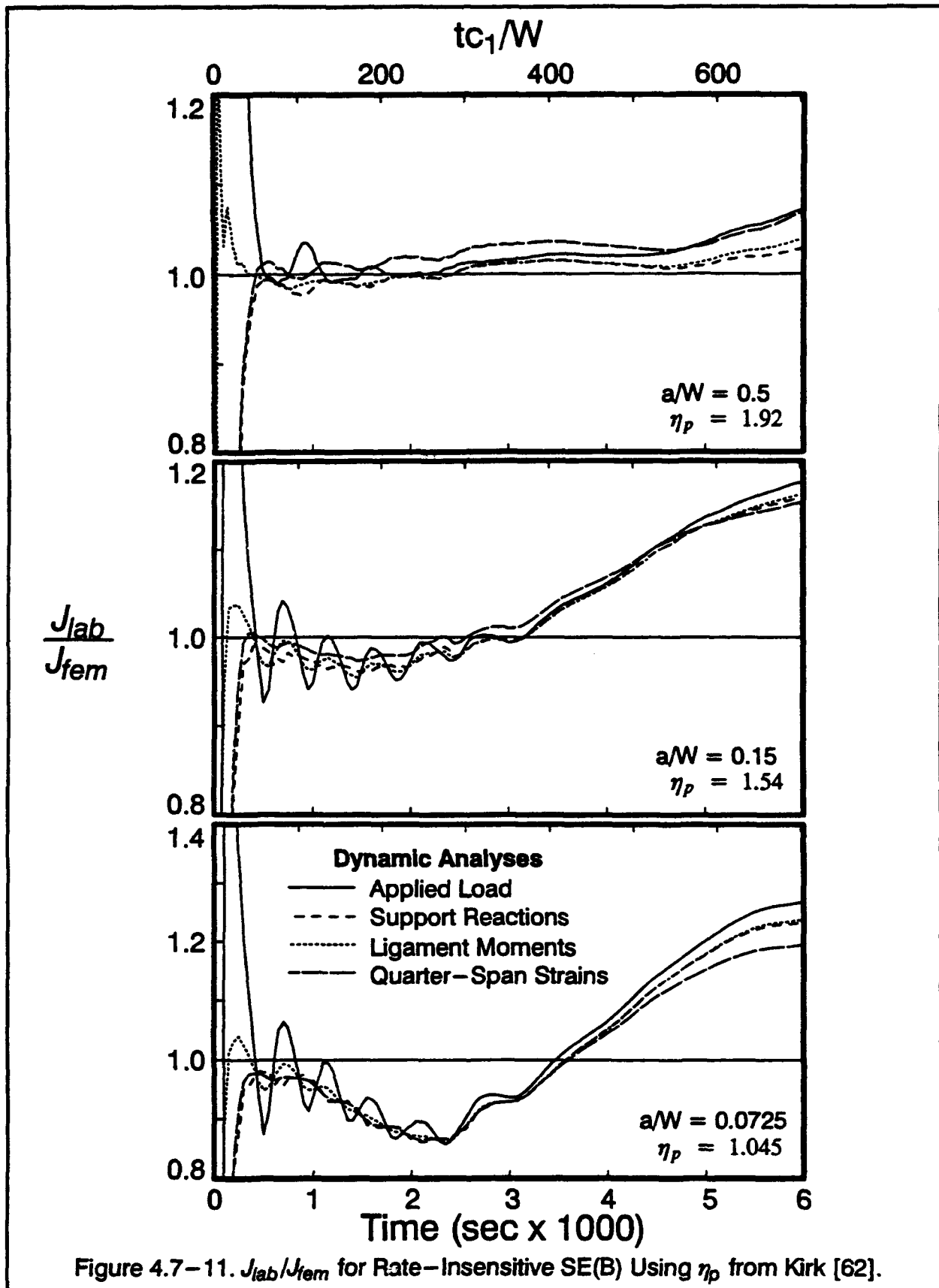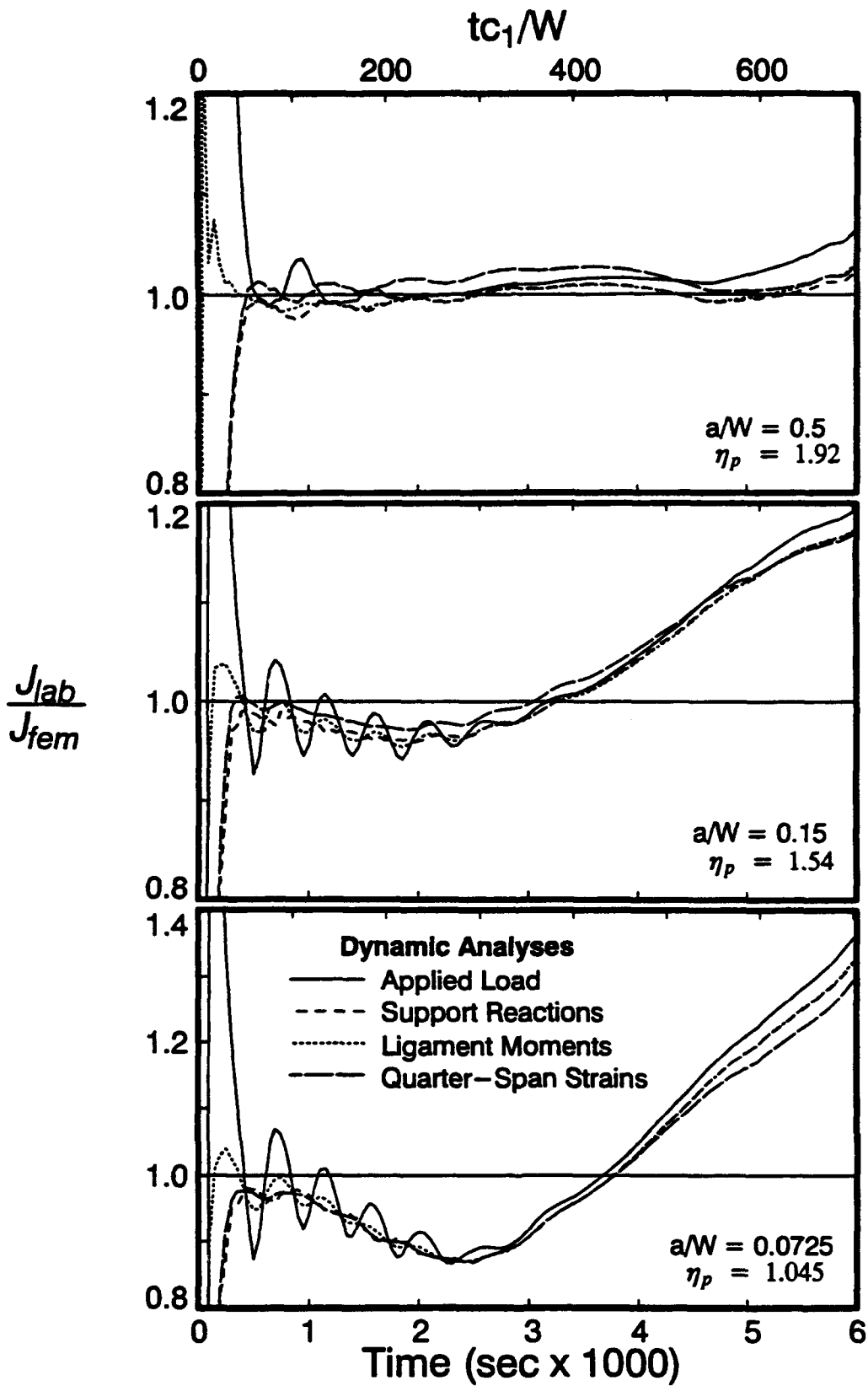
Figure 4.7–12. J_{lab}/J_{fem} for Rate–Sensitive SE(B) Using η_p from Kirk [62].
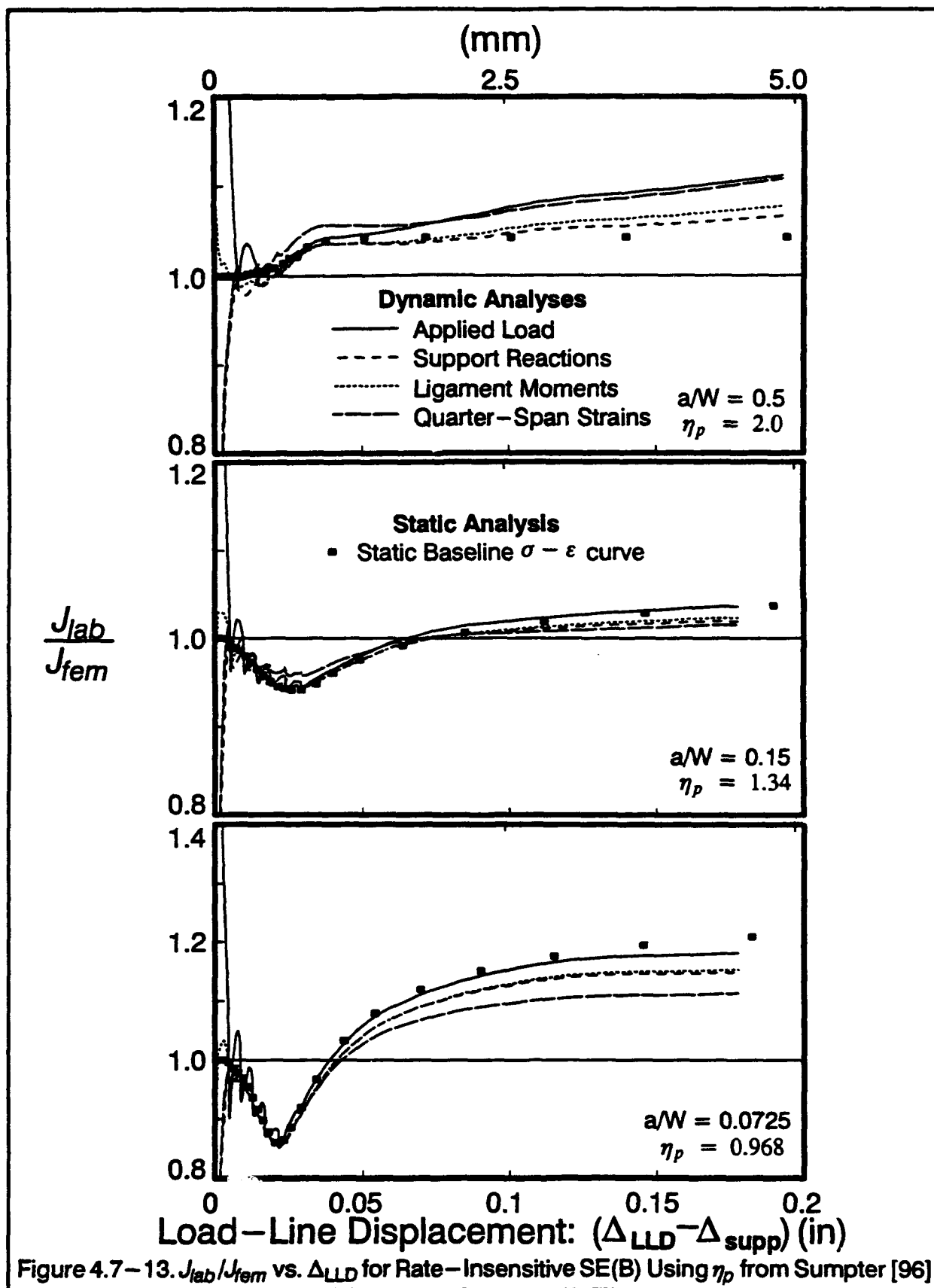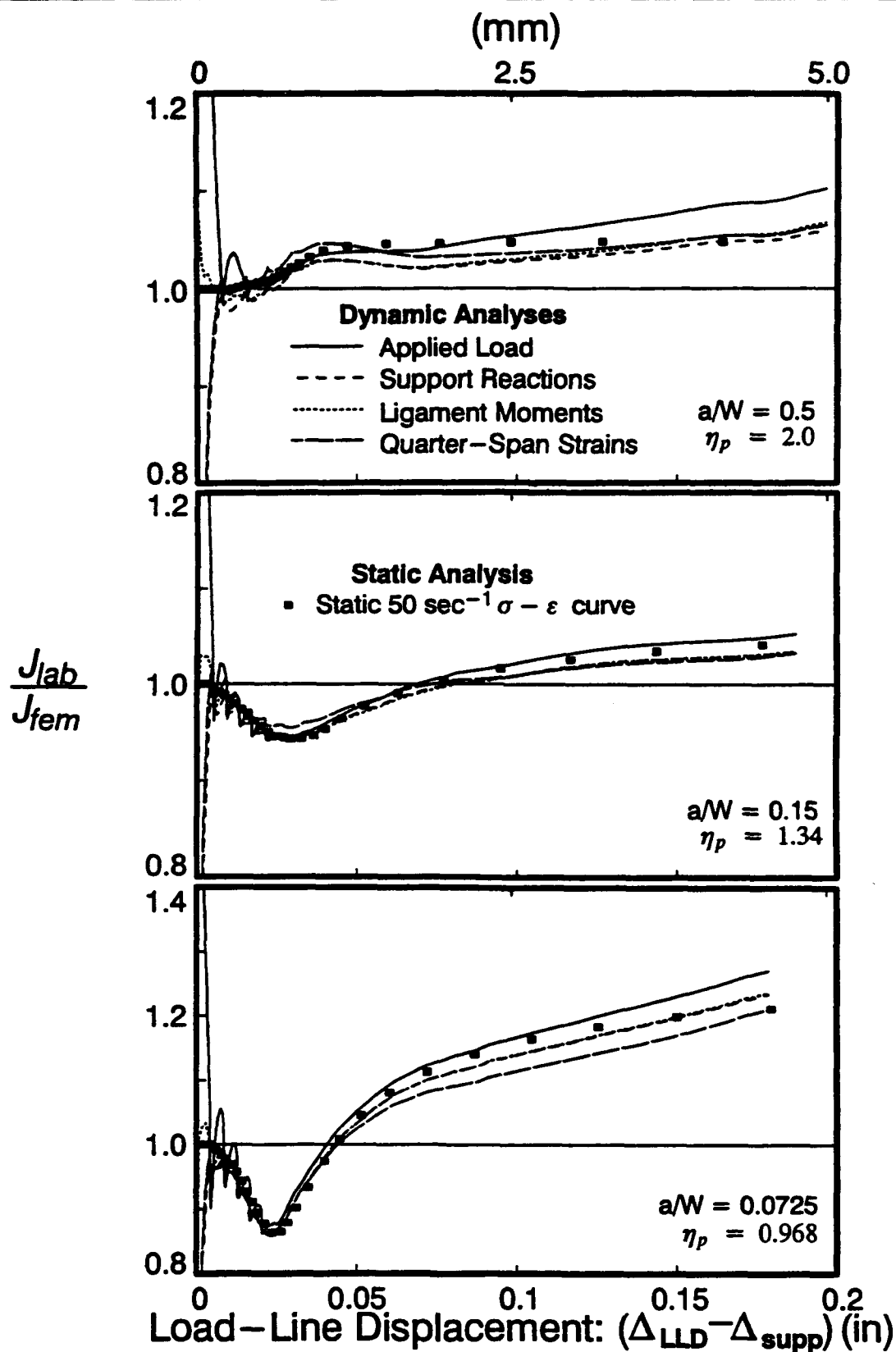
Figure 4.7–13. J_{lab}/J_{fem} vs. Δ_{LLD} for Rate–Insensitive SE(B) Using η_p from Sumpter [96].

Figure 4.7−14. J_{lab}/J_{fem} vs. Δ_{LLD} for Rate−Sensitive SE(B) Using η_p from Sumpter [96].

Figure 4.7-15. J_{lab}/J_{fem} vs. Δ_{LLD} for Rate-Insensitive SE(B) Using η_p from Kirk [62].
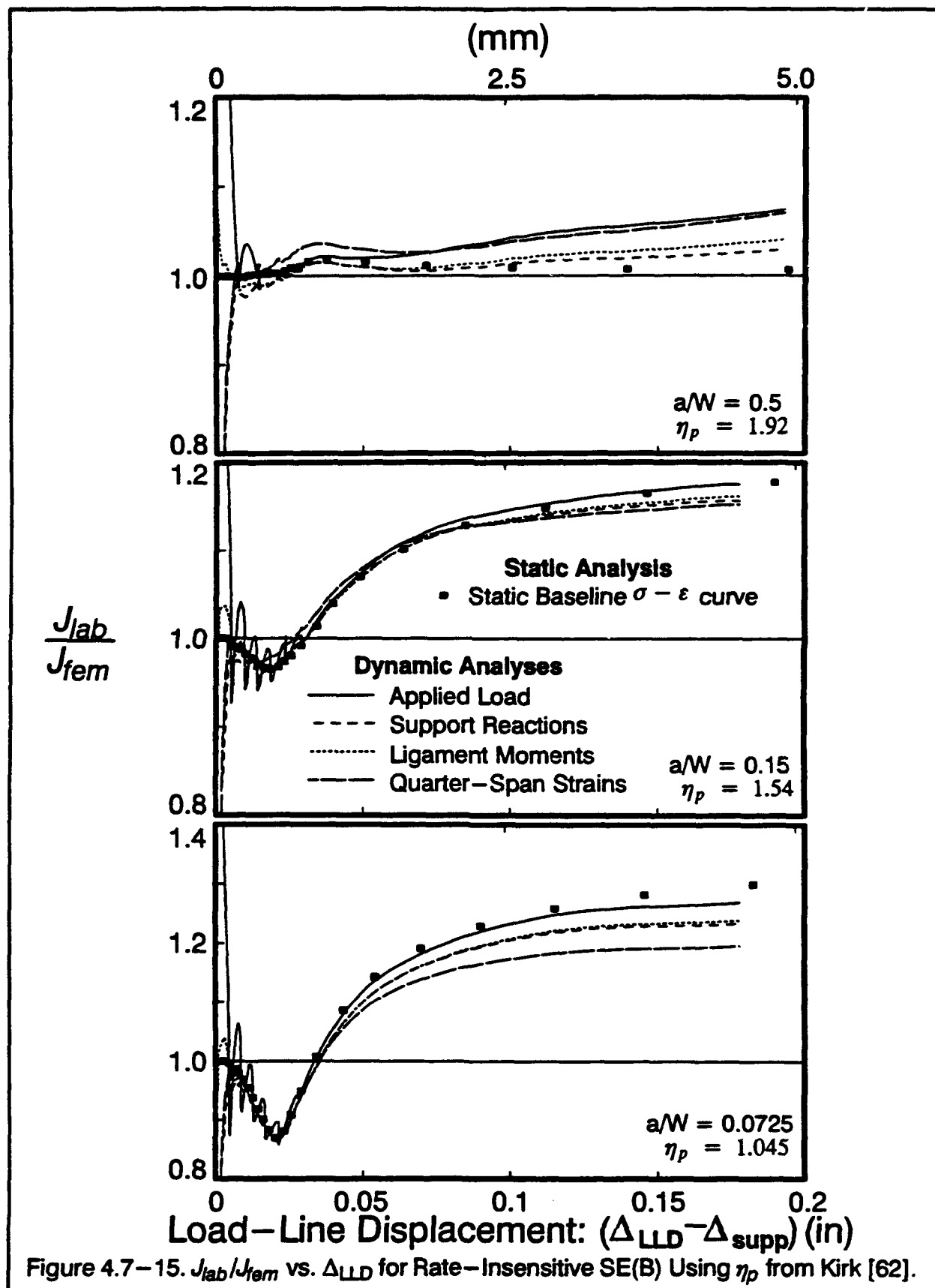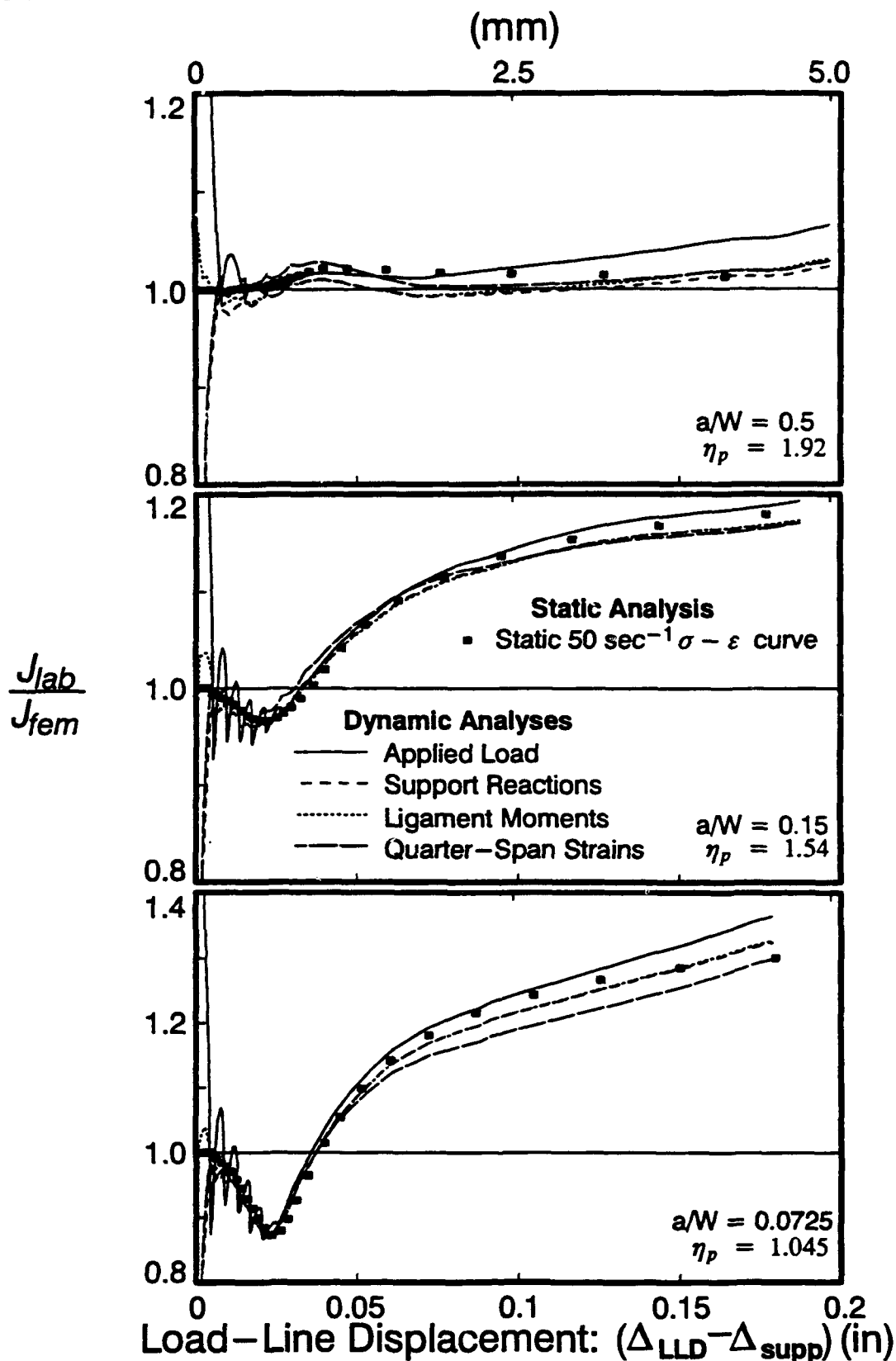
Figure 4.7–16. J_{lab}/J_{fem} vs. Δ_{LLD} for Rate–Sensitive SE(B) Using η_p from Kirk [62].

$$\eta_p = \left[J_{fem} - P^2 J_e^{1kip} \right] bB \left[\int_0^{\Delta_f} P_{equiv} \, d\Delta_p \right]^{-1} \qquad (4.7-7)$$

where all terms appearing in this expression are defined in the previous section. Eqn. 4.7−7 defines η_p at each time step during the analysis. Figure 4.7−17 shows the computed values of η_p versus load−line displacements (corrected for the support displacement). The load−displacement histories as inferred from the ligament moments are used to evaluate the integral in Eqn. 4.7−7. This inferred load−displacement history is chosen as it most closely reflects the actual conditions at the crack tip. Also shown in the figure are the computed values of η_p from the 3−D static analyses.

η_p values begin to approach a constant value when the load−line deflection exceeds 0.025 inches (0.635 mm) for the deep crack specimen, and 0.050 inches (1.27 mm) for the medium and shallow crack specimens. This behavior occurs for both static and dynamic analyses, and for both rate−sensitive and rate−insensitive material models, making it independent of inertial loadings and rate−sensitivity. Early in the response, large fluctuations in η_p−values develop due to the dynamic effects and to the small relative size of J_p vs. J_e.

A single value of η_p for each specimen is calculated from these results in the following manner:

1. A weighted average η_p, $\overline{\eta_p}$ is calculated from each analysis. The area under the $\eta_p - \Delta_{LL}$ curve is integrated from a load−line displacement of 0.04 inches (1.02 mm) to the end of the response. This area is then divided by the total load−line displacement from 0.04 inches to the end of the response to give the desired $\overline{\eta_p}$:

$$\overline{\eta_p} = \frac{\int_{0.04\,in}^{\Delta_f} \eta_p \, d\Delta_{LL}}{\int_{0.04\,in}^{\Delta_f} d\Delta_{LL}} \qquad (4.7-8)$$

2. The resulting four values of $\overline{\eta_p}$ per specimen, one from each analysis shown in Fig. 4.7−17, are then averaged to provide η_p^{3d}.

A load−line displacement of 0.04 inches is chosen as the starting point since stabilized values of η_p are computed at larger deformations for all three specimens. J−values computed with the resulting η_p^{3d} should be more accurate toward the end of the response where: 1) the loading

Figure 4.7–17. η_p vs. Δ_{LLD} for Both Dynamic and Static Analyses.
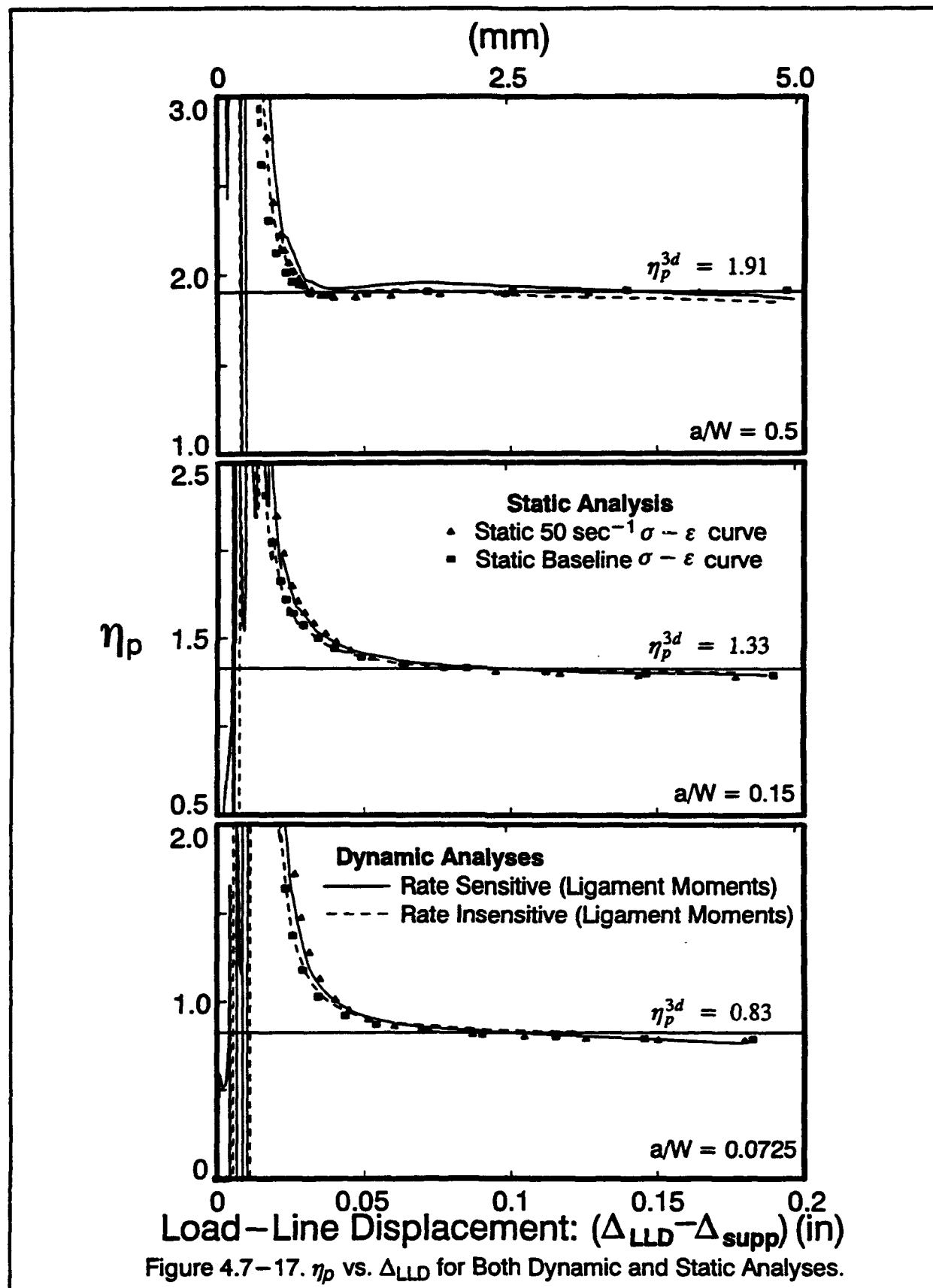
point of the specimen has reached the terminal velocity of the tup; and 2) the specimen has undergone large amounts of plasticity. The values of η_p^{3d} are 1.905, 1.327, 0.826, for the deep, medium and shallow crack, respectively. These values are shown as horizontal lines in Fig. 4.7-17. As expected, the computed values of η_p^{3d} for the deep crack and the medium crack specimen are very similar to the η_p values that produced the most accurate J-values in the previous section.

Figures 4.7-18 and 4.7-19 show the normalized J-values computed using η_p^{3d} with the different inferred loads as a function of response time. All three specimens show improvement in accuracy over the computations with η_p based on 2-dimensional models. At approximately $2.5 \times$ the transition time in each specimen the inertial effects become negligible.

For the shallow crack specimen, the static estimates of J are too small for a large portion of the response. Figures 4.7-18 and 4.7-19 show errors approaching 15% of J_{fem} for both material models. The medium crack results also show the same tendency to underestimate J, but with errors of only 5%. Once inertial effects have diminished after approximately 0.0005 seconds, and toward the end of the response after 0.004 seconds, accurate J-values are obtained with η_p^{3d} for both the medium and the shallow crack specimens. Computed J-values for the deep crack specimen are accurate throughout the response once the inertial effects have diminished.

Figures 4.7-20 through 4.7-21 show the normalized J-values as a function of load-line displacement (corrected for the support deformation). Results from the static analyses are also included in the figures. Significant improvements in the accuracy of the J-values are obtained for computations using η_p^{3d}. Once the inertial effects diminish, J-values computed for the deep crack specimen show less than 5% error throughout the analyses. Errors in the computed J approach 10% and 18% for the medium and shallow crack specimen, respectively, prior to load-line deflections of 0.05 inches (1.27 mm). At larger load-line deflections, however, the computed J-values for the medium and shallow crack specimens show less than 5% deviation from the finite element values. Aside from the inertial effects, the static and dynamic analysis provide similar accuracy in the J computations using η_p^{3d}.

4.7.7 Calculation of J from Total Work

The separation of J into elastic and plastic components [3,62] is somewhat arbitrary. Other separation techniques, such as the deformation that represents the structure without the crack and the additional deformation that occurs due to the crack, are equally valid [7]. The original

Figure 4.7–18. J_{lab}/J_{fem} for Rate–Insensitive SE(B) Using $\eta_p{}^{3d}$

Figure 4.7-19. J_{lab}/J_{fem} for Rate-Sensitive SE(B) Using $\eta_p{}^{3d}$

Figure 4.7–20. J_{lab}/J_{fem} vs. Δ_{LLD} for Rate–Insensitive SE(B) Using $\eta_p{}^{3d}$.
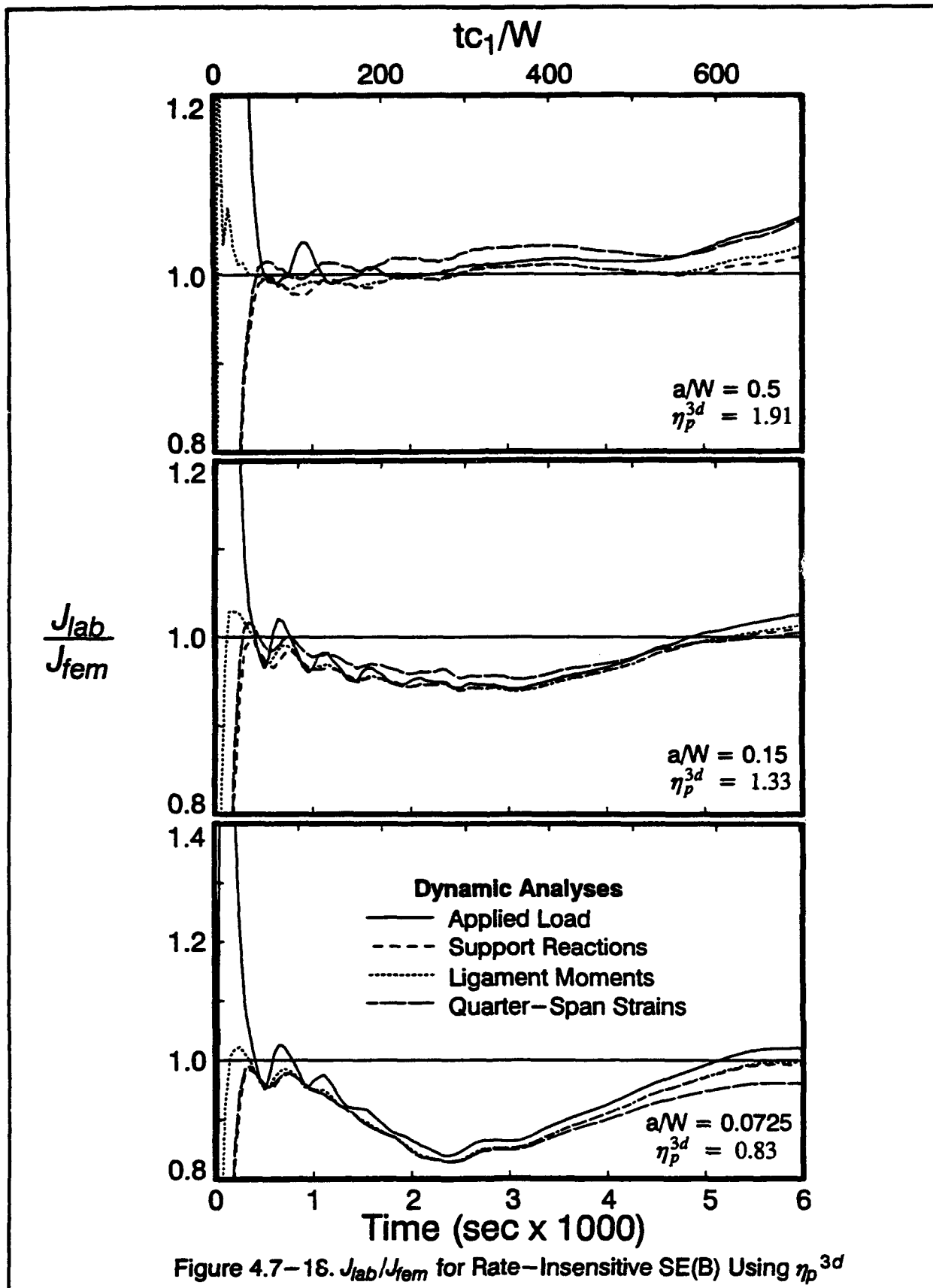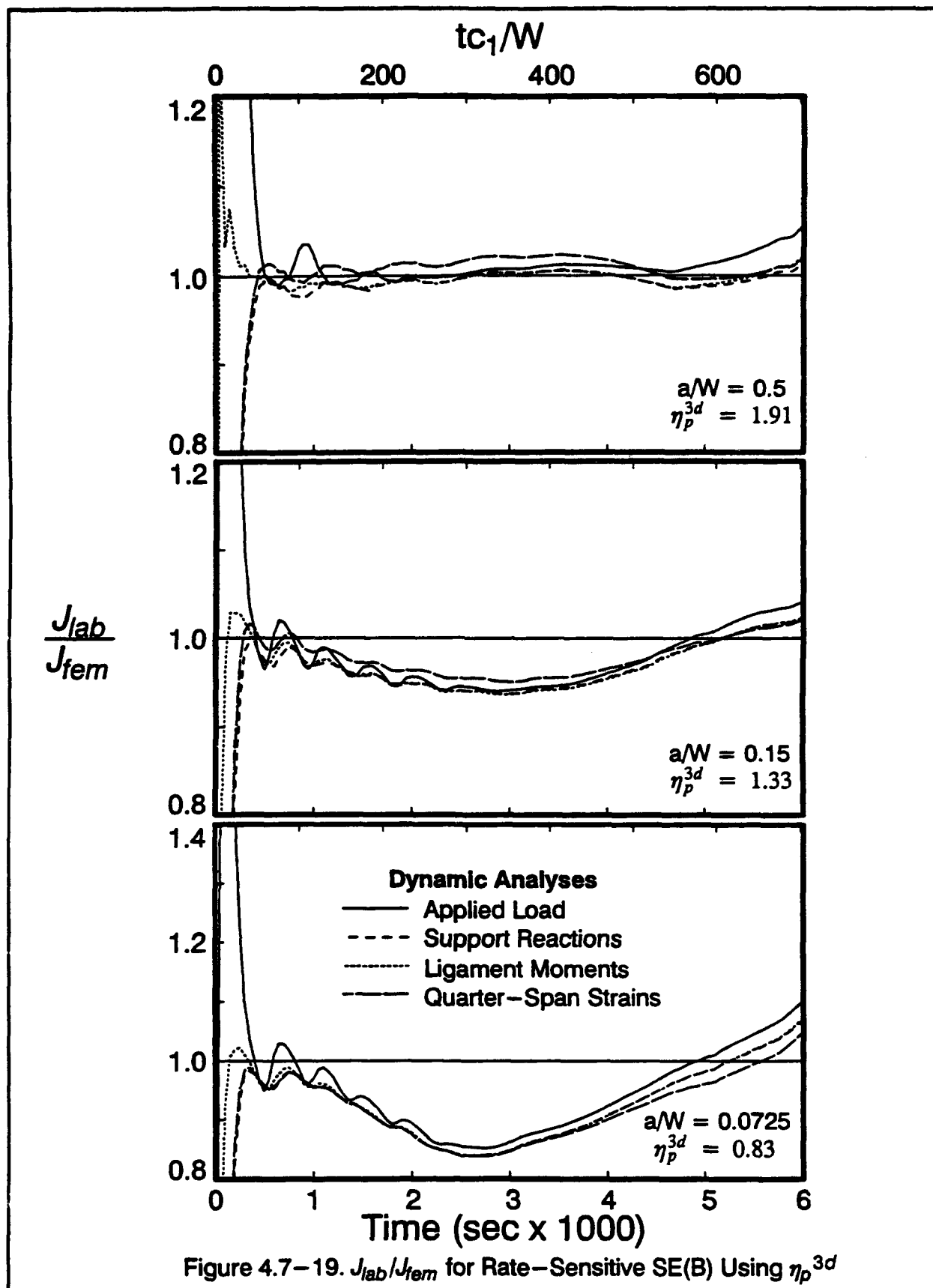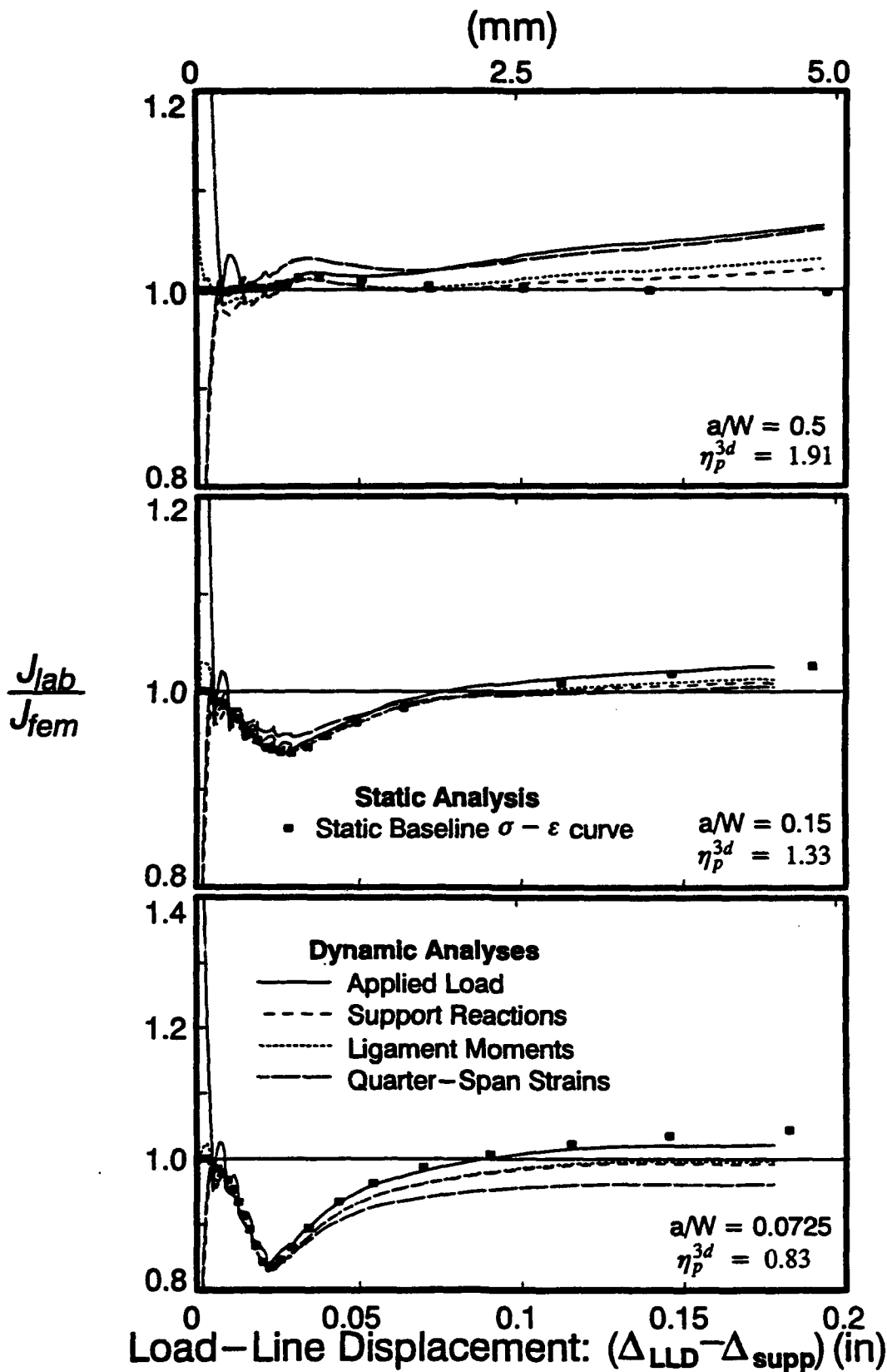
Figure 4.7−21. J_{lab}/J_{fem} vs. Δ_{LLD} for Rate−Sensitive SE(B) Using $\eta_p{}^{3d}$.
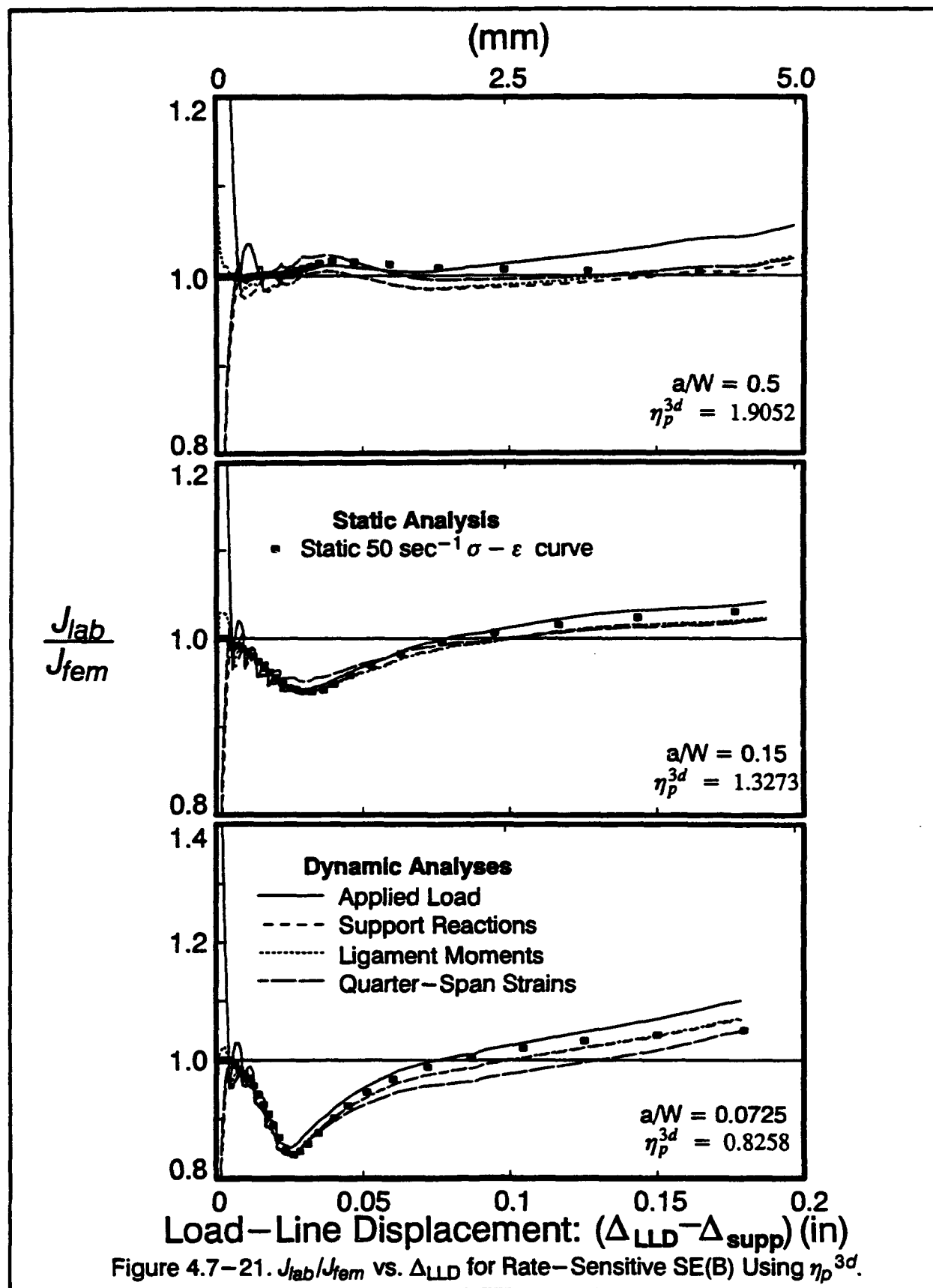
derivation by Rice [86] does not assume any separation of the total J. This section investigates the computation of J_{lab} without the separation into J_e and J_p.

Figure 4.7−17 shows large oscillations in η_p for the initial 0.01 inches of load−line displacement. The specimens are predominantly elastic at this stage, making J_p near zero, and the computation of η_p subject to large error. Since the external work of a statically applied load for an elastic specimen is one half the product of the load and the load−line displacement, a 3−dimensional η_e, the dimensionless constant that relates the elastic work to J_e, (See Eqn 2.2−5) can be calculated as follows:

$$J_e = \frac{\eta_e}{bB} \frac{1}{2} P_{equiv} \Delta_e = \frac{\eta_e}{bB} \frac{1}{2} P_{equiv} PC_\Delta = \frac{\eta_e}{bB} \frac{1}{2} P^2 a_{load} C_\Delta \qquad (4.7-9)$$

where all terms are as defined in the previous section. For the SE(B) specimens in this study, a relationship between the applied load and the resulting elastic J is stated in Eqn.4.7−3. Solving for η_e from these two equations yields:

$$\eta_e^{3d} = \frac{2J_{el}^{1kip} Bb}{C_\Delta a_{load}} \qquad (4.7-10)$$

Using the values in Table 4.7−1, values for η_e^{3d} are: 0.758, 1.257, and 1.967 for the shallow, medium and shallow crack, respectively. These values are nearly identical to values of η_t obtained by Srawley [95] for 2−dimensional models of elastic SE(B) specimens:

$$\eta_t^{Srawley} = 2.0 - \left(0.3 - 0.7\frac{a}{W}\right)\left(1.0 - \frac{a}{W}\right) - e^{\left(1.0 - \frac{a}{W}\right)} \qquad (4.7-11)$$

which yields η_t = 0.776, 1.257, and 1.975 for the shallow, medium and deep crack specimens respectively. These values are numerically similar to the computed η_p^{3d} in the previous section, which suggests the combination of elastic and plastic components, i.e. using a single η_t that relates the total energy to the fracture parameter J.

By relating the total applied external work to the fracture parameter J, the static formula becomes:

$$J_{lab} = \frac{\eta_t}{bB} \int_0^{\Delta_f} P_{equiv} \, d\Delta_t \qquad (4.7-12)$$

141

where η_t is the proportionality factor that relates the total energy to J, P_{equiv} is the applied loading corrected for the finite loading area, and Δ_t is the total load—line displacement corrected for support deformation:

$$\Delta_t = \Delta - \Delta_{support} \qquad (4.7-13)$$

Following the procedure used to compute η_p^{3d}, Eqn. 4.7—12 is set equal to J_{fem} and solved for η_t. Figure 4.7—22 shows the resulting values of η_t as a function of specimen deformation. Dynamic analyses with loads inferred from the ligament moments and companion static analyses are used to compute η_t. A single value for each specimen, η_t^{3d}, is obtained with the averaging technique shown in Eqn. 4.7—8.

As shown in Fig. 4.7—22, the variation of computed η_t values with increasing load—line displacement is much smoother than variations of η_p shown in Fig. 4.7—7. η_t reaches a near—constant value beyond 0.05 inches (1.27 mm) of load—line deformation. The deep crack specimen exhibits very little change in η_t over the response from fully elastic to fully plastic conditions. The medium and shallow crack specimens, however, show a small "hump" followed by a near—constant value. All analyses show the same behavior, independent of inertial and rate—sensitivity effects. Use of the averaging procedure defined in Section 4.7.6, values of η_t^{3d} = 0.8151, 1.3171, and 1.9095 are found for the shallow, medium and deep crack specimen, respectively. These values are shown as horizontal lines in Fig. 4.7—22.

Figures 4.7—23 and 4.7—24 show J from Eqn. 4.7—12 using computed η_t^{3d} values. Large inertial effects are present for the initial 0.0006 seconds of the deep crack specimen, and for the initial 0.0004 seconds of the medium and shallow crack specimens. This represents approximately 2.5 $\times$ the respective transition time of the specimen. After this time, all three methods to infer the load produce less than 5% error in J for the deep and medium crack specimens, and 12% error in J for the shallow crack specimen. Rate sensitivity of the material model does not affect the accuracy of J—values given by Eqn 4.7—12.

Figures 4.7—25 and 4.7—26 show the evolution of J—values with increasing specimen deformation. After the initial 0.01 inches (0.25 mm) of load—line displacement, all J—values are within 5% of the correct values for the deep and medium crack specimens, and within 12% for the shallow crack specimen.

Use of the total work for computation of J_{lab} improves the accuracy relative to the separation techniques, but with a small reduction of accuracy during the initial elastic response of the specimen.

142

Figure 4.7−22. η_t vs. Δ_{LLD} for Both Dynamic and Static Analysis.

Figure 4.7–23. J_{lab}/J_{fem} for Rate–Insensitive SE(B) Using η_l^{3d}.

144
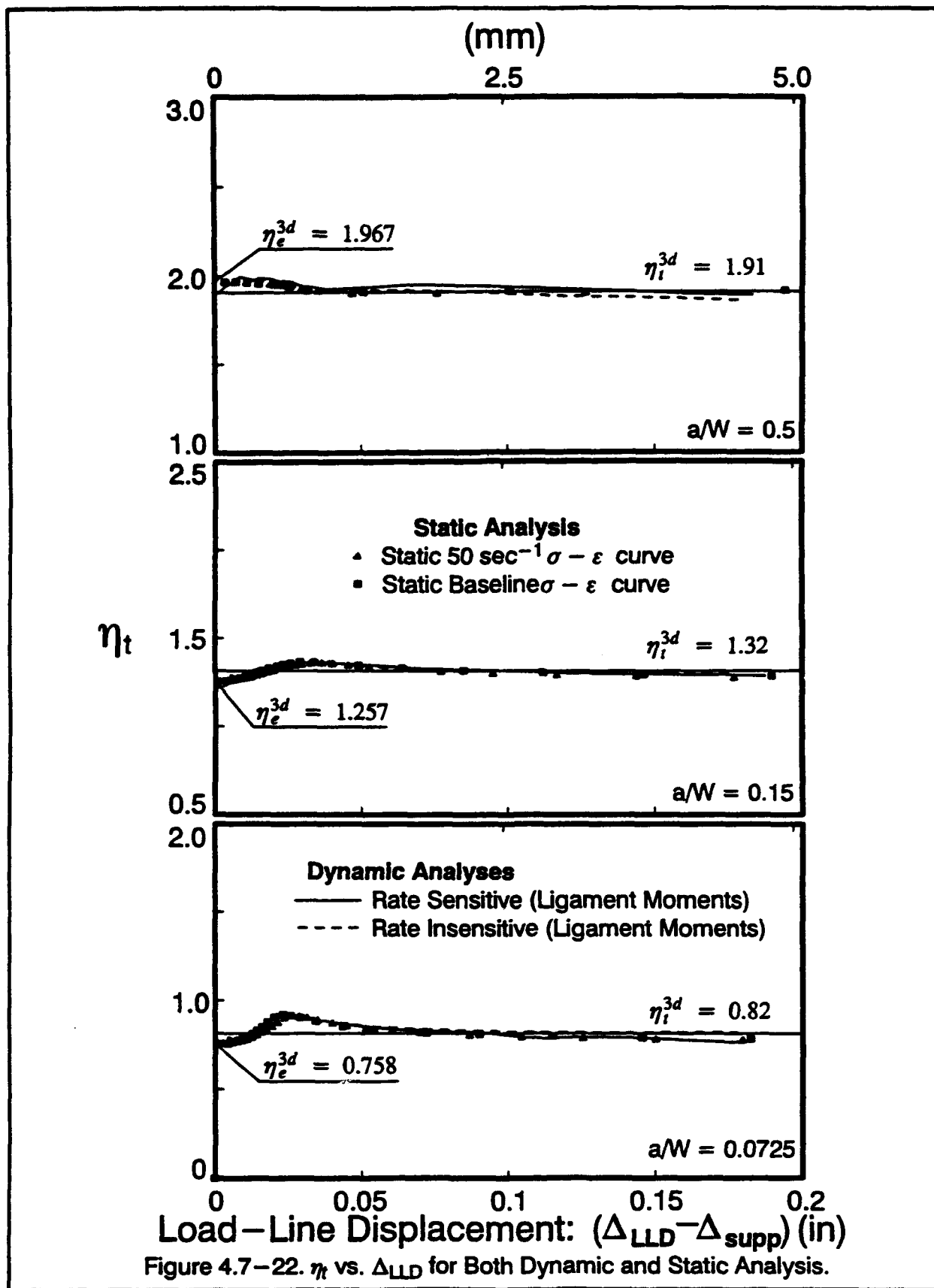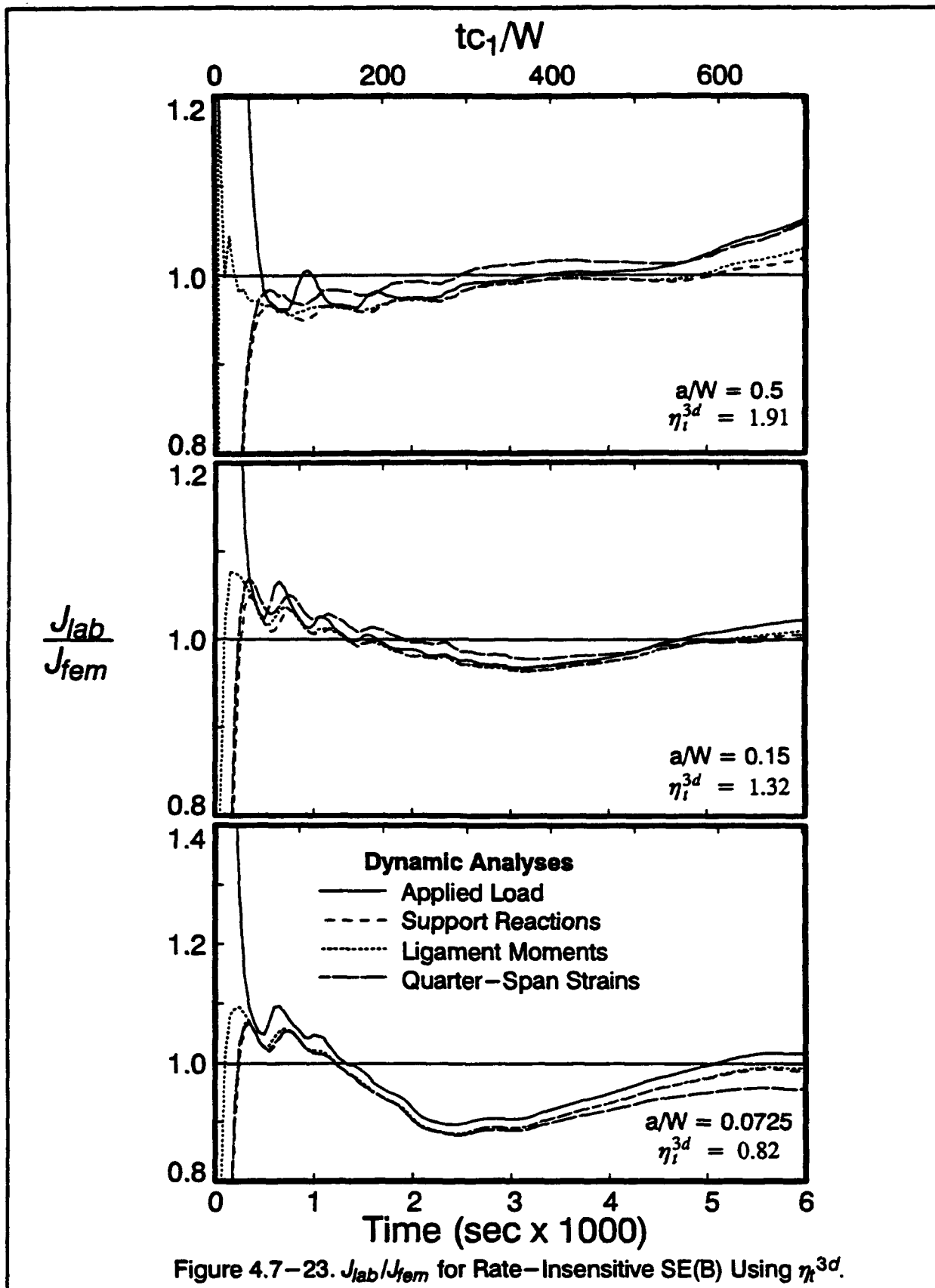
Figure 4.7–24. J_{lab}/J_{fem} for Rate–Sensitive SE(B) Using η_t^{3d}.

145

Figure 4.7-25. J_{lab}/J_{fem} vs. Δ_{LLD} for Rate-Insensitive SE(B) Using $\eta_t{}^{3d}$.

Figure 4.7–26. J_{lab}/J_{fem} vs. Δ_{LLD} for Rate–Sensitive SE(B) Using η_t^{3d}.
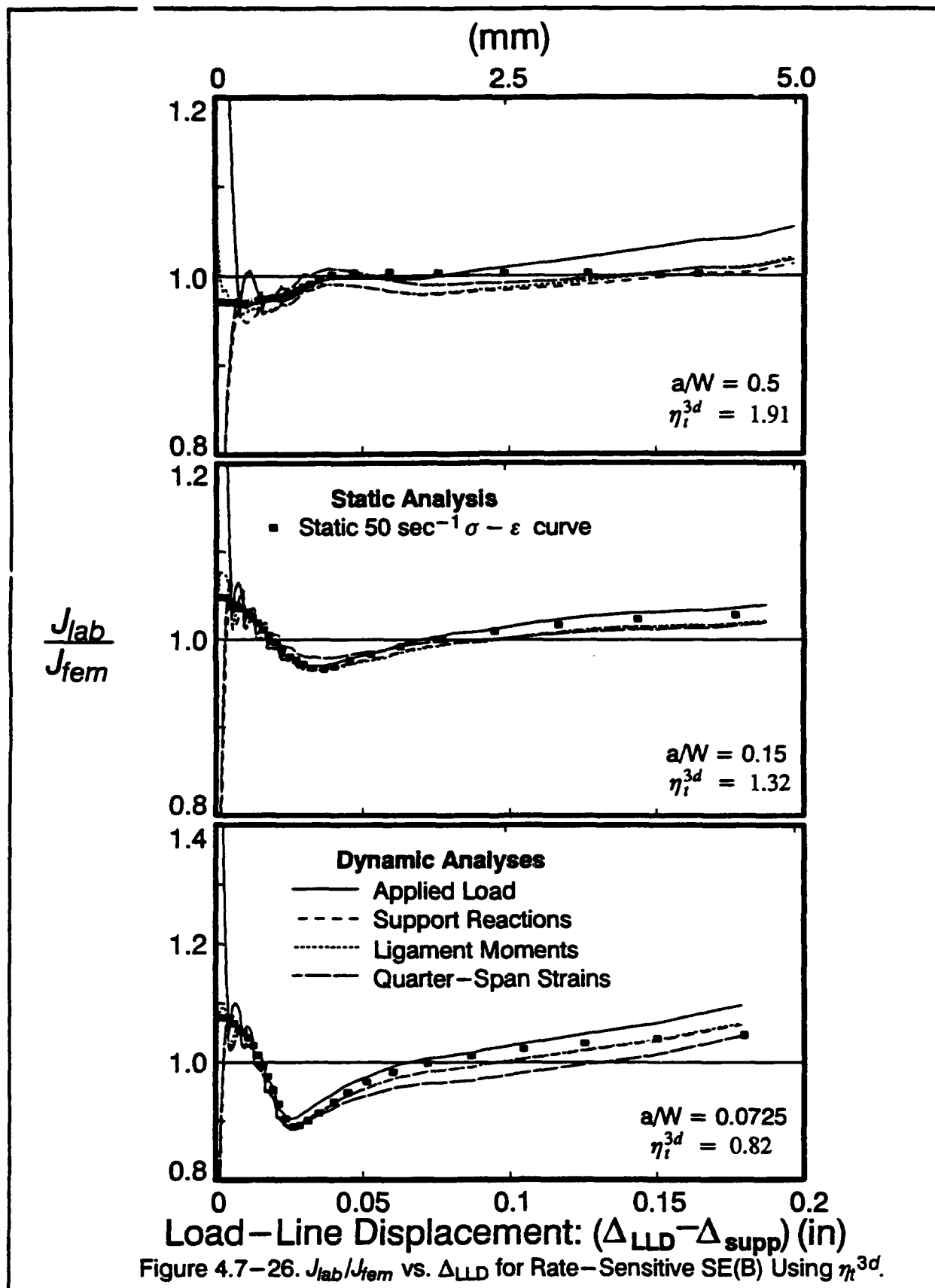
4.7.8 J–Integral Calculations: Summary

Rate sensitivity elevates J–values by approximately 17% for the deep and medium crack specimens, but only 5% for the shallow crack specimen. For the shallow crack specimen, rate sensitivity increases the ligament stresses and stiffens the ligament sufficiently to force deformation away from the crack tip. This shields the crack tip of the shallow crack specimen from the rate sensitivity induced increases in J for the deep and medium crack specimens.
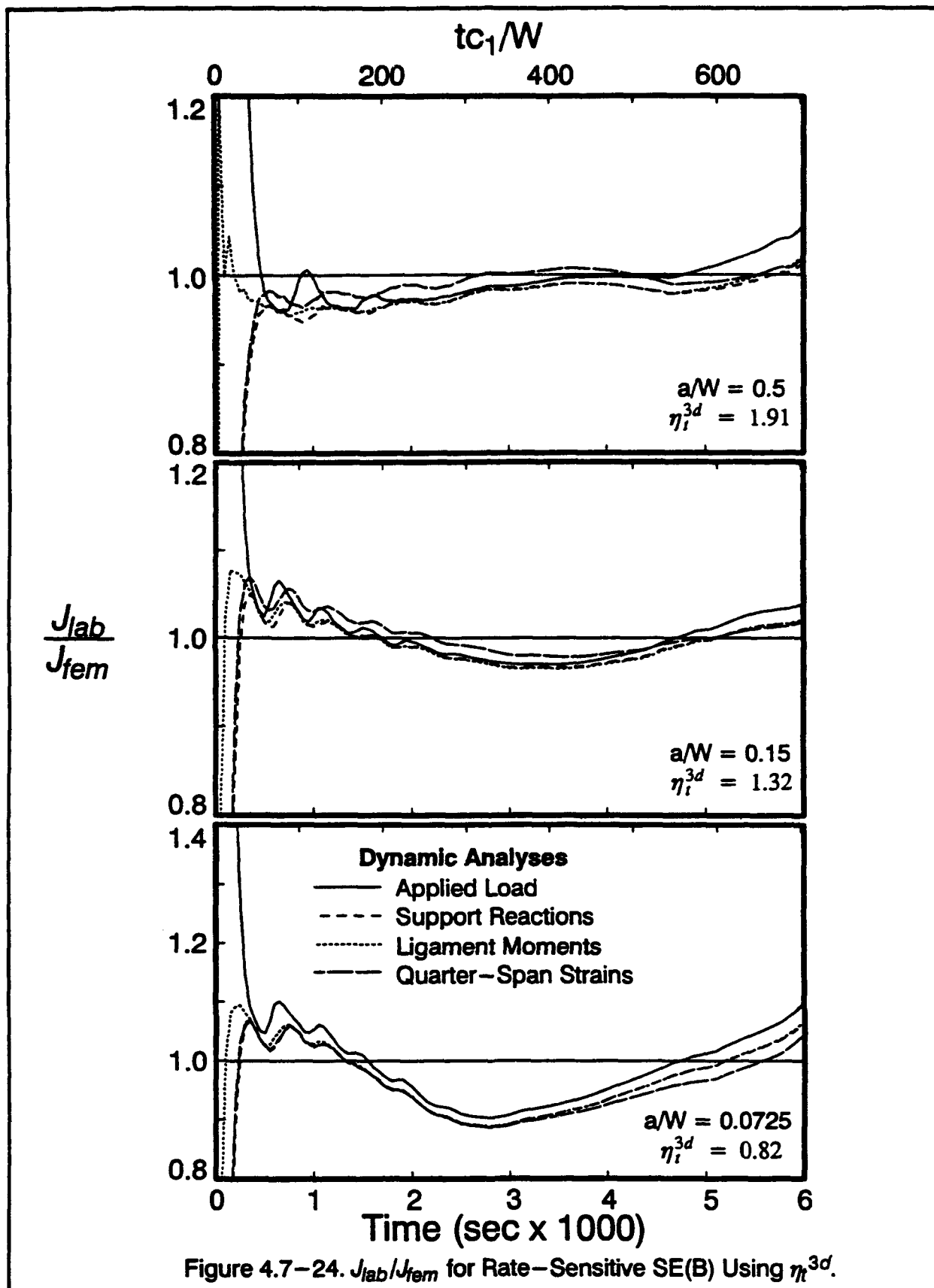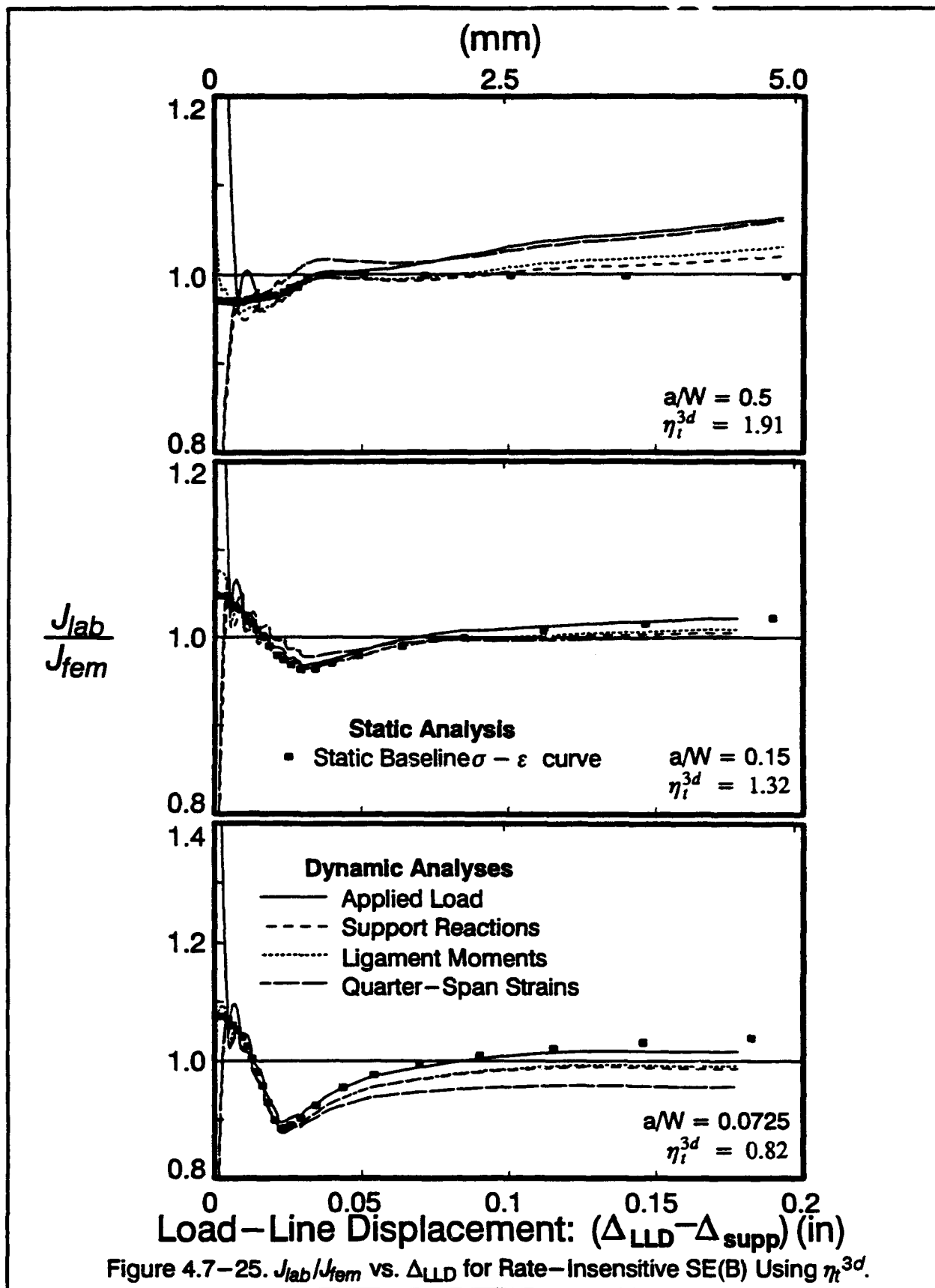
For all three specimens, the static formula to compute J is applicable at times after $2.5 \times$ the transition time of each specimen. Beyond this time the accuracy of J computed with the static formula is not dependent on inertial effects, but is dependent on the plastic proportionality factor used (η_p).

The static formula for J based on ligament work with η_p obtained from solutions based on 2–dimensional models produces unacceptable errors. Sumpter's η_p values [96] produce errors approaching 20% for the shallow SE(B) specimen. Kirk's η_p values [62] produce errors approaching 20% for the medium crack specimen and 30% error for the shallow crack specimen. For use in laboratory tests these errors are *unconservative*, and can lead to considerable overestimation of the actual capacity of the fracture resistance. η_p^{3d}–values derived from 3–D analyses increase the accuracy of the static formula. Use of η_p^{3d} produces less than 5% error once load–line deformation is greater than 0.05 inches for both statically and impact loaded specimens.

A modification of the static formula in which the fracture parameter is related to the total area under the load–displacement curve improves the accuracy in J computations. While sacrificing accuracy during the initial elastic response (up to 8% error for the shallow crack specimens), the overall accuracy in the computed J–values is improved. Sorem [94] reached similar conclusions for a high hardening steel (A36 steel) SE(B) specimen with $a/W = 0.15$ loaded statically. Utilizing a 3–D finite element analysis, Sorem obtained an η_t value of 1.34, which is nearly identical to the value obtained in this study, $\eta_t = 1.32$, for the medium crack specimen.

Both methods to infer the applied load during an impact test (from the quarter–span strains and from the support reactions) produce acceptable J–values (<5% error) after the initial elastic response once appropriate values of η_p are utilized in Eqns 2.2–6 and 4.7–12.

4.8 J Variation Along the Crack Front

Finite element meshes for the SE(B) specimens contain five layers of elements through the half thickness. A pointwise value of J at each plane of nodes over the crack front is obtained

using the domain integral approach. The four q-function variations indicated in Fig. 4.7-1 are applied in each plane of nodes. All nodes that lie outside of a given plane are assigned zero q-values. This form of the domain integral produces a weighted value of J on the crack front at the plane of the nodes. All elements incident to nodes that have nonzero q-values are included in the domains. For each plane of nodes intersecting the crack tip, an average J computed from the domains denoted *Ring 2* through *Ring 4* in Fig. 4.7-1 defines the pointwise value.

Figures 4.8-1 and 4.8-2 show the pointwise J-values normalized by the average J-value over the thickness. The figures show $J(z)$, (where z is measured from the specimen centerplane to the outer surface), as a function of the normalized through-thickness distance for each milli-second of the dynamic response. Arrows are provided to indicate the change with time of the $J(z)$ distributions.

Figure 4.8-3 shows the crack front J-values for the companion static analyses with the baseline stress-strain curve. The figure shows six distributions, each one corresponding to the load-line displacement at indicated times in the dynamic analyses of Figs. 4.8-1 and 4.8-2. These figures indicate that the variation of J across the crack front is strongly dependent on the specimen geometry, and relatively independent of both inertial effects and rate sensitivity of the material. Both the deep and the medium crack specimens show relative increases of J at the centerplane, with decreasing relative values at the free surface. The maximum J-values for the deep and medium crack specimens are 15% and 10% larger than the average J-value at 0.006 seconds. The maximum J for the shallow crack specimen occurs near the free surface at $z/B = 0.4$. For the shallow crack specimen an elevation of approximately 10% of the average J occurs at this location. The centerplane value of J for the shallow crack specimen remains very near the average J throughout the response.

Figure 4.8-4 shows the J distribution across the crack front at the end of the dynamic analyses together with the corresponding static analysis distribution at the same, final load-line displacement. The relatively small differences between the three sets of results confirm the strong similarity of the J variation across the crack front for both the dynamic and static analyses.

The larger centerplane J-values in the deep and medium crack SE(B) specimens reflect the high constraint due to confinement against plastic flow. Near the free surface this constraint decreases. As shown in the figures, the boundary effect of the free surface of these two specimens extends to approximately 0.15 inches (3.81 mm). The figures also show that the loss of constraint is progressive: as plastic deformation increases, the relative J-value at the
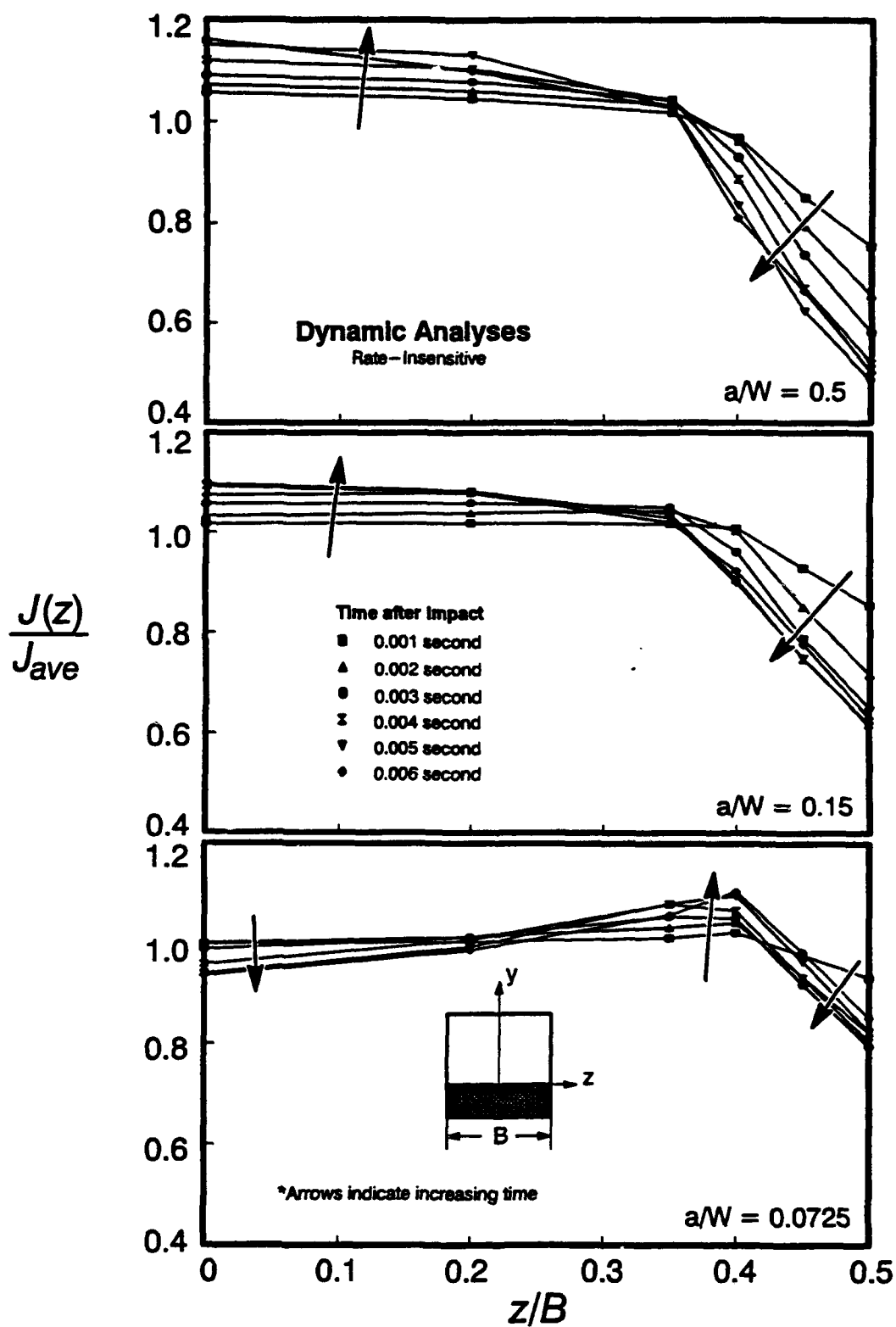
149

Figure 4.8-1. Crack Front $J(z)/J_{ave}$ Variation for Rate-Insensitive SE(B)
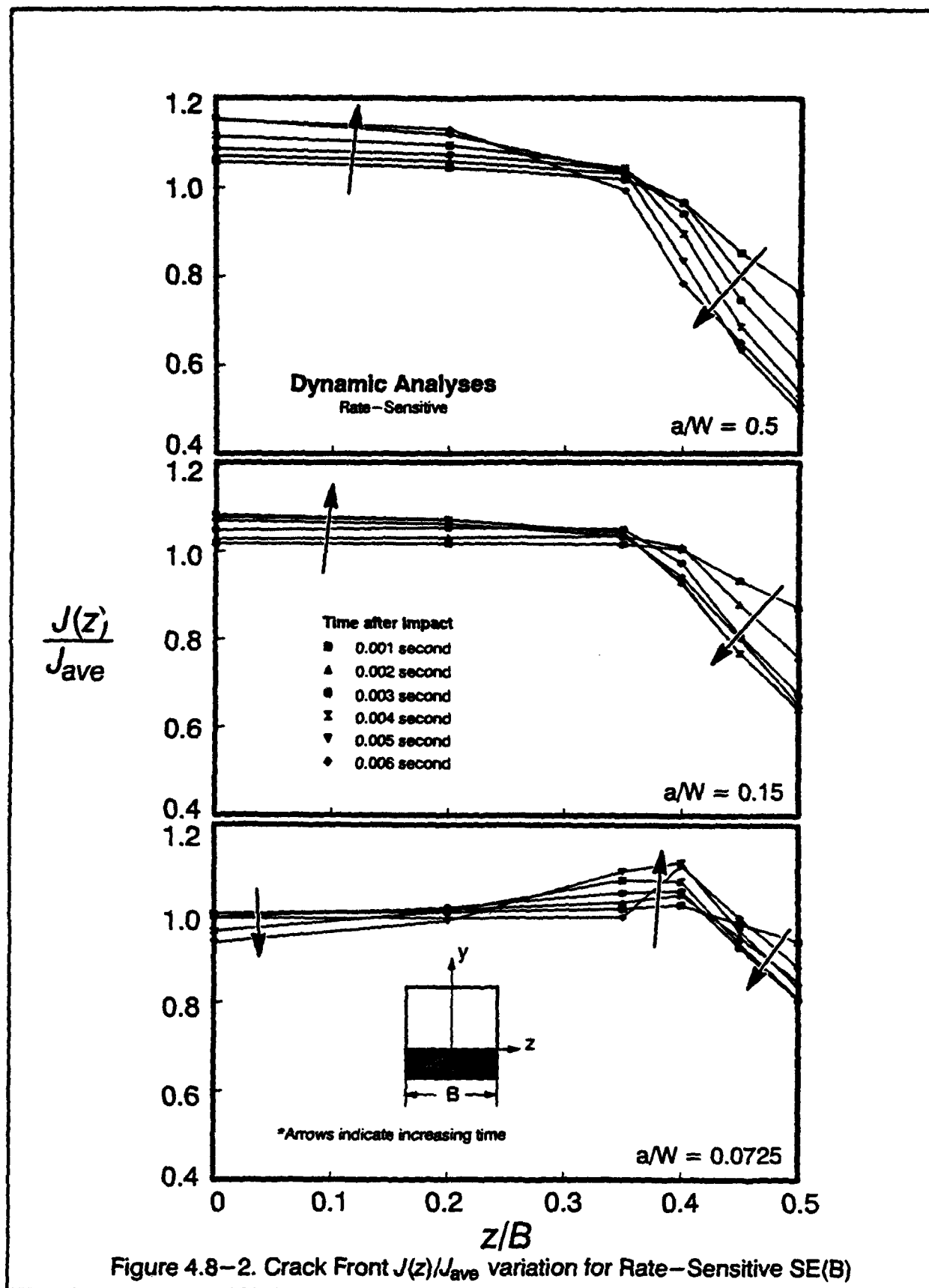
Figure 4.8–2. Crack Front $J(z)/J_{ave}$ variation for Rate–Sensitive SE(B)
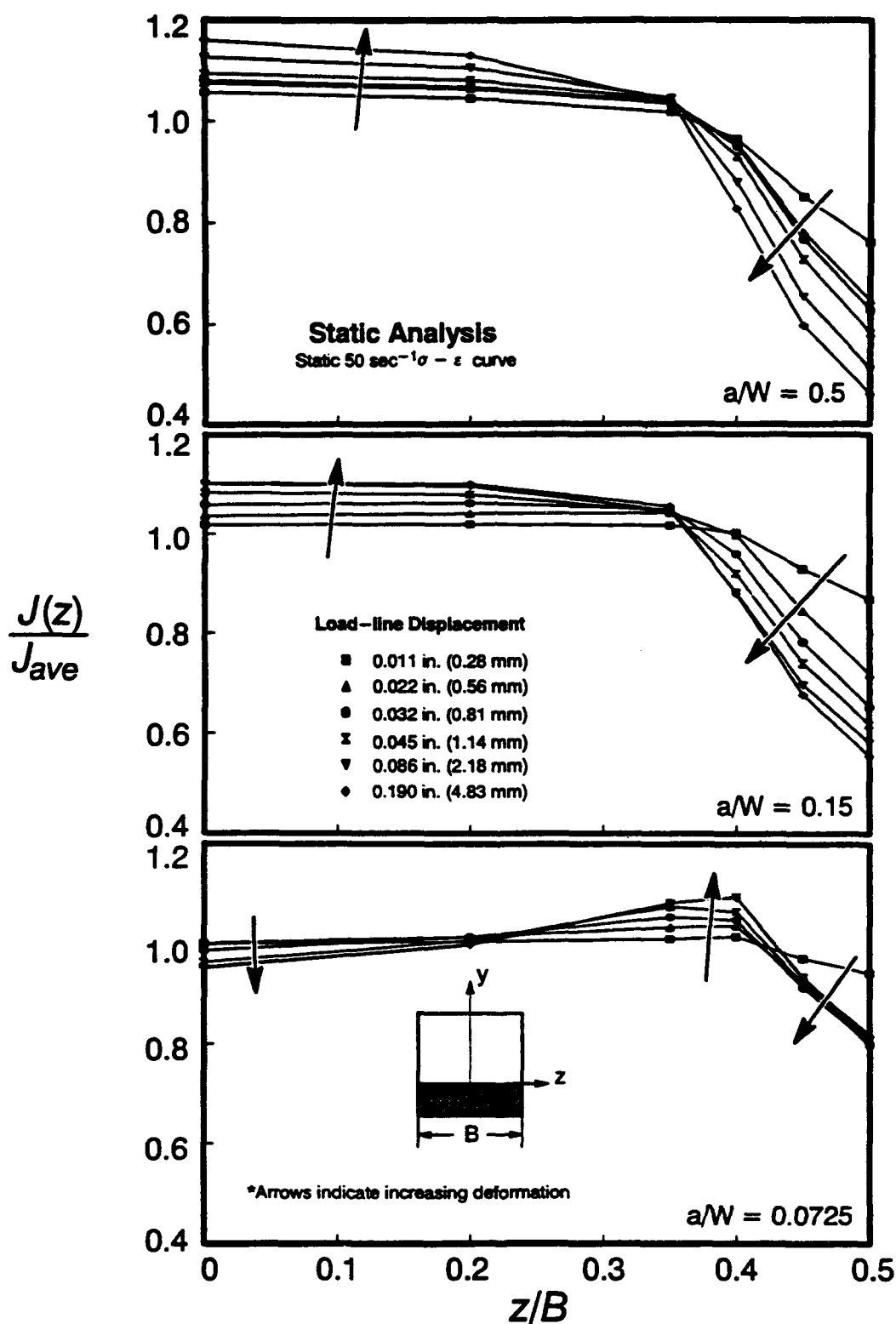
Figure 4.8–3. Crack Front $J(z)/J_{ave}$ Variation for Baseline Static Analysis
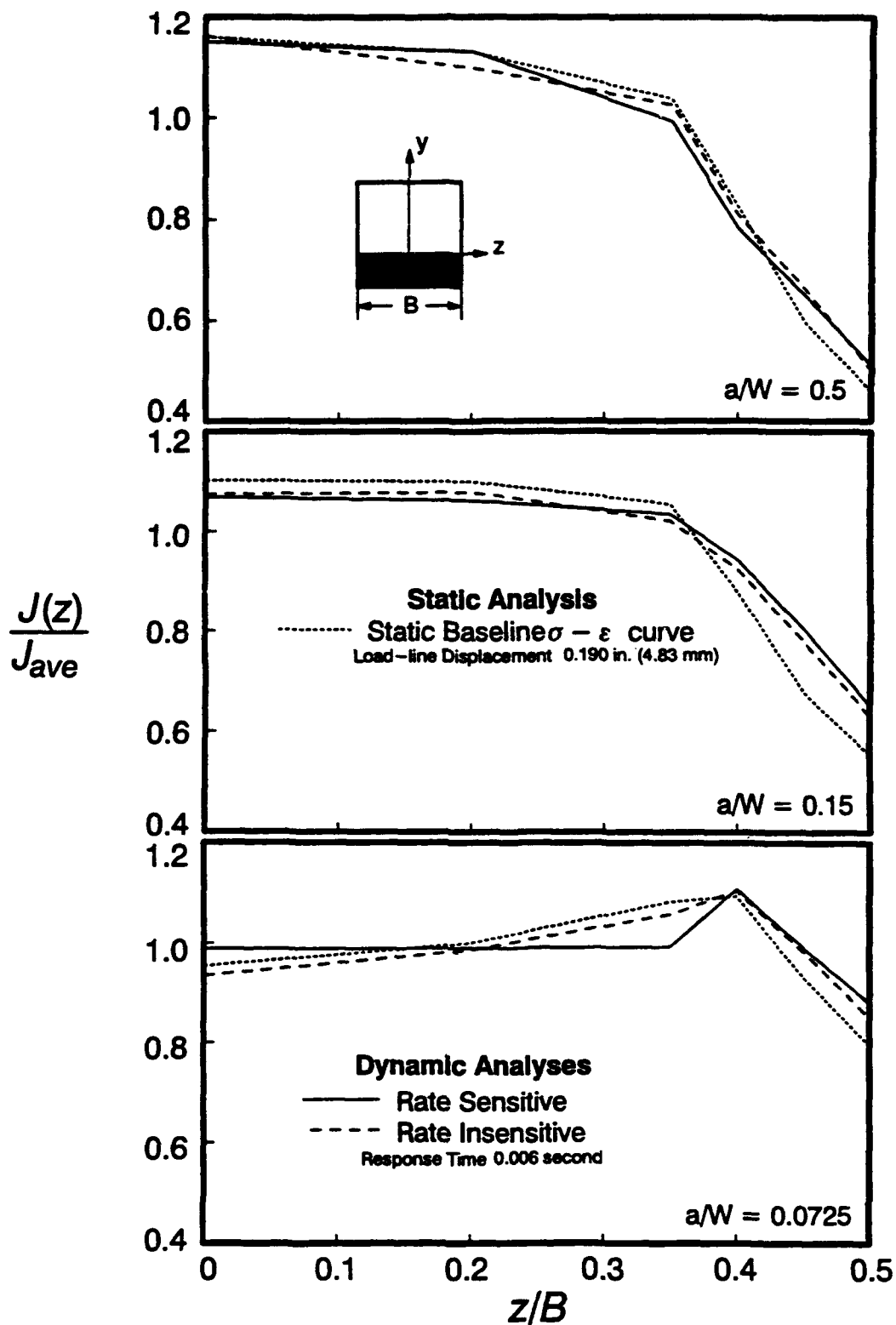
Figure 4.8−4. Crack Front $J(z)/J_{ave}$ Variation at End of Analysis.

153

free surface decreases. As a result, the distribution of *J* across the crack front becomes highly non—uniform as deformation increases.

The shallow crack specimen, however, shows a more uniform distribution of *J* across the crack front. The plastic zone impinges on the bottom surface of the specimen over the full thickness. Thus, the loss of constraint is relatively uniform through the thickness. Consequently the *J* distribution is more uniform than the deep and medium crack specimens.

4.9 Crack Tip Opening Displacements (CTOD)

Figure 1.2—2 shows the definition employed for the Crack—Tip Opening Displacement (CTOD), δ_t. Under load, the initially coincident nodes of the collapsed elements at the crack tip displace in the manner indicated in Fig. 4.1—5. The CTOD is computed by extending a line 45° line from the crack tip and determining the intersection on the deformed crack profile. The opening displacement of this intersection point is one—half of the CTOD. The arrangement of five element layers through the thickness in the finite element models defines six nodal planes that intersect the crack front. CTOD values are computed at each of these nodal planes. A weighted average of the six crack—front CTODs defines the average through—thickness value. (Each nodal—plane value of CTOD is assigned a weight according to it's relative length along the crack front.)

Figure 4.9—1 shows the average CTODs for the different specimens for the dynamic analyses. As shown in the figure, the medium crack exhibits the largest CTOD values, followed by the deep crack and the shallow crack SE(B) specimens. When plotted as a function of response time, the CTODs do not decrease monotonically with decreasing crack depth. For each specimen, the CTOD values at a given response time (or load—line displacement) are relatively independent of rate—sensitivity. The shallow crack specimen exhibits a small increase in the CTOD values for the rate—insensitive material model.

From Dodds [31], Eqn. 1.2—4 is recast as follows:

$$J = m\sigma_{fl}\delta_t \qquad (4.9-1)$$

where σ_{fl} is the flow stress, taken as the average of the yield and ultimate stress of the material, and m is the dimensionless proportionality factor that linearly relates the CTOD to the *J*—integral. By using σ_{fl} instead of the yield stress (Eqn. 1.2—4), m values become relatively independent of the strain hardening. The m factor indicates the extent of crack tip deformation that
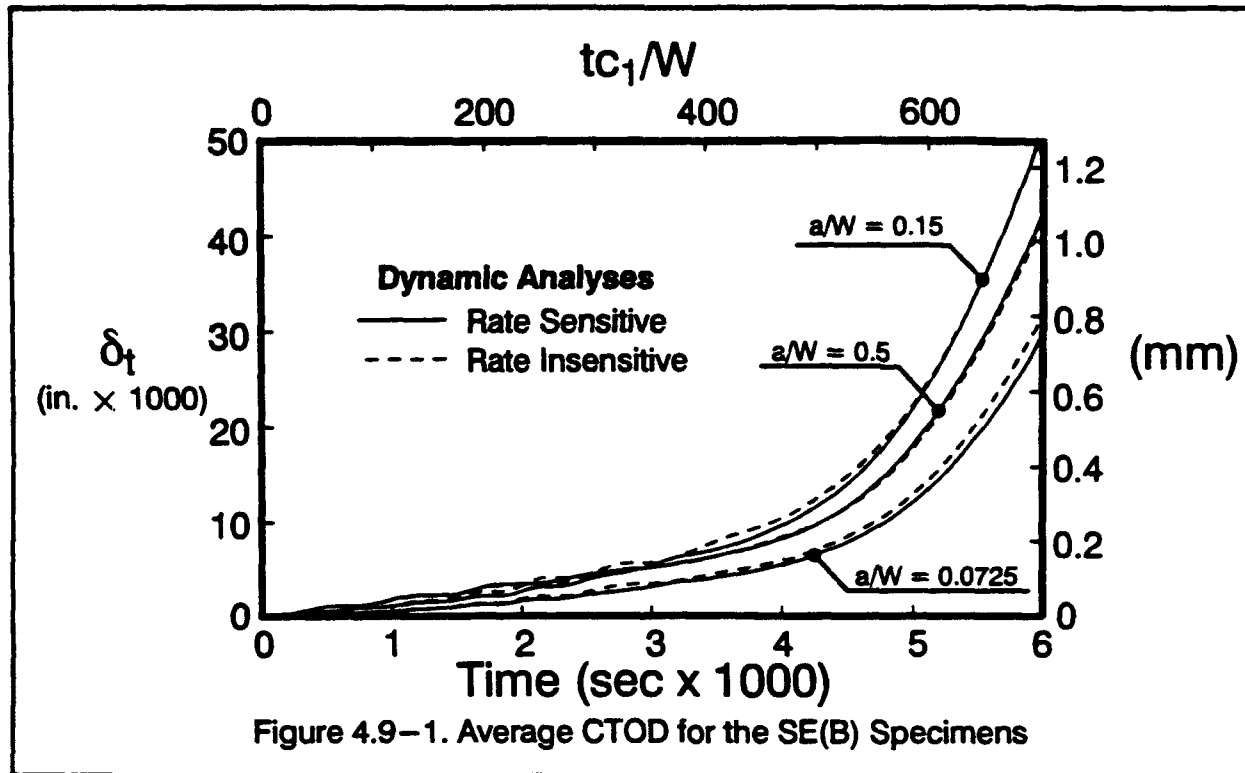
Figure 4.9−1. Average CTOD for the SE(B) Specimens

results from the applied J and is a weak measure of stress triaxiality. A larger value of m means that more J is needed to achieve the same δ_t, and thus indicates an increase in constraint at the crack tip [31,94]. An average m for the SE(B) specimens is computed using average values for J and δ_t in Eqn. 4.9−1.

Figure 4.9−2 shows the relationship of average J−values with average δ_t for the dynamic and static analyses (with the baseline stress−strain curve). The linear relationship between the δ_t and J confirm the validity of Eqn. 4.9−1. Results for the static analyses match the rate−insensitive dynamic analyses well. The slope of the curves in Fig. 4.9−2 correspond to $m\sigma_{fl}$. (Thus the higher the slope in the figure, the higher the near−tip constraint.)

Table 4.9−1 summarizes values of m from the analyses in Fig. 4.9−2. A flow stress of 75.6 ksi, corresponding to the average of the yield and ultimate stress for A533B steel (see Table 2.3−1), is used for evaluation of m. Nearly identical values of m are obtained for the static and the rate−insensitive dynamic analyses, indicating similar constraint. The strain rate sensitive material model elevates the constraint parameter m for all three specimens. The percentage elevation of m as a percentage of the rate−insensitive results is also included in the table. Kirk [61] reports m values for plane−strain SE(B) finite element models using material models with different hardening characteristics. For a hardening exponent of $n = 10$, the corresponding m values are: 1.79, 1.57 and 1.51 for the deep, medium and shallow crack, respectively. The

155
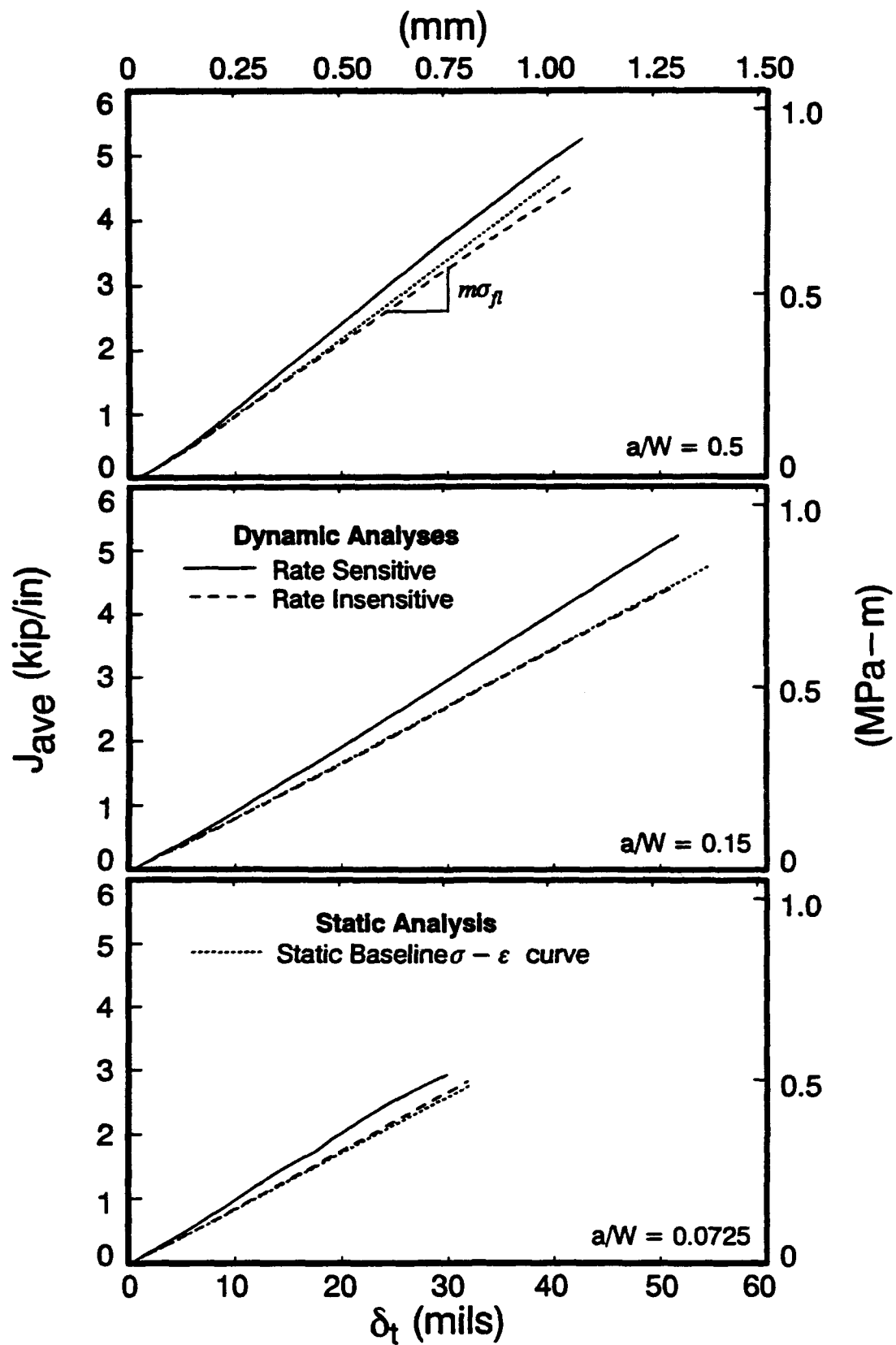
Figure 4.9–2. J_{ave} vs. Average δ_t for the Three SE(B) Specimens.

	Deep Crack	Medium Crack	Shallow Crack
Rate Sensitive (% elevation)	1.628 (13.8)	1.340 (16.3)	1.301 (10.7)
Rate Insensitive	1.430	1.141	1.175
Quasi–Static	1.434	1.152	1.136

Table 4.9–1 m Values for the SE(B) Analyses.

plane–strain values are not surprisingly larger than the 3–D values in Table 4.9–1. Dodds [31] computed the m variation across the crack front for a quasi–static SE(B) specimen with the same dimensions as the medium crack in this study. The low hardening material resulted in an average m between 1.1 and 1.2, similar to results reported in Table 4.9–1.

The larger m values for the rate sensitive material can be interpreted as an increase in the apparent flow stress of the material at the crack tip. Using the m for the rate–insensitive dynamic analyses, the apparent flow stresses for the rate–sensitive results are: 85.99, 87.88, 83.64 ksi for the deep, medium and shallow crack, respectively. These values are approximately equal to the apparent yield stress of the crack–tip stress–strain curve for the rate–sensitive analyses as shown in Fig. 4.7–4.

The distributions of J and δ_t determine the constraint parameter m across the crack front. Figure 4.9–3 shows m across the crack front for the three specimens. The rate–insensitive material model closely matches the m values for the static analyses. Rate sensitivity elevates the constraint parameter in a nearly uniform manner across the crack front. This elevation is approximately 0.2 for all three specimens.

4.10 Stresses Near the Crack Front

This section examines stresses near the crack front in the SE(B) specimens for the static and dynamic analyses. The levels of mesh refinement used in these analyses do not permit the detailed resolution of near tip fields of the type reported in [6,30,80,81]. Due to the large displacement formulation of the elements, crack tip blunting affects the stress distributions in the near tip elements (for the dynamic analyses). However, for material that is sufficiently removed from the crack tip (r = several × the CTOD), the blunting effects diminish rapidly. Cleavage fracture is controlled by stresses in the *fracture process zone*, defined as a finite volume ahead of the crack tip, extending a distance of approximately 2 to 6 δ_t ahead of the tip. The significance of stress distributions in the fracture process zone and their direct relationship to the cleavage fracture resistance are described in [6,30].

157

Figure 4.9–3. Variation of *m* Across Crack Front.
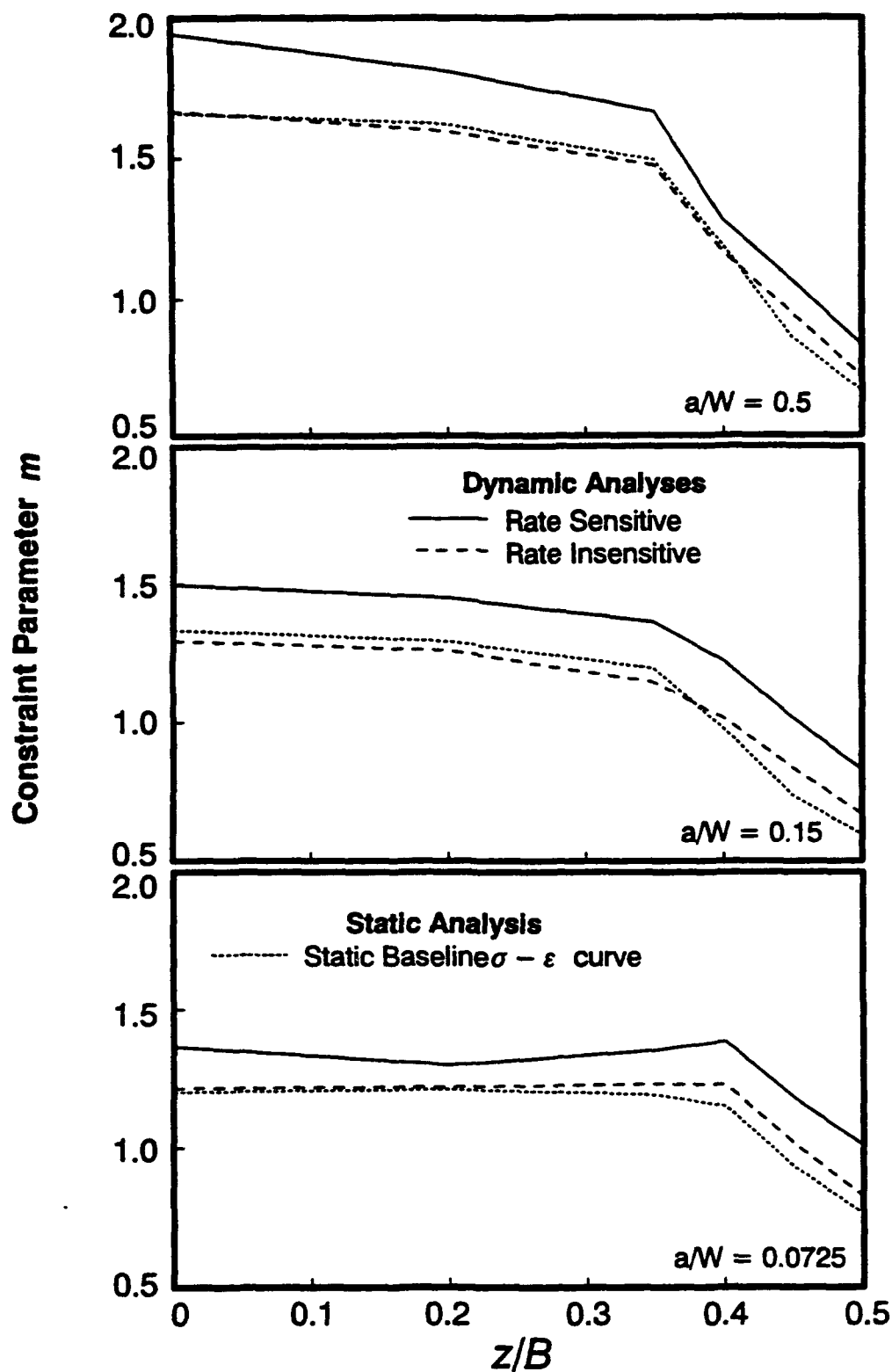
Figure 4.10−1 shows the innermost four rings of elements surrounding the crack tip. The stresses from the shaded row of elements in the figure are used to compare the crack front stress distributions for the three SE(B) specimens. The location of these elements, removed one element−ring from the crack tip element, reduces the blunting effect on the stress fields. The one−point integration scheme of the elements defines a stress sampling point at a distance of 0.0529 inches (1.32 mm) from the crack tip as shown in the figure. This integration point lies within the fracture process zone for cleavage over most of the response of all three SE(B) specimens.
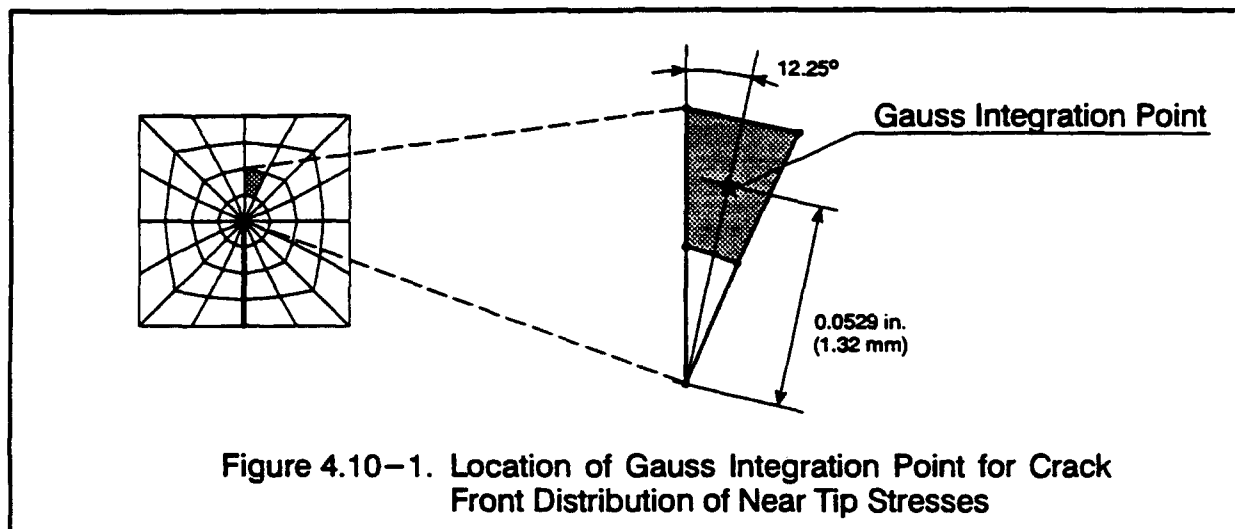
Figure 4.10−1. Location of Gauss Integration Point for Crack Front Distribution of Near Tip Stresses

Figures 4.10−2, 4.10−3 and 4.10−4 show the distribution of stresses for the deep, medium and shallow crack specimens, respectively. The figures show the opening mode, mean and von Mises stresses (labelled $\sigma_{\theta\theta}$, σ_m, and σ_{VM} respectively) across the specimen thickness for the row of elements shown in Fig. 4.10−1. The stresses in the figures are normalized with respect to the static yield stress of 64.5 ksi (445 MPa); the crack front location is normalized by the specimen thickness, B. (Due to symmetry, only one−half of the distributions are shown, $z/B=0.0$ at centerplane, and $z/B=0.5$ at the free surface). Six distributions are given for the dynamic analyses, which correspond to 0.001s time increments. Six distributions are given for the static analyses conducted with the baseline stress−strain curve. The Δ_{LLD} shown for each static distribution matches the Δ_{LLD} of the dynamic distribution at the 0.001s intervals.

These figures lead to the following observations:

1) Rate sensitivity elevates the opening mode stresses, $\sigma_{\theta\theta}$, for all three specimens. At the end of the analyses, this elevation is approximately 18%, 23% and 17% for the deep, medium and shallow crack, respectively.

159
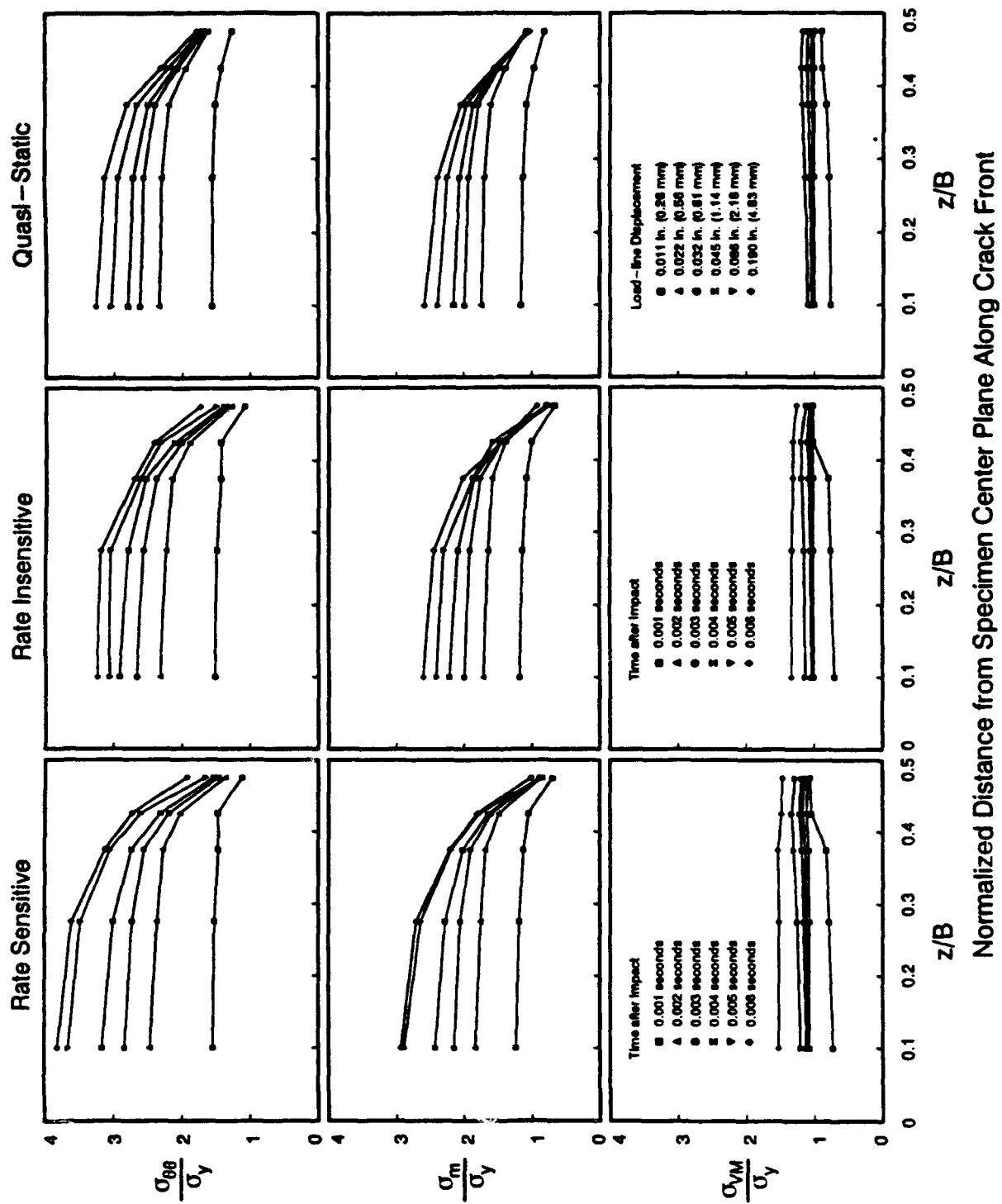
Figure 4.10-2. Normalized Crack-Front Stresses for the Deep Crack,
a/W = 0.5, SE(B) Specimen.
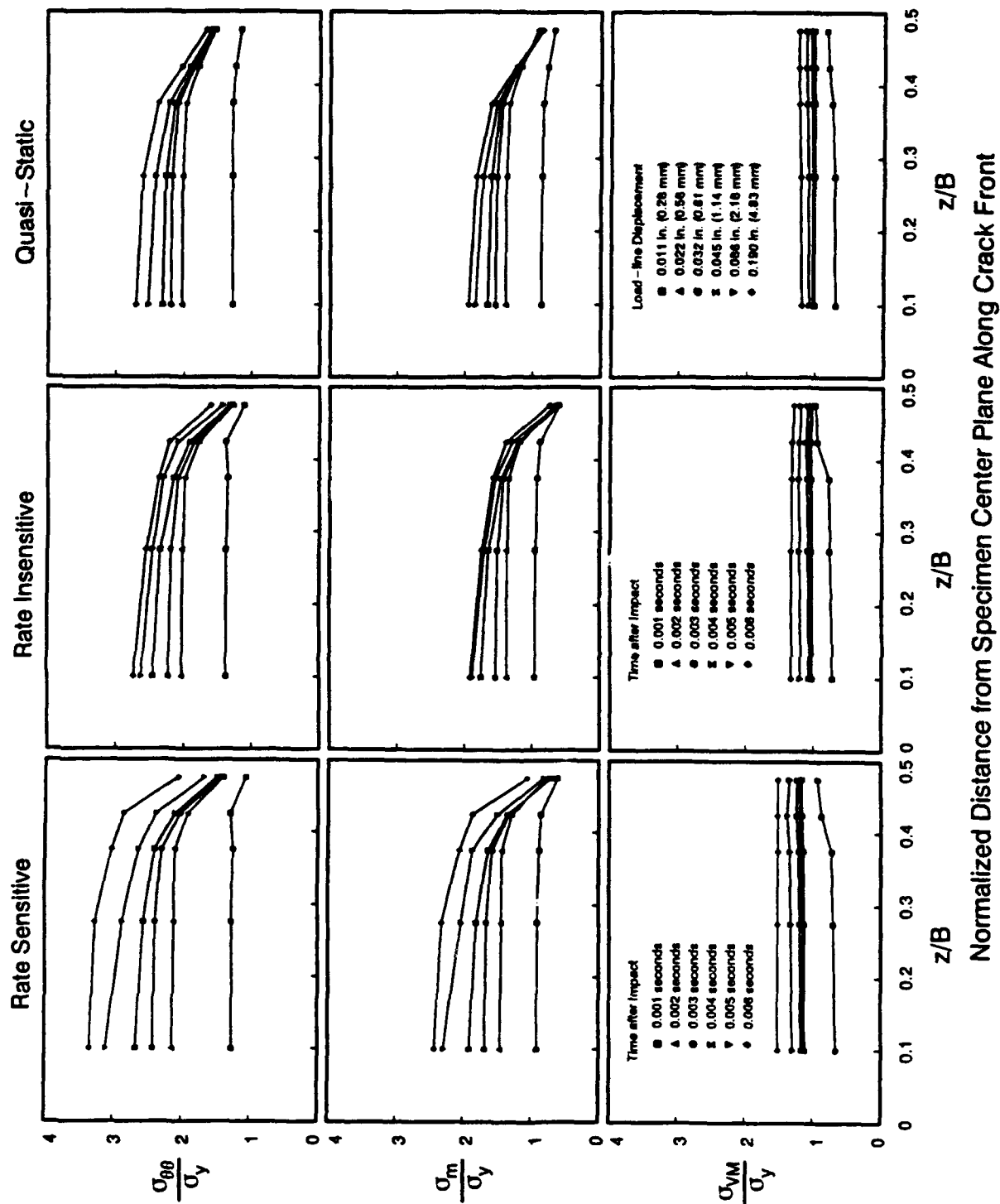
Figure 4.10-3. Normalized Crack-Front Stresses for the Medium Crack, a/W = 0.15, SE(B) Specimen.
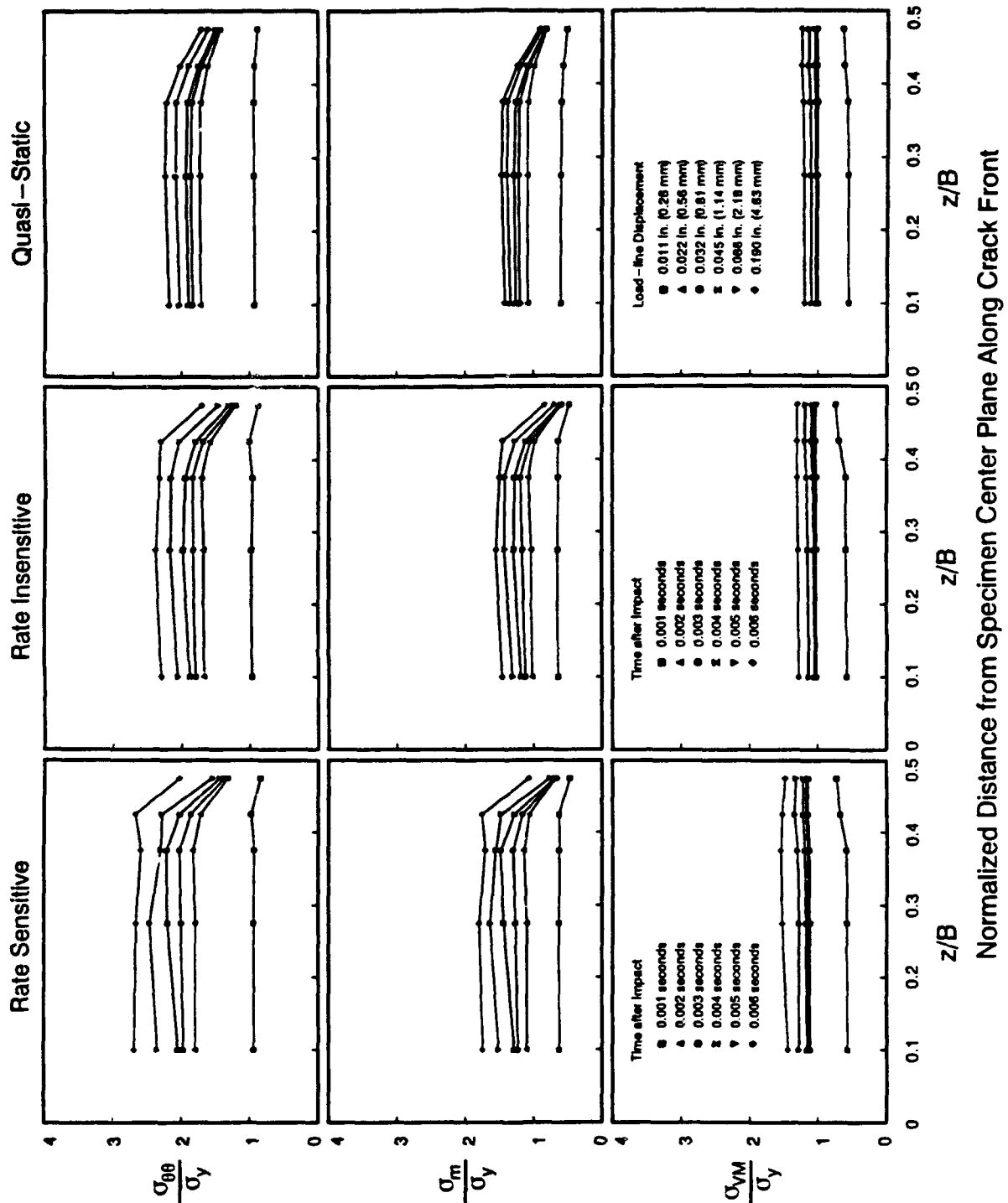
Figure 4.10–4. Normalized Crack–Front Stresses for the Shallow Crack, a/W = 0.0725, SE(B) Specimen.

2) For all three specimens, the crack−front stress distributions of the static analyses match the rate−insensitive dynamic analyses well. Stress distributions are thus not influenced by inertial effects for all three specimens.

3) Initially, the von Mises stresses are slightly elevated near the free surface for all three specimens. At increased levels of plastic deformation, the von Mises stress distribution becomes approximately constant across the crack front. The maximum amplitude of the normalized von Mises stresses is 1.2 for the rate−insensitive and 1.5 for the rate−sensitive material models.

4) Crack front variations of the opening mode stress and the mean stress become more uniform with decreasing a/W ratio.

5) Both the opening mode stress and the mean stress distribution for the rate−sensitive shallow crack specimen show a local peak near $z/B=0.4$ at 0.0006 seconds. This trend is also observed in the crack front distribution of $J(z)$ shown in Fig. 4.8−4.

Figure 4.10−5 shows the opening mode stresses along $\theta = 0$ on the centerplane as a function of normalized radial distance, r, from the crack tip. Results for two loading levels of the three specimens are shown, $J \cong 1.5$ k/in, and $J \cong 3.0$k/in (0.263 MPa−m and 0.525 MPa−m). The factor J/σ_y normalizes the radial distance. The plots also show the small−scale yielding (SSY) stresses for a Ramberg−Osgood material under plane−strain conditions with a hardening exponent of 10 [6]. (Figure 4.7−10 shows the A533B steel quasi−static stress−strain curve together with a corresponding Ramberg−Osgood material model with a hardening exponent of 10). Under small scale yielding conditions, J uniquely characterizes the near−tip stress fields. The difference between the SSY stresses and the actual opening mode stresses form the basis for the two parameter $J-Q$ description of near−tip fields. O'dowd and Shih [80,81] showed that the opening mode stresses in large scale yielding can be expressed as a hydrostatic stress field superimposed onto the SSY solution. The operational value of Q is defined as the difference between the actual opening mode stresses (normalized by the yield stress) and the SSY solution at $r/(J/\sigma_y)=2$.

The opening mode stresses for the medium and shallow crack specimens show distributions similar to the SSY distributions. For the shallow crack, the value for Q is approximately −1.3 for J values greater than 1.5 k/in for both the rate insensitive and quasi−static distributions. For the shallow crack specimen rate sensitivity makes Q less negative by approximately 20%. The medium crack stress distributions give $Q=-0.75$ for $J=1.5$ k/in, and $Q=-1.0$ for $J=3.0$ k/in for both the rate insensitive and quasi−static analyses. For the medium crack specimen, rate−sensitivity makes Q less negative by approximately 25%. The stresses for the deep crack specimens reflect the very strong bending gradients in the ligament at high load levels. Q cannot be calculated for the deep crack specimen due to the lack of similarity of the stress distributions with the SSY solution.
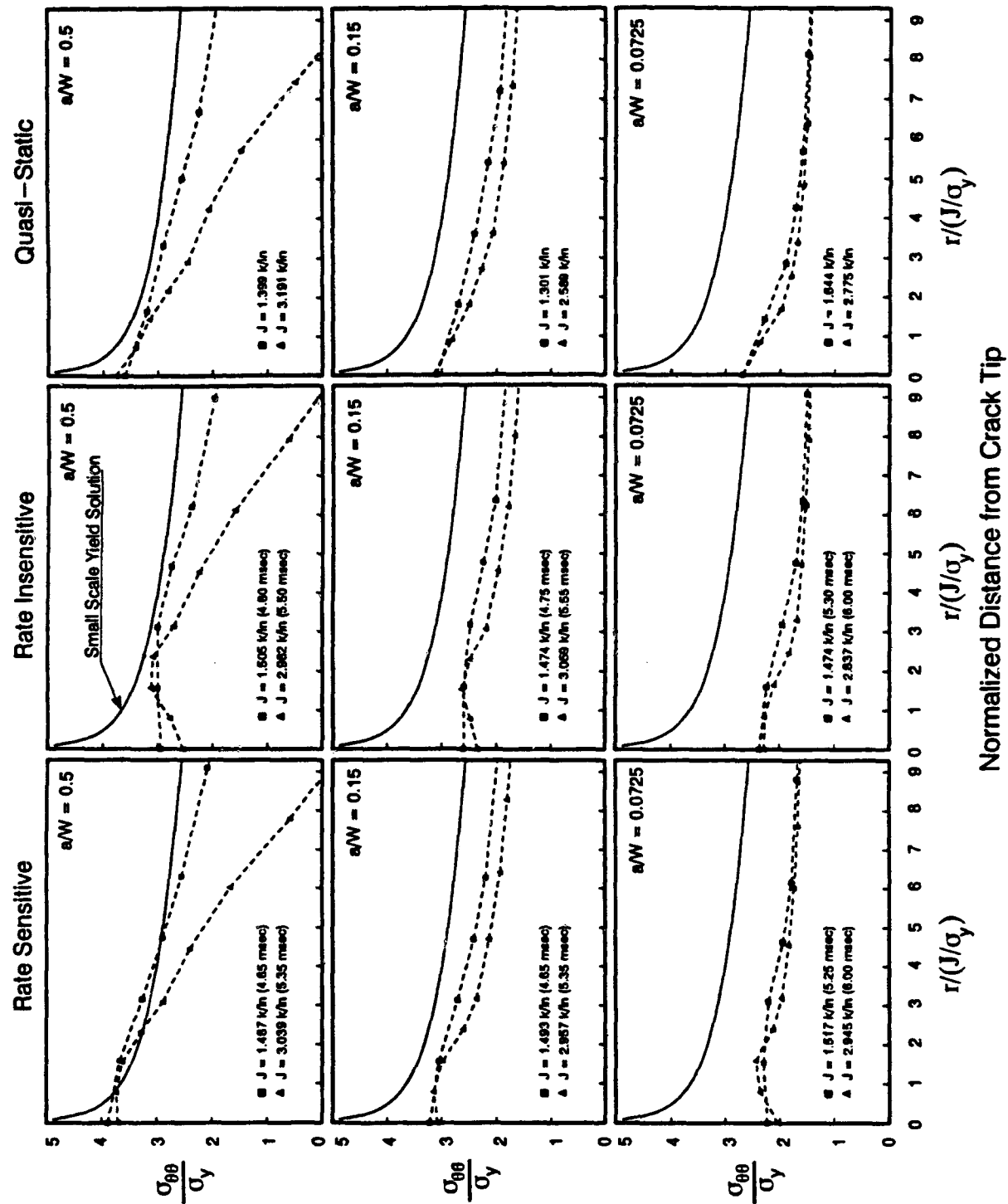
Figure 4.10-5. Normalized Opening Mode Stresses on the Center Plane.

164

4.11 Significance of the J_{acc} Term

Equations 2.1−5 through 2.1−7 describe the contributions to the J−integral for dynamic loading. J_1 and J_2 are independent of inertial effects and their sum is the J−integral for static loading. Inertial effects enter the computation of J through J_3:

$$J_3 = -\int_V \left(T\frac{\partial q_k}{\partial x_k} - \varrho\frac{\partial^2 u_i}{\partial t^2}\frac{\partial u_i}{\partial x_k}q_k + \varrho\frac{\partial u_i}{\partial t}\frac{\partial^2 u_i}{\partial t\partial x_k}q_k \right) dV \qquad (4.11-1)$$

The first and third term of Eqn. 4.11−1 arise from the kinetic energy and the explicit derivative of the kinetic energy in the integration domain, respectively. These two terms become significant for situations that occur with unstable crack propagation where large velocities and large velocity gradients exist near the crack tip [71,70]. For the non−propagating cracks investigated in this study, these two terms are less than 0.1% of J_3. For the present study, the second term in Eqn. 4.11−1, denoted J_{acc}, dominates the value of J_3:

$$J_{acc} = \int_V \varrho\frac{\partial^2 u_i}{\partial t^2}\frac{\partial u_i}{\partial x_k}q_k \ dV \qquad (4.11-2)$$

Figure 4.11−1 shows the average through thickness value of J_{acc} for the domain labelled *Ring 4* in Fig. 4.7−1. As shown in the figure, J_{acc} remains near zero for the initial 0.003 seconds in all analyses. After 0.003 seconds, J_{acc} shows relatively large oscillations. However, the magnitudes of J_{acc} are extremely small compared to the total J−integral (see Fig. 4.7−3). For all analyses, the contribution of J_{acc} to J_{ave} is less than 0.1% for most of the response. Thus for loading rates typical of those in drop tower tests, accurate computation of J−values does not require the J_3 term. This confirms the quasi−static nature of the experiment with respect to the computation of J and explains the good agreement between static (baseline stress−strain curve) and dynamic rate−insensitive analyses in this study.

Very early in the response ($t < 1 \times 10^{-4}$ s), when discrete stress waves are still prevalent, J_{acc} contributes significantly to the total J−integral. In particular, for times less than 1×10^{-4} s, J_{acc} is *needed* to obtain domain independence of the J−values. In addition to the four domains shown in Fig. 4.7−1, six additional (larger) domains are defined to examine the domain dependance of the J values. The vertical distance from the crack tip to the domain edge defines the domain radius and is used to quantify the domain size. Figure 4.11−2 illustrates the largest domain studied with the corresponding domain radius. The distribution of the q−function follows the form described in Section 4.7.1. A unit value of q is applied at every node that resides on the domain interior. The q−value for all other nodes is set to zero.

Figure 4.11-1. $\bar{J}_{acc}$ for the SE(B) Specimens
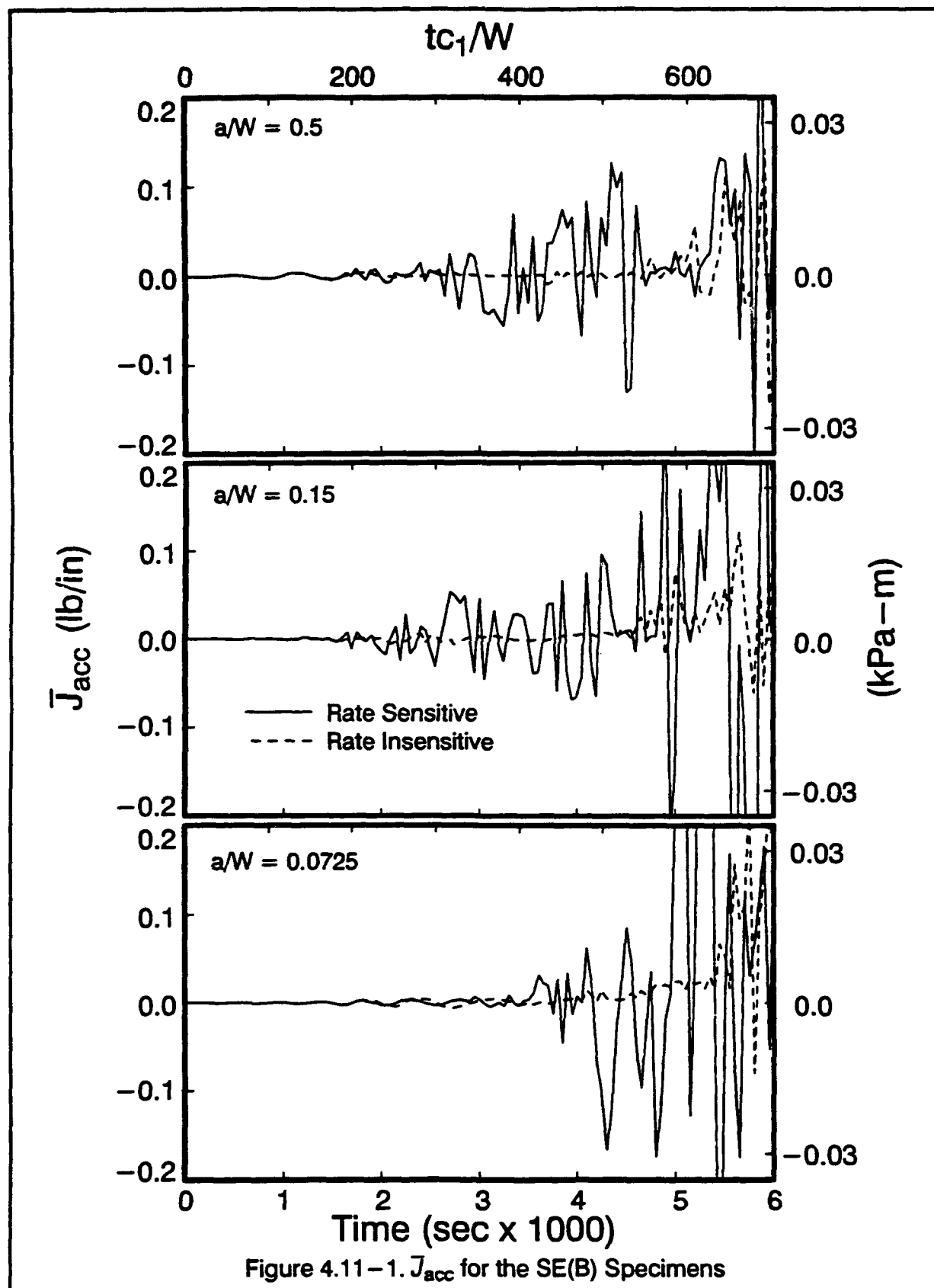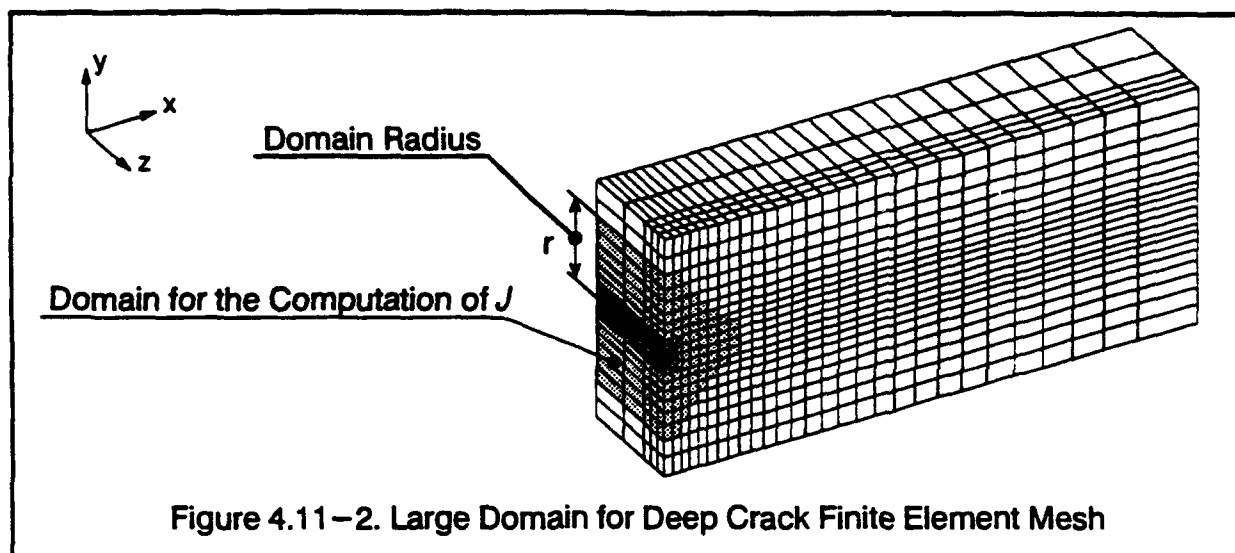
Figure 4.11-2. Large Domain for Deep Crack Finite Element Mesh

Figure 4.11-3 shows the normalized values of J_1, (defined in Eqn. 2.1-5), J_{acc}, and the sum: $J_1 + J_{acc}$, as a function of normalized domain radius for the rate-sensitive deep-crack SE(B) analysis. The values of J_{acc} and J_1 correspond to response times of 0.02 to 0.07 milli-seconds. The the specimen is predominantly elastic over these response times. The average of all the domains (excluding the domain that contains crack tip elements only, i.e. *Ring 1* in figure 4.7-1) of J_{fem} (Eqn. 4.7-1) is used as J_{ave} for the normalization. The J-value for the specimen at these response times is less than 0.01 lb/in (a negligible value for most practical applications). The medium and the shallow crack SE(B) specimens show similar trends and are not repeated here.

As shown in the figure, J_1 exhibits domain dependance at these early response times. At 0.02 milli-seconds, J_1 is negative for the larger domains, and approaches the domain independent value with decreasing domain radius. J_{acc} exhibits the opposite behavior, and approaches zero with decreasing domain radius. The sum of these two values is domain independent. At 0.05 milli-seconds, J_1 alone is equal to the total J-integral for all domains. The use of small domains near the crack tip provides accurate J values using J_1 alone. J_1 from the smallest four domains predicts the total J-integral accurately by as early as 0.03 milli-seconds. Similar path dependence of J_1 is found in [76,98] for the case of thermal loadings.

4.12 Summary

The detailed results for six dynamic analyses and six static analyses have been discussed in this chapter. The static analyses provide a reference solution to assess the relative importance of strain rate and inertial effects in the dynamic analyses. Loading rates imposed in the dynam-

167
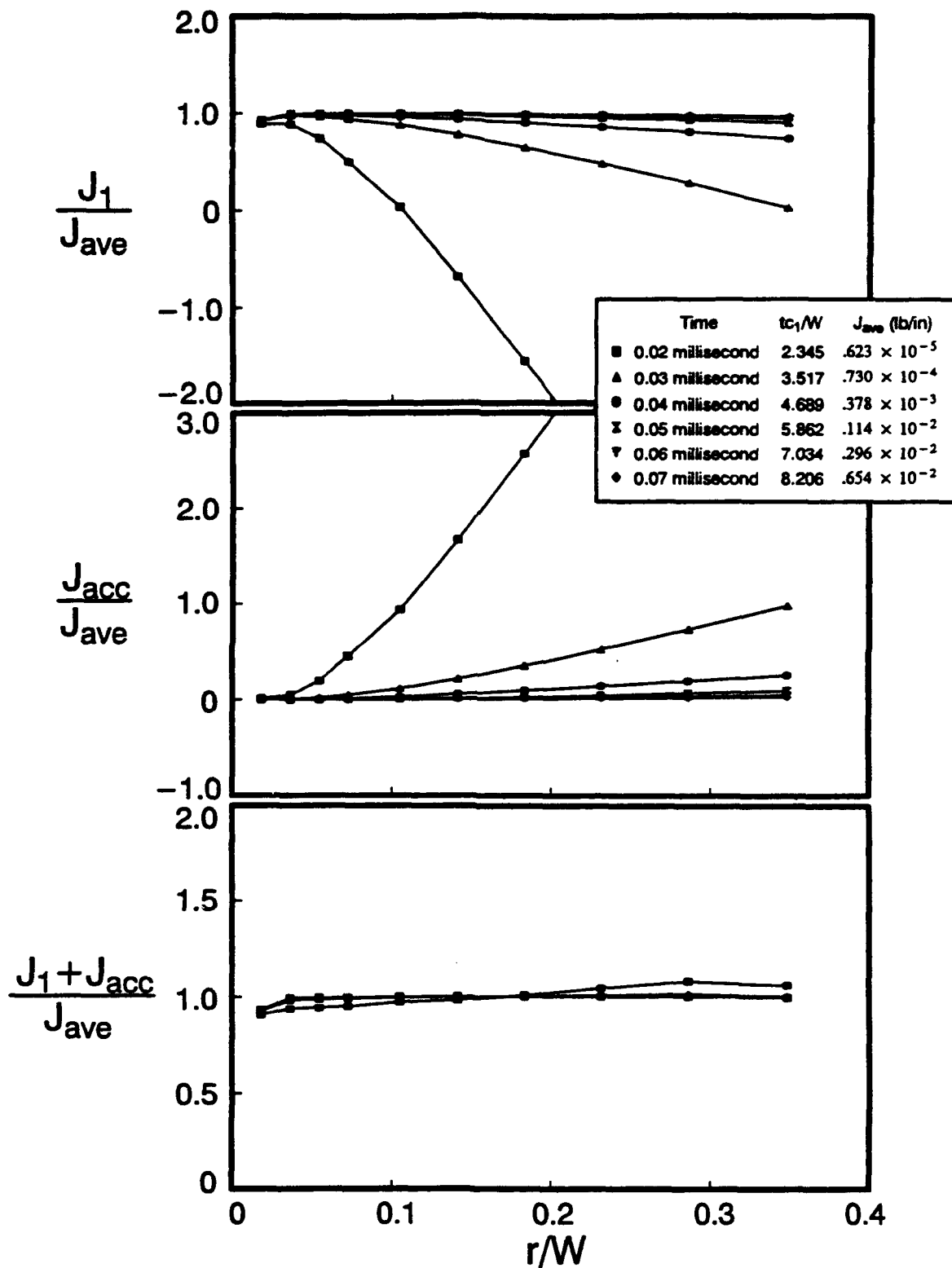
Figure 4.11−3. Domain Radius Dependence of *J* for the Deep Crack
Rate Sensitive SE(B) Specimen.

ic analyses are comparable to the rates routinely found in drop tower testing. The following items summarize the important observations and conclusions obtained from these analyses:

1) A methodology is presented and verified to load the dynamic models which produces load–displacement histories measured experimentally. This method involves two analyses: one in which a displacement response is directly applied to the specimen, and a second analysis in which the extracted nodal loads from the first analysis are smoothed and then applied as a pressure loading to the detailed model for the specimen.

2) The transition time occurs while the specimen remains essentially elastic. The transition time is a function of the fundamental elastic period of the specimen. For loading rates considered, (and up to an order of magnitude higher), the transition time is $-0.4 \times$ the first period of vibration.

3) Strain rates of up to 50/sec occur near the crack tip in the specimens at the imposed loading rate of 100 inches/sec.

4) Plasticity remains confined to the ligament for the deep crack specimen. For the shallow crack specimen, the plastic zone grows through the entire width of the specimen, and impinges on the quarter–span gage locations. The low hardening A533B steel restricts further growth of the plastic zone in the shallow crack specimen after plasticity has spread through the width of the specimen.

5) Three techniques to infer the applied load are studied: quarter–span strains, end reactions and ligament moments. All three methods underestimate the actual applied load toward the end of the response due to the large increase in kinetic energy of the specimen. Longitudinal strains for the shallow crack specimen remain sufficiently linear at the quarter–span gage locations to enable accurate load estimation from measured values.

6) The static formula to compute J from applied work with η_p values derived from plane–strain models produces large (>20%) errors in the medium and shallow crack specimens. However, the static J formula produces accurate results (<5% errors) when η_p values derived from three–dimensional (static and dynamic) analyses are used. Accuracy of the static formula is improved even further when modified to relate the total energy absorbed by the specimen to J. For response times after approximately 2.5 × the transition time, inertial effects diminish sufficiently for the static formula to apply. This time is approximately equal to the first period of each specimen.

7) The crack–front distribution of J, normalized by the through thickness average J, is independent of strain rate for the specimens in this study. The deep and medium crack specimens have a local maximum of J at the centerplane. For the shallow crack specimens, however, the local maximum J occurs at a small distance (10% B) from the free surface.

8) Rate sensitivity elevates crack–front J–values 17% for the deep and shallow crack specimen, but only 5% for the shallow crack specimen. Rate sensitivity in the shallow crack specimen elevates the stresses in the ligament sufficiently so that the increase in stiffness forces deformation away from the crackplane.

169

9) Rate sensitivity has little effect on the CTOD for the deep and medium crack specimens, but it decreases the CTOD for the shallow crack specimen. This is due to the increase in stiffness that results with the rate–sensitive material for the shallow crack specimen.

10) At the same response time, the medium crack specimen exhibits the largest CTOD, followed by the deep crack specimen, and finally the shallow crack specimen. However, the constraint parameter m increases monotonically with increasing a/W.

11) Opening mode stresses ahead of the crack tip obtained for the dynamic analyses reveal the same trends obtained from static analyses. The deep crack specimen maintains a high level of constraint (and thus high stresses) well into the fully plastic regime. The medium and shallow crack specimens reveal significant reductions of crack tip stresses under increased plastic deformation (loss of constraint). Rate sensitivity partially restores the constraint and elevates crack–tip stresses. Estimates for the constraint parameter Q are given for the shallow and medium crack specimens. The strong bending field of the deep crack specimen makes Q radially dependent at high loads. Rate sensitivity decreases the amplitude of Q [80] 20% for the medium crack and 25% for the shallow crack specimen.

12) At the same response time, the opening mode stresses ahead of the crack tip increase with increasing a/W. Elevation of the opening mode stresses is due to increased constraint against plastic flow as shown by similar increases in the hydrostatic stress state.

13) The material acceleration component of the J–integral is negligible except very early in the response. At response times less than 5×10^{-5} s, the acceleration term of the J–integral is necessary to achieve domain independence.

5 Summary, Conclusions and Recommendations

This study extends the understanding of SE(B) fracture specimens subjected to loading rates characteristic of drop tower testing through the use of advanced finite element techniques. Three–dimensional models of three different specimen configurations, $a/W = 0.5$, 0.15, 0.0725, are analyzed to investigate constraint effects. Static analyses provide baseline results from which inertial effects are assessed. Dynamic analyses with a rate–insensitive material model provide baseline results for the assessment of strain rate effects. The detailed evaluation of dynamic effects including viscoplasticity, inertia, and the acceleration component of the J–integral, significantly improves our understanding of impact fracture tests.

Key aspects and conclusions of this study include:

- Computational techniques are implemented that compute efficiently the dynamic, viscoplastic behavior of the SE(B) specimens. Explicit time integration is used to evaluate the dynamic response. The Bodner–Partom material model is implemented for rate–sensitivity. A one point domain integration technique is used for J calculations.

- Transition time concepts are evaluated for the three SE(B) geometries. At response times after 2.5 × the transition time, the static formula to compute J from work on the ligament applies. Numerical results demonstrate that this limit corresponds to the elastic period of the specimen.

- For the medium and shallow crack specimens, use of η_p derived from 2–D analyses leads to overpredictions of the applied J values. Accurate computation of J from static formulas requires the use of plastic proportionality factors derived from results of 3–D finite element models.

- Strain–rate sensitivity elevates the loading levels and the opening mode stresses for all three specimens. Rate sensitivity also elevates the applied J and constraint parameter m for all three specimens, however, this effect is less pronounced in the shallow crack specimen. Rate sensitivity elevates the ligament stresses in the shallow crack specimen sufficiently to force deformation away from the crack tip, thereby lowering the applied J.

- The inertial component of J is negligible (less than 0.1% of the total J) for the three specimens except very early (< 0.05 milli–sec) in the response when this component is needed to maintain domain independence of J.

- Oscillations of loads inferred from strain gage readings and load–line displacements occur due to the inertial response of the specimen. However, the accuracy of J values computed from the static formulas is not significantly affected.

- Constraint loss that occurs in the medium and shallow crack specimens decreases the opening mode stresses well below the SSY solution. This leads to the well known elevation in cleavage fracture toughness for shallow notch SE(B) specimens. Crack front distribution of J and CTOD become more uniform with decreasing a/W.

171

Each of the above items is summarized in greater detail in this chapter. The chapter concludes with recommendations for further research.

5.1 Summary of Computational Techniques

The following computational techniques support the detailed examination of fracture quantities reported in this study:

1) Explicit time integration coupled with one–point Gaussian integration of 8–node, iso-parametric elements is used for the efficient computation and monitoring of both discrete stress waves and global dynamic behavior of the SE(B) specimens.

2) Numerical integration techniques are developed that compute accurately the applied J values through a domain integral approach.

3) The Bodner–Partom viscoplastic model is implemented to characterize the strain–rate sensitivity of medium strength pressure vessel steels. A newly developed iterative technique to integrate the stiff rate equations maintains the overall efficiency of one–point Gaussian integrated elements.

4) A procedure is developed that reproduces accurately the desired load–line displacement histories for all specimens.

Essential aspects of the computational techniques are provided below.

5.1.1 Explicit Time Integration

Computational economy is maintained with the use of an explicit time integration technique which incorporates single point integration of the element divergence operator. Explicit dynamic analyses reproduce accurately both the localized stress waves and the global behavior of the SE(B) specimen. The critical time step size required for stability is approximately the time required for a dilatational wave to traverse the smallest element in the finite element mesh. Thus, the mesh refinement of the finite element model determines the critical time step size and establishes two important limits: the total number of time steps required for the solution (amount of CPU time), and the maximum number of time steps (total time of the dynamic analysis) before a loss of precision occurs. The single precision storage of Spectrom–331 enforces approximately a 10 million step limit for acceptable precision. The critical time step of the refined finite element models in this study is approximately 2.2×10^{-7} seconds. Approximately 300,000 total time steps are needed to compute the 6 milli–second response.

5.1.2 J–Integral Computations

The domain form of the J–integral, extended to include inertial effects, is implemented for the computations in this study. Techniques to evaluate the volumetric integrals parallel those for the one–point Gaussian integration used to compute the element internal forces.

5.1.3 Bodner–Partom Constitutive Model

The Bodner–Partom viscoplastic constitutive model is used to represent strain rate effects on the material flow properties. The strong dependence of plastic strain rates on stresses requires an iterative technique to integrate the stiff rate equations. A new, efficient technique that minimizes the number of iterations required for convergence is described. The small time step size needed for stability of the globally explicit dynamic computations makes possible the use of a stress–updating scheme which avoids sub–incrementing of the time step. The newly developed iterative technique exhibits monotonic convergence for the materials, time steps, and strain rates of this study.

Through careful modification of the Bodner–Partom material constants, a rate–independent response for A533B steel is developed which elevates stress due to rate sensitivity by less than 2%. When used in a dynamic analysis, this material model provides the basis to examine the relative significance of strain rate effects.

5.1.4 Loading of Finite Element Models

A technique is developed to define applied loads that generate a pre–determined displacement history. An SE(B) model is first loaded by applying the desired displacement history on a finite loading area. The reactions at the displaced nodes are extracted and smoothed to generate the loading history. For computational efficiency, a relatively coarse finite element model is used to generate the applied loading for each specimen. The generated loading is then applied as a time dependent pressure on the refined model to examine the specimen's response in detail. This methodology enables comparisons of the responses for the three SE(B) specimens having different a/Ws with each specimen subjected to the same "displacement" controlled loading.

The displacement history characteristic of a drop tower test is chosen for this study. This displacement history consists of an initial phase in which deformation concentrates in the impact absorber, and a final phase in which the load–line velocity of the specimen reaches the terminal velocity of the falling tup. The resulting load–line displacement curve consists of two

173

well defined segments of constant velocity. The terminal load–line velocity of 100 in/sec (2.45 m/sec) equals the tup velocity. SE(B) specimens of high toughness material fail during the terminal phase of the load–displacement trace.

These analyses represent the first detailed examination of the 3–dimensional response of SE(B) specimens under realistic impact loadings.

5.2 Transition Time Concepts

The transition time at which the internal energy of deformation exceeds the kinetic energy occurs very early in the response while the specimen behavior is predominantly linear–elastic. Transition times obtained in this study are: 0.240×10^{-3}, 0.161×10^{-3} and 0.157×10^{-3} seconds for the deep, medium, and shallow crack respectively. (Normalized with respect to t_W, the time it takes a dilatational wave to travel the depth of the specimen, these are: 28.1, 18.9, and 18.4 respectively). Since the early response is elastic, the transition time is independent of viscoplastic effects. A single degree of freedom system models accurately the energy content of the SE(B) specimen and provides accurate estimates for the transition time.

The transition time is consistently demonstrated to be a fraction of the first elastic period of the specimen ($0.4 \times T_1$), and relatively independent of loading rate. At response times greater than $2.5 \times$ the transition time, the initial dynamic effects due to impact subside sufficiently so that static formulas predict accurately the applied J. The first elastic period provides a simple practical limit after which static formulas for J apply.

5.3 Applied Loads from Laboratory Measurements

The calculation of J using the static formula requires numerical integration of the load displacement history for an SE(B) specimen. Direct measurement of the applied load in an impact test is not generally practical. Instead, the applied load is inferred from more simply measured quantities. Three techniques to infer the load are examined: 1) measured support reactions, 2) strains measured by quarter–span gages, and 3) computed ligament moments. The first two methods can be used in laboratory settings. Assumptions of a static response are used to relate measured quantities to the applied load, i.e. 1) support reactions sum to equal the applied load, and 2) the distribution of strains at the quarter–span location is correlated to the applied load. The third method infers the dynamically applied load as the equivalent static load that produces the same ligament moment. Although the ligament moment cannot be measured in the laboratory, it is a direct indicator of crack–tip deformation.

All three methods infer well the actual applied load with maximum errors on the order of 6%. Early in the dynamic response, while the specimens are predominantly elastic, simple elastic vibrations of the SE(B) specimens produce oscillations of the inferred loads about the actual applied load. All three methods underestimate the applied load by approximately 3% during the terminal (constant velocity) stage of the response. This error is attributed to the rapid increase in the kinetic energy experienced by the specimen during the terminal stage.

For the shallow crack specimen, plastic deformation impinges on the quarter−span locations. Linearity of the strain distributions at the quarter−span locations is preserved at the specimen centerplane, while surface strains exhibit warping effects. A simple setup using strain gages mounted on top and bottom of the specimen at the centerplane provides surprisingly accurate load estimates.

5.4 Computation of *J* Using Static Formulas

Loads inferred with the three methods and the applied load are used to compute *J* values with the static formula (Eqn. 2.2−6). After the initial impact, very similar *J* values are obtained with a maximum deviation of 5%. In general, the *J* values computed with the applied load are larger than those computed from the inferred loads (which are slightly smaller).

The average (through thickness) *J* value (computed via domain integrals from the finite element models) provides the basis to evaluate the accuracy of the static formula which uses plastic work on the ligament. Published values of η_p (derived from plane−strain models) yield accurate *J* values for the deep crack specimen. For the medium and the shallow crack specimen, however, use of the plane−strain η_p values overpredict applied *J* values by 20 to 30%. Static analyses of the same specimens indicate that the errors are not due to rate sensitivity or dynamic effects, but instead are due to 3−dimensional effects.

Accurate values of *J* can be obtained by using η_p values derived from 3−dimensional static finite element models (η_p^{3d}). The computed values are: $\eta_p^{3d} = 1.91, 1.33, 0.83$, for the deep, medium and shallow crack, respectively. Maximum errors of 3%, 7%, and 18% in J are then predicted for the deep, medium and shallow crack, respectively.

An alternate form of the *J* estimation formula which uses the total work (not just the plastic component) done by the applied load (Eqn. 4.7−12), further improves the accuracy. η_t^{3d} relates the total external work to the applied *J*. The computed values for η_t^{3d} are: $\eta_t^{3d} = 1.91, 1.32$, and 0.82 for the deep, medium and shallow crack, respectively. Maximum errors of the static *J*− formula with η_t^{3d} are 3%, 4%, and 12% for the deep, medium, and shallow crack, respec-

tively. After the initially elastic response, this scheme based on total external work predicts the most accurate J values of the methods surveyed.

With η_p^{3d} and η_t^{3d} (factors derived from 3−D analyses), the simple ligament−work approach to compute J applies equally well to all analyses conducted in this study. The accuracy of this approach is independent of rate sensitivity and inertial effects.

5.5 Effects of Strain Rate Sensitivity

Strain rate sensitivity increases the applied loads by approximately 20% for all three specimen configurations. Stresses in the crack tip elements increase to levels that correspond to a strain rate of approximately $50 \sec^{-1}$. Rate sensitivity elevates the opening mode stresses 18%, 23% and 17% for the deep, medium and shallow crack specimen, respectively. In terms of $J-Q$ theory [81], rate sensitivity decreases (less negative) the amplitude of Q 25% for the medium and shallow crack specimens. For the deep crack specimen, rate sensitivity elevates the near−tip stresses above the small scale yielding solution comupted for the static yield stress.

Applied J−integral values also increase with strain rate sensitivity. The average through thickness J value is approximately 17% larger for the deep and medium crack specimens due to rate sensitivity. J increases by only 5% for the shallow crack specimen. Rate sensitivity in the shallow specimens elevates the ligament stresses sufficiently so that deformation is forced away from the crack tip which shields the crack tip from increases in J observed in the deep and medium crack specimens. Crack front variations of the pointwise J−values are independent of strain−rate effects.

Thickness average CTODs for a given specimen geometry are relatively independent of rate sensitivity. However, since the applied J values increase with rate sensitivity, the relationship between CTOD and J is affected. Rate sensitivity increases the constraint parameter m. This effect can be explained as well by the apparent increase in the yield stress that occurs with rate sensitive materials.

Rate sensitivity has no effect on the different techniques used to infer the applied load. Also, since the transition time occurs while the specimen is predominantly elastic, transition times are independent of rate effects. The computations of η_p^{3d} and the resulting simple schemes to estimate J are not affected by rate−sensitivity.

5.6 Inertial Component of J

The inertial component of the J−integral, J_3, quantifies material acceleration effects on the crack tip deformation. The term containing the material accelerations, J_{acc}, numerically

176

dominates J_3 for the analyses of this study. For most of the response, J_{acc} contributes less than 0.1% to the total J. Thus the computation of J_{acc} is unnecessary for the loading rates studied.

Early in the response, while discrete stress wave effects are predominant, J_{acc} contributes a significant amount of the total J. In particular, for times less than 0.05 milliseconds, J_{acc} is needed to obtain *domain—independence* of J. The domain dependence of J decreases with decreasing domain size. Domain—independence is observed for all domains beyond 0.05 milli—second response. This time corresponds to approximately six traversals of a dilatational wave over the width of the specimen.

The amplitude of the total applied J prior to 0.05 milli—second of response is on the order of 0.01 lb/in. This amplitude is negligible for metals, making the computation of J_{acc} unnecessary for the loading rates studied.

5.7 Inertial Effects

Three types of inertial effects are identified in this study: 1) local stress waves affect the domain independence of J up to approximately 0.1 milli—seconds response, 2) first mode oscillatory behavior of the SE(B) specimen affects the computation of J with the static formula up to approximately 3 milli—seconds response, and 3) increases in the kinetic energy of the SE(B) specimen at the end of the response affect the accuracy of the inferred loads. The local stress waves occur prior to significant deformation in the specimen, and thus do not affect the elastic—plastic fracture behavior.

Both the load—line displacements and the inferred loads are affected by the elastic oscillations. As a result, the J values computed from the static formula using these quantities also exhibit oscillatory behavior. However, the amplitude of the oscillations of J are quite small, and the static formula yields accurate results.

The inferred loads are smaller than the applied load as the specimen approaches terminal velocity. A portion of the applied work is translated into the increase in kinetic energy, and is thus not available for an increase in the specimen deformation (used to infer the load). Accurate values of J result with the static formula during this stage.

5.8 Specimen Configuration and Constraint Effects

Constraint effects in the SE(B) specimen as a function of crack depth are examined. The numerical analyses lead to the following conclusions:

177

1) The local J along the crack front decreases near the outside free surface of the specimen. This is due to the loss of constraint against plastic flow that occurs near the traction free surfaces. For the deep and medium crack specimens, the maximum local J occurs at the center-plane. For the shallow crack specimen, however, the maximum local J occurs at a distance of 10% of the specimen thickness from the outside free surface. Additional loss—of—constraint occurs in the shallow crack specimen due to plastic flow to the bottom (crack face) free surface. The variation of local J along the crack front becomes more uniform with decreasing a/W ratios. The crack front variations of opening—mode stresses, CTOD, and m also become more uniform with decreasing a/W ratio.

2) Strain rate effects elevate the near tip stresses approximately 20% for all three specimen configurations. The deep and medium crack specimens experience a 20% elevation in J, while the shallow crack specimen experiences only a 5% elevation of J. The elevated stresses in the ligament due to rate sensitivity stiffen the midsection, forcing deformation away from the crack plane. Thus the effect of rate sensitivity on J and CTOD for the shallow crack specimen is less than for the deep or medium crack specimen.

3) The deformation patterns for the deep and medium crack specimens are effectively two rigid arms rotating about the ligament plane. For this deformation pattern, the CTOD at a given load—line displacement increases with remaining ligament length. The deformation of the shallow crack specimen, however, is more beam—like; a pattern which produces a smaller CTOD than the rigid—arm—rotation deformation at the same load—line displacement. This explains the order of CTOD values obtained in this study. At a given load—line displacement, the medium crack specimen shows the largest CTOD values, followed by the deep crack specimen and finally the shallow crack specimen. (The constraint parameter m, however, decreases monotonically with a/W.)

4) Loss of constraint due to specimen geometry is also quantified through the comparison of near—tip stresses at the same global J levels. The near—tip stresses in the deep crack specimen approach those of the SSY solution which indicates a high degree of stress triaxiality. The near—tip stresses of the medium crack and shallow crack specimens, however, fall below the SSY solution by amounts approaching the yield stress of the material. This loss of stress triaxiality and, consequently, the opening mode stresses, greatly increases the applied J needed for cleavage fracture.

5.9 Recommended Directions for Future Research

Impact testing of instrumented elastic—plastic fracture specimens is the most recent effort to evaluate the behavior of structures under short duration loadings expected in blast or accident type loadings. As a result, research in this area is limited, and this study presents the first detailed investigation of the 3—dimensional behavior of different SE(B) specimens under impact loading. Further understanding of fracture behavior under impact loadings can be achieved through more detailed examination of the near—tip fields at global loading rates examined in this study.

5.9.1 Micro−Mechanical Studies for Cleavage Fracture

Dodds et. al. [30] provide a framework to predict the cleavage fracture in one geometry based on the toughness data from another. Under a large range of static loadings (in 2−dimensions), different specimen configurations exhibit self−similar principal stress contours ahead of the crack tip, even after a significant amount of plasticity has occurred. A stress−volume criteria dictates cleavage failure once the volume inside of a pre−determined principal stress contour (generally taken over the range $2.5\sigma_y$ to $3.5\sigma_y$) has reached a critical value. The micro−mechanical model postulates that this critical volume for cleavage fracture is independent of geometry and mode of loading. Dodds et. al. takes this critical volume concept further by establishing a reference from which a specimen independent J is obtained. The equivalent J that produces the critical volume in the small scale yielding solution defines the specimen independent J.

Extension of the Dodds−Anderson model for impact loading requires very detailed computation of crack−tip stress fields to obtain the principal stress contours ahead of the crack tip. Variations of the strain rates near the crack tip, and the resulting elevated viscoplastic stresses, may nullify the self−similar distribution of the principal stresses near the crack tip observed for static loading. Thus three key aspects merit attention in the extension of the micro−mechanical model to include the impact test:

1) Examination of the near tip stress fields is needed to determine if sufficient self−similarity across different specimens exists for application of the Dodds−Anderson model. Provided self−similar stress fields exist, relationships based upon the micro−mechanical model may be generated for a specific impact test, facilitating the determination of J required for cleavage fracture of shallow flaws encountered in structures under short duration loading. Once obtained, such a relationship will predict the fracture performance of different specimens from deep crack specimens that are easily tested under impact loadings, and will reduce the need to test shallow crack specimens.

2) Examination of the near tip stress fields may reveal that sufficient similarity exists with corresponding statically loaded specimens so that extension of the Dodds−Anderson model for the purpose of predicting fracture performance in impact loadings may proceed directly from static tests alone.

3) Loading rate dependence may require modification of the Dodds−Anderson model to account for the apparent increase in the yield stress at high strain rates. Alternatively, relationships may be developed that apply to ranges of loading rates.

As shown in Section 4.10, the through−thickness distributions of the opening mode stresses near the crack tip are dependent on specimen geometry. This study shows that 3−di-

179

mensional representations of stressed volumes in will not be self similar, even for static loadings. This phenomena may necessitate modifications of the equivalent stressed−volume approach that forms the basis of the Dodds−Anderson micro−mechanics model in 2−dimensions. An approach that has been reported recently treats the maximum local value of J along the crack front as the equivalent 2−dimensional plane strain value of J for the purpose of applying the micro−mechanics model [33].

5.9.2 Higher Loading Rates

The Charpy−V notch test provides an inexpensive impact method to estimate the toughness temperature curve. A small bend specimen with a 0.4 inch square cross section is notched and loaded to fracture by a swinging pendulum. The loading duration of the Charpy test is on the order of 200 μ−seconds [78,9]. The difference between the energy levels of the pendulum before and after impact with the specimen provides the total energy absorbed by the specimen. By using a pre−cracked Charpy specimen, (i.e., a sharp crack is introduced in the specimen through fatigue loading), a fracture test occurs that is an order of magnitude shorter in duration than the impact loading of much larger specimens examined in this study. The fatigue pre−crack is intended to make the dynamic stress fields resemble those of conventional statically loaded specimens.

The Charpy test is predominantly a displacement controlled loading in which the pendulum imparts a displacement history to the specimen. Computational aspects of the Charpy pre−cracked specimen involve:

1) *Method of specimen loading*: To quantify dynamic effects, modelling of the kinematic behavior of the specimen is essential. The lack of knowledge about the distribution of displacements at the loaded edge (impact edge) does not allow a displacement controlled finite element analyses. Schemes similar to those explained in Section 3.4 need to be examined so that an applied pressure load can be used to reproduce the required kinematic history.

2) η_p: For shallow flaws, the published values (based on 2−dimensional studies) of the plastic proportionality factor for use in the J estimation formula (Eqn. 2.2−6) produced unacceptably large errors in J. Possible extension of the proportionality ratio approach so that the absorbed energy as measured by the Charpy test can be directly utilized for the estimation of J should also be considered.

5.9.3 Implicit Techniques for Dynamic Analyses

Spatial refinement of the finite element meshes utilized in this study are very near the maximum levels to obtain valid results with the single precision computations used in Spec-

trom−331. These finite element meshes are not refined sufficiently for the accurate evaluation of near−tip stresses needed in micro−mechanical models. Increasing the model refinement to obtain sufficient resolution of the near−tip stress fields with explicit integration techniques will result in a small critical time step that will make the analyses computationally prohibitive.

Generation of micro−mechanical models for impact loading can proceed through the use of implicit dynamic techniques. Although implicit techniques are computationally more intensive than explicit techniques per time step, solution stability is not a function of mesh refinement and much larger time steps can be taken. For larger time steps, however, the ability to monitor discrete stress waves is lost. Since the discrete stress waves occur at times prior to plasticity development in the specimens, this is not a concern for loading rates of this study. Suitable time step sizes can then be taken that capture strain rate and global inertial effects while ignoring the stress wave effects that occur immediately after impact.

Use of implicit dynamic techniques for higher loading rates is possible provided that specimen failure occurs well beyond the time at which discrete stress waves predominate. This may allow implicit techniques to be used for Charpy specimen loadings.

References

[1]   ASTM E8–90a, Standard Test Methods of Tension Testing of Metallic Materials, *1991 Annual Book of ASTM Standards*, Section 3, Metals Test Methods and Analytical Procedures, Volume 03.01, pp. 130–145, 1991.

[2]   ASTM E616–89, Standard Terminology Relating to Fracture Testing, *1991 Annual Book of ASTM Standards*, Section 3, Metals Test Methods and Analytical Procedures, Volume 03.01, pp. 622–633, 1991.

[3]   ASTM E813, Standard Test Method for J_{Ic}, A Measure of Fracture Toughness, *1991 Annual Book of ASTM Standards*, Section 3, Metals Test Methods and Analytical Procedures, Volume 03.01, pp. 713–727, 1991.

[4]   ASTM E1152–87, Standard Test Method for Determining $J–R$ Curves, *1991 Annual Book of ASTM Standards*, Section 3, Metals Test Methods and Analytical Procedures, Volume 03.01, pp. 825–835, 1991.

[5]   ASTM E1290–89, Standard Test Method for Crack–Tip Opening Displacement (CTOD) Fracture Toughness Measurement, *1991 Annual Book of ASTM Standards*, Section 3, Metals Test Methods and Analytical Procedures, Volume 03.01, pp. 924–939, 1991.

[6]   Anderson, T. L., and Dodds, R. H., "Specimen size requirements for fracture toughness testing in the ductile–brittle transition region," *Journal of Testing and Evaluation* Vol. 19, pp. 123–134 (1991).

[7]   Anderson, T. L., *Fracture Mechanics, Fundamentals and Applications*, 1st Edition, CRC Press, Boca Raton, Florida, (1991).

[8]   Atluri, S. N., Nishioka, T., "Numerical Studies in Fracture Mechanics," *International Journal of Fracture*, Vol. 25, (1985).

[9]   Ayres, D. J., "Dynamic Plastic Analysis of Ductile Fracture – the Charpy Specimen," *International Journal of Fracture*, Vol. 12, No. 4, August (1976).

[10]   Bathe, K. J., *Finite Element Procedures in Engineering Analysis*, Prentice Hall, Inc., Englewood Cliffs, New Jersey 07632, (1982).

[11]   Belytschko, T., Ong, J. S., Liu, W. K., and Kennedy, J. M., A., et. al., "Hourglass Control in Linear and Nonlinear Problems", *Computer Methods in Applied Mechanics and Engineering*, Vol. 43, pp. 251–276, (1984).

[12]   Bennallal, A., et. al., "Validation of Structural Computation Codes in Elastoviscoplasticity", *International Journal for Numerical Methods in Engineering*, Vol. 29, pp. 1109–1130, (1990).

[13]   Bodner, S. R., and Partom, Y., "Constitutive Equations for Elastic−Viscoplastic Strain Hardening Materials," *Journal of Applied Mechanics*, Vol. 42, pp. 385−389, June (1975).

[14]   Bodner, S. R., "Review of a Unified Elastic−Viscoplastic Theory (The Bodner Equations)," Interim Scientific Report, Air Force Office of Scientific Research/NA, Building 410, Bolling A.F.B., D.C. 20332, Oct (1984).

[15]   Bodner, S. R., "Material Modeling at High Rates of Strain," *Proceedings, International Conference on Impact Loading and Dynamic Behavior of Materials*, Bremen, FRG, May (1987).

[16]   Bodner, S. R., and Chan, K. S., "Modeling of Continuum Damage for Application in Elastic−Viscoplastic Constitutive Equations," *Engineering Fracture Mechanics*, Vol. 25, Nos. 5/6, pp. 705−712, (1986).

[17]   Brocks, W., and Olschewski, J., "On J−Dominance of Crack Tip Fields in Largely Yielded 3−D Structures," *International Journal of Solids and Structures*, Vol. 22, No. 7, (1986).

[18]   Brocks, W., and Yuang, H., "Numerical Investigations on the Significance of J for Large Stable Crack Growth," *Engineering Fracture Mechanics*, Vol. 32, No. 3, (1989).

[19]   Carpenter, W. C., Read, D. T., and Dodds, R. H., "Comparison of Several Path Independent Integrals Including Plasticity Effects," *International Journal of Fracture*, Vol. 31, pp. 303−323, (1986).

[20]   Chan, K. S., Bodner, S. R., and Lindholm, U. S., "Phenomenological Modeling of Hardening and Thermal Recovery in Metals," *Journal of Engineering Materials and Technology*, Vol. 110, pp. 1−8, Jan. (1988).

[21]   Cook, R. D., Malkus, D. S., Plesha, M. E., *Concepts and Applications of Finite Element Analysis*, 3rd Edition, John Wiley and Sons, New York, New York, (1989).

[22]   de Lorenzi, H. G., "Energy Release Rate Calculations by the Finite Element Method," *Technical Information Series*, No. 82CRD205, General Electric Company, Corporate Research and Development, New York 12345, August (1982).

[23]   de Lorenzi, H. G., "On the Energy Release Rate and the J−integral for 3−D Crack Configurations," *International Journal of Fracture*, Vol. 19,(1982).

[24]   Dexter, R. J., and Chan, K. S., "Viscoplastic Characterization of A533B Steel at High Strain Rates," *Transactions of the ASME*, Vol. 112, August (1990).

[25]   Dexter, R. J., Private correspondence. August, (1990)

[26]   Dexter, R. J., Hudak, S. J. Jr., Reed, K. W., Polch, E. Z., and Kannimen, M. F., "Dynamic−Viscoplastic Analysis and Small−Specimen Experimental Methods for the study of

Fracture in A533B Steel," *Proceedings of the Forth International Conference on Numerical Methods in Fracture Mechanics*, San Antonio, Texas, March 23−27, 1987, Pineridge Press, Swansea, U.K. 1987 p. 807.

[27]   Dienes, J. K.,"On the Analysis of Rotation and Stress Rate in Deformable Bodies," *Acta Mechanica*, Vol. 32, pp. 217−232, (1979).

[28]   Dodds, R. H., and Read, D. T., "Experimental and Numerical Studies of the J−integral for a Surface Flaw," *International Journal for Fracture*, Vol. 43, pp. 47−67, (1990).

[29]   Dodds, R. H., Carpenter, W. C., and Sorem, W. A., "Numerical Evaluation of a 3−D J−integral and Comparison with Experimental Results for a 3 Pt. Bend Specimen," *Engineering Fracture Mechanics*, Vol. 29, pp. 275−285, (1988).

[30]   Dodds, R. H., and Anderson, T. L.,"Numerical Correlation of Size Effects on Elastic−Plastic Fracture Toughness (J_c) in SENB Specimens," Report to David Taylor Research Center, Department of Civil Engineering, University of Illinois at Urbana−Champaign, (1990).

[31]   Dodds, R. H., and Mark, T. Kirk.,"An Analytical and Experimental Comparison of J_I Values for Shallow Through and Part Through Surface Cracks," *Civil Engineering Studies*, Structural Research Series No. 553, UILU−ENG−90−2008, ISSN: 0069−4274, Department of Civil Engineering, University of Illinois at Urbana−Champaign, July (1990).

[32]   Dodds, R. H., and Vargas, P. M.,"Numerical Evaluation of Domain and Contour Integrals for Nonlinear Fracture Mechanics: Formulation and Implementation Aspects," *Civil Engineering Studies*, Structural Research Series No. 542, UILU−ENG−88−2006, ISSN: 0069−4274, Department of Civil Engineering, University of Illinois at Urbana−Champaign, August (1988).

[33]   Dodds, R. H., Shih, C. Fong, Anderson, L. Ted.,"Continuum and Micromechanics Treatment of Constraint in Fracture," *Civil Engineering Studies*, Structural Research Series No. 573, UILU−ENG−92−2014, ISSN: 0069−4274, Department of Civil Engineering, University of Illinois at Urbana−Champaign, November (1992).

[34]   Dodds, R. H., "Finite Element Evaluation of J parameters in 3−D," *International Journal for Fracture*, Vol. 33, pp. R7−R15, (1987).

[35]   Dodds, R. H., and Lopez, L. A., "Software Virtual Machines for Development of Finite Element Systems," *Engineering Computations*, Vol. 3, pp. 18−26, (1986).

[36]   Ewing, D. J. F., "Topics in Plane Strain Plasticity," PhD Thesis, Cambridge University, (1969).

[37]   Flanagan, D. P., and Belytchko, T., "A Uniform Strain Hexahedron and Quadrilateral with Orthogonal Hourglass Control," *International Journal for Numerical Methods in Engineering*, Vol. 17, pp. 679−706 (1981).

184

[38] Flanagan, D. P., and Belytchko, T., "Eigenvalues and Stable Time Steps for the Uniform Stress Hexahedron and Quadilateral," *Journal of Applied Mechanics*, Vol. 51, pp. 35–40, (1984).

[39] Green, A. P., and Hundy, B. B., "Inelastic Plastic Yielding in Notch Bend Tests," *Journal of the Mechanics and Physics of Solids*, Vol. 4, pp. 128–144, (1956).

[40] Grebner, H., and Strathmeier, U., "Stress Intensity Factors for Circumferential Semi-elliptical Surface Cracks in a Pipe under Thermal Loading," *Engineering Fracture Mechanics*, Vol. 22, pp. 1–7, (1985).

[41] Grebner, H., and Strathmeier, U., "Stress Intensity Factors for Circumferential Semi-elliptical Surface Cracks in a Pipe under Thermal Loading," *Engineering Fracture Mechanics*, Vol. 22, pp. 1–7, (1985).

[42] Hackett, E. M., Joyce, J. A, and Shih, C. F., "Measurement of Dynamic Fracture Toughness of Ductile Materials," Presented at the Third International Symposium on Non–Linear Fracture Mechanics, 6–8 Oct. 1986, Knoxville, Tennessee.

[43] Healy, B. E., and Dodds, R. H.,"A Large Strain Plasticity Model for Implicit Finite Element Analysis," *Computational Mechanics*, Vol. 9, pp. 95–112, (1992).

[44] Hellen, T. K., "On the Method of Virtual Crack Extension," *International Journal of Numerical Methods in Engineering*, Vol. 9, pp. 187–207, (1975).

[45] Hellen, T. K., "Numerical Post–Yield Fracture Criteria Comparisons on Plane Strain Test Specimens," *Engineering Fracture Mechanics*, Vol. 39, No. 2, pp. 269–285, (1991).

[46] Hughes, T. J. R.,"Generalization of Selective Integration Procedure to Anisotropic and Nonlinear Media", *International Journal for Numerical Methods in Engineering*, Vol. 16, pp. 1413–1418, (1980).

[47] Hutchinson, J. W., "Singular Behavior at the End of a Tensile Crack in a Hardening Material", *Journal of the Mechanics and Physics of Solids*, Vol. 16, pp. 13–31, (1968).

[48] Hutchinson, J. W., "Fundamentals of the Phenomenological Theory of Nonlinear Fracture Mechanics", *Journal of Applied Mechanics and Physics of Solids*, Vol. 50, (1983).

[49] Joyce, J. A., "Static and Dynamic J–R Curve Testing of A533B Steel Using the Key Curve Analysis Technique," *Fracture Mechanics: fourteenth Symposium*, Vol I: Theory and Analysis, ASTM STP 791, American Society for testing and materials, (1983).

[50] Joyce, J. A, and Hackett, E. M., "Dynamic J–R Curve Testing of a High Strength Steel Using the Key Curve and Multispecimen Techniques," *Fracture Mechanics: Seventeenth Volume*, ASTM STP 905, American Society for Testing and Materials, Philadelphia, PA (1986).

[51] Joyce, J. A, and Hackett, E. M., "Application of the Key Curve and Multi–Specimen Techniques to Dynamic J–R Curve Testing of Alloy Steel," U.S. Nuclear Regulation Commission NUREG/CP - 4579, April, (1986).

[52] Joyce, J. A, and Hackett, E. M., "Development of an Analytic Key Curve Approach to Drop Tower J–R Curve Measurement," U.S. Nuclear Regulation Commission NUREG/CR–4782, December, (1986).

[53] Joyce, J. A, and Hackett, E. M., "Transition Range Drop Tower J–R Curve Testing of A106 Steel," U.S. Nuclear Regulation Commission NUREG/CR–4818, February, (1987).

[54] Joyce, J. A., "Ductile to Brittle Toughness Transition Characterization of A533B Steel," U.S. Nuclear Regulation Commission NUREG/CR–5142, June, (1988).

[55] Kanninen, M. F., Dexter, R. J., Hudak, S. J., Couque, H. R., and O'Donoghue, P. E., "Viscoplastic–Dynamic Crack Propagation: Experimental and Analysis Research for Crack Arrest in Engineering Structures," *International Journal of Fracture*, Vol. 42, 1975, pp. 239–260 (1990).

[56] Kalthroff, J. F., "On the Measurement of Dynamic Fracture Toughness – a'A Review of Recent Work", *International Journal of Fracture*, Vol. 27, (1985).

[57] Key, Samuel W.,"Spectrom–331, A Finite Element Computer Program for the Large Deformation, Elastic and Inelastic, Transient Dynamic Response of Three Dimensional Solids and Structures," Topical Report RSI–0299, RE/SPEC Inc, P. O. Box 14984, Albuquerque, NM 87191, (1988).

[58] Key, Samuel W., "Hondo III, Theoretical and Users Manual, Computer Program Document," Topical Report RSI(ALO)–0194, RE/SPEC Inc, P. O. Box 14984, Albuquerque, NM 87191, (1982).

[59] Kirk, M. T., Waskey, J. P., and Dodds, R. H.,"Procedure for Drop Tower Testing of Shallow Cracked Single Edge Notched Bend Specimens," David Taylor Research Center, Ship Materials Engineering Department, Research and Development Report, Bethesda, MD DTRC–SME–90/18 July 1990.

[60] Kirk, M. T., and Dodds, R. H.,"An Analytical and Experimental Comparison of J_i–values for Shallow Through and Part–Through Surface Cracks,"*Engineering Fracture Mechanics*, Vol. 39, No. 3, pp. 535–551, (1991).

[61] Kirk, M. T., and Dodds, R. H.,"Experimental *J* Estimation Formulas for Single Edge Notch Bend Specimens Containing Mismatched Welds," *1992 ASME Symposium on Off–Shore Mechanics and Arctic Engineering,* Calvary, Canada, (1992).

[62] Kirk, M. T., and Dodds, R. H.,"Effect of Weld Mismatch on Elastic–Plastic Fracture Parameters," *Civil Engineering Studies,* Structural Research Series No. 570, UILU–

ENG–92–2008, ISSN: 0069–4274, Department of Civil Engineering, University of Illinois at Urbana–Champaign, August (1992).

[63] Kordisch, H., Sommer, E., and Schmitt, W., "The Influence of Triaxiality on Stable Crack Growth," *Nuclear Engineering and Design*, Vol. 112, (1989).

[64] Lamain, L. G., "Numerical Analysis in EPFM", *Elastic Plastic – Fracture Mechanics*, L. H., Larsson, Editor, Reidel Publishing Co. 227–261, (1985).

[65] Lee, F. Z., Shih C. F., and Needleman, A., "A Comparison of methods for calculating Energy Release Rates," *Engineering Fracture Mechanics*, Vol. 21, (1985).

[66] Levy, N., Marçal, P. V., Ostergren, W. J., and Rice, J. R., "Small Scale Yielding Near a Crack in Plane Strain: a Finite Element Analysis," *International Journal of Fracture Mechanics*, Vol. 7, pp. 143–157, (1971).

[67] Li, F. Z., Needleman, A., and C. F. Shih, "Creep Crack Growth by Grain Boundary Cavitation and Crack Growth Rates under Transient Conditions," *International Journal of Fracture*, Vol. 38, (1988).

[68] Miller, A. G., "Review of Limit Loads of Structures Containing Defects," *International Journal of Pressure Vessels and Piping*, Vol. 32, pp. 197–327, (1988).

[69] Nagtegaal, J. C., Parks, D. M., and Rice, J. R.,"On Numerically Accurate Finite Element Solutions in the Fully Plastic Range," *Computer Methods in Applied Mechanics and Engineering*, Vol. 4, pp. 153–178, (1974).

[70] Nakamura, T., Shih C. F., and Freund L. B., "Analysis of a Dynamically loaded Three–Point–Bend Ductile Fracture Specimen," *Engineering Fracture Mechanics*, Vol. 25, (1986).

[71] Nakamura, T., Shih C. F., and Freund L. B., "Elastic–Plastic Analysis of a Dynamically loaded Circumferentially Notched Round Bar," *Engineering Fracture Mechanics*, Vol. 22, (1985).

[72] Nakamura, T., Shih C. F., and Freund L. B., "Three–Dimensional Transient Analysis of a Dynamically Loaded Three–Point–Bend Ductile Fracture Specimen," Office of Naval Research ONR0365/3, September, (1986).

[73] Nakamura, T., Shih C. F., and Freund L. B., "Computational Methods Based on an Energy Integral in Dynamic Fracture," *International Journal of Fracture*, Vol. 27, (1985).

[74] Nakamura, T., "Effects of Rate–Sensitivity in Dynamically Loaded 3D Fracture Specimen," Proceedings of the 7th International Conference on Fracture (ICF7), Houston, Texas March 20–24, 1989, Vol. 1, pp. 795–802.

[75] Naus, D., et.al., "Crack–Arrest Behavior in SEN Wide Plates of Quenched and Tempered A533 Grade B Steel Tested under Nonisothermal Conditions," NUREG/

CRD–4930 (ORNL–6388), Martin Marietta Energy Systems, Inc., Oak Ridge National Laboratory, Oak Ridge, Tennessee, August, (1987).

[76] Nikishkov, G. P., Atluri, S. N., "An Equivalent Domain Integral Method for Computing Crack–Tip Integral Parameters in Non–Elastic, Thermo–Mechanical Fracture," *Engineering Fracture Mechanics*, Vol. 26, No. 6, pp. 851–867, (1987).

[77] Nikishkov, G. P., Atluri, S. N., "Calculation of Fracture Mechanics Parameters for an Arbitrary Three–Dimensional Crack by the 'Equivalent Domain Integral' Method," *International Journal for Numerical Methods*, Vol. 24, No. 6, pp. 1801–1821, (1987).

[78] Norris, D. M., Jr.,"Computer Simulation of the Charpy V–Notch Toughness Test," *Engineering Fracture Mechanics*, Vol. 11, pp. 261–274, (1979).

[79] Norton, F. H., *Creep of Steel at High Temperature*. Mcgraw–Hill, New York, 1929.

[80] O'dowd N. P., and C. F. Shih, "Family of Crack–Tip Fields Characterized by a Triaxiality Parameter: Part I – Structure of Fields," *Journal of the Mechanics and Physics of Solids*, (1990).

[81] O'dowd N. P., and C. F. Shih, "Family of Crack–Tip Fields Characterized by a Triaxiality Parameter: Part I – Fracture Applications," *Journal of the Mechanics and Physics of Solids*, (1991).

[82] Parks, D. M. "A Stiffness Derivative Finite Element Technique for Determination of Crack Tip Stress Intensity Factors," *International Journal of Fracture*, Vol. 10 pp. 487–502, (1974).

[83] Parks, D. M., and Wang, Y. Y., "Elastic–Plastic Analysis of Part–Through Surface Cracks," *Analytical, Numerical and Experimental Aspects of Three Dimensional Fracture Processes*, ASME, AMD–Vol. 91 pp. 19–32, (1988).

[84] PATRAN–II Modelling Software, PDA Engineering, 1560 Brookhollow Dr., Santa Ana, California, 92705.

[85] Rice, J. R.,"A Path–Independent Integral and the Approximate Analysis of Strain Concentration by Notches and Cracks," *Journal of Applied Mechanics*, Vol.35, pp.37 (1968).

[86] Rice, J. R., Paris, P. C., and Merkle, J. G., "Some Further Results of *J* Integral Analysis and Estimates," *ASTM STP536*, pp. 231–235, (1973).

[87] Rice, J. R., and Rosengren, G. F., "Plane Strain Deformation Near a Crack Tip in a Power Law Material", *Journal of the Mechanics and Physics of Solids*, Vol. 16, pp. 1–12, (1968).

[88] Rice, J. R., Tracey, D. M., "Computational Fracture Mechanics", *Numerical and Computer Methods in Structural Mechanics*, pp. 555–624, Academic Press, (1973).

[89]   Schmitt, W., and Kienzler, R., "The J–Integral Concept for Elastic–Plastic Material Behavior," *Engineering Fracture Mechanics*, Vol. 32, No. 3, pp 409–418, (1989).

[90]   Shih, C. F., Moran, B., and Nakamura, T., "Energy Release Rate Along a Three–Dimensional Crack Front in a Thermally Stressed Body," *International Journal of Fracture*, Vol. 30, (1986).

[91]   Shih, C. F., Moran, B., "A General Treatment of Crack Tip Contour Integrals," *International Journal of Fracture*, Vol. 35, (1987).

[92]   Shih, C. F., and German, M. D., "Requirements for a one parameter characterization of crack tip fields by the HRR singularity," *International Journal of Fracture*, Vol. 17, (1981).

[93]   Shih, C. F., "Relationships between the *J*–integral and the Crack Tip Opening Displacement for Stationary and Extending Cracks," *Journal of the Mechanics and Physics of Solids*, Vol. 29, pp. 305–326, (1981).

[94]   Sorem, W. A., "The Effect of Specimen Size and Crack Depth on the Elastic–Plastic Fracture Toughness of a Low–Strength High–Strain Hardening Steel," Ph.D. Dissertation, Unicersity of Kansas, Lawrence, Kansas, (1989).

[95]   Srawley, J., "On the Relationship of J_I to Work Done per Unit Area: 'Total,' or Component 'Due to Crack'," *International Journal of Fracture*, Vol. 12, pp. 470–474, (1976).

[96]   Sumpter, J. D. G., "J_c Determination for Shallow Notch Welded Bend Specimens," *Fatigue and Fracture of Engineering Materials and Structures*, Vol. 10, No. 6, pp. 479–493, (1987).

[97]   Tada, H., Paris, P. and Irwin, G., "The Stress Analysis of Cracks Handbook," 2nd Edition, Del. Research Corp., St. Louis, Mo. (1985).

[98]   Vargas, P. M., and Dodds, R. H., "Numerical Evaluation of Energy Release Rates," *Structural Materials, Proceedings Structural Congress '89*, Orofino, J. F., Editor, ASCE, pp. 206–215, (1989).

[99]   Yagawa, G., and Ueda, H., "Behavior of Surface Crack in Plates Subjected to Tensile Loads: Analysis based on Fully Plastic Solutions," *Nuclear Engineering and Design*, Vol. 111, pp. 189–196, (1989).

[100]   Zienkiewics, O. C., and Taylor, R. L., *The Finite Element Method*, 4th Edition, Volume 1, McGraw–Hill Book Company (UK) Limited, London, England, 1988.

INITIAL DISTRIBUTION

OUTSIDE CENTER

Copies

1   DDRE/Lib

1   CNO/OP 098T

2   OCNR
     1 1132 (Rajapakse)
     1 1132 (Vasudivan)
     1 0225
     1 432S
     1 Lib

1   NAVPGSCOL

1   USNROTCU
     NAVADMINU MIT

2   NRL
     1 Code 6380
     1 Code 6384

8   NAVSEA
     1 (SEA05M)
     1 (SEA05M2)
     1 (SEA05P)
     1 (SEA05P1)
     1 (SEA05P2)
     1 (SEA05P3)
     2 (SEA08S)

2   DTIC

5   USNRC
     1 (M. Mayfield)
     2 (Dr. S.N. Malik)
     1 (A. Hiser)
     1 (Dr. E.M. Hackett)

1   DOE, Oak Ridge

2   NIST, Boulder
     1 Lib
     1 (J. Berger)

4   NIST, Washington
     1 Lib
     1 (R. Fields)
     1 (R. DeWitt)
     1 (J.T. Fong)

1   Brown Univ.
     1 (Dr. C.F. Shih)

1   Univ. of Illinois
     1 (Dr. R.H. Dodds, Jr.)

1   Texas A&M Univ.
     1 (Dr. T.L. Anderson)

2   NASA/Langley
     1 Lib
     1 (Dr. J.C. Newman)

1   Hibbit, Karlsson and Sorenson, Inc.

CENTER DISTRIBUTION

Copies

1	0115
1	60
1	60A
1	60D
1	601
1	602
1	603
1	65
2	65.4
1	66
2	66.3
1	68.
1	68.3
5	61
1	612
1	613
12	614
5	614 (R. Link)
1	615
1	3421
1	3422

NAVSSES

1	62
1	624
1	625